UNIVERSITY OF CALIFORNIA,
IRVINE

Reliable and Energy Efficient Battery-Powered Cyber-Physical Systems

DISSERTATION

submitted in partial satisfaction of the requirements
for the degree of

DOCTOR OF PHILOSOPHY

in Computer Engineering

by

Korosh Vatanparvar

Dissertation Committee:
Associate Professor Mohammad Al Faruque, Chair
Professor Fadi Kurdahi
Professor Nikil Dutt

2018

DEDICATION

To my parents for their unbelievable sacrifices, love, and support.

TABLE OF CONTENTS

Page

LIST OF FIGURES **vii**

LIST OF TABLES **x**

ACKNOWLEDGMENTS **xi**

CURRICULUM VITAE **xii**

ABSTRACT OF THE DISSERTATION **xv**

1 Introduction and Background **1**
- 1.1 Cyber-Physical System - Electric Vehicle . . . 2
- 1.2 Energy Storage - Battery . . . 3
- 1.3 Battery and Energy Management . . . 5
- 1.4 Major Challenges and Thesis Contributions . . . 6

2 Reliable Battery Management **8**
- 2.1 Introduction and Related Work . . . 9
  - 2.1.1 Motivational Case Study . . . 10
  - 2.1.2 Problem and Research Challenges . . . 11
  - 2.1.3 Novel Contributions and Concept Review . . . 12
- 2.2 System Modeling and Estimation . . . 13
  - 2.2.1 Battery Model . . . 13
  - 2.2.2 Ultracapacitor Model . . . 16
  - 2.2.3 Hybrid Electrical Energy Storage Model . . . 17
  - 2.2.4 Active Battery Cooling System Model . . . 18
- 2.3 Thermal and Energy Management . . . 21
  - 2.3.1 Methodology Description . . . 21
  - 2.3.2 Optimization Formulation . . . 22
  - 2.3.3 Control Algorithm . . . 24
- 2.4 Experimental Results . . . 25
  - 2.4.1 Experiment Setup . . . 25
  - 2.4.2 Results and Analysis . . . 26
- 2.5 Concluding Remarks . . . 30

3 Battery-Aware Climate Control **31**
3.1 Introduction and Related Work . . . 32
3.1.1 Motivational Case Study . . . 32
3.1.2 Problem and Research Challenges . . . 35
3.1.3 Novel Contributions and Concept Review . . . 35
3.2 Electric Vehicle Modeling and Estimation . . . 37
3.2.1 Drive Profile . . . 38
3.2.2 Power Train . . . 39
3.2.3 HVAC . . . 41
3.2.4 Battery . . . 44
3.3 Battery-Aware Automotive Climate Control . . . 47
3.3.1 Methodology Description . . . 47
3.3.2 Optimization Formulation . . . 49
3.4 Experimental Results . . . 52
3.4.1 Experiment Setup . . . 52
3.4.2 Results and Analysis . . . 53
3.5 Concluding Remarks . . . 62

4 Eco-Friendly Navigation System **63**
4.1 Introduction and Related Work . . . 64
4.1.1 Motivational Case Study . . . 65
4.1.2 Problem and Research Challenges . . . 66
4.1.3 Novel Contributions and Concept Overview . . . 67
4.2 System Components . . . 68
4.2.1 Map Database . . . 69
4.2.2 Route Behavior . . . 69
4.2.3 Electric Vehicle . . . 70
4.3 Control and Optimization . . . 75
4.3.1 Routing Algorithm . . . 75
4.3.2 Route Prediction . . . 78
4.3.3 Automotive Climate Control . . . 79
4.3.4 Automotive Navigation System . . . 81
4.4 Experimental Results . . . 83
4.4.1 Experiment Setup . . . 83
4.4.2 Results and Analysis . . . 84
4.5 Concluding Remarks . . . 90

5 Drive Profile Optimization **91**
5.1 Introduction and Related Work . . . 92
5.1.1 Motivational Case Study . . . 93
5.1.2 Problem and Research Challenges . . . 95
5.1.3 Novel Contributions and Concept Review . . . 96
5.2 System Modeling and Estimation . . . 97
5.2.1 Drive Profile . . . 98
5.2.2 Power Train . . . 99

5.2.3 Battery Pack . . . 101
5.2.4 Power Grid . . . 104
5.3 Optimized Charge and Drive Management . . . 106
5.3.1 Methodology Details . . . 106
5.3.2 MILP Optimization Problem . . . 108
5.4 Experimental Results . . . 115
5.4.1 Experiment Setup . . . 115
5.4.2 Results and Analysis . . . 116
5.5 Concluding Remarks . . . 125

6 Quality-Aware Control **126**
6.1 Introduction and Related Work . . . 127
6.1.1 Motivational Case Study . . . 128
6.1.2 Problem and Research Challenges . . . 130
6.1.3 Main Contributions and Concept Review . . . 131
6.2 System Modeling and Estimation . . . 132
6.2.1 Design-Time Mathematical Modeling . . . 132
6.2.2 Dynamically Data-Driven Modeling . . . 135
6.3 ACQUA Control Design . . . 140
6.3.1 ACQUA-based Navigation System . . . 141
6.4 Experimental Results . . . 145
6.4.1 Experiment Setup . . . 145
6.4.2 Results and Analysis . . . 146
6.5 Concluding Remarks . . . 150

7 Driving Behavior Estimation **151**
7.1 Introduction and Related Work . . . 152
7.1.1 Motivational Case Study . . . 153
7.1.2 Problem and Research Challenges . . . 154
7.1.3 Main Contributions and Concept Review . . . 155
7.2 System Modeling and Estimation . . . 156
7.2.1 Electric Vehicle . . . 157
7.2.2 Driving Behavior . . . 160
7.3 Driving Behavior within Energy Management . . . 165
7.4 Experimental Results . . . 169
7.4.1 Experiment Setup . . . 169
7.4.2 Results and Analysis . . . 170
7.5 Concluding Remarks . . . 177

8 Self-Secured Control **178**
8.1 Introduction and Related Work . . . 179
8.1.1 Motivational Case Study . . . 180
8.1.2 Novel Contributions and Concept Review . . . 181
8.2 Control Loop Vulnerabilities . . . 182
8.2.1 Control Loop Design . . . 182

8.2.2 Physical System Attack . . . 183
8.2.3 Sensor Attack . . . 184
8.2.4 Vulnerable Model . . . 185
8.3 Self-Secured Control . . . 185
8.3.1 Machine Learning Architecture . . . 186
8.3.2 Training and Adjusting . . . 188
8.3.3 Anomaly Detection . . . 189
8.3.4 Recovering Prediction . . . 190
8.4 Self-Secured BMS . . . 191
8.4.1 Attack Models . . . 191
8.4.2 Integrating Novel Architecture . . . 191
8.5 Experimental Results . . . 192
8.5.1 Experiment Setup . . . 192
8.5.2 Results and Analysis . . . 192
8.6 Concluding Remarks . . . 195

Bibliography **196**

LIST OF FIGURES

Page

1.1 Contributors to EV Power Consumption 4

2.1 Battery Cells' Temperature while Driving an EV 10
2.2 Optimized Thermal and Energy Management Methodology for HEES 13
2.3 Different HEES Architectures for Battery and Ultracapacitor 18
2.4 Active Battery Cooling System Design for the Battery Pack 19
2.5 Battery Temperature Analysis for Different Methodologies 27
2.6 Illustrating TEB Preparation for HEES Using OTEM 27
2.7 Battery Lifetime Comparison for Different Methodologies and Drive Cycles . 28
2.8 Power Consumption Comparison for Different Methodologies and Drive Cycles 28

3.1 Contribution of Power Consumers in EV and ICE Vehicle 33
3.2 Range Reduction Resulted by HVAC Power Consumption 33
3.3 Battery-Aware Automotive Climate Control Methodology for EV 37
3.4 Modeling and Abstracting Driving Route as a Drive Profile 38
3.5 Road Load and Driving Forces on Vehicle 39
3.6 Scheme of a Single-Zone HVAC in Automotive 42
3.7 Control and Monitoring of Automotive Climate Control 42
3.8 Battery SoC Behavior in Terms of SoC Average and Deviation 45
3.9 Automotive Climate Control Variables and Control Inputs 47
3.10 Scheme of MPC Implemented for Battery-Aware Automotive Climate Control 48
3.11 HVAC Power Adjustment by Battery-Aware Climate Control 53
3.12 Cabin Temperature Analysis for Battery-Aware Climate Control 54
3.13 Execution Time of Optimizer at Each Time Step 55
3.14 Memory Usage of Optimizer at Each Time Step 55
3.15 Cost Analysis for Different Control Window Sizes 55
3.16 Performance Analysis for Different Control Window Sizes 56
3.17 Average HVAC Power Consumption Analysis and Improvement 57
3.18 Performance Analysis for Different Ambient Temperatures 58
3.19 Battery-Aware Climate Control Performance Versus Route Behavior 59
3.20 Cost Analysis for Different Cabin Thermal Capacitance Modeling Error Rates 60

4.1 EV Energy Analysis for Various Routes and Ambient Temperatures 64
4.2 Eco-Friendly Automotive Climate Control and Navigation System Methodology 68
4.3 Sources Used to Create the Map Database 69

4.4 Battery Cell Electrical Circuit Model 74
4.5 Flowchart of the Automotive Climate Control 80
4.6 Flowchart of the Automotive Navigation System. 82
4.7 Experimental Test Bed Hardware 83
4.8 Selected Routes by Navigation System Methodologies 85
4.9 Time-Domain Analysis of Climate Control and Navigation System Integration 86
4.10 HVAC Energy Consumption for Different Ambient Temperatures 87
4.11 EV Energy Consumption for Different Ambient Temperatures 87
4.12 Battery Capacity Loss for Different Ambient Temperatures 88

5.1 Fuel Economy Comparison Between EV and ICE Vehicle 93
5.2 Battery Capacity Loss for Various Depths of Discharge 93
5.3 Illustration of Optimized Charge and Drive Management for EV 97
5.4 System-Level EV Model Developed in AMESim Tool 99
5.5 Estimated EV Range w/ or w/o Considering the Rate-Capacity Effect 103
5.6 Battery Lifetime Cycles for Various Depths of Discharge 103
5.7 State Variables for Optimization Over a Day 109
5.8 Battery Power and Estimated Power of House Over a Day 117
5.9 Battery SoC Change Regarding the Discharging/Charging Processes 118
5.10 Analysis of Energy Consumption and Driving Time for Each Case Study . . 119
5.11 Analysis of Battery Lifetime for Each Case Study 120
5.12 Analysis of EV Charging Process and Its Influence on Power Grid 120
5.13 Analysis of EV Recharging Cost for Each Case Study 121
5.14 OCDM Scalability Analysis in Terms of Execution Time and Memory Usage 123
5.15 Battery Power and SoC During Daily and Weekly Cycles 124

6.1 Analysis of Driving Routes for Driving Time and Energy Consumption . . . 129
6.2 Abstract Illustration of Contributions in Our ACQUA Control Design for CPS 131
6.3 Modules of ACQUA-based Control Design for SUD 140
6.4 ACQUA-Based Navigation System Cooperating with EV Control Systems . 143
6.5 Model Estimation Error and Fit Model Adjustment at Run Time 146
6.6 Regression Accuracy and Fit Model Histogram 147
6.7 Best Fit Regression Models and Data Values 147
6.8 Energy Consumption vs. Control Design and Route 149
6.9 Battery Capacity Loss vs. Control Design and Route 149

7.1 Impact of Driving Behavior on EV Power Variation and Driving Range . . . 153
7.2 Context-Aware Driving Behavior Modeling and Estimation 156
7.3 RF Architecture to Predict Each of the Future Speed Values 162
7.4 FFNN Architecture to Predict Future Speed Values 163
7.5 NARX Architecture to Predict Future Speed Values 164
7.6 Portion of the Real-Life Vehicle Speed Data for Two Route Conditions . . . 169
7.7 Estimation Delay for Different Methodologies for Various Window Sizes . . . 172
7.8 Estimation Error for Different Methodologies for Various Window Sizes . . . 173
7.9 Distribution of Total Cost Improvement for Different Methodologies 173

7.10 Energy Saving, Battery Lifetime Improvement, and Cost Reduction 174
7.11 Temperature Variation when Integrating Driving Behavior Estimation 175
7.12 Impact of Estimation Window Size on Climate Control Performance 176

8.1 Examples of Different Attacks on the Control in a Compromised CPS 180
8.2 Self-Secured Machine Learning Architecture Integrated into Automotive CPS 181
8.3 Compromised Control Loop in BMS from Multiple Aspects 184
8.4 Conditional Generative Adversarial Network for Self-Secured Control 187
8.5 CGAN Generator and Discriminator Loss Function at Train-Only Phase . . 193
8.6 Discriminator Performance in Detecting DoS and Physical Attack 193
8.7 Generator Performance in Terms of Prediction Error When an Attack Happens194

LIST OF TABLES

Page

1.1 Challenges Addressed by Our Contributions in Thesis 7

2.1 Analyzing the Influence of Ultracapacitor Size in Different Methodologies . . 29

3.1 Battery-Aware Climate Control Performance for Different Drive Profiles . . . 59

4.1 Performance Analysis of Navigation System Methodologies for Different Routes 88

5.1 Specifications of the Utility Pricing Policy 105
5.2 Components Specifications for Multiple Benchmark EV 115
5.3 Driver Information Regarding Locations and Timing Preferences 116

6.1 Multiple real-life route benchmarks. 145
6.2 Complexity Analysis of Different Control Designs 148

7.1 Components Specifications of Nissan Leaf EV 160
7.2 Complexity of the Driving Behavior Estimation 171

ACKNOWLEDGMENTS

I would like to express the deepest appreciation to my committee chair, Professor Mohammad Al Faruque, who has the attitude and the substance of a genius: he continually and convincingly conveyed a spirit of adventure in regard to research and scholarship, and an excitement in regard to teaching. Without his guidance and persistent help this dissertation would not have been possible.

I would like to thank my committee members, Professor Fadi Kurdahi and Professor Nikil Dutt, for guiding and supporting me throughout these years.

I would like to give special thanks to my family for their unbelievable sacrifices, unconditional love, unstoppable support, encouraging me in all of my pursuits, and inspiring me to follow my dreams.

To all my friends and colleagues at UCI and AICPS lab, thank you for offering me advice, supporting me through this entire process, and making my graduate study an unforgettable experience, to name a few: Maral Amir, Jiang Wan, Haeseung Lee, Sujit Rokka Chhetri, Sina Faezi, Anthony Lopez, Igor Burago, and Marco Levorato.

The work reported in this dissertation was partially supported by the National Science Foundation under Grant No. ECCS 1611349. I thank IEEE and ACM for the permission to include the content of my dissertation, which portion of it was originally published in transactions and conference papers.

CURRICULUM VITAE

Korosh Vatanparvar

EDUCATION

Doctor of Philosophy in Computer Engineering **2018**
University of California, Irvine *Irvine, CA*

Master of Science in Electrical and Computer Engineering **2015**
University of California, Irvine *Irvine, CA*

Bachelor of Science in Electrical Engineering **2013**
Sharif University of Technology *Tehran, Iran*

RESEARCH EXPERIENCE

Graduate Research Assistant **2013–2018**
University of California, Irvine *Irvine, CA*

Research Scientist Intern **2017–2017**
NEC Laboratories America, Inc. *Cupertino, CA*

TEACHING EXPERIENCE

Teaching Assistant and Lecturer **2015–2018**
University of California, Irvine *Irvine, CA*

Teaching Assistant **2011–2013**
Sharif University of Technology *Tehran, Iran*

BOOK PUBLICATIONS

Control-as-a-Service in Cyber-Physical Energy Systems over Fog Computing **2017**
Fog Computing in the Internet of Things (Intelligence at the Edge), Springer

JOURNAL PUBLICATIONS

Design and Analysis of Battery-Aware Automotive Climate Control for Electric Vehicles **2018**
ACM Transactions on Embedded Computing Systems (TECS)

Extended Range Electric Vehicle with Driving Behavior Estimation in Energy Management **2018**
IEEE Transactions on Smart Grid (TSG)

Electric Vehicle Optimized Charge and Drive Management **2017**
ACM Transactions on Design Automation of Electronic Systems (TODAES)

Path to Eco-Driving: Electric Vehicle HVAC and Route Joint Optimization **2017**
IEEE Design & Test

A Security Perspective on the Battery Systems of the Internet of Things **2017**
Journal of Hardware and Systems Security, Springer

Compartmentalization-Based Design Automation Method for Power Grid **2017**
IET Cyber-Physical Systems: Theory & Applications

Application-Specific Residential Microgrid Design Methodology **2016**
ACM Transactions on Design Automation of Electronic Systems (TODAES)

Energy Management-as-a-Service Over Fog Computing Platform **2016**
IEEE Internet of Things Journal (IoT)

Design Space Exploration for the Profitability of a Rule-Based Aggregator Business Model Within Residential Microgrid **2014**
IEEE Transactions on Smart Grid (TSG)

CONFERENCE PUBLICATIONS

Battery Optimal Approach to Demand Charge Reduction in Behind-The-Meter Energy Management Systems — **Aug 2018**
IEEE Power & Energy Society General Meeting (PES GM)

ACQUA: Adaptive and Cooperative Quality-Aware Control for Automotive Cyber-Physical Systems — **Nov 2017**
ACM/IEEE International Conference on Computer-Aided Design (ICCAD)

Driving Behavior Modeling and Estimation for Battery Optimization in Electric Vehicles — **Oct 2017**
International Conference on Hardware/Software Codesign and System Synthesis (ESWEEK)

Eco-Friendly Automotive Climate Control and Navigation System for Electric Vehicles — **Apr 2016**
ACM/IEEE International Conference on Cyber-Physical Systems (ICCPS)

OTEM: Optimized Thermal and Energy Management for Hybrid Electrical Energy Storage in Electric Vehicles — **Mar 2016**
ACM/IEEE Design Automation & Test in Europe (DATE)

Modeling, analysis, and optimization of Electric Vehicle HVAC systems — **Jan 2016**
ACM/IEEE Asia and South Pacific Design Automation Conference (ASP-DAC)

Battery-Aware Energy-Optimal Electric Vehicle Driving Management — **Jul 2015**
ACM/IEEE International Symposium on Low Power Electronics and Design (ISLPED)

Battery Lifetime-Aware Automotive Climate Control for Electric Vehicles — **Jun 2015**
ACM/IEEE Design Automation Conference (DAC)

Demo abstract: Energy Management as a Service over Fog Computing Platform — **Apr 2015**
ACM/IEEE International Conference on Cyber-Physical Systems (ICCPS)

Home Energy Management as a Service over Networking Platforms — **Feb 2015**
IEEE PES Conference on Innovative Smart Grid Technologies (ISGT)

ABSTRACT OF THE DISSERTATION

Reliable and Energy Efficient Battery-Powered Cyber-Physical Systems

By

Korosh Vatanparvar

Doctor of Philosophy in Computer Engineering

University of California, Irvine, 2018

Associate Professor Mohammad Al Faruque, Chair

Cyber-Physical Systems (CPS) were presented as a solution to multidisciplinary integration and control in embedded systems. They provide seamless interactions between cyber and physical domains, enabling more intelligent and complicated control applications. However, CPS face the challenges of reliability and energy efficiency since they mainly rely on batteries for power supply. We investigate these issues with Electric Vehicles (EV) which are common battery-powered CPS. EV were introduced as a mean of transportation to address environmental problems like air and noise pollution. However, their stringent design constraints, especially on battery packs, create challenges of limited driving range and battery lifetime for daily drivers and manufacturers. Design automation community has been addressing these by developing more efficient and dependable devices and control methodologies. Our contributions in this thesis will embrace: 1) novel machine learning and physics-based modeling techniques to capture CPS dynamics more accurately; 2) unique optimization problem formulations to make optimal control decisions; and 3) intelligent control methodologies that leverage the modeling and interaction within CPS to achieve reliable and efficient operation. These contributions are applied to the systems in EV such as navigation system, climate control, and battery management system. Our objectives are to further extend the EV driving range and prolong the battery lifetime while maintaining similar driving experience and comfort for passengers.

Chapter 1

Introduction and Background

1.1 Cyber-Physical System - Electric Vehicle

Embedded systems contain dedicated computational hardware and software elements that implement monitoring and control functions responsible for multiple physical systems (e.g., mechanical or electrical). These computational elements consider the physical system behavior in order to make control decisions for the proper operation of the whole system. Advancement of technology and fabrication process have enabled production of smaller sensors and actuators [31, 65]. Adding more sensors and actuators in the control process have provided intense interactions and integrations among the computational (cyber) and the physical systems. The multidisciplinary interconnections between the physical and cyber domains have transformed embedded systems into Cyber-Physical Systems (CPS). The ultimate objective of CPS is to provide performance and efficiency improvement for the system by jointly designing the computing and control aspects [25, 156]. Interdisciplinary integrations and coordination introduced in CPS have initiated new domains of applications that are more complex and intelligent in areas as diverse as automotive, aerospace, health care, manufacturing, and transportation. For instance, development of tiny sensors, responsive actuators, and low-power microcontrollers have enabled advancement in automotive industry towards commercial production of Electric Vehicles (EV), complicated Battery Management Systems (BMS), and Advanced Driver-Assistance Systems (ADAS) [36, 38, 39, 96, 154].

On the other hand, unpredictability and indeterministic variations in the process of control and physical domains enforce robust requirements on the design of CPS. Since CPS will not be operating in a controlled and predictable environment, the requirements are more stringent than for embedded systems [81]. Furthermore, the CPS will face the challenges of reliability and energy efficiency since they mainly rely on batteries for power supply. The unpredictable availability and behavior of energy and power of the battery add uncertainty, and thereby may degrade the lifetime and efficiency of a battery-powered CPS. In this thesis, we investigate these issues with EV as an example of similar battery-powered CPS [157].

Transportation in the U.S. is mainly facilitated by roads and the vast majority of passenger trips occur by automobiles [49]. Passenger vehicles are major pollution contributors, producing significant amounts of nitrogen oxides, carbon monoxide, and other pollutants; in 2013, transportation accounted for about 27% of total U.S. greenhouse gas emissions [2]. The environmental concerns such as global warming, air pollution, and noise pollution impact the human health significantly. EV have been accepted as the most common zero-emission and sustainable mean of transportation for commercial, non-commercial, and industrial purposes in many countries [18, 32, 51, 62, 118, 128]. EV have had the potential to address the environmental issues caused by greenhouse gases and other pollutants coming from road transportation [29, 56, 91]. Moreover, governments provide incentives to promote EV deployment and proliferation and help with addressing the above-mentioned global issues [107]. Furthermore, the EV power train architecture is much simpler compared to the one in Internal Combustion Engine (ICE) vehicles. Therefore, this simplicity has benefited the drivers towards a more economical and sustainable mean of transportation even for longer terms considering maintenance [33, 92]. However, EV consumers have been demotivated by the poor driving range, high price, and troublesome recharging facing the EV [161]. Consumers have not been able to gain the trust of using EV as their daily mean of transportation.

1.2 Energy Storage - Battery

Energy storage and specifically battery is the major component in the EV providing the power. Major issues with EV have been mainly caused by the behavior of the commonly used family of lithium-ion battery cells and EV stringent constraints especially on the battery pack [34, 103, 122]. The EV pose challenges regarding trade-offs between cost and performance [33]. The cost, volume, and weight constraints in the battery pack design make them the major bottleneck restricting the amount of energy stored for driving [34, 92]. Fur-

thermore, the recharging process of the EV battery is significantly slow compared to the refueling process of ICE vehicles. Both factors influence the EV usage for daily and/or long trips causing *"range anxiety"* for the drivers [51, 78, 103, 105, 137, 147].

Besides driving range issue, the battery capacity degrades over time due to the increase in its internal resistance with every cycle of charging and discharging. In long-term, due to the special behavior of lithium-ion, the battery becomes useless after 20% of capacity loss which is considered as the battery lifetime [64, 98, 123, 152]. This creates more limitation on the driving range and introduces huge battery replacement costs for the drivers/manufacturers. Since battery production requires complex process and expensive material, the battery replacement gets sophisticated and costly which causes economic and sustainability issues [110]. For instance, the cost to replace a battery pack is more than 12,000$ for Tesla Model S 85 KWh [3] and 5,500$ for Nissan Leaf S [4]. Nevertheless, the battery pack itself costs significantly more than the above-mentioned cost.

The driving range and battery lifetime are the parameters affected by the power consumption of the EV. The power requests from the electric motor and other auxiliary systems define the battery consumption [131, 151, 158]. Figure 1.1 illustrates how much each of these systems contribute to the EV power consumption. The power and energy consumption affects the stress put on the battery, and thereby the driving range and battery lifetime. This influence becomes significant when considering the rate-capacity effect in the battery [107, 111]. In other words, the available battery capacity decreases when discharging the battery at higher rates.

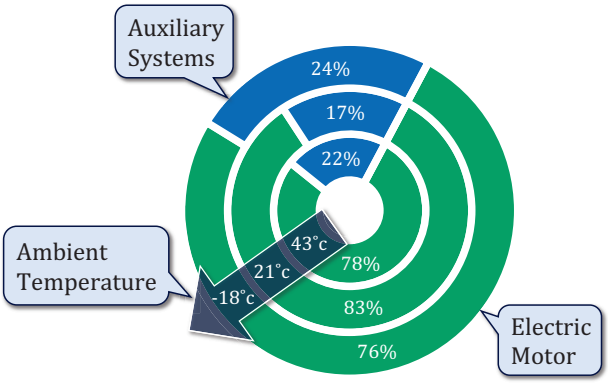

Figure 1.1: Contributors to EV power for various ambient temperatures.

1.3 Battery and Energy Management

Battery-powered CPS implement controllers to address the above-mentioned challenges with the battery while maintaining proper operation of the CPS. They are responsible to monitor system state variables and decide on control inputs. They typically utilize integrated design-time models towards their estimation, optimization, and decision making purposes. The domain of these controllers may range from device level to system level depending on their objectives [19, 139, 141, 145, 146].

For instance, at device level, a BMS observes the state of the battery cells by monitoring their temperature, voltage, and current. Based on the observed state, the BMS decides the amount of power request from each battery cell such that they are under equal load for better efficiency and longevity of operation. Furthermore, the BMS is responsible to meet the power requirements while preventing the battery cells from over charging, over discharging, over heating, and over loading [38, 90, 107, 108, 131, 147, 159]. On the other hand, at system level, controllers may monitor the state of the battery in order to schedule the load of the systems on the battery. For instance, the EV power request can be split among battery cells, ultracapacitors, or power generators in order to improve the total energy efficiency and battery lifetime while putting the battery to rest. However, the battery behavior may vary over time due to degradation and the inaccurate estimation may cause the BMS to make unreliable decision and trigger over loading or over heating the cells. Moreover, the BMS has limited knowledge of the systems utilizing the battery that may cause the BMS to operate the battery cells in an inefficient manner and degrade the operation time of the systems.

The systems such as electric motor and auxiliary systems (see Figure 1.1) are the major contributors to the battery power. Therefore, these systems will indirectly influence the energy efficiency and battery lifetime, creating trade-offs between control quality of the systems and efficiency or reliability of the battery. Control methods have been introduced to optimize the

consumption [87] of these systems given the battery state. These methods will improve the energy efficiency and battery lifetime in the EV and battery-powered CPS. Their primary element is the modeling of the multi-domain systems and implicit dependencies between them. However, the growing complexity and lack of scalability of modeling the interdisciplinary systems in CPS such as EV make the high-level management of CPS, impractical.

1.4 Major Challenges and Thesis Contributions

Previously, we discussed the main issues with battery-powered CPS especially electric vehicles in term of energy efficiency and reliability. There are state-of-the-art sophisticated controllers implemented to monitor the systems and address these issues in device level or system level. However, they pose major challenges that are listed below and will be discussed in details throughout the thesis:

1. Control systems running separately have limited flexibility of control that results in limited and non-optimal control quality of the whole system of EV.

2. Battery dynamics - energy efficiency and battery lifetime - are not considered in control systems decision making process which may put excessive load and stress on the battery.

3. Limited design-time behavioral knowledge and inaccurate future estimation of the systems dynamics restrict the quality and optimality of the control system decision.

4. Implicit trade-offs existing between different systems within a CPS like an EV are neglected which results in a limited system-level performance of the EV.

5. Lack of scalability to integrate multi-domain systems for optimizing a higher-level quality rather than the quality of individual systems.

6. Controllers lack necessary mechanisms to secure the control loop, to prevent a compromise, and to recover from the attack while maintaining the proper system operation.

We address these existing challenges facing battery-powered CPS such as EV by implementing novel modeling, machine learning, and control methodologies that improve the energy efficiency and reliability of the systems:

1. Co-scheduling the utilization of multiple systems and joint optimization of their control inputs help the CPS to achieve a better system-level control quality and performance.

2. Modeling battery behavior and dynamics and incorporating them into decision making and optimization enable the controller to consider battery lifetime and energy efficiency.

3. Machine learning and data-driven modeling that capture the behavior of the systems and provide long-term prediction to be integrated in their optimization and control without overhead.

4. Self-secured control design by leveraging a machine learning architecture that monitors the control loop and enables anomaly detection and secured recovery estimation for vulnerable control loops in CPS.

Table 1.1: Challenges addressed by our contributions in the thesis.

Contribution	Challenges	Chapters	References
1 Co-Scheduling	1, 4	2, 3, 4, 5, 6	[131, 133, 134, 135, 137, 138, 140, 147]
2 Battery Modeling	2, 3	2, 3, 4, 5	[20, 131, 133, 134, 137, 140]
3 Machine Learning	3, 4, 5	6, 7	[135, 142, 143]
4 Self-Secured Control	3, 6	8	[88]

Table 1.1 provides a high-level map of the contributions discussed in each chapter to address the above-mentioned challenges with their corresponding publications. Detailed introduction of the challenges facing the EV will be discussed in each chapter. Related work are analyzed and novel methodologies are provided to address their issues. Experimental results are provided to justify and analyze the performance of the systems and controllers in EV from every aspect.

Chapter 2

Reliable Battery Management

2.1 Introduction and Related Work

Driving range and Battery LifeTime (BLT) or operational time are major challenges in battery-powered CPS such as EV considering the stringent design constraints (see Chapter 1). Researchers have been trying to extend these operating parameters by designing more efficient materials for the batteries such as lithium-ion family, to provide more energy or power density while diminishing the battery capacity degradation rate [69, 92, 111]. On the other hand, intelligent control methodologies have been introduced to manage the battery utilization more efficiently and reliably.

Sophisticated BMS with the capability of energy management have been implemented to utilize the battery cells more efficiently by monitoring their status, while meeting the safety requirements (e.g., thermal and power limits) and preventing over charging, over discharging, and over heating [38, 90, 91, 131, 147]. Moreover, the utilization of the battery cells may get balanced by evenly distributing the power requests by the BMS in order to improve the driving range and extend the battery lifetime [38, 76, 122]. To further improve the energy efficiency, Hybrid Electrical Energy Storage (HEES) [107, 108, 158, 159] design has been introduced which comprises of batteries and ultracapacitors connected in different architectures, e.g. parallel [121] or dual [123]. In HEES design, pulsed loads may be redirected to ultracapacitors which have higher power density [121] to improve the total energy efficiency. Since the battery capacity loss is significantly dependent on the battery operating temperature, decreasing the battery temperature may reduce its capacity loss thus extending the BLT [98, 123]. Hence, HEES has been also used to alleviate the thermal issues [109] caused by the heat generated from the battery cells [123].

2.1.1 Motivational Case Study

We conduct experiments to further analyze the performance of battery thermal managements. In this case study, the ultracapacitors are used when the temperature of battery cells reaches a certain threshold [123]. Figure 2.1 illustrates the thermal management performance using an HEES for different ultracapacitor sizes. As shown in the figure, the temperature can be maintained using large ultracapacitors, however, the safe threshold for the battery cells' temperature may get violated while using smaller ultracapacitors. If the ultracapacitors' capacity is not sufficient, they will deplete before the batteries are cooled down well enough. Also, the batteries are required to recharge the ultracapacitors again, which may increase the battery temperature further than before in some circumstances. This will cause drastic battery capacity loss and decrease in BLT.

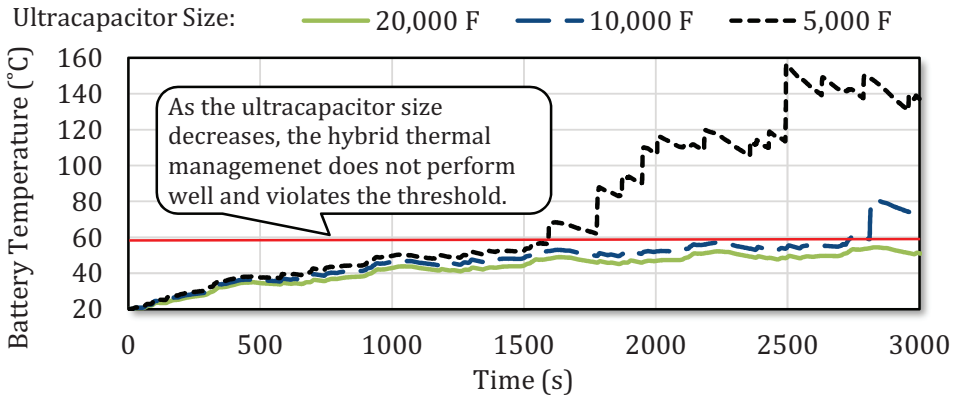

Figure 2.1: Battery cells' temperature while driving an EV simulated in ADVISOR (Advanced Vehicular Simulator) for US06 drive cycle [123, 155].

Summary and conclusion from observations: the above analysis shows that ultracapacitors may not suffice to maintain the battery temperature and may not be a reliable solution for avoiding thermal issues (unsafe states). On the other hand, adding more ultracapacitors may significantly increase the HEES cost ($\approx \$12,000$ for $20,000F$) [5], volume, and mass which are constrained during the design time [29]. Hence, having an active battery cooling system is necessary for the energy storage in order to prevent thermal violations.

Moreover, the above-mentioned energy managements and BMS have not considered the battery energy efficiency in different temperatures; it has been shown that lithium-ion battery cells have higher usable capacity in higher temperatures [6]. On the other hand, the influence of ultracapacitors' high voltage swing on the HEES energy efficiency needs to be considered; power efficiency of the DC/DC converter used for the ultracapacitors may decrease as the voltage of the ultracapacitors drop while being overused [33, 40, 108]. Knowing these characteristics will help the thermal and energy management in BMS to efficiently distribute the energy among the battery cells or ultracapacitors. Since the active battery cooling system consumes power to maintain the battery temperature, an Optimized Thermal and Energy Management (OTEM) is necessary to know when to use the active battery cooling system or the ultracapacitors such that it improves the driving range, extends the BLT, and maintains the battery temperature in the safe range [123]. Furthermore, when OTEM decides to utilize the ultracapacitors, it needs to make sure there is enough charge allocated in them. On the other hand, when OTEM decides to utilize the battery, it needs to make sure the battery is cooled enough. In this chapter, this quality metric is termed as Thermal and Energy Budget (TEB). The OTEM should provide enough TEB (i.e., pre-cool battery or pre-charge ultracapacitors) efficiently before utilizing the HEES.

2.1.2 Problem and Research Challenges

The problem of controlling the battery temperature and energy consumption for improving the driving range and battery lifetime poses the following key challenges:

1. Considering the HEES design combined with active battery cooling system for the thermal and energy management.
2. Accounting the total energy efficiency and battery lifetime while controlling the energy consumption and maintaining the temperature constraints.
3. Having an efficient and reliable methodology to avoid the thermal and energy violations while utilizing HEES.

2.1.3 Novel Contributions and Concept Review

To address the above-mentioned challenges, a novel HEES thermal and energy management methodology for improving the driving range and extending the battery lifetime is provided which employs:

1. **Hybrid Electrical Energy Storage (Section 2.2):** in which the detailed electrical and thermal characteristics of the battery, ultracapacitor, and hybrid architectures are modeled and estimated.

2. **Active Battery Cooling System (Section 2.2.4):** in which the thermal dynamics, power consumption, and influence on the battery temperature are modeled and estimated.

3. **Optimized Thermal and Energy Management (Section 2.3):** which provides enough TEB for the HEES by optimizing the utilization of different energy storage and active battery cooling system power. The controller may pre-charge the ultracapacitor or pre-cool the battery efficiently upto the perfect amount, in order to extend the BLT, improve HEES efficiency, and minimize the energy consumption while maintaining the thermal constraints. This methodology is formulated using Model Predictive Control (MPC) [28, 131] in Section 2.3.2.

Figure 2.2 further describes our optimized thermal and energy management methodology for HEES. Different architectures for HEES design and ultracapacitor sizing are analyzed in Sections 2.2 and 2.4. Although the design space exploration for the HEES and active battery cooling system in terms of size and cost [34, 50, 71] is out of the scope of this thesis, the methodology will be economical for any design variation.

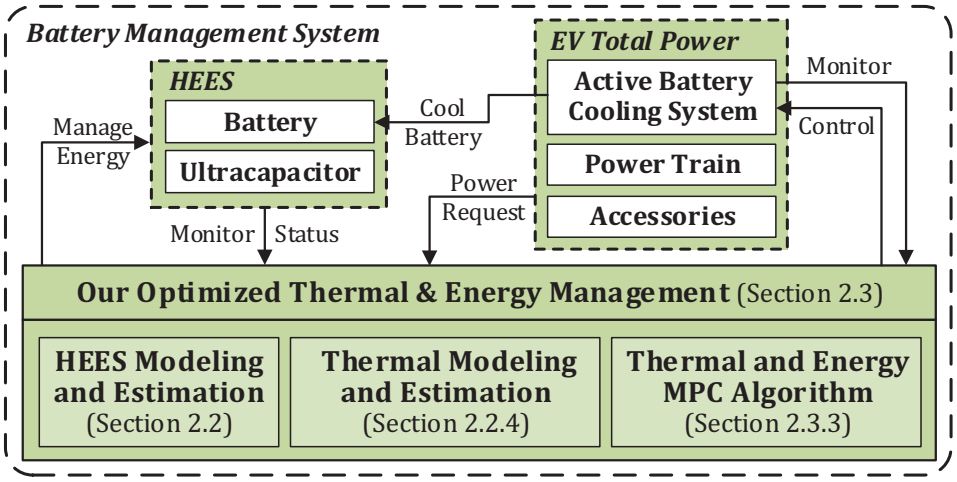

Figure 2.2: Optimized thermal and energy management methodology for HEES.

2.2 System Modeling and Estimation

More knowledge about the future will help our OTEM to provide adequate TEB and control the components efficiently. Hence, the contributing components, e.g. battery, ultracapacitor, and active battery cooling system, are modeled to provide the OTEM (see Section 2.3) with sufficient estimation of their behaviors; an EV power train and its drive cycle have been modeled in ADVISOR [155], in order to estimate the power requests from the EV. The power requests are then handled by the controller in OTEM (see Section 2.3.3). An optimized MPC algorithm will monitor and control the HEES (see Section 2.2.3) comprising of batteries (see Section 2.2.1) and ultracapacitors (see Section 2.2.2), and the active battery cooling system (see Section 2.2.4).

2.2.1 Battery Model

Battery packs are designed according to the requirements specified for each EV. Typically, EV deploy lithium-ion battery cells as their primary electrical energy storage [33]. For instance, Tesla Model S utilizes a battery pack made out of 18650A battery cells [3, 6].

Although, the electrical and thermal characteristics of these cells vary for each type, the lithium-ion battery cells used for EV (18650A), are mostly modeled as the following.

Electrical model for each battery cell is described using an equivalent electric circuit model [123]; the battery cell is modeled as a variable voltage power supply in series with an internal resistance (see Figures 2.3(a) and 2.3(b)). The ratio of the available charge to the battery capacity is represented by State-of-Charge (SoC). Open-circuit voltage (V_{OC}) of the battery (the variable voltage power supply) and the battery internal resistance (R_{bat}) depend on SoC value, which are modeled by:

$$SoC_t = SoC_0 - 100 \times \int_0^t \frac{I_{bat}}{C_{bat}} \tag{2.1}$$

$$V_{OC} = v_1 e^{v_2 SoC_t} + v_3 SoC_t^4 + v_4 SoC_t^3 + v_5 SoC_t^2 + v_6 SoC_t + v_7 \tag{2.2}$$

$$R_{bat} = r_1 e^{r_2 SoC_t} + r_3 \tag{2.3}$$

where C_{bat} is the rated battery capacity (in Ah) evaluated in nominal discharge rate [6]. I_{bat} is the current drawn from the battery. SoC_0 represents the initial SoC at time 0. v_x and r_x parameters can be empirically measured for each specific battery type [6, 123].

The energy production by a battery depends on its chemical metabolism and internal resistance which change by the operating temperature; elevated battery temperature improves the energy production by lowering the internal resistance and speeding up the chemical metabolism. This behavior is modeled as temperature-sensitive r_x parameters in Equation 2.3. The value for this parameter can be extracted from the battery manufacturer's datasheet [6].

Lithium-ion batteries generate internal heat (Q_{bat}) while charging/discharging. The heat generated is caused by the power loss due to the internal resistance or the entropy change in the ions [71, 123]. Based on the current battery utilization, the heat generated from each

battery is approximated using:

$$Q_{bat} = I_{bat}(V_{OC} - V_{bat}) + I_{bat}T_{bat}\frac{dV_{OC}}{dT_{bat}} \tag{2.4}$$

where V_{bat} is the battery terminal voltage (which may be measured under load), T_{bat} is the current battery temperature, and $\frac{dV_{OC}}{dT_{bat}}$ is a constant for approximating the entropy change influence on the heat generated. The values for these parameters can be empirically measured for each specific battery type [123]. It needs to be noted that although more detailed battery electrical model may increase behavior modeling accuracy, it will not contradict our methodology.

The internal heat generated from each battery will increase the battery temperature. A battery may be comprised of multiple materials with different density and thermal characteristics [71]. A thermal capacity variable (C_b) in a **thermal model** is used to approximate the changing temperature behavior regarding the internal heat and the convection heat from the environment, e.g. air or active battery cooling system. HEES thermal behaviors are modeled with details in Section 2.2.4.

The battery capacity degrades over time based on the battery utilization. Battery stress, number of discharge cycles, discharge current, and temperature influence the capacity loss [98]. In this chapter, the capacity loss is modeled considering the discharge current and temperature:

$$Q_{loss} = l_1 e^{-l_2/(RT_{bat})} I_{bat}^{l_3} \tag{2.5}$$

where R is the ideal gas constant. l_x parameters are the coefficients in the model that can be measured empirically [98, 123].

2.2.2 Ultracapacitor Model

Ultracapacitors are used as secondary energy storage for EV [33]. Since ultracapacitors unlike batteries do not conduct chemical reactions to provide electrical energy, they can be charged/discharged faster than batteries. Due to their higher power density, they are used in parallel with batteries to handle the high-rate pulsed load [121]. Ultracapacitors are modeled as a variable voltage power supply and an internal resistance [121] (see Figures 2.3(a) and 2.3(b)). Ratio of the available energy stored in an ultracapacitor to its energy capacity (maximum energy that can be stored - E_{cap}) is represented by State-of-Energy (SoE). The voltage across the ultracapacitor (V_{cap}) varies significantly with the SoE. The **electrical model** is described as follows:

$$E_{cap} = 1/2\ C_{cap} V_r^2 \tag{2.6}$$

$$I_{cap} = C_{cap}\ dV_{cap}/dt \tag{2.7}$$

$$V_{cap} = V_r \sqrt{SoE_t/100} \tag{2.8}$$

$$SoE_t = SoE_0 - 100 \times \int_0^t \frac{V_{cap} I_{cap}}{E_{cap}} \tag{2.9}$$

where C_{cap} is the rated capacitance [5], V_r is the rated voltage of the ultracapacitor, I_{cap} is the current drawn from the ultracapacitor. SoE_0 represents the initial SoE at time 0. Since the internal resistance of an ultracapacitor is very inconsiderable ($\approx 2.2m\Omega$), it has been omitted in the model. Also, because ultracapacitors do not generate considerable heat, we can ignore them in the **thermal model**.

2.2.3 Hybrid Electrical Energy Storage Model

HEES design is composed of multiple battery cells and ultracapacitors. There are different hybrid architectures in the literature defining the way of connecting and managing the energy storage:

1. Dual/Parallel: as shown in Figure 2.3(a), in this architecture which was recently used for thermal management in [123], two switches (S_b, S_c) are used to change the connection to the battery or the ultracapacitor. In the dual architecture, the battery and the ultracapacitor can be connected in parallel or individually to the EV (see Figure 2.3(a)). When each energy storage is connected individually to the EV, the electrical model is described using the equations defined in Sections 2.2.1 and 2.2.2. Otherwise, when they are connected in parallel, we use the following equations [123]:

$$P_l = V_l I_l \tag{2.10}$$

$$I_l = I_b + I_c \tag{2.11}$$

$$V_l = V_b - R_b I_b \tag{2.12}$$

$$V_l = V_c - R_c I_c \tag{2.13}$$

where P_l, I_l ,and V_l are the load requested by the EV, the current drawn from the HEES, and the voltage output to the load, respectively. V_b, R_b, and I_b are the open-circuit voltage, the internal resistance, and the current drawn for the total battery pack (see Section 2.2.1). V_c, R_c, and I_c are the open-circuit voltage, the internal resistance (it can be omitted), and the current drawn for the total ultracapacitor pack (see Section 2.2.2).

2. Hybrid: as shown in Figure 2.3(b), in this architecture, each energy storage is connected indirectly using a DC/DC converter to a DC bus in EV [107]. Hence, each energy storage can be independently used with the capability of energy migration and allocation [159]. This

(a) Dual/Parallel architecture.

(b) Hybrid architecture.

Figure 2.3: Different HEES architectures for battery and ultracapacitor.

architecture is mainly used for our optimized HEES thermal and energy management, since it provides the flexibility to control the utilization of each energy storage.

Performance of the DC/DC converters used for the energy storage changes for various voltages. As the voltage domain drops, the conversion efficiency decreases. Hence, the conversion efficiency is modeled as a parameter η_{DC}, which affects the power requests to the ultracapacitors, batteries, or the dual/parallel architecture. The value for this parameter can be measured empirically [40].

2.2.4 Active Battery Cooling System Model

Although the heat generated from the batteries are significantly dependent on the EV and the battery type (see Section 2.2.1), having energy-dense and high-power batteries necessitate the existence of a methodology to prevent over heating. Recently, EV utilize active battery cooling system to maintain the battery temperature in the safe range. Another approach is through constraining the battery utilization by redirecting the power to another energy storage - ultracapacitor - as in [123]. However, as shown in Section 2.1, HEES is not sufficient for preventing the battery over heating and the active battery cooling system is necessary to maintain the battery performance and reliability.

As stated in Section 2.2.1, the battery cells are connected together in parallel or series inside a battery pack (see Figure 2.4). In the existence of an active battery cooling system, the battery cells are surrounded by a flowing coolant. The coolant may be gas or liquid depending on the configuration. However, the coolant material is orthogonal to the methodology provided and may only change the parameter values for the equations, we have considered the details for the coolant as in [71]. The coolant is pumped to the battery pack using an electric motor (pump). The hot coolant returned from the battery pack is cooled down by a cooler and pumped back to the system again. Since the ultracapacitors do not generate considerable internal heat, they are not considered in the cooling system and they may be packed separately from the battery pack.

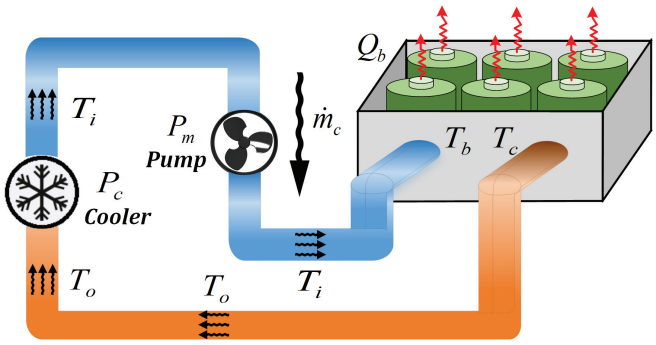

Figure 2.4: Active battery cooling system design for the battery pack.

The battery temperature (T_b) is influenced by the internal heat generated from the battery (Q_b) and the heat exchange with the coolant. Since the battery pack is completely isolated from outside, the ambient temperature does not influence the battery temperature directly. The energy balance for a battery cell is described as:

$$C_b \frac{dT_b}{dt} = h_{cb}(T_c - T_b) + Q_b \tag{2.14}$$

where C_b is the battery cell heat capacity (see Section 2.2.1), h_{cb} is the heat transfer coefficient between the coolant and the battery, and T_c is the coolant temperature in the battery pack. Hence, the battery temperature changing rate ($\frac{dT_b}{dt}$) can be evaluated using Equation 2.14.

The coolant temperature inside the battery pack (T_c) is influenced by the heat exchange with the battery cells and the coolant pumped to the battery pack. Since the battery cells are small, we can simplify the heat exchange model between the battery and coolant further without affecting the concept in this chapter. Hence, both the battery cells and the coolant are lump modeled by their heat capacity. The energy balance for the coolant is described as:

$$C_c \frac{dT_c}{dt} = h_{bc}(T_b - T_c) + C_c(T_i - T_c) \tag{2.15}$$

where C_c is the coolant heat capacity [71] and h_{bc} is the heat transfer coefficient between the coolant and the battery. Hence, the coolant temperature changing rate ($\frac{dT_c}{dt}$) can be evaluated using Equation 2.15.

The coolant returned from the battery pack is cooled down by a cooler. The cooler power consumption (P_c) is proportional to the energy difference between its inlet and outlet coolant flow. Moreover, the heat exchange among the coolant, environment air, and potential secondary coolant in the cooling system is modeled as an efficiency parameter (η_c), which is influenced by the operating conditions.

$$P_c = \frac{C_c}{\eta_c}(T_o - T_i) \tag{2.16}$$

The pump is needed for maintaining the coolant flow rate. The pump power consumption (P_m) is related to the coolant flow rate ($\dot{m}_c$). In this chapter, the coolant flow rate is considered fixed which makes the pump power consumption a constant.

2.3 Thermal and Energy Management

In the previous sections, battery (see Section 2.2.1), ultracapacitor (see Section 2.2.2), and HEES design (see Section 2.2.3) have been modeled in order to estimate their electrical and thermal characteristics, e.g., energy consumption, battery lifetime, and generated internal heat. This information is leveraged by our OTEM to maintain the battery temperature, extend the battery lifetime, reduce the energy consumption by the active battery cooling system, and improve the energy efficiency of the HEES (reducing the energy loss in battery, ultracapacitor, or DC/DC converters).

2.3.1 Methodology Description

In OTEM, based on the models of the components contributing to the system, we may predict the future state of the system for defined period of time (control window). Knowing more information about the future may help the controller to configure and utilize the system, e.g. HEES, in a more desirable and efficient way while minimizing a cost function, e.g. improve the BLT and reduce the energy consumption/loss. This method of controlling is known as Model Predictive Control (MPC) [28, 131].

The novelty of this methodology is to simultaneously consider the battery temperature, energy consumption of active battery cooling system, and energy consumed (including energy loss) in the HEES while considering the energy efficiency in different conditions. These values are estimated for a time period in future. Hence, the OTEM provides sufficient TEB before the EV power requests arrive. And, the HEES will be at the most efficient state for handling the power requests.

2.3.2 Optimization Formulation

Since the controlling is conducted in discrete time, the model equations need to be also discretized. For instance, Equation 2.15 which models the thermal behavior of the battery, is defined in discrete time as follows:

$$C_b \frac{T_b^+ - T_b}{\triangle t} = h_{cb}(\frac{T_c^+ + T_c}{2} - \frac{T_b^+ + T_b}{2}) + Q_b \tag{2.17}$$

where "+" symbol represents the value of the variable at the next time step $t + \triangle t$. Here, $\triangle t$ is the time step duration (sampling period).

EV power requests predicted by modeling the power train and driving route [107] are passed as input variables to the controller. Let P_e^t be the estimated EV power at time t. In the OTEM, let $x^{k|t}$ be the value of the state variables vector $[T_b, T_c, SoE, SoC]$, $i^{k|t}$ be the value of the controlling input variables vector $[T_i, P_{bat}, P_{cap}]$, and $u^{k|t}$ be the value of the auxiliary variables vector $[P_e, P_c, Q_{loss}, T_o, dE_{bat}, dE_{cap}]$ at time $t + k \triangle t$, predicted at time t.

The control requirements and physical restrictions state the following inequality constraints on state variables, controlling input variables, and auxiliary variables:

$$\begin{aligned}
&\boldsymbol{C1:} && \underline{T_b} \leq T_b \leq \overline{T_b} && \text{safety restrictions on battery temperature} \\
&\boldsymbol{C2:} && T_i \leq T_o && \text{cooler always decreases the temperature} \\
&\boldsymbol{C3:} && P_c \leq \overline{P_c} && \text{cooler maximum power output} \\
&\boldsymbol{C4:} && 20\% \leq SoC \leq 100\% && \text{charge restriction on battery} \\
&\boldsymbol{C5:} && 20\% \leq SoE \leq 100\% && \text{energy restriction on ultracapacitor} \\
&\boldsymbol{C6:} && P_{bat} \leq \overline{P_{bat}} && \text{battery power restriction} \\
&\boldsymbol{C7:} && P_{cap} \leq \overline{P_{cap}} && \text{ultracapacitor power restriction}
\end{aligned} \tag{2.18}$$

The discrete-time model equations, system dynamics are defined as the equality constraints (C_{eq}) for the optimization process of the controller. Moreover, initial conditions for the state variables are dictated using equality constraints. For instance, the initial value of T_b to estimate $T_b^{k+1|t}$ should be equal to $T_b^{k|t}$. $T_b^{0|t+1}$ should be equal to estimated T_b^+ at time t:

$$C_{eq}^j\left(\begin{bmatrix} x^{k|t} \\ i^{k|t} \\ u^{k|t} \\ x^{k+1|t} \end{bmatrix}\right) = 0 \qquad\qquad C^i \begin{bmatrix} x^{k|t} \\ i^{k|t} \\ u^{k|t} \\ x^{k+1|t} \end{bmatrix} \leq b^i \tag{2.19}$$

where C_{eq}^j is a non-linear function describing the equality constraints. C^i and b^i are matrices stating the linear inequality constraints.

Our OTEM mainly attempts to decrease the energy consumption by the active battery cooling system, energy consumption/loss in the HEES, and battery capacity loss. This goal is represented by the following cost function which needs to be minimized:

$$F = \sum_{\tau=t}^{t+N\triangle t} w_1(P_c \triangle t) + w_2 Q_{loss} + \ w_3(dE_{bat} + dE_{cap}) \tag{2.20}$$

where N is the MPC control window size. w_1 represents the weight for reducing the active battery cooling power consumption (P_c), w_2 represents the weight for reducing the capacity loss (Q_{loss}) in the battery in order to improve its BLT, and w_3 represents the weight for reducing the energy used from the HEES which is the sum of energy consumed/lost in the battery and the ultracapacitor. The values of these variables in the MPC control window are summed as the cost.

2.3.3 Control Algorithm

The optimized thermal and energy management system monitors and controls the components at the driving-time. Using the estimated values by the implemented models, the optimization problem (see Equation 2.19 and 2.20) is solved at each instances of time.

ALGORITHM 1: Our Optimized Thermal and Energy Management

Input: Estimated Power Request $\widehat{P_e} = \{P_e^t \mid 0 \leq t \leq T\}$
Output: Measured Capacity Lost in Battery Q_{loss}
Output: Measured Energy Consumed in HEES *Energy*
`// the total route duration`
$T =$ length $(\widehat{P_e})$
$Q_{loss} = 0$
$Energy = 0$
$N =$ control window duration
$x = N \times 4$ matrix `// state variable`
$i = N \times 3$ matrix `// control inputs`
$u = N \times 6$ matrix `// auxiliary variables`
$x^+ = N \times 4$ matrix `// state variable`
$x^0 \leftarrow [298, 298, 100, 100]$ `// initial conditions`
`// driving-time thermal and energy management`
for $t = 1$ *to* T **do**
  for $\tau = 0$ *to* $N - 1$ **do**
    $u^\tau[P_e] \leftarrow P_e^{\tau+t}$
  `// control window optimization variables`
  $z \leftarrow [x, i, u, x^+]$
  $z_{opt} =$ Optimize (z) `// call optimizer`
  `// apply control inputs & measure the states`
  $[T_b^+, T_c^+, P_c] =$ Package (z_{opt})
  $[SoC^+, SoE^+, dE_{bat}, dE_{cap}, Q_l] =$ HEES (z_{opt})
  `// accumulate the capacity loss in battery`
  $Q_{loss} \leftarrow Q_{loss} + Q_l$
  `// accumulate the energy consumed in HEES`
  $Energy \leftarrow Energy + dE_{bat} + dE_{cap}$
  $x^0[T_b] \leftarrow T_b^+$ `// next time step initial` T_b
  $x^0[T_c] \leftarrow T_c^+$ `// next time step initial` T_c
  $x^0[SoC] \leftarrow SoC^+$ `// next time step initial SoC`
  $x^0[SoE] \leftarrow SoE^+$ `// next time step initial SoE`
return $[Q_{loss}, Energy]$

Algorithm 1 is the pseudo-code representing the methodology used in our OTEM. The estimated values for EV power requests are added as vector $\widehat{P_e}$. The driving duration is

saved as T and two variables Q_{loss} and *Energy* are defined to store the values for capacity loss in battery and energy consumed in HEES, respectively (lines 1-3). The size of the control window for MPC algorithm is defined in line 4. The state variables (x, x^+), control input variables (i), and auxiliary variables (u) for the control window are defined (lines 5-8). The initial conditions for the state variables at time zero are defined in line 9. The for-loop in lines 10-22 represents the driving-time thermal and energy management. In lines 11 and 12, the estimated values for EV power requests during the control window are initialized. These state, control input, and auxiliary variables are combined in a vector as optimization variables (z) (lines 13). The optimization variables are passed to the solver to solve the optimization problem defined in Equation 2.19 and 2.20 (line 14). The optimized values will be passed to the package (containing active battery cooling system and the battery pack) for thermal management and the HEES for energy management and the outcome states are evaluated (lines 17-18). The capacity loss in the battery and energy consumed in the HEES are estimated and accumulated in Q_{loss} and *Energy*, respectively (lines 17-18). The estimated values of the state variables in this time step will be used as the initial conditions for the next time step (lines 19-22). Eventually, the values of Q_{loss} and *Energy* are returned.

2.4 Experimental Results

2.4.1 Experiment Setup

The model equations defined in Section 2.2 contain multiple parameters which are mostly defined by the real-life specifications of the system. The values of the parameters are set and adjusted so that the system dynamics are verified by the experimental data gathered from the existing references. Our OTEM methodology defined in Section 2.3 is implemented in MATLAB/Simulink [7] and the EV power consumption is estimated using ADVISOR

(Advanced Vehicular Simulator) [155]. For evaluation, we use multiple standard driving cycles [147] as the driving routes, different environment temperatures, and conduct the simulation using these two platforms.

2.4.2 Results and Analysis

We compare the performance of our optimized thermal and energy management methodology with other state-of-the-art methodologies:

1) ***Parallel Architecture [121]:*** where the simple parallel architecture (Section 2.2.3) is used in the HEES design. There is no thermal or energy management implemented.

2) ***Active Battery Cooling System [71]:*** where only battery is used as the energy storage and active battery cooling system is utilized to maintain the battery temperature in the safe range.

3) ***Dual Architecture [123]:*** where the dual architecture with switches (Section 2.2.3) is used in the HEES design in order to maintain the battery temperature by switching to ultracapacitor.

For fairness of the comparisons, all methodologies have been applied for the same system configuration, drive cycle, and physical restriction (unless otherwise specified).

a) Battery Temperature Analysis: the battery temperature has been monitored for the listed methodologies. As shown in Figure 2.5, the dual architecture methodology reacts when the battery temperature reaches a threshold, in which may not be sufficient for extending BLT. However, the OTEM attempts to decrease the battery temperature further by managing the utilization of different energy storage and the cooler in order to extend the battery lifetime.

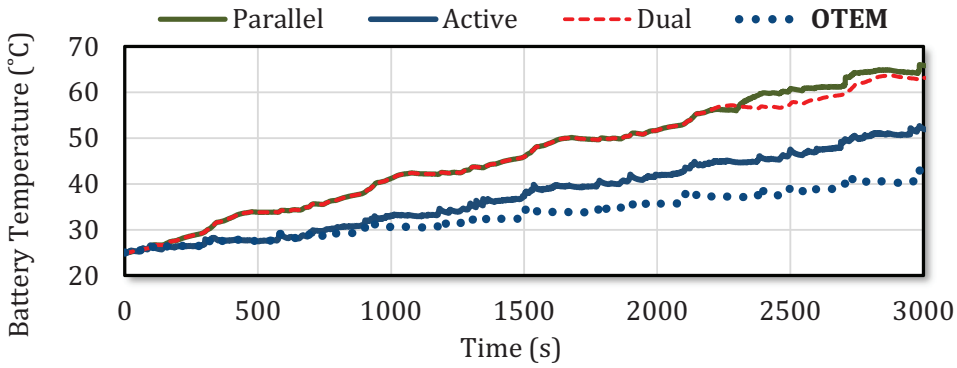

Figure 2.5: Battery temperature analysis for different methodologies.

To further analyze the OTEM methodology, we have performed the temporal analysis on the battery temperature, the ultracapacitor SoE, and the EV power requests. As shown in Figure 2.6, the OTEM provides enough TEB when it notices large EV power requests in the near-future; it allocates more charge to the ultracapacitor or cools the battery to the right amount so that the HEES stays in the most efficient state. This will decrease the capacity loss and increase the energy efficiency of the HEES. Analyses shown in Figures 2.5 and 2.6 have been done using $25,000F$ ultracapacitors and driving in US06 five times.

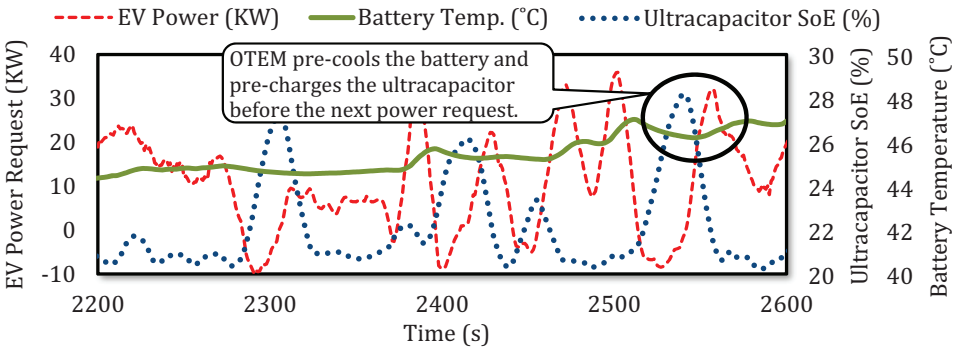

Figure 2.6: Illustrating the TEB preparation for the HEES using the OTEM.

b) Battery Lifetime Analysis: the EV has been driven for multiple drive cycles under control by different methodologies and the battery capacity loss has been monitored and compared. Figure 2.7 illustrates the ratio of the battery capacity loss in each methodology compared to the parallel architecture methodology. The OTEM decreases the capacity loss by 16.38% on average compared to the parallel architecture methodology and by 11.3% on

average compared to the dual architecture methodology. The performance of each methodology varies for different drive cycles, since the EV requires different amount of power and the battery may not get heated the same.

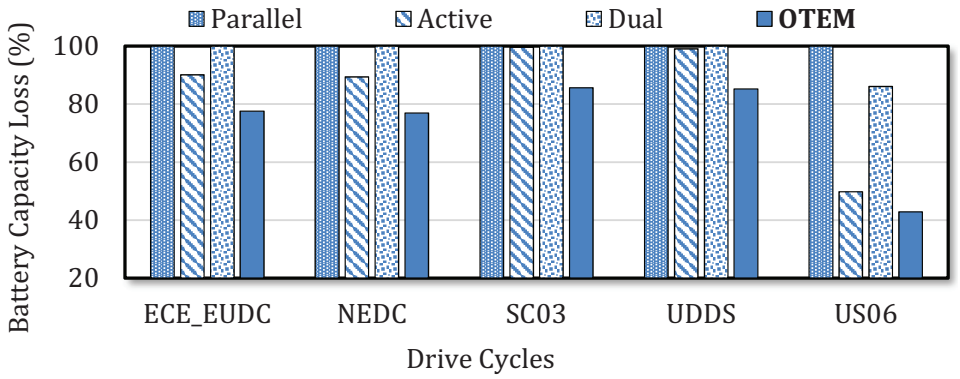

Figure 2.7: Battery lifetime comparison for different methodologies in multiple drive cycles.

c) Energy Consumption Analysis: as we have stated, the HEES energy efficiency depends significantly on the battery temperature and the ultracapacitor *SoE*. In Figure 2.8, we have compared the average power consumption of the EV and the active battery cooling system (if available). As shown in the figure, the methodologies which use active battery cooling system have consumed more energy compared to others, since they attempt to decrease the battery temperature and extend BLT by cooling. However, in the OTEM, the average power consumption has been decreased by 12.1% on average compared to the pure active battery cooling system architecture, since HEES design has also contributed.

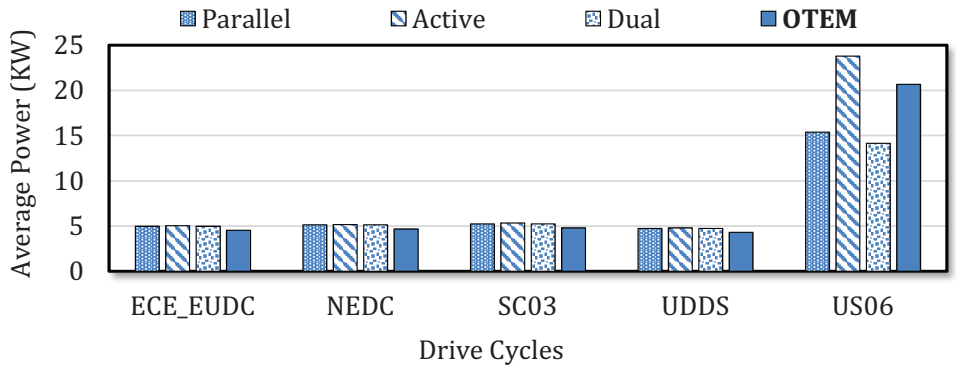

Figure 2.8: Power consumption comparison for different methodologies and drive cycles.

d) Ultracapacitor Size Analysis: in previous analyses we have considered the ultracapacitor size fixed ($25,000F$). However, the HEES efficiency and the methodologies' performance may vary significantly based on the ultracapacitor size. In Table 2.1, we have illustrated the average power consumption and the capacity loss (compared to the parallel architecture using $25,000F$ ultracapacitor) for different ultracapacitor sizes controlled by different methodologies. The experiment has been done using the US06 drive cycle, since it is a highly power consuming drive cycle. The table shows that, by decreasing the ultracapacitor size, the average power consumption increases significantly in parallel and dual architectures. Also, the capacity loss while using the dual architecture increases by decreasing the size, since the methodology significantly depends on the ultracapacitor size. In the OTEM, the increase in the ultracapacitor size will help the efficiency of the HEES and the OTEM performance. However, since the OTEM has the flexibility of using active battery cooling system, it is not much dependent on the ultracapacitor size.

Table 2.1: Analyzing the influence of ultracapacitor size in different methodologies.

Ultracapacitor Sizes	Average Power (W)			Capacity Loss (%)		
	Parallel	Dual	**OTEM**	Parallel	Dual	**OTEM**
5,000 F	16,919	15,239	22,391	175.24	85.53	49.03
10,000 F	16,893	14,381	22,274	136.02	82.84	48.61
20,000 F	16,856	13,891	21,094	107.21	78.30	44.40
25,000 F	16,846	14,156	20,662	100.00	84.70	42.85

2.5 Concluding Remarks

In literature, active battery cooling system or HEES has been considered as solutions to address the thermal issues influencing the battery performance and longevity. However, active battery cooling system alone may not be efficient for improving the EV driving range. Moreover, the HEES alone is an unreliable and costly solution to maintain the battery temperature in the safe zone, which is highly dependent on the ultracapacitor size. Hence, in this chapter, we have integrated both the solutions and implemented an OTEM methodology that provides optimized TEB for the HEES before handling the power requests; it may pre-charge the ultracapacitor or pre-cool the battery to put the HEES in the most efficient state. Our methodology demonstrates significant improvement in BLT (on average 16.8%) and average power consumption (on average 12.1% reduction) compared to the state-of-the-art methodologies. We have also shown that the decrease in the ultracapacitor size, which is preferable for HEES design, may not influence the OTEM performance.

Chapter 3

Battery-Aware Climate Control

3.1 Introduction and Related Work

EV as a whole CPS contain multiple physical systems that are governed by cyber systems or controllers. For instance, we observed that the battery cells can be directly monitored and controlled by BMS (see Chapter 2). However, there are physical systems that their behavior indirectly depends on operation of other systems. In particular, the battery utilization is defined by the power requests from the whole EV in which the electric motor (engine) is the main continual contributor [45]. The electric motor power consumption/generation is mainly influenced by the route and driving behavior [63, 147]. However, the power requests are not only defined by the electric motor. For instance, other high-load components like Heating, Ventilation, and Air Conditioning (HVAC) system may also affect the battery utilization [20, 70, 131, 140]. The HVAC system power consumption is mainly influenced by the cabin temperature and outside weather. To further demonstrate these characteristics, we look into the following motivational example (see Figure 4.1).

3.1.1 Motivational Case Study

The electric motor is the major component that provides the required force for propelling the EV. The energy goes to overcoming the driving forces on the EV (for details see Section 3.2.2). Moreover, the electric motor may generate power in the regenerative mode while decelerating the EV [107]. On the other hand, the accessory systems comprise of the Heating, Ventilation, and Air Conditioning (HVAC) system and other computing, communication, and entertainment devices in the vehicle. The HVAC system is the major consumer among the accessories (see Figure 3.1). The heating coils, cooling coils, and fans in the HVAC system consume power according to their architecture design, control target, and the ambient temperature (for details see Section 3.2.3) [131, 140]. For instance in ICE vehicles, the heat generated from the combustion engine is utilized to heat the supply air to the cabin.

While in EV, negligible heat is generated by the electric motor and is not sufficient enough to heat the supply air. Hence, electric heating coils are necessary as well for heating which increase the power consumption further (up to 21% of total power consumption), compared to the ICE vehicles (see Figure 3.1).

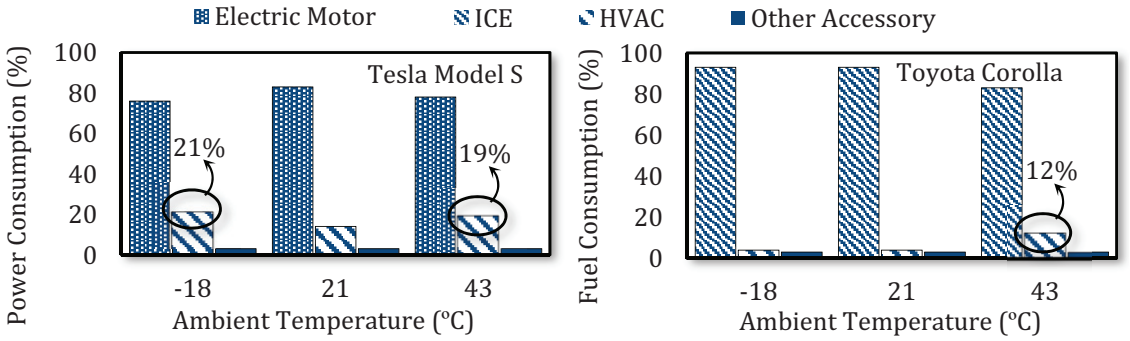

Figure 3.1: Contribution of three types of power consumers in EV [3] and ICE vehicle [77] for different ambient temperatures [131, 140].

As shown in the figure, the influence of the HVAC system on the battery in EV can be more significant than on the fuel consumption in ICE vehicles, especially in severe weathers. This becomes more challenging considering the limited energy available in a battery of an EV. The amount of the power consumption by the HVAC system results in further driving range reduction by up to 13% in cold weather as shown in Figure 3.2.

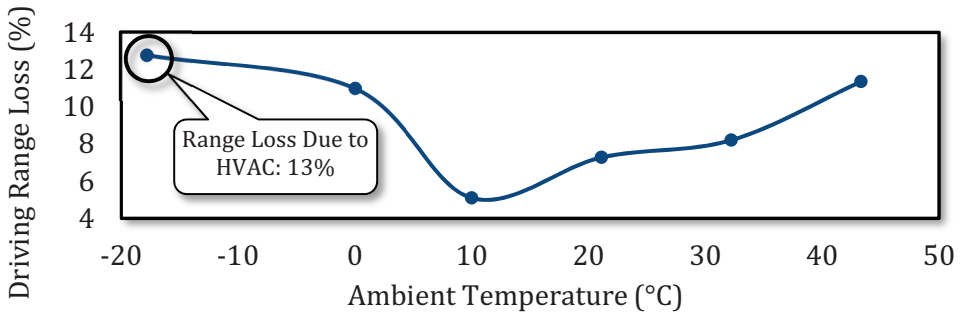

Figure 3.2: Range reduction resulted by HVAC power consumption [20].

Summary and conclusion from observations: primarily, the electric motor power consumption is defined by the driving behavior and route. Although the electric motor power consumption can be optimized by adjusting the driving behavior and route, it is not flexible

within the EV itself. However, the analysis explained above illustrates that the HVAC system has flexible and large power consumption; the power consumption can be controlled by adjusting the control parameters such as cooling/heating temperature, and fan speed [131]. These HVAC control parameters are mainly adjusted according to the cabin temperature. Managing the limited energy in the battery of an EV is problematic and the HVAC system is a major factor impacting the battery. Hence, it becomes the challenge of how to reduce the influence of the HVAC on the battery behavior (battery lifetime and energy consumption) without losing the thermal comfort for the passengers. By looking into the relationships between HVAC, EV power, and battery characteristics, the flexibility of the HVAC system in terms of its power consumption can be beneficial in reducing these impacts by controlling its inputs while being aware of the battery behavior and the EV power consumption.

Automotive climate controls are responsible for monitoring and controlling the HVAC system. The main objective of the control has been to maintain the passenger thermal comfort[1] [20, 89, 131]. There are various automotive climate controls and HVAC system designs in the literature with different performances in terms of energy consumption and thermal comfort maintenance for the passengers. They may implement different control algorithms, e.g., on-off controller, feedback control, Proportional-Integrator-Derivative (PID), Linear-Quadratic Regulator (LQR), and Model Predictive Control (MPC) [59, 86, 107]. Some of the automotive climate controls attempt to provide uniform thermal environment for the passengers by maintaining the whole cabin temperature (single-zone). While, other methodologies maintain the temperature in multiple zones of the cabin separately providing higher thermal comfort for the passengers (multi-zone). In these methodologies, multiple variables, e.g. the cabin temperature, ambient temperature, and solar radiation, may be monitored and the HVAC system is controlled accordingly to cool/heat the cabin [20]. They only consider

[1]The modeling of the passenger thermal comfort is important to the automotive climate control design, however, the details of the modeling is out of the scope of this thesis. Moreover, the thermal comfort modeling approach is orthogonal to our methodology. Hence, temperature deviation from the target temperature is considered as a metric for thermal comfort (see Section 3.3.2).

the behavior of the HVAC system (e.g. cabin and environment thermodynamics) during their operation. However, they may also be capable of rejecting the disturbance caused by the environment (e.g., solar radiation). Moreover, in these classical methodologies, the control parameters are set based on the design-time thermal loads and are not adaptive to the environmental factors.

On the other hand, the BMS do not consider the influence of the automotive climate control which controls the HVAC system - a flexible and large power consumer - on the battery behavior. Moreover, the automotive climate control does not account the battery operation behavior, e.g. driving range and battery lifetime, into the HVAC system control.

3.1.2 Problem and Research Challenges

In summary, the problem of designing an automotive climate control in EV to improve the battery lifetime and driving range poses the following challenges:

1. Accounting the influence of the detailed HVAC load besides the electric motor on the battery operation behavior, e.g. driving range and battery lifetime.
2. Considering and integrating the battery behavior in the automotive climate control while managing the HVAC.
3. Applicability and scalability of the battery-aware automotive climate control ensuring the passenger thermal comfort for any driving route and weather.

3.1.3 Novel Contributions and Concept Review

To address the above-mentioned challenges, we propose a novel methodology of battery-aware automotive climate control which employs:

1. **EV Modeling and Estimation (Section 3.2):** dynamic behavior of the EV components is described, modeled, and estimated:

   - **Drive Profile (Section 3.2.1):** behavior of the EV driving route is described. The drive profile models the driving speed, acceleration, and route slope.
   - **Power Train (Section 3.2.2):** power consumption/generation of the electric motor which provides the propelling force for the EV or regenerate power is modeled and estimated by considering the driving forces.
   - **HVAC System (Section 3.2.3):** thermodynamics and power consumption of the HVAC system and the automotive climate control are modeled and estimated.
   - **Battery (Section 3.2.4):** battery behavior such as rate-capacity effect and battery lifetime regarding the power request by the EV is modeled and estimated.

2. **Battery-Aware Automotive Climate Control (Section 3.3):** our novel methodology estimates the battery behavior and takes it into consideration for controlling the HVAC system in order to improve the driving range and extend the battery lifetime while ensuring the passenger thermal comfort:

   - Predicting and optimizing the system state variables in the near-future control window (receding horizon) using a Model Predictive Control (MPC) algorithm.
   - Ensuring the passenger thermal comfort by predicting and maintaining the cabin temperature in a convenient range around a target temperature.

3. **Experiment, Exploration, and Analysis of Methodology (Section 3.4):** the performance of the methodology in terms of execution time, memory usage, improvement on the battery lifetime, and energy consumption has been measured and analyzed for various conditions and has been compared to the state-of-the-art methodology:

   - Availability of the predicted data in the near-future in terms of the control window size, e.g. number of estimated states and time duration of the each predicted state.

- Environment factors such as the driving route and ambient temperature.
- Modeling and estimation error of the HVAC system as the physical plant.

As shown in Figure 3.3, our novel methodology of automotive climate control for EV considers the battery behavior such as driving range and battery lifetime while monitoring and controlling the HVAC system. The drive profile is utilized to describe and model the driving route (Section 3.2.1). The power consumption of the EV power train is then modeled and predicted for the input drive profile (Section 3.2.2). Moreover, the HVAC system state variables such as cabin temperature and the power consumption are modeled and estimated (Section 3.2.3). Finally, the total EV power request is evaluated and used for battery energy consumption and battery lifetime estimation. These EV state variables are estimated and optimized for better driving range and battery lifetime. Eventually, the optimal control inputs are applied to the HVAC system.

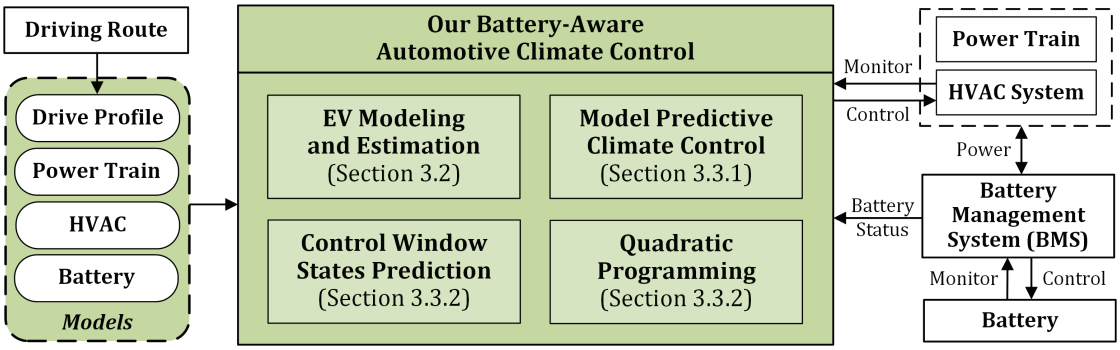

Figure 3.3: Our novel battery-aware automotive climate control methodology for EV.

3.2 Electric Vehicle Modeling and Estimation

In our novel methodology of battery-aware automotive climate control, modeling of the EV components are required to estimate the dynamics of the power train, HVAC system, and battery operation. (Non-)linear and Ordinary Differential Equations (ODE) are utilized in order to describe the dynamic behavior of these components.

3.2.1 Drive Profile

The driving route is a factor influencing the power consumption of the electric motor in the power train[2]. The estimation of the driving route is required for predicting the power consumption and our automotive climate control near-future optimization.

A driving route is modeled and termed as a *drive profile* in this chapter. A drive profile encapsulates the behavior of the driving route at each time instance. The drive profile contains the information about 1) velocity, 2) acceleration, 3) road slope, and 4) time step, for each route segment (see Figure 3.4). The route segments may have uniform or non-uniform time steps according to the abstracting and modeling level.

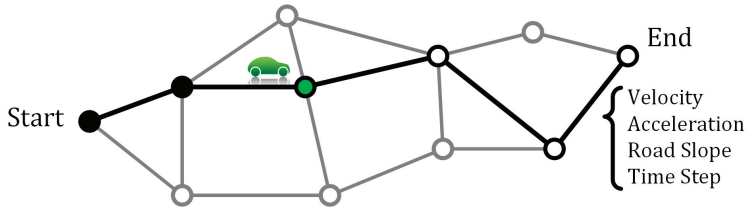

Figure 3.4: Modeling and abstracting the driving route as a drive profile.

Nowadays, navigation systems are the common method of finding the route to the destination. The driving route may be estimated by utilizing the map databases of the navigation systems [8, 147]. The map databases may represent an abstracted version (model) of the geographical map of the surrounding area using graphs (see Figure 3.4). Hence, the selected route by the navigation system can be modeled and abstracted as a drive profile for our battery-aware automotive climate control using this graph. There also exist other algorithms that are capable of predicting the driving route behavior with various performances for the purposes of navigation and safety that can be utilized [82, 83, 137, 142, 143, 147].

[2]The power consumption of the electric motor is dependent on the driving behavior. However, estimating the driver behavior on route is out of the scope of this chapter (it will be further discussed in Chapter 7). Hence, the driving route is only considered for estimating the power consumption which might be sufficient for adjusting the HVAC utilization.

Moreover, multiple standard drive cycles are created by United States Environmental Protection Agency (EPA) or United Nations Economic Commission for Europe (ECE) for experimenting and testing the performance of the vehicles in terms of fuel/energy consumption, air pollution, etc. Therefore, these standard drive cycles can also be used as the drive profiles for modeling the typical driving routes [9, 14, 147].

3.2.2 Power Train

The power train which contains the electric motor is the major power consumer in EV. It is responsible for generating the required power and driving force using the electric motor and transferring it to the wheels.

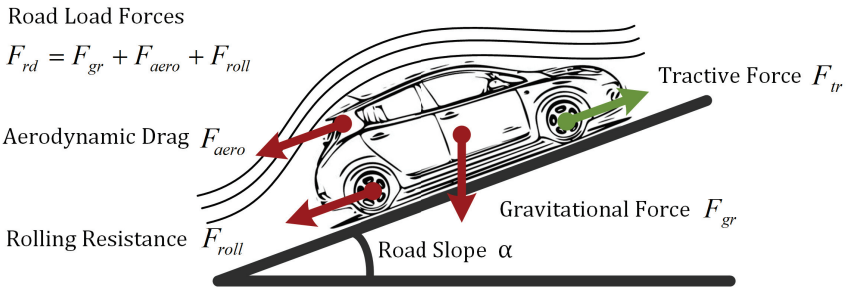

Figure 3.5: Road load and driving forces on vehicle.

The tractive force (F_{tr}) provided by the power train overcomes the road load force (F_{rd}) imposed on the vehicle. It propels the vehicle forward at a desired speed and acceleration [117]. F_{rd} consists of the aerodynamic drag, the gravitational force, and the rolling resistance (see Figure 3.5).

$$F_{rd} = F_{gr} + F_{aero} + F_{roll} \tag{3.1}$$

The aerodynamic drag (F_{aero}) is the viscous resistance of the air working against the vehicle motion which is quadratically proportional to the vehicle speed (v).

$$F_{aero} = \frac{1}{2}\rho_{air} C_x A \left(v + v_{wind}\right)^2 \tag{3.2}$$

where ρ_{air} is the air density, C_x is the aerodynamic drag coefficient, A is the effective frontal area of the vehicle, and v_{wind} is the head-wind velocity.

The gravitational force (F_{gr}) is the force caused by the gravity and is mainly dependent on the road slope.

$$F_{gr} = mg \sin\left(\arctan\left(\frac{\alpha}{100}\right)\right) \tag{3.3}$$

where m is the total mass of the vehicle, g is the gravitational acceleration constant, and α is the percentage of the road slope; 100% represents the slope of 45°.

The rolling resistance (F_{roll}) is produced by the flattening of the tire at the contact surface of the road.

$$F_{roll} = mg\left(c_0 + c_1 v^2\right) \tag{3.4}$$

where c_0 and c_1 are the rolling resistance coefficients.

F_{tr} is generated by the electric motor to overcome F_{rd} so that the vehicle maintains the desired acceleration (a) and speed.

$$F_{tr} = F_{rd} + ma \tag{3.5}$$

When F_{rd} is positive and the speed needs to be maintained, the vehicle should provide enough forward force to prevent deceleration. In this case, the force is generated only by the electric motor (F_{tr}). On the other hand, when F_{rd} is negative and the speed needs to be maintained, the vehicle needs to provide backward force to prevent acceleration. In this case, the force

may be generated by the electric motor and the braking system. The later force generated by the electric motor is due to the regenerative mode ($F_{tr} < 0$), is limited to F_{min}, and may not provide enough backward force to neutralize the resistive force (Equation 3.6). Therefore, the rest of the backward force is generated by the braking pads (Equation 3.7).

$$F_{tr} = max\,(\,F_{min}\,,\,F_{tot}\,) \quad (N) \tag{3.6}$$

$$F_{brake} = F_{tr} - F_{tot} \quad (N) \tag{3.7}$$

The electric motor power (P_e) is calculated based on the tractive force and speed.

$$P_e = \frac{F_{tr} v}{\eta_m} \tag{3.8}$$

where η_m represents the electric motor efficiency when converting electrical to mechanical energy in the motor mode and converting mechanical to electrical energy in the regenerative mode (regenerative brake). η_m is dependent on the motor rotational speed and the generated torque [86, 93, 162, 162].

In this chapter, the specifications for the EV Nissan Leaf S have been used to validate the power train model and to demonstrate the EV power consumption behavior while driving [131]. The parameters regarding the specifications are extracted from the manufacturers' forums and experimental data provided by the third-parties testing the vehicles [4, 63].

3.2.3 HVAC

The HVAC in modern vehicles mainly uses the Variable Air Volume (VAV) system [67]. The advantage of this system is the precise control of the temperature and humidity in multi-zone or single-zone with lower energy consumption [67]. The HVAC structure [101, 130] in

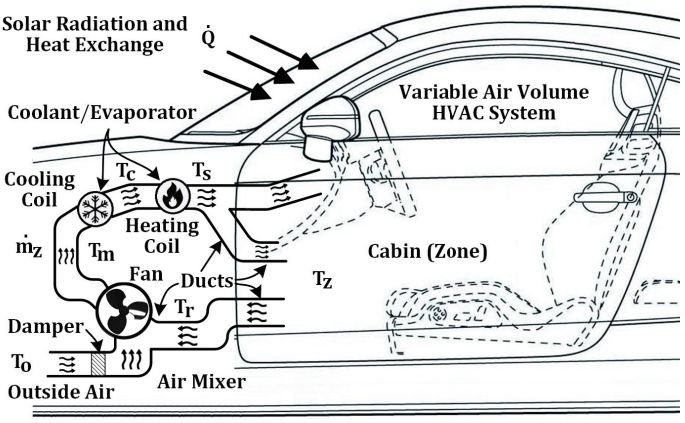

Figure 3.6: Scheme of a single-zone HVAC in an automotive [131].

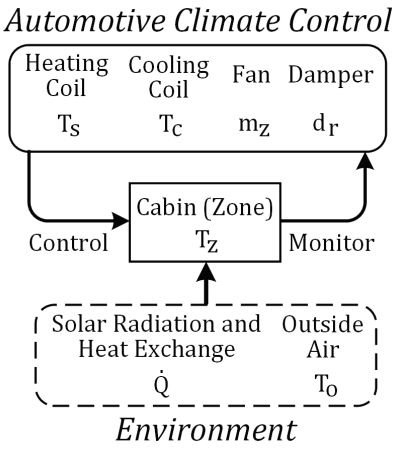

Figure 3.7: Control and monitoring of an automotive climate control.

an EV is depicted in Figure 3.6. The system contains a variable-speed fan to provide the supply air to the zone(s). A valve damper is used to control the mix of the outside air and the recirculated air back into the system. The cooler and the heater will control the air temperature by exchanging heat. In this chapter, we assume a single-zone HVAC and model the corresponding behavior and dynamics in different parts of the system using low-order ODEs. Despite the simplicity (compared to higher-order thermodynamic equations), the model provides sufficient information for analyzing the transient behavior of the system. The humidity can be an important factor affecting the HVAC power consumption, but it is not typically directly measured or controlled [73]. Therefore, in this chapter, the temperature represents an equivalent dry air temperature at which the dry air has the same specific enthalpy as the actual moist air mixture.

As shown in Figure 3.7, the state-of-the-art automotive climate control methodologies monitor the cabin (zone) temperature and adjust the controlling inputs of the system such as heating coils, cooling coils, fan, and damper valves. Moreover, the temperature inside the cabin (T_z) is influenced by the supply air (T_s) to the cabin, the heat exchange with outside, and the solar radiation. The energy balance in the cabin model is described as:

$$M_c \frac{dT_z}{dt} = \dot{Q} + \dot{m}_z c_p (T_s - T_z) \tag{3.9}$$

where M_c is the thermal capacitance of the air, wall, and the seats inside the cabin and c_p is the heat capacity of the air. The cabin temperature changing rate ($\frac{dT_z}{dt}$) is also controlled by the air flow rate into the cabin ($\dot{m}_z$).

The exchanged heat with outside and the solar radiation are modeled as thermal loads $\dot{Q}$:

$$\dot{Q} = \dot{Q}_{solar} + c_x A_x (T_o - T_z) \tag{3.10}$$

where the solar radiation ($\dot{Q}_{solar}$) and outside temperature (T_o) are time-varying factors. The values of T_o and $\dot{Q}_{solar}$ are assumed to be constant during driving (ambient temperature and thermal load offset). The heat exchange through the walls with outside is proportional to the difference between T_z and T_o, the heat exchange coefficient c_x, and the area separating the cabin and outside (A_x).

The air returned from the cabin is mixed with the outside air and recirculated back to the system. The fraction of the returned air from the cabin is d_r, which is controlled by a damper. Then, the energy balance in the air mixer gives the temperature of the system inlet air (T_m) as following:

$$T_m = (1 - d_r) T_o + d_r T_r \tag{3.11}$$

where T_r is the returned air temperature which is as same as the cabin temperature (T_z) in a single-zone HVAC.

We consider the cooling and heating coil power consumption in terms of the energy difference between their inlet and outlet air flow. Moreover, the heat exchange between the

coolant/evaporator and air is modeled as efficiency parameters:

$$P_h = \frac{c_p}{\eta_h}\dot{m}_z(T_s - T_c) \tag{3.12}$$

$$P_c = \frac{c_p}{\eta_c}\dot{m}_z(T_m - T_c) \tag{3.13}$$

where P_c and P_h are cooling coil and heating coil power consumption, respectively. η_h and η_c are the efficiency parameters describing the operating characteristics of the heating and cooling processes. T_c is the temperature of the cooling coil outlet air.

The fan power consumption (P_f) is quadratically related to $\dot{m}_z$.

$$P_f = k_f(\dot{m}_z)^2 \tag{3.14}$$

where k_f is a parameter that captures the fan efficiency and the duct pressure losses.

The parameters for the HVAC model have been extracted from the HVAC specifications provided in the literature [101, 130, 131] and to accurately match the thermodynamic behavior of an HVAC system similar to the Nissan Leaf in different conditions [66, 77].

3.2.4 Battery

Lithium-ion batteries are widely used as the primary electrical energy storage [90, 92, 122] in the EV. Despite their high energy density, they have specific characteristics. They demonstrate less usable capacity in higher discharge rates (rate-capacity effect). This characteristic is described using the Peukert's Law [38, 48, 107, 148]. Therefore, the battery SoC which shows the available charge in the battery can be estimated by having the battery current [106].

$$SoC^{t} = SoC^{0} - 100 \times \int_{0}^{t} \frac{I_{eff}}{C_n}\, dt \tag{3.15}$$

$$I_{eff} = I \left(\frac{I}{I_n}\right)^{pc-1} \tag{3.16}$$

where C_n is the nominal capacity of the battery measured at the nominal current (I_n) predefined by the battery manufacturer. I_{eff} represents the effective current draining the chemical energy. pc is the Peukert's constant typically measured empirically for the type of the battery cell [48, 148]. SoC^{t} represents the SoC at time t.

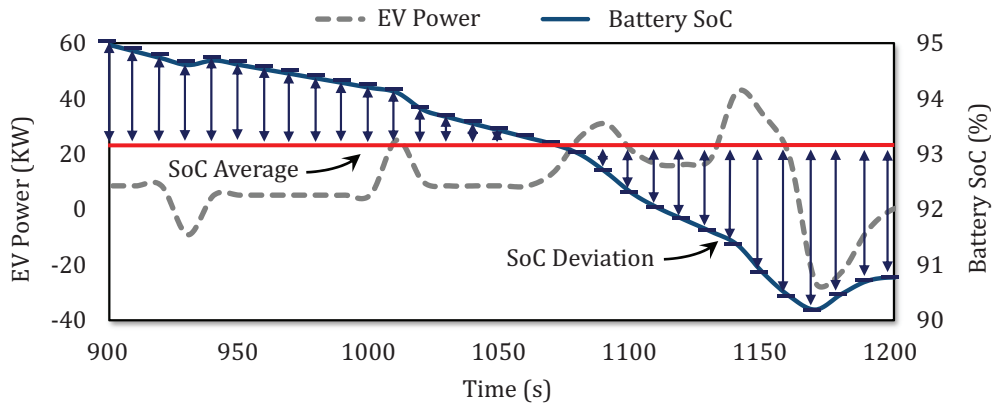

Figure 3.8: Battery SoC behavior in terms of SoC average (horizontal line) and SoC deviation (vertical arrows).

Moreover, the battery lifetime in other words, State-of-Health (SoH) - the ratio of the current capacity to the nominal capacity - degrades over time in Lithium-ion battery cells (capacity fade effect). The SoH degradation ($\bigtriangledown SoH$) is mainly influenced by the stress on the battery cell which may be modeled as SoC deviation (SoC_{dev}) and the SoC average (SoC_{avg}) [98]. $\bigtriangledown SoH$ is measured based on the SoC pattern over a time period:

$$\bigtriangledown SoH = f\ (SoC_{dev}, SoC_{avg}) = \ (a_1 e^{\alpha SoC_{dev}} + a_2)(a_3 e^{\beta SoC_{avg}}) \tag{3.17}$$

where α, β, a_1, a_2, and a_3 are the parameters empirically evaluated at design time for estimating $\bigtriangledown SoH$ accurately based on the battery type. Consideration of the battery temperature for estimating $\bigtriangledown SoH$ is out of the scope of the chapter and is modeled as a constant

in Equation 3.17. SoC_{dev} and SoC_{avg} are calculated based on a discharging/charging cycle (see Figure 3.8).

$$SoC_{avg} = \frac{1}{T} \int_0^T SoC(t)dt \tag{3.18}$$

$$SoC^2_{dev} = \frac{1}{T} \int_0^T (SoC(t) - SoC_{avg})^2 dt \tag{3.19}$$

where T is the period of the discharging/charging cycle. However, in this chapter, the charging part of the cycle is assumed to have a fixed pattern and duration. Hence, the effect of the charging part on SoC_{dev} and SoC_{avg} are modeled as constants. The battery cell capacity decreases with the rate of $\bigtriangledown SoH$. When the battery capacity reaches 80% of its nominal capacity, it will be useless. Therefore the number of discharging/charging cycles, the battery can be used (the battery lifetime), is dependent on battery lifetime degradation ($\bigtriangledown SoH$). Although, the battery lifetime degradation is effected by both SoC_{dev} and SoC_{avg}, the influence and flexibility of SoC_{dev} is more significant on the battery lifetime [98]. Hence, in this chapter, we further focus on the battery SoC deviation for reducing the battery stress.

The parameters for modeling the battery cell is empirically evaluated using the data for a family of lithium-ion battery cells which are commonly used in EV like Nissan Leaf. Moreover, the structure of the battery package is defined according to the Nissan Leaf specifications [4, 63, 148].

3.3 Battery-Aware Automotive Climate Control

3.3.1 Methodology Description

The HVAC system in the automotive has multiple actuators and sensors for monitoring and controlling the operating parameters such as air speed, temperature set points, and valve damper ratio. The automotive climate control is responsible for sensing these values and making decision on the control inputs. Figure 3.9 illustrates the control inputs and variables in the system from the controller's perspective.

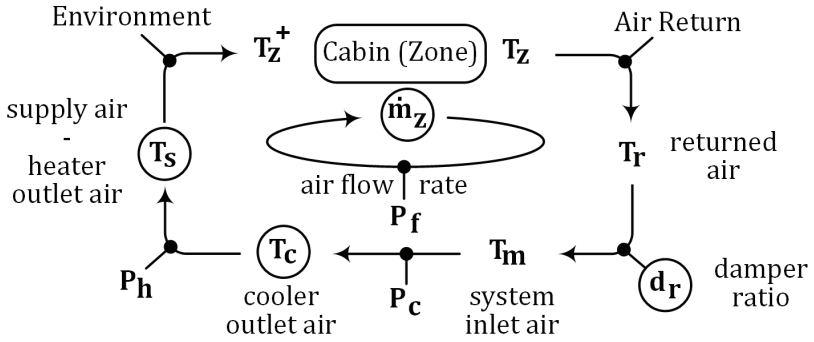

Figure 3.9: Automotive climate control variables and control inputs (circled).

In our battery-aware automotive climate control methodology, the goal is to improve the driving range and extend the battery lifetime while maintaining the thermal comfort for the passengers. In abstract, the methodology predicts the EV electric motor power consumption regarding the route behavior and attempts to adjust the HVAC system power consumption by deciding on the operating parameters such that the stress on the battery is reduced. The route behavior is predicted and modeled using a drive profile (Section 3.2.1). The power consumption of the electric motor is modeled and estimated by knowing the driving forces on the EV (Section 3.2.2). The HVAC system thermodynamics and power consumption regarding the operating parameters and control inputs are modeled and estimated (Section 3.2.3). Therefore, our automotive climate control enables us to adjust the

HVAC system variables while knowing the EV electric motor power consumption in order to reduce the SoH degradation and energy consumption of the battery predicted according to its power request (Section 3.2.4).

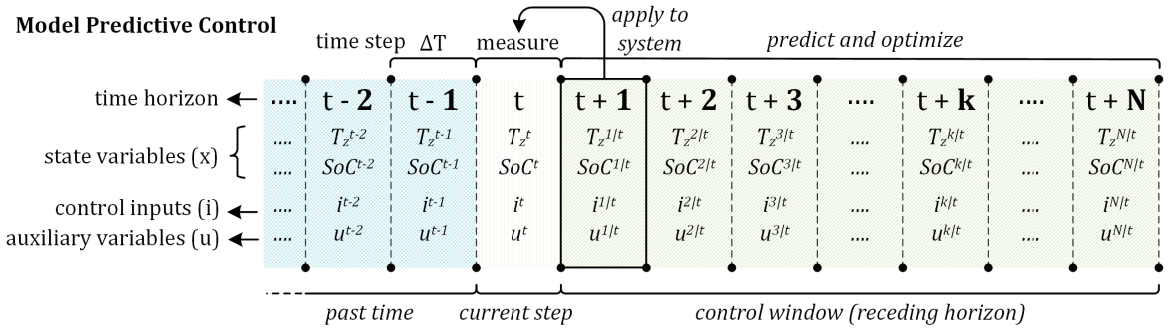

Figure 3.10: Scheme of MPC implemented for battery-aware automotive climate control.

The operation state of the HVAC can be defined by multiple state variables $x = \{T_z, SoC\}$, control inputs $i = \{T_s, T_c, d_r, \dot{m}_z\}$, and auxiliary variables $u = \{T_m, P_h, P_c, P_f, P_e\}$ for each time step.

MPC is an advanced method of control that relies on dynamic models of the process or physical plant (HVAC). The main advantage of MPC is the fact that it allows the current time step to be optimized, while keeping future time steps in account (EV states). This is achieved by optimizing a finite time horizon (control window), but only implementing the current time step. MPC has the ability to anticipate future events and can take control actions accordingly. PID and LQR controllers do not have this predictive ability [73].

Our battery-aware climate control is implemented based on a MPC algorithm (Figure 3.10). For each time step of the control (t), the current system state is monitored. Then, the state variables, control inputs, and auxiliary variables are predicted in the near-future control window. $x^{k|t}$, $i^{k|t}$, and $u^{k|t}$ are the values of the state variables, control inputs, and auxiliary variables at time $t + k \triangle T$, respectively predicted at time step t. The estimation of the variables in the control window enables the controller to optimize the variables of the system such that it minimizes a cost function. Moreover, in the MPC, the variables

can be explicitly constrained which is important and beneficial to defining the temperature range limits for thermal comfort and component control restrictions. After optimizing the variables of the control window at each time step, the optimal values of the control inputs for the first predicted step will be applied to the system. The controller will continue to the next time step for predicting, optimizing the variables, and applying them to the system again (receding horizon).

3.3.2 Optimization Formulation

The equations modeling the system (e.g. EV power train, HVAC, and battery) are the main equations defining the constraints of the optimization problem in the MPC algorithm for the battery-aware automotive climate control. Since the control has to take place in a discrete-time domain, the continuous-time equations need to be discretized into different discrete-time states. These constraints need to be applied for each time step of the control window in order to model the dynamics of the system. The equations modeling the HVAC system and the battery are discretized and used as the equality constraints in the following.

The thermodynamic behavior of the cabin regarding supply air and environment is described as the following constraint (Equation 3.20). T_z^+ represents the cabin temperature at the next time step $t + \triangle T$. Here, $\triangle T$ is the time step duration of the controller (sample period). The average of the temperature in the current step and the next step has been used as the method of discretization.

$$\boldsymbol{C_{EQ}1:} \quad M_c \frac{T_z^+ - T_z}{\triangle t} = \dot{Q}_{solar} + c_x A_x (T_o - \frac{T_z^+ + T_z}{2}) + \dot{m}_z c_p (T_s - \frac{T_z^+ + T_z}{2}) \tag{3.20}$$

Other equations describing the behavior of the air temperature and HVAC system power consumption comprise the following equality constraints (Equation 3.21).

$$\boldsymbol{C_{EQ}2:} \quad T_r = T_z$$

$$\boldsymbol{C_{EQ}3:} \quad T_m = (1 - d_r) \times T_o - d_r \times T_r$$

$$\boldsymbol{C_{EQ}4:} \quad P_h = \frac{c_p \times m_z}{n_h} \times (T_s - T_c)$$

$$\boldsymbol{C_{EQ}5:} \quad P_c = \frac{c_p \times m_z}{n_c} \times (T_m - T_c)$$

$$\boldsymbol{C_{EQ}6:} \quad P_f = k_f \times m_z^2 \tag{3.21}$$

The battery SoC behavior has been modeled using the Puekert's Law as a non-linear exponential equation (Section 3.2.4). However, for implementation of the optimization constraint, the equation can be approximated. Hence, the battery SoC estimation for the next time step (SoC^+) has been abstracted into a quadratic equation (Equation 3.22). $I = \frac{P_c+P_h+P_f+P_e}{V_{dc}}$ is the current drawn from the battery with the voltage of V_{dc}. Parameters α_x are evaluated by fitting Equations 3.15 and 3.16 into the quadratic form.

$$\boldsymbol{C_{EQ}7:} \quad SoC^+ = SoC - (\alpha_2 I^2 + \alpha_1 I + \alpha_0) \tag{3.22}$$

The electric motor power consumption is predicted for each time step of the control window and is applied to the $P_e^{k|t}$ variables by an equality constraint at each time step $k|t$. The values of the state variables at the beginning of the control window ($T_z^{0|t}, SoC^{0|t}$) should be assigned to the currently measured values of the system using equality constraints. Moreover, the values of the predicted state variables at end of each time step ($T_z^{+k|t}, SoC^{+k|t}$) should be assigned to the current values of the state variables at the next time step of the control window ($T_z^{k+1|t}, SoC^{k+1|t}$).

The control requirements and restrictions state the following time-varying constraints on control inputs and state variables. They comprise of the limits for heating/cooling coil power consumption and fan speed; tolerance of 10% for cabin temperature[3]; and restrictions

[3]The temperature tolerance is the maximum temperature deviation from the target temperature. Although this tolerance has been selected arbitrarily, our methodology is orthogonal to this value or any other value.

on the values of the variables for correct operation of the system and right solution of the optimization.

$$
\begin{aligned}
&\boldsymbol{C_{NEQ}1:} && \underline{\dot{m}}_z \leq \dot{m}_z \leq \overline{\dot{m}}_z && \text{maximum and minimum air flow to the cabin}\\
&\boldsymbol{C_{NEQ}2:} && \underline{T_z} \leq T_z \leq \overline{T_z} && \text{comfort zone restrictions on cabin temperature}\\
&\boldsymbol{C_{NEQ}3:} && T_c \leq T_s && \text{heater always increases the temperature}\\
&\boldsymbol{C_{NEQ}4:} && T_c \leq T_m && \text{cooler always decreases the temperature}\\
&\boldsymbol{C_{NEQ}5:} && \underline{T}_c \leq T_c && \text{minimum outlet air temperature by cooler}\\
&\boldsymbol{C_{NEQ}6:} && T_s \leq \overline{T}_h && \text{maximum outlet air temperature by heater}\\
&\boldsymbol{C_{NEQ}7:} && 0 \leq d_r \leq \overline{d}_r && \text{limitation on recirculated air fraction}\\
&\boldsymbol{C_{NEQ}8:} && P_h \leq \overline{P}_h && \text{heater maximum power output}\\
&\boldsymbol{C_{NEQ}9:} && P_c \leq \overline{P}_c && \text{cooler maximum power output}
\end{aligned}
\tag{3.23}
$$

The cost function for the optimization problem is defined in the following (Equation 3.24). $(T_z^{k|t} - T_{target})^2$ is the thermal comfort cost added for minimizing the deviation of the temperature from the target temperature with weight variable w_1. It ensures that thermal comfort of the passengers is not sacrificed in the optimization. $(SoC^{+k|t} - SoC^{k|t})^2$ is the battery SoC cost added for minimizing the SoC deviation with weight variable w_2. Since, the battery lifetime and energy consumption is affected by the battery SoC change, this cost will result in extending the battery lifetime and decreasing the energy consumption for further driving range. The sum of the costs has been normalized by dividing them by N and $\triangle t^2$.

$$
C^t = \frac{1}{N}\sum_{k=1}^{N} w_1\ (T_z^{k|t} - T_{target})^2 + w_2\ (SoC^{+k|t} - SoC^{k|t})^2/\triangle t^2 \tag{3.24}
$$

Although maintaining the cabin temperature is addressed by minimizing the cost function (thermal comfort cost) and defining a constraint on the comfort zone, there might be multiple

optimizer solutions with different temperature behavior in the control window which might not be acceptable; since the first step of the control window is applied to the system, the temperature behavior may not be the acceptable optimal solution. Hence, another equality constraint (Equation 3.25) is added to limit the solution space by enforcing the temperature of the first step and last step of the control window to be equal. It needs to be noted that this equality constraint is just one constraint for the whole control window, unlike the previous constraints which were defined for each time step in the control window.

$$\boldsymbol{C_{EQ}8:} \quad T_z^{+1|t} = T_z^{+N|t} \tag{3.25}$$

The non-linear equations of the system model which define the constraints and the cost function of the optimization problem are convex and quadratic equations. Therefore, the best option might be to apply Sequential Quadratic Programming (SQP) which is an iterative method for non-linear optimization. The optimization problem is solved for the MPC algorithm in each time step. The non-convex non-linear equations have been approximated by adding a convex quadratic term to the cost function using Lagrangian multiplier method [73].

3.4 Experimental Results

3.4.1 Experiment Setup

We need to implement the system modeling for our battery-aware automotive climate control. All the equations in Section 3.2 have been formulated in MATLAB/Simulink [7] for modeling the EV system including the power train, HVAC, and battery as the plant of the controller. The optimization cost function, non-equality constraints, and equality constraints formulated in Section 3.3.2 are implemented in MATLAB. *fmincon* toolbox has been used with the sequential quadratic programming (*sqp*) solver. Multiple drive cycles (see Table 3.1) are modeled as the drive profiles for our experiment benchmarks using AMESim [9].

3.4.2 Results and Analysis

The performance of our methodology is compared with a baseline in which the power consumption of the HVAC system is adjusted such that the cabin temperature is maintained constant. Fuzzy-based control is implemented which has been the state-of-the-art methodology with the objective of maintaining smooth cabin temperature [67]. In the fuzzy-based control, cooling/heating set points are adjusted based on the cabin temperature which makes the temperature and the HVAC power almost constant. The resulted energy consumption is the lowest compared to the other methodologies such as the on/off methodology [101, 130].

a) Temporal Analysis: our battery-aware automotive climate control adjusts the HVAC power consumption regarding the electric motor power requests such that the battery stress is reduced for better driving range and battery lifetime. However, the cabin temperature is also affected due to the change in the HVAC power consumption.

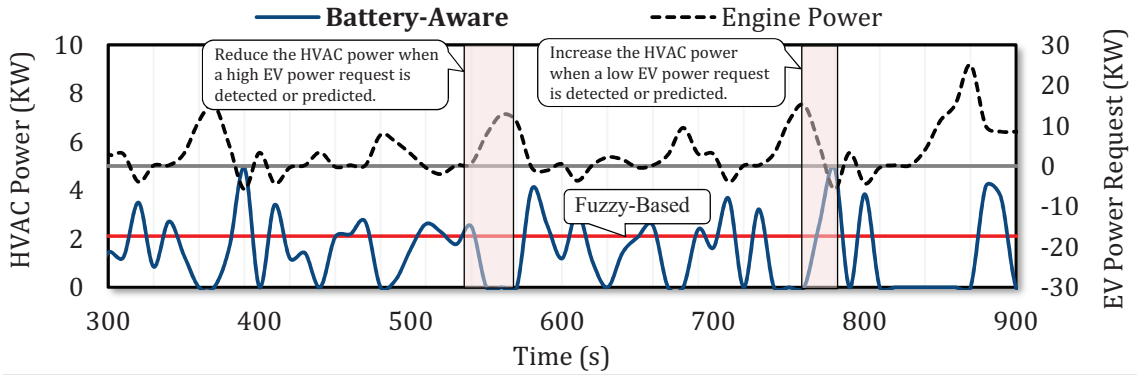

Figure 3.11: HVAC power adjustment by the battery-aware climate control.

We experimented the battery-aware and fuzzy-based methodologies in the 35°C weather with the target temperature of 25°C while driving the *ECE_EUDC* drive cycle. In Figure 3.11, the HVAC power consumption with regards to the electric motor power consumption is shown. When our battery-aware automotive climate control predicts or detects a high electric motor power request in the near-future (control window), it adjusts the HVAC power such that the energy consumption and battery stress reduce.

In Figure 3.12, the behavior of the cabin temperature is illustrated while using our battery-aware climate control. Our methodology ensures that the cabin temperature is maintained around the target temperature. Hence, the methodology (pre-)cools the cabin when the electric motor is estimated or detected to be using more power in the control window. In the state-of-the-art fuzzy-based methodology, the HVAC power is adjusted such that the cabin temperature is maintained around the target temperature. However, in our methodology, the cabin temperature fluctuates around the target temperature while adjusting the HVAC power. As a result, the battery stress (battery SoC deviation) reduces for better energy efficiency and battery lifetime. The temperature deviation from the target temperature and increase in the thermal comfort cost are the trade-offs for improving the battery lifetime and driving range.

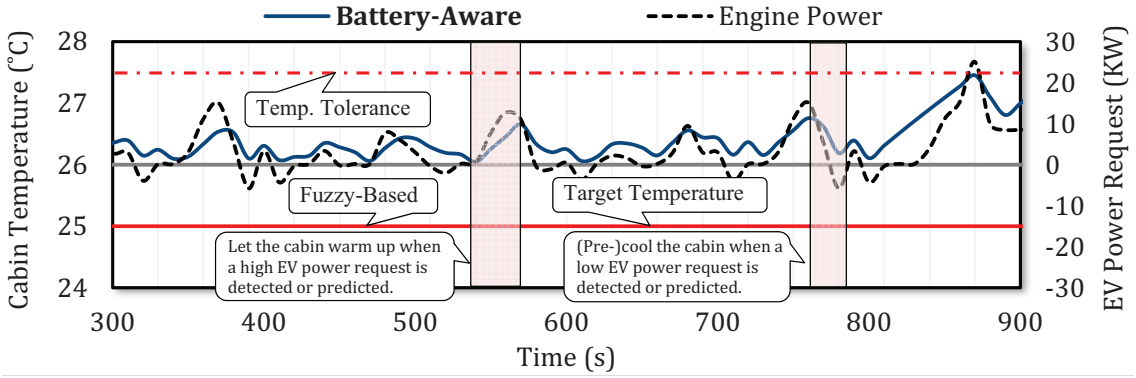

Figure 3.12: Cabin temperature analysis for battery-aware climate control.

b) Scalability and Performance Analysis: the control window size for the MPC is variable depending on the number of estimated states and time step duration. As the number of states increases, more state variables of the system are being considered for the optimization. Hence, as shown in Figures 3.13 and 3.14, more memory and longer execution time are required by the optimizer to converge and find the solution. The execution time and memory usage will be roughly the constant for the same number of states. However, the slight difference is mainly due to the low accuracy and non deterministic nature of the memory usage and execution time of the MPC optimization when solving a problem and converging

to an optimal solution. Although designing a real-time embedded system controller is out of the scope of this chapter, we need to analyze and design control window size such that not to violate the timing and memory constraints. For instance, the maximum execution time of the controller at each time step can be limited to the sampling time or time step duration of the controller. The computing platform used for the experiments is comprised of an Intel Core-i7 3770 CPU with 3.4 GHz clock frequency and an 8 GB of DDR3 RAM.

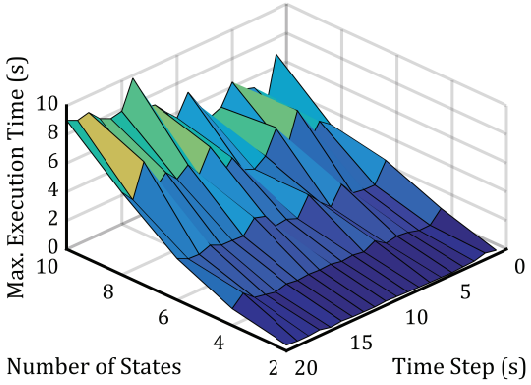

Figure 3.13: Execution time of optimizer at each time step.

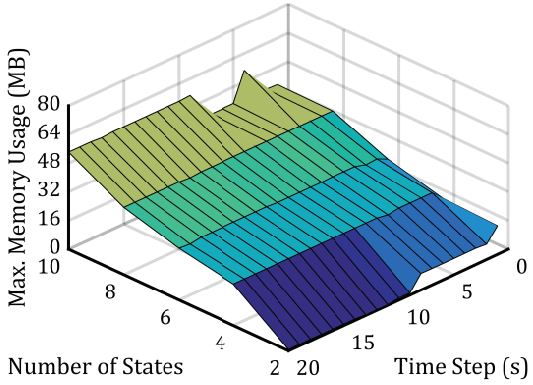

Figure 3.14: Memory usage of optimizer at each time step.

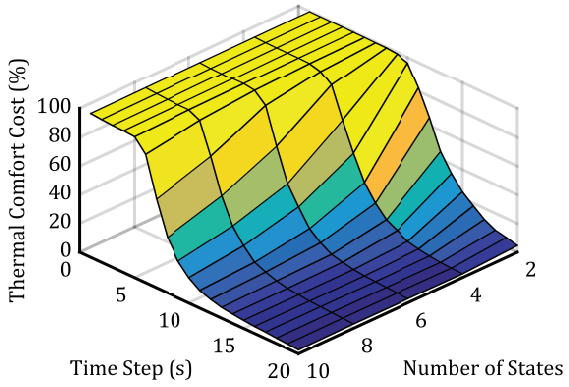

(a) Normalized thermal comfort cost.

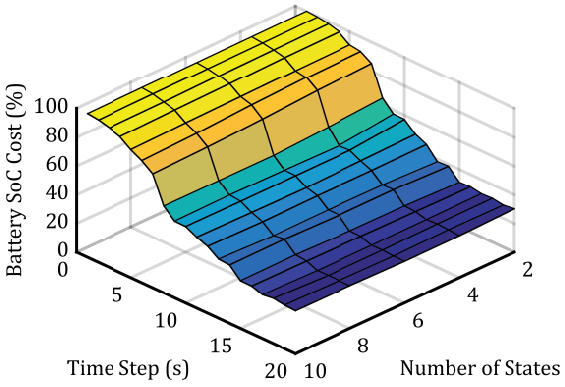

(b) Normalized battery SoC cost.

Figure 3.15: Cost analysis for different different control window sizes.

On the other hand, by increasing the control window size, the optimization gets more flexibility and reaches to a better solution in terms of the cost (smaller cost value). Figures 3.15(a) and 3.15(b) show the optimization cost of the final solution for thermal comfort and battery SoC objectives normalized by the maximum value.

The thermal comfort cost is based on the sum of the cabin temperature deviations from the target temperature (see Section 3.3.2). Therefore, as shown in Figure 3.15(a), increasing the control window size decreases the thermal comfort cost which results in better maintenance of the cabin temperature and improving the thermal comfort. It needs to be noted that the thermal comfort cost evaluated for the fuzzy-based methodology is nearly zero which is better than our methodology. This is the trade-off of our methodology for reaching better driving range and battery lifetime. However, the cabin temperature limits specified for the thermal comfort are always met.

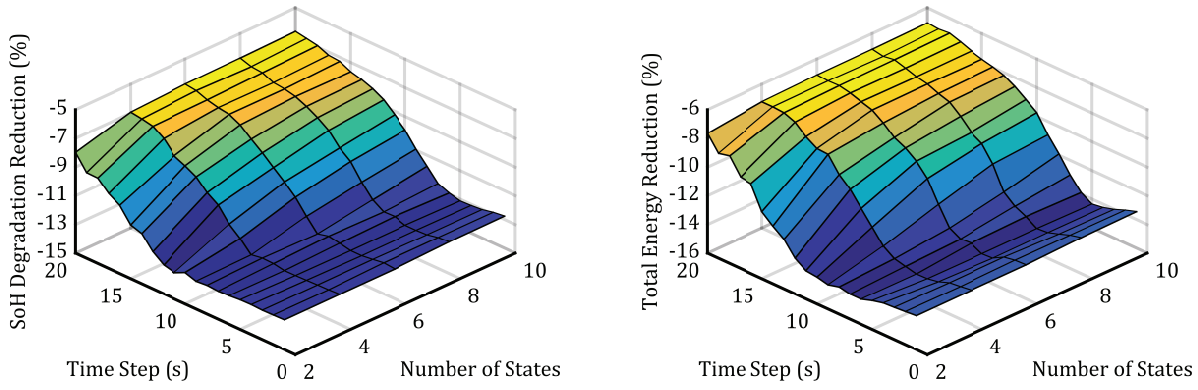

(a) SoH degradation reduction.

(b) Energy consumption reduction.

Figure 3.16: Performance analysis for different control window sizes.

The battery SoC cost is based on the sum of the battery SoC differences over time (see Section 3.3.2). This optimization cost does not have an absolute target like thermal comfort cost. Hence, reducing the battery SoC cost does not necessarily reflect on better battery SoH degradation and energy consumption. As shown in Figures 3.16(a) and 3.16(b), the battery lifetime and energy consumption improve compared to the fuzzy-based methodology. However, by increasing the control window size, the battery SoC cost reduction does not reflect in better battery lifetime and energy consumption. The battery SoH degradation reduction reaches up to 13.2% and energy consumption reduction reaches up to 14.4% with 5 states estimated in the control window with time step of 10s. Increasing the number of states, reduces the improvement of the methodology. This is due to the fact that the final

battery SoC deviation of the solution is different from the optimization cost. Therefore, increasing the number of states in the control window reduces the MPC algorithm influence on the final battery SoC deviation although the optimization cost function for the battery SoC decreases.

c) Environment Analysis: environment factors such as driving route behavior and ambient temperature influence the performance of our methodology. This is due to the fact that our methodology requires the knowledge of the route behavior for electric motor power estimation and the HVAC system optimization. Moreover, the ambient temperature affects the HVAC system power consumption.

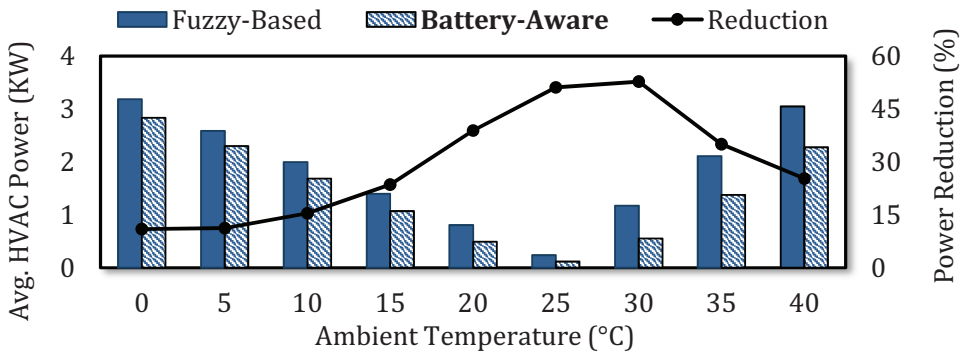

Figure 3.17: Average HVAC power consumption analysis and improvement over fuzzy-based.

Figure 3.17 illustrates the average HVAC power consumption for the fuzzy-based methodology and our battery-aware climate control. As you can see the HVAC average power consumption increases as the ambient temperature deviates further from the target temperature (25°C). The reduction of the average HVAC power consumption while using our battery-aware methodology is shown on the right axis of the figure in percentage. When the ambient temperature deviates from the target temperature, the optimizer has less flexibility of adjusting the HVAC variables for maintaining the cabin temperature in these harsh weathers which results in smaller power reduction.

Figure 3.18(a) shows that the maintenance of the cabin temperature is harder as the ambient temperature deviates from the target temperature, which will result in higher thermal com-

fort cost. The total energy consumption of the EV has been evaluated for different ambient temperatures and has been compared with the fuzzy-based methodology. As Figure 3.18(b) shows, the reduction in the total energy consumption is more noticeable in higher temperatures as the HVAC energy consumption is higher. It needs to be noted that heating the cabin in cold weather is easier than cooling the cabin in hot weather, since the solar radiation heats the cabin as well. Moreover, the SoH degradation has been compared for both methodologies and its reduction has been illustrated in Figure 3.18(c). The SoH degradation reduction is due to the fact that the SoC deviation has been reduced using the battery-aware climate control.

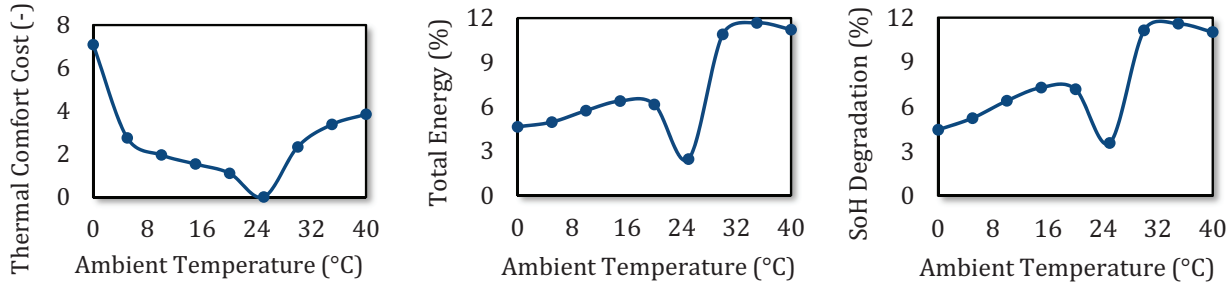

(a) Thermal comfort cost. (b) Energy consumption reduction. (c) SoH degradation reduction.

Figure 3.18: Performance analysis for different ambient temperatures.

Automotive manufacturers utilize standard driving cycles and drive profiles to test their vehicles for performance and energy consumption. Table 3.1 lists these drive profiles with the metric showing the variance in the profile. The route coefficient variance is the normalized standard variance (standard variance over average) of the route behavior for the drive profile. The route coefficient variance affects the variation of the electric motor power requests along the route. The performance of the battery-aware methodology has been evaluated for the selected drive profiles. The table also illustrates the energy consumption and SoH degradation reduction achieved by the battery-aware methodology compared to the fuzzy-based methodology with the corresponding thermal comfort cost.

Table 3.1: Performance of the battery-aware climate control for different drive profiles [14].

Drive Profile	Route Coefficient Variance (-)	Energy Consumption Reduction (%)	SoH Degradation Reduction (%)	Thermal Comfort (-)
C1015	2.43	16.02	14.68	1.94
ECE_EUDC	1.98	11.68	11.59	3.38
ECE_EUDC_AT	2.02	11.60	11.53	3.28
ECE_EUDC_MT	1.98	11.68	11.59	3.38
FTP	1.90	12.98	13.85	5.27
HWFET	0.67	8.15	7.56	5.76
JC08_cold	2.07	14.56	14.40	2.57
JC08_hot	2.07	14.31	14.72	3.09
NEDC	1.95	11.58	11.48	3.40
NEDC_AT	1.99	11.50	11.41	3.32
NEDC_MT	1.95	11.58	11.48	3.40
NEDC_min	2.02	12.07	11.94	3.12
SC03	1.72	11.65	9.93	2.86
UDDS	1.64	13.17	12.47	4.06
US06	1.14	6.34	5.59	5.78

The route coefficient variance influences the electric motor power requests and thereby the control performance. Hence, we have analyzed the performance of the battery-aware control with respect to the variance (see Figure 3.19). It is shown that our battery-aware methodology reduces the energy consumption, the SoH degradation, and thermal comfort cost further when the coefficient variance is higher. This shows that our methodology benefits from the higher variance of the electric motor power requests in order to reduce the battery stress by adjusting the HVAC power.

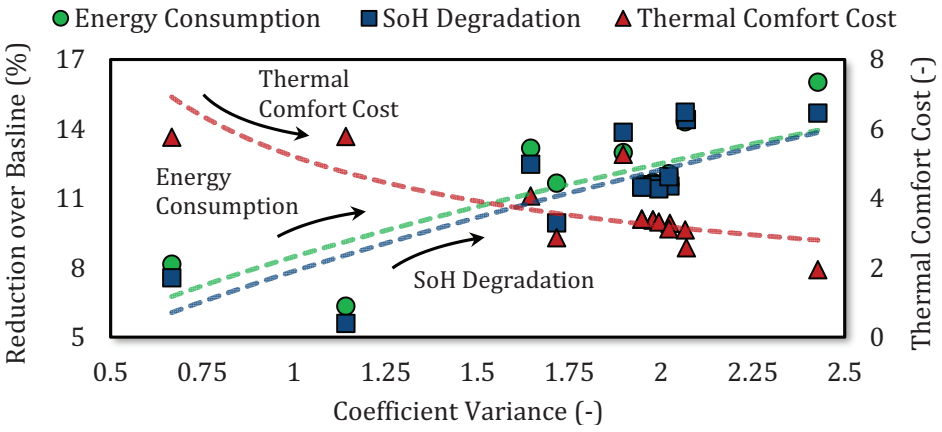

Figure 3.19: Battery-aware climate control performance versus route behavior.

It needs to be noted that the estimation error of the driving route behavior that depends on its prediction algorithm may influence the performance of the climate control. However, the MPC algorithm implemented in the climate control is very stable with regards to limited outliers in the estimation window. Moreover, the optimization always ensures a safe and comfort range of cabin temperature using the constraints. Therefore, the safe range of HVAC control inputs and passenger comfort will not be violated for any estimation error.

d) Plant Modeling Error Analysis: the EV system, especially the HVAC system and the cabin are modeled and estimated as part of our battery-aware automotive climate control methodology (Section 3.2). However, the cabin thermodynamic behavior may not be accurate in the model and may change according to the interior, e.g. seat material, passenger body heat, etc. Hence, inaccurate estimation of the system behavior may result in different performance of the climate control.

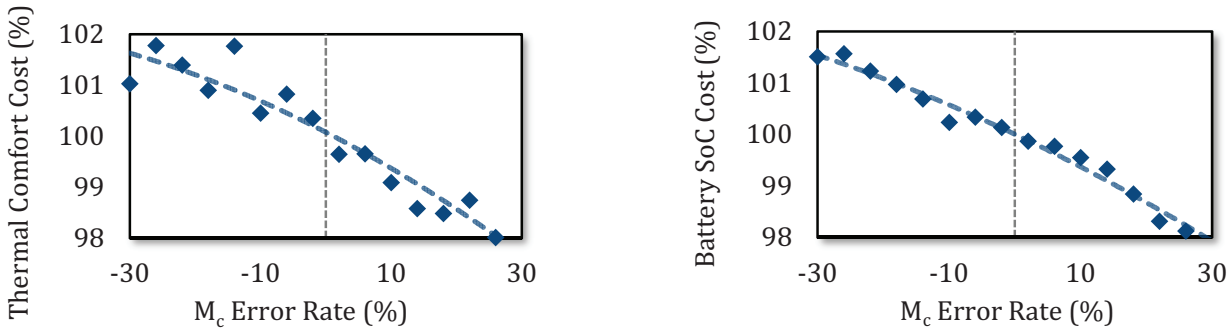

(a) Thermal comfort cost change.

(b) Battery SoC cost change.

Figure 3.20: Cost analysis for different cabin thermal capacitance modeling error rates.

The performance of the battery-aware climate control methodology has been analyzed in terms of the thermal comfort cost and the battery SoC cost for different modeling error rate of the cabin thermal capacity (M_c). As shown in Figures 3.20(a) and 3.20(b), the methodology attempts to make up for the cabin temperature estimation error and maintain the thermal comfort and minimize the battery SoH degradation. Therefore, 30% of the modeling error rate only changes the thermal comfort cost and battery SoC cost up to 2% from their nominal value (when there is no error). This shows that our battery-aware

automotive climate control is adequately robust and tolerant to the modeling and estimation error of the physical plant.

It needs to be noted that as the battery cell degrades, their capacity and internal resistance change which will result in lower performance in the charging and discharging cycles. Hence, the implemented model may underestimate the discharge-rate effect of the battery cell. We have analyzed the performance resulted from this modeling and estimation error for HVAC which will behave the same. It shows that the battery-aware automotive climate control is robust and tolerant to the modeling and estimation error. Moreover, this can be compensated by generating a more detailed model which is out of the scope this thesis and the methodology of the climate control.

3.5 Concluding Remarks

Design of EV has been challenging due to the battery restrictions and characteristics which hinder the process of its development as a zero-emission mean of transportation. Different battery management systems to manage battery cells and automotive climate controls to maintain the passenger thermal comfort have been developed. However, it has been observed that the HVAC system contributes a lot to the power consumption which significantly influences the EV driving range and battery lifetime. This influence on the battery has not been considered in the state-of-the-art battery management systems and automotive climate control methodologies. In this chapter, we proposed a novel methodology of automotive climate control which considers the battery behavior in terms of energy consumption and battery lifetime while monitoring and controlling the HVAC system. Our battery-aware automotive climate control predicts the power requests from the electric motor and adjusts the HVAC power consumption such that the battery stress reduces. The methodology has been implemented and experimented for different control window sizes, ambient temperatures, drive profiles, and modeling error rates. The performance and scalability of the methodology has been analyzed and compared to the state-of-the-art. It has been shown that our methodology diminishes the battery lifetime degradation by up to 13.2% and decreases the total energy consumption by up to 14.4% with prediction of 5 states in the future with time step of 10s.

Chapter 4

Eco-Friendly Navigation System

4.1 Introduction and Related Work

In Chapter 1, we noticed that there are multiple contributors to the EV power consumption. The electric motor and HVAC are the two systems that have the major influence on the EV power consumption, and thereby on energy consumption and battery lifetime. As explained in Chapter 2, the BMS was implemented to manage the power requests to the battery cells at device level regardless of the type of the power request. The BMS can optimize the power split among battery cells and ultracapacitor such that the driving range is extended and battery capacity loss is minimized. Moreover, in Chapter 3, a battery-aware automotive climate control was implemented that could reduce the stress on the battery by co-scheduling the load of HVAC given the future electric motor power requests. The proposed climate control can prolong the battery lifetime and extend driving range while maintaining the same passenger thermal comfort. The implemented methodologies estimate the electric motor power consumption given a static driving route. For instance, a navigation system may choose the fastest driving route and provide that to the driver and control methodologies in order for them to make their optimal control decisions. The fastest driving route will be the best option considering that it has the shortest driving time. However, the climate control or BMS are not aware of and do not have any influence in the routing process. This lack of knowledge may result in the selection of a driving route that mandates higher EV energy consumption and battery capacity loss.

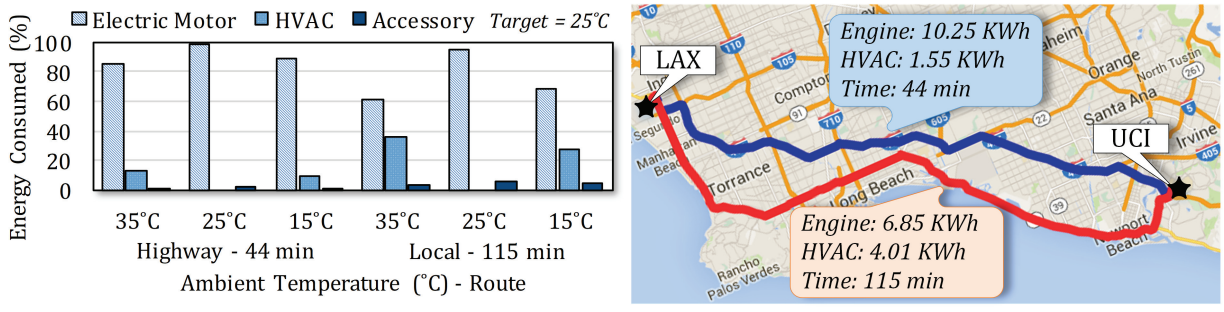

Figure 4.1: EV energy consumption analysis for various routes and ambient temperatures [8, 63, 131, 147].

4.1.1 Motivational Case Study

We further analyzed the energy consumption of an EV (Nissan Leaf S) considering the electric motor, HVAC system, and other accessories [63, 131, 147], while driving on local/highway routes and hot/cold weather from University of California, Irvine (UCI) to Los Angeles International Airport (LAX) (see Figure 4.1).

Summary and conclusion from observations: We noticed that the route behavior significantly influences the electric motor energy consumption; energy is saved by driving on the local route while sacrificing significant driving time (+50 min). Moreover, the HVAC system makes up a significant amount of the EV energy consumption ($\sim$ 40%) depending on the ambient temperature. Moreover, the route behavior also influences the HVAC energy consumption significantly; the HVAC energy consumption increases on the local route, since the driving time increases.

In the existing works, the main objective for automotive climate controls has been to maintain the cabin temperature in a comfort range [89]. Hence, stabilizing the cabin temperature and reducing the HVAC energy consumption have been the major objectives in these climate controls [27, 67, 89, 101]. In [131], it has been shown that the HVAC system may increase the battery stress significantly, which results in major battery lifetime and driving range degradation. Hence, a battery lifetime-aware automotive climate control has been introduced in Chapter 3, which controls the HVAC optimally considering the EV power requests. This methodology has reduced the battery stress in order to improve the battery lifetime and driving range for the EV.

However, the HVAC energy consumption is significantly dependent on the route behavior, especially in the battery lifetime-aware climate control which optimizes the HVAC based on the route behavior. Moreover, the performance of these climate controls is mainly limited by lack of route behavior prediction and optimization.

On the other hand, existing automotive navigation systems attempt to only find the shortest or the fastest route to a specific destination [8, 72]. Moreover, to reduce the energy consumption of EV, new concept of energy-aware routing has been introduced; the EV energy consumption is estimated for each route segment and used to select the route with the least energy consumption. The estimation has been done using the real data gathered by monitoring the EV [54] or by estimating the electric motor energy consumption considering the driving forces on the EV [150]. Furthermore, to account the battery lifetime in the navigation system, [147] introduced a driving management which estimates the battery lifetime resulted from driving multiple route alternatives to a specific destination; it selects the one with the longest battery lifetime while preventing significant sacrifice of the driving time.

Moreover, the route behavior influences the EV energy consumption and battery lifetime. Existing navigation systems have attempted to improve these parameters by optimizing the route. However, the performance of these navigation systems is only limited to considering the electric motor behavior. In other words, other high-load components in the EV and their control dynamics (e.g. HVAC [131]) have not been considered for optimization. Therefore, the integration of automotive climate control and navigation system and the trade-off between electric motor, HVAC, and route behavior have not been considered for joint optimization of the HVAC and route, which may cause sub-optimal results.

4.1.2 Problem and Research Challenges

In summary, the above-mentioned state-of-the-art methodologies implemented in EV for navigation and control suffer from the following three major limitations:

1. Battery lifetime has not been considered in the route optimization, especially while considering the influence of the high-load components and their control dynamics (e.g. climate control in HVAC) on the battery behavior.

2. Lack of route behavior prediction and optimization has been limiting the battery lifetime-aware automotive climate control performance.

3. Implicit trade-off existing in automotive climate control and navigation system has been neglected.

4.1.3 Novel Contributions and Concept Overview

To address the above-mentioned challenges, a novel eco-friendly automotive climate control and navigation system methodology for extending the battery lifetime and driving range in EV is proposed that employs:

1. **System Behavior Estimation (Section 4.2):** in which a detailed map database is created and utilized to model the route behavior and estimate the power consumption of the electric motor and HVAC while considering their influence on the battery parameters.

2. **Automotive Climate Control (Section 4.3.3):** which optimizes the HVAC system control inputs and variables by having the predicted route behavior in the near-future using Model Predictive Control (MPC) [131] algorithm in order to reduce the battery stress for extending the battery lifetime and driving range.

3. **Automotive Navigation System (Section 4.3.4):** which optimizes the route towards a specific destination using Bellman-Ford algorithm [42] for longer battery lifetime and driving range while providing a predicted route behavior for the automotive climate control.

As shown in Figure 4.2, we present a novel methodology in which automotive navigation system optimizes the route of the EV for longer battery lifetime and driving range while

considering the behavior of the electric motor and the HVAC system and their influence on the battery degradation. Also, the navigation system provides a predicted route behavior for our novel automotive climate control. Hence, the climate control optimizes the HVAC utilization at driving time for further battery lifetime and driving range improvement.

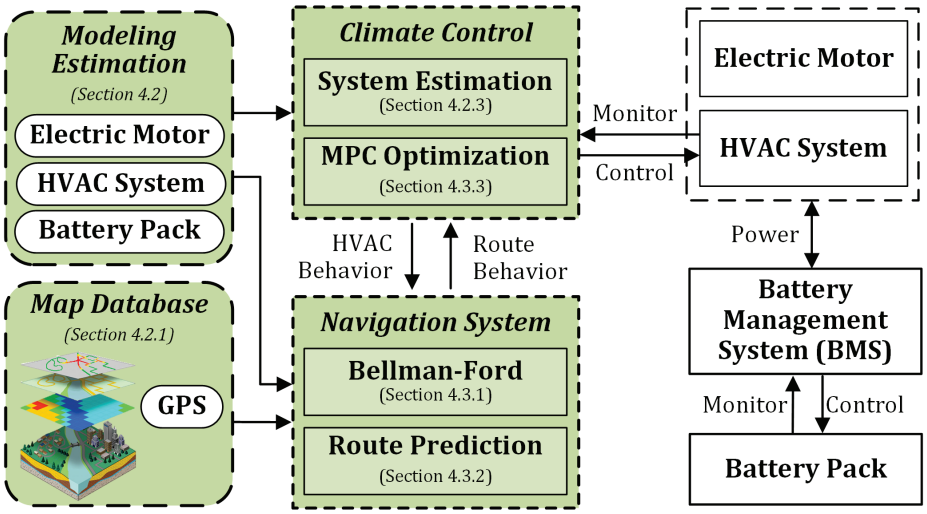

Figure 4.2: Our eco-friendly automotive climate control and navigation system.

The integration of automotive climate control and navigation system in our methodology helps us to handle the trade-off between the electric motor, HVAC, and route behavior for better joint optimization of the route and HVAC system. It needs to be noted that the driving behavior is affected not only by the route behavior, but also by the driver's behavior [74]. However, considering the driver's behavior into the methodology is out of the scope of this chapter (see Chapter 7 for further details).

4.2 System Components

Implementation of our eco-friendly automotive climate control and navigation system requires the behavior knowledge of the contributing cyber and physical components in this automotive CPS (EV). Hence, in the following sections, these components are described and modeled. In Section 4.2.1, the map database containing the required geographical and traffic

information is generated. Section 4.2.2 explains how the route behavior is modeled using the map database. Finally, in Section 4.2.3, the EV components such as the electric motor and HVAC system are modeled and their power consumption is estimated by knowing the route behavior and their control dynamics. Then, their influence on battery operating parameters is modeled and estimated.

4.2.1 Map Database

The automotive navigation system needs to know the current location and the surrounding map for optimizing the route towards a specific destination. Multiple types of data of the surrounding map are required for different purposes. OpenStreetMap [60] database is used for locating the nodes (latitude and longitude values) and segments connecting these nodes (graph). Also, map labels are used to find out the driveability of each segment. Google Maps Elevation API [8] provides the elevation for each node on the map. Google Maps Directions API [8] also provides the average speed at each segment (see Figure 4.3). The data extracted from these databases is leveraged to generate the map database for our automotive navigation system.

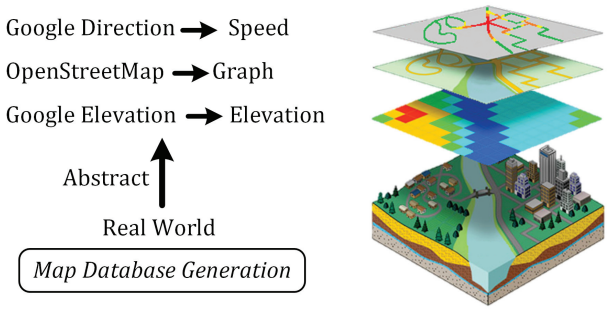

Figure 4.3: Sources used to create the map database.

4.2.2 Route Behavior

In the map database, a node matrix ($\overline{n}$) is created where each row holds the node id, elevation, latitude, and longitude values. A segment matrix ($\overline{s}$) consisting of driveable segments is also created where each row contains the starting node id, ending node id, time duration, length, average speed, and road slope (see Equation 4.1). The automotive navigation system utilizes

the map database to model the route behavior. The model contains a series of sequentially-connected segments with their respected information. The route behavior model is used as the input to EV components' model in order to estimate their utilization behavior.

$$\overline{s} = \begin{bmatrix} \text{start} & \text{end} & \text{time} & \text{length} & \text{speed} & \text{slope} \\ n_1 & n_2 & t_1 & d_1 & v_1 & \alpha_1 \\ . & . & . & . & . & . \\ . & . & . & . & . & . \\ n_m & n_{m+1} & t_m & d_m & v_m & \alpha_m \end{bmatrix} \tag{4.1}$$

4.2.3 Electric Vehicle

In the previous section, the route where the EV is being driven has been modeled. Here in this section, the behavior of the contributing EV components such as the electric motor, HVAC, and battery pack is described and modeled which is influenced by the environment, e.g. route behavior.

Electric Motor in EV as described in [9, 131, 147] provides the requested force for the vehicle to overcome the road load forces (F_{rd}) for propelling the vehicle at a desired speed and acceleration. The road load forces are caused by the rolling resistance (F_{roll}), aerodynamic drag (F_{aero}), and gravitational (F_{gr}) forces. These forces are affected by the route behavior, i.e. vehicle speed (v) and road slope (α):

$$F_{roll} = mg\left(c_0 + c_1 v^2\right) \tag{4.2}$$

$$F_{aero} = \frac{1}{2}\rho_{air} C_x A \left(v + v_{wind}\right)^2 \tag{4.3}$$

$$F_{gr} = mg \sin\left(\arctan\left(\frac{\alpha}{100}\right)\right) \tag{4.4}$$

$$F_{rd} = F_{roll} + F_{aero} + F_{gr} \tag{4.5}$$

where c_0 and c_1 are the rolling resistance coefficients, m is the total mass of the vehicle, g is the gravitational acceleration constant, ρ_{air} is the air density, C_x is the aerodynamic drag coefficient, A is the effective frontal area of the vehicle, v_{wind} is the head-wind velocity, and α is the percentage of the road slope; 100% represents the slope of 45°. The values for the speed and road slope in each segment are provided by the map database (see Section 4.2.1).

The tractive force (F_{tr}) to overcome the road load forces is provided by the electric motor either in the motor mode or regenerative braking mode, depending on the required torque direction (see Equation 4.6). The power consumed or generated by the electric motor is described by Equation 4.7.

$$F_{tr} = F_{rd} + ma \tag{4.6}$$

$$P_e = \frac{F_{tr} v}{\eta_m} \tag{4.7}$$

where η_m represents the electric motor efficiency when converting electrical to mechanical energy in the motor mode or converting mechanical to electrical energy in the regenerative braking mode. η_m is highly dependent on the motor rotational speed and the generated torque [45, 155]. The parameters used in the equations are extracted from the specifications for Nissan Leaf S [63, 131].

HVAC System is a component under the control of the automotive climate control which is responsible for maintaining the cabin temperature [67, 89, 131]. HVAC system controls heating/cooling coils in order to adjust the air supply temperature. Besides, recent HVAC systems benefit from the Variable Air Volume (VAV) system for more precise control of the temperature and humidity in multi-zone or single-zone with lower energy consumption. These systems utilize variable-speed fans and air ducts to provide the supply air to the zone(s).

The thermodynamics of the cabin (zone) temperature (T_z) is modeled by energy balance equations according to [131] (see Equation 4.8). T_z is influenced by the supply air to the cabin (T_s) and other thermal loads ($\dot{Q}$) including the heat exchange with outside (T_o) and the solar radiation ($\dot{Q}_{solar}$) (see Equation 4.9).

$$M_c \frac{dT_z}{dt} = \dot{Q} + \dot{m}_z c_p (T_s - T_z) \tag{4.8}$$

$$\dot{Q} = \dot{Q}_{solar} + c_x A_x (T_o - T_z) \tag{4.9}$$

where M_c is the thermal capacitance of the air, wall, and the seats inside the cabin and c_p is the heat capacity of the air. The cabin temperature changing rate ($\frac{dT_z}{dt}$) is also controlled by the air flow rate into the cabin ($\dot{m}_z$). The solar radiation ($\dot{Q}_{solar}$) and ambient temperature (T_o) are time-varying factors which can be monitored. The heat exchange through the walls with outside is proportional to the difference between T_z and T_o, the heat exchange coefficient c_x, and the area separating the cabin and outside (A_x).

The cabin air is mixed with the outside air and recirculated back to the system as the system inlet air (T_m). The fraction of the returned air (T_z) from the cabin is d_r, which is controlled by a damper.

$$T_m = (1 - d_r)\, T_o + d_r T_z \tag{4.10}$$

The power consumption of the cooling and heating coils (P_c and P_h) is modeled based on the energy difference between their inlet and outlet air flows. Moreover, the heat exchange between the coolant/evaporator and air is modeled as efficiency parameters (η_h and η_c). Also, the fan power consumption (P_f) is quadratically related to $\dot{m}_z$.

$$P_h = \frac{c_p}{\eta_h}\dot{m}_z(T_s - T_c) \tag{4.11}$$

$$P_c = \frac{c_p}{\eta_c}\dot{m}_z(T_m - T_c) \tag{4.12}$$

$$P_f = k_f(\dot{m}_z)^2 \tag{4.13}$$

where k_f is a parameter capturing the fan efficiency and duct's pressure losses. T_c is the temperature of the cooling coil outlet airflow going to heating coil. The model parameters have been set based on an HVAC specifications [70, 131]. The humidity can be an important factor affecting the HVAC power consumption, but it is not typically directly measured or controlled. Hence, in this chapter, the temperature represents an equivalent dry air temperature at which the dry air has the same specific enthalpy as the actual moist air mixture.

Battery Pack mainly provides the requested power to the EV components. The battery pack contains multiple battery cells connected together in series or parallel. The battery packs are designed according to the requirements specified for each EV [34]. In this chapter, we focus on lithium-ion battery cells which are typically used in existing EV. These battery cells are constantly monitored by the Battery Management System (BMS) for ensuring the reliability and safety requirements [64, 74, 75]. The BMS also distributes and balances the power request to the battery cells in order to extend the battery lifetime and driving range[1].

Battery cell electrical model is described using an equivalent electric circuit model [10, 123, 134]; the battery cell is modeled as a variable-voltage power supply in series with an internal resistance (see Figure 4.4). The ratio of the available charge to the battery capacity is represented by State-of-Charge (SoC). Open-circuit voltage (V_{OC}) of the battery (the variable voltage power supply) and the battery internal resistance (R_b) depend on the SoC value which are modeled by:

[1]Battery packs design space exploration and the BMS design and features review are out of the scope of this thesis.

$$SoC^{+} = SoC - 100 \times \frac{I_b}{C_b} dt \tag{4.14}$$

$$V_{OC} = v_1 e^{v_2 SoC} + v_3 SoC^4 + v_4 SoC^3 + v_5 SoC^2 + v_6 SoC + v_7 \tag{4.15}$$

$$R_b = r_1 e^{r_2 SoC} + r_3 \tag{4.16}$$

where C_b is the rated battery capacity (in Ah) evaluated in nominal discharge rate [10]. I_b is the current drawn from the battery. SoC^{+} represents the resulted SoC after time duration of dt. v_x and r_x parameters can be empirically measured for each specific battery type [10, 123, 134].

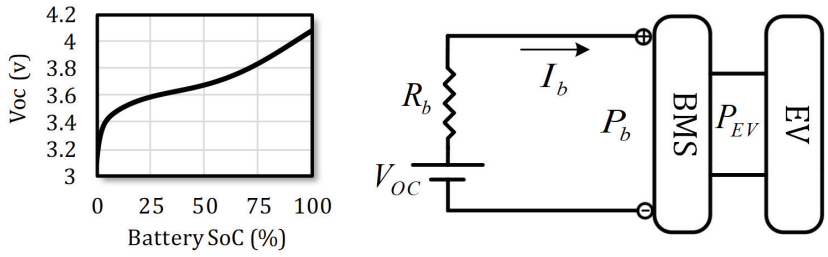

Figure 4.4: Battery cell electrical circuit model.

Battery capacity degrades over time depending on the battery utilization. The battery stress, number of discharge cycles, discharge current, and battery temperature influence this capacity loss (Q_{loss}) [64, 75, 98]. In this chapter, Q_{loss} is modeled considering the discharge current:

$$Q_{loss} = l_1 e^{-l_2/(RT_{bat})} I_b^{l_3} \tag{4.17}$$

where R is the ideal gas constant. l_x parameters are the coefficients in the model that can be measured empirically [6, 98, 123, 134]. The battery temperature T_{bat} is assumed to be maintained and its influence on the battery operation [75] is out of the scope of this chapter.

4.3 Control and Optimization

In the previous sections, the primitive data and CPS models required for implementation of our eco-friendly automotive climate control and navigation system methodology have been defined in details. The map database generated in Section 4.2.1 is traversed by the automotive navigation system for routing purpose. The equation-based models defined for route behavior and EV components will be used to evaluate the battery lifetime and EV energy consumption with respect to each route and weather. Thereby, we are able to estimate how eco-friendly a route is. On the other hand, the predicted route will be provided by the automotive navigation system for the automotive climate control in order to optimize the HVAC system utilization; the equation-based models defined for EV components will be used to estimate the EV states in the near-future in order to optimize the HVAC control inputs while maintaining the cabin temperature. This integration helps the methodology to consider the trade-off existing in the climate control and navigation system in order to jointly optimize the route and HVAC system for further battery lifetime and driving range improvement.

4.3.1 Routing Algorithm

A routing algorithm is required as part of our automotive navigation system in order to find the optimal route for longer battery lifetime and driving range. Although different routing algorithms and data structures exist with various complexities and performances [42], our navigation system is orthogonal to any routing algorithm and map data structure. In this chapter, the Bellman-Ford algorithm is used as the routing algorithm. The routing algorithm searches through the weighted directed graph (map database) which may be structured as multiple matrices (see Section 4.2.1). The weight function of the routing algorithm evaluates a cost metric of driving on each segment; as shown in Algorithm 2, the route behavior infor-

mation for the respected *segment* connecting a *target* node to a *neighbor* node is extracted (lines 1-4). In lines 5-7, the power consumption of the electric motor, HVAC, and the EV is estimated for the *segment* using the modeling equations (see Section 4.2.3), route behavior, and current EV state (*target_state*) [*Distance_Driven*, *Time_Driven*, *Energy_Used*, *Capacity_Lost*, *weight*, SoC, T_z]. In line 8, the energy consumed in EV (*Energy*), change in the battery *SoC* (*dSoC*), and the amount of battery capacity lost (Q_{loss}) are estimated using the battery model. In line 9, the variables contributing to weight function are stored in a vector. These values will be accumulated later to find the EV state at each node and to select the node with the least total weight. In line 10, the weight of the segment is calculated. The weight parameters (w_x) define the priority of minimizing each variable. They are adjusted based on the following order of priorities from high to low: Q_{loss} for improving the battery lifetime, *Energy* for further driving range, and *time* to avoid sacrificing too much driving time.

ALGORITHM 2: Evaluate Segment Weight

Input: Target Node *target*
Input: Neighbor Node *neighbor*
Input: Target Node EV State *target_state*
Input: Connecting Segment *segment*
Output: Segment Weight Vector $\overline{weight}$
Output: Segment Weight *weight*

`// extracting segment information`
1 *distance* = *segment* (distance)
2 *speed* = *segment* (speed)
3 *time* = *segment* (time)
4 *slope* = *segment* (slope)

`// estimating system power consumption`
5 P_{motor} = **Electric_Motor_Model** (0, *speed*, *slope*)
6 P_{HVAC} = **HVAC_Model** (*target_state* (T_z))
7 $P_{EV} = P_{HVAC} + P_{motor}$

`// energy consumption & capacity loss estimation`
8 [*Energy*, *dSoC*, Q_{loss}] = **Battery_Model** (P_{motor}, ... *target_state* (SoC), *time*)

`// segment weight calculation`
9 $\overline{weight}$ = [*distance*, *time*, *Energy*, *dSoC*, *Qloss*]
10 $weight = \omega_1 \times distance + \omega_2 \times time + \omega_3 \times Energy + \omega_4 \times Q_{loss}$
11 **return** [$\overline{weight}$, *weight*]

► **Lemma 1:** Having a weighted directed graph with no negative-weight cycle, Bellman-Ford algorithm can be applied to find the minimum weight routes to the nodes.

► **Lemma 2:** In any segment in graph, *distance*, *time*, and Q_{loss} variables have positive values. However, there can be a segment where *Energy* variable has positive or negative value when EV is consuming or generating power. Hence, there is a segment where *weight* variable is positive or negative.

► **Lemma 3:** The law of conservation of energy states that there cannot be a cycle in the graph where the accumulated *Energy* variable has a negative value.

► **Theorem:** Due to Lemmas 2 and 3, there cannot be a negative-weight cycle in the graph. Hence, according to Lemma 1 and the defined weight function (Algorithm 2), Bellman-Ford algorithm can be applied to find the minimum weight route, which will improve the battery lifetime and driving range while not sacrificing the driving time.

The main routing problem in this chapter is a single-pair shortest-path problem. However, this problem can be solved by solving the single-destination shortest-path problem without adding any complexity [42]. The Bellman-Ford routing algorithm is implemented in Algorithm 3. The number of nodes in the map is saved in line 1. Matrix $\overline{state}$ which consists the EV state variables at each node is initialized (line 2). In line 3, matrix $\overline{t}$ is created to store the predecessor of each node. Since the algorithm is traversing from the destination node, the EV state is initialized to zero for the *fid* node (line 4). In the for loop (lines 5-15), the weights of the nodes get updated ($\#\_nodes - 1$) times regarding the segment weights. *target* and *neighbor* nodes are swapped since the algorithm is traversing from the destination (lines 7-8). The weight for each segment is evaluated and the **update** function adds the *segment* weight to the current *target*'s state and weight (lines 9-10). In lines 11-14, the current weight and estimated weight (after traversing *segment*) of the *neighbor* node are evaluated and the *neighbor*'s state is updated to the one with the less weight. In line 15, the predecessor of *neighbor* node is updated with the better possible node (*target*) in the $\overline{t}$ matrix.

ALGORITHM 3: Single-Destination Routing Algorithm

Input: Segments $\overline{s}$
Input: Nodes $\overline{n}$
Input: Destination Node *fid*
Output: Trace $\overline{t}$

```
1  #_nodes = |n̄|                                          // number of nodes
2  state̅ = inf (#_nodes, 7)                               // nodes' current state
3  t̄ = zeros (#_nodes, 1)                                 // predecessors of nodes
4  initialize state̅ (fid)                                 // initialize destination node
   // multiple passes over the segments
5  for i = 1 in (#_nodes − 1) do
       // checking each segment
6      for segment in s̄ do
           // selecting nodes of edge
7          target = segment (end)
8          neighbor = segment (start)
           // evaluate the segment weight
9          seg_weight = eval_seg_weight (neighbor, ...
                                target, state̅ (target), segment)
           // neighbor state prediction
10         pred_state = update (state̅ (target), seg_weight)
           // current and predicted neighbor weight
11         neighbor_weight = (state̅ (neighbor)) (weight)
12         pred_neighbor_weight = (pred_state) (weight)
           // relaxing the neighbor node
13         if neighbor_weight > pred_neighbor_weight then
14             state̅ (neighbor) = pred_state
15             t̄ (neighbor) = target
               // update state and predecessor
16 return [t̄]
```

4.3.2 Route Prediction

The route may change while driving due to any unexpected events, e.g. turns. Despite this, the automotive navigation system is responsible for providing the optimal route to the destination node, starting from any node where the EV is located. Using the routing algorithm described in Section 4.3.1 (Algorithm 3), the route with the least weight from any node to the destination node is evaluated. On the other hand, the navigation system is required to provide a sufficient predicted route for the automotive climate control. Hence, a route prediction algorithm needs to be implemented for the navigation system.

We use the least-weighted route to the destination, starting from a specific node as the predicted route for that node. The **route_prediction** algorithm utilizes the $\overline{t}$ matrix provided by the routing algorithm to evaluate the route (single-pair shortest-path problem). In Algorithm 4, $\overline{t}$ matrix which contains the predecessors of nodes is iterated through, in order to evaluate the predicted route (*route*).

ALGORITHM 4: Route Prediction

Input: Starting Node *sid*
Input: Trace $\overline{t}$
Output: Optimal Route *route*

1 $iterate = sid$
2 $route = [iterate]$
`// iterate through the nodes until the end`
3 **while** $\overline{t}\,(iterate) \neq 0$ **do**
4 $\quad iterate = \overline{t}\,(iterate)$ `// find predecessor node`
5 $\quad route = [route; iterate]$ `// add the node to route`
6 **return** $[route]$

4.3.3 Automotive Climate Control

The behavior of an HVAC system has been described in Section 4.2.3 using ordinary differential equations. The current state of an HVAC system is defined by multiple variables. Automotive climate control is responsible for adjusting the control inputs to the HVAC system for maintaining the system output and state variables in a specific range and target. The battery lifetime-aware automotive climate control methodology in [131] has utilized an MPC algorithm for estimating all the variables contributing to the system in a receding horizon (control window) by having the EV power requests before hand. In each time segment, the MPC algorithm optimizes these variables in order to minimize a cost function considering the constraints put by the physical behaviors and control limits. Then, the optimized control inputs are applied to the HVAC system and the variables are updated according to the new system state. Since the control is done in discrete time, the model equations also need to be defined in discrete time. The time segments are specified according to the segments of the predicted route provided by the automotive navigation system.

As shown in Figure 4.5, the automotive climate control receives the predicted route behavior from the automotive navigation system and utilizes the electric motor model (Section 4.2.3) in order to estimate the EV power requests for the control window (steps 1-3). Then, according to the current HVAC state, estimated EV power requests, and HVAC model (Section 4.2.3) the optimization variables and their relationships are defined and initialized (steps 4-7):

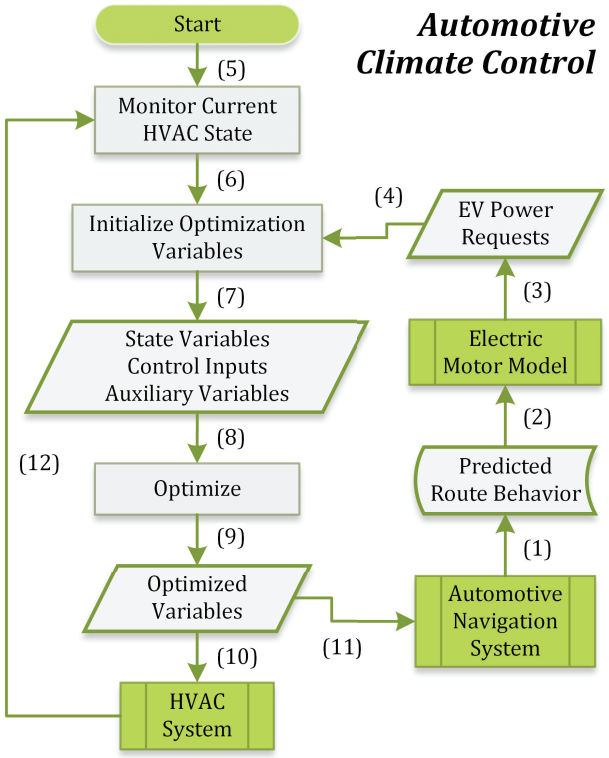

Figure 4.5: Flowchart of the automotive climate control.

$$x^{k|t} = [T_z, SoC]' \tag{4.18}$$

$$i^{k|t} = [T_s, T_c, d_r, \dot{m}_z]' \tag{4.19}$$

$$u^{k|t} = [T_m, P_h, P_c, P_f, P_e, dt]' \tag{4.20}$$

where $x^{k|t}$, $i^{k|t}$, and $u^{k|t}$ are respectively the values of the state variables, control inputs, and auxiliary variables at time t_k predicted at time t; k is the index of the segment in the control window. The model equations, system dynamics, and constraints can all be expressed in the following form:

$$F_j\left(\begin{bmatrix} x^{k|t} \\ i^{k|t} \\ u^{k|t} \\ x^{k+1|t} \end{bmatrix}\right) = 0 \qquad A^{k|t}\begin{bmatrix} x^{k|t} \\ i^{k|t} \\ u^{k|t} \\ x^{k+1|t} \end{bmatrix} \leq b^{k|t} \tag{4.21}$$

where F_j is the j^{th} non-linear equality constraint function for the optimization problem.

The matrices $A^{k|t}$ and $b^{k|t}$ define the linear inequality constraints at time t_k. Also, inside the control window, the predicted values for the state variables T_z^+ and SoC^+ need to be applied to the state variables of the next segment (t_{k+1}).

The cost function for optimization at time t is as follows:

$$C^t = \sum_{\tau=t_1}^{t_N} w_1(P_f + P_c + P_h) + w_2(Q_{loss}) + w_3(T_z - T_{target})^2 \tag{4.22}$$

where N is the number of segments in the control window of the MPC, $w_1(P_f+P_c+P_h)$ is for reducing the HVAC power consumption with the weight value of w_1, $w_2(Q_{loss})$ is minimized for battery lifetime improvement with the weight value of w_2, and $w_3(T_z - T_{target})^2$ stabilizes the cabin temperature around the target temperature (T_{target}) with the weight value of w_3. The values for the weight parameters are adjusted arbitrary for battery lifetime improvement mainly. It needs to be mentioned that a trivial trade-off exists between extending the battery lifetime, minimizing the HVAC power consumption, and stabilizing the cabin temperature.

The optimization problem formulated in Equation 4.18-4.22 is executed and optimized variables are saved (steps 8-9). The optimal control inputs are applied to the HVAC system at each segment (step 10). The optimal state variables are sent to the navigation system for routing purposes (step 11). Finally, the climate control goes to the next segment.

4.3.4 Automotive Navigation System

The automotive navigation system is responsible for providing the EV with the optimal route and the automotive climate control with a predicted route. As shown in Figure 4.6, the routing algorithm (see Section 4.3.1) is executed in the pre-processing stage to evaluate all the optimal routes from any node to the destination node (steps 1-2). This data is stored for the run-time algorithm after step 3. The *current* node is lo-

cated using the Global Positioning System (GPS) and one of the segments connecting to the *current* node is selected (steps 4-5). The *neighbor* node connected to the *segment* is input to the **route_prediction** function (see Section 4.3.2) in order to evaluate the predicted route (steps 6-8). The predicted route is sent to the automotive climate control methodology for estimating the optimized HVAC state variables (steps 9-11). The predicted route and the optimized variables of the HVAC system are used to evaluate the accumulated weight of driving the route to the destination (see Section 4.3.1) (steps 11-13). The segment with the minimum estimated route weight will be selected and suggested to the driver (using an in-vehicle infotainment) (steps 13-15). The navigation system will continue to the next segment and if the destination is reached, it will terminate (steps 16-17).

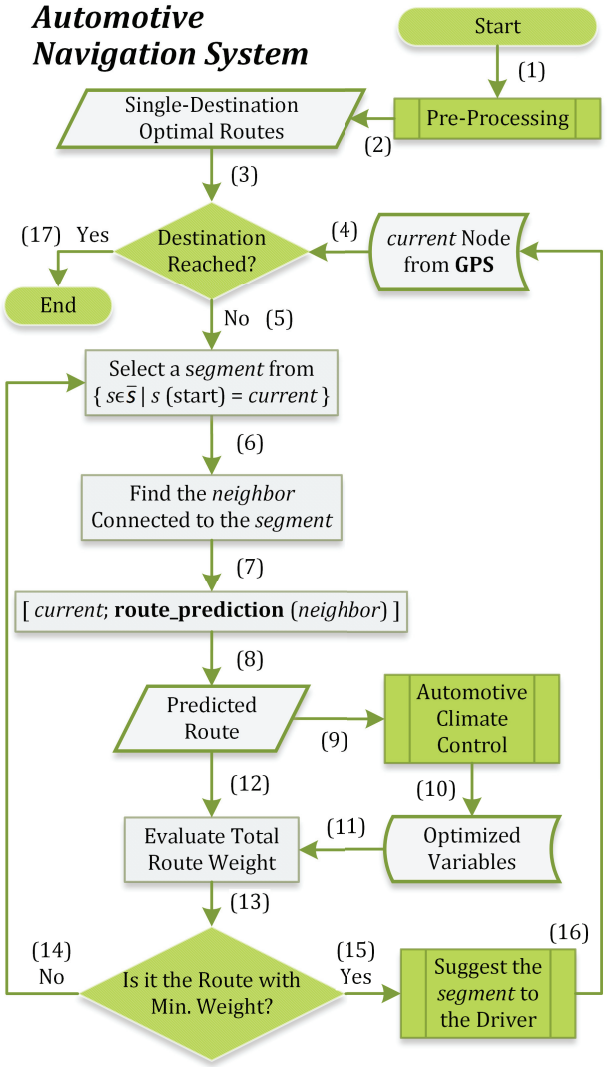

Figure 4.6: Flowchart of the automotive navigation system.

4.4 Experimental Results

4.4.1 Experiment Setup

The map database and route behavior data (see Sections 4.2.1 and 4.2.2) are extracted from the real-life databases [8, 60] considering the map of Orange County in California, U.S.A. The parameters in equations defined in Section 4.2.3 for describing the electric motor, HVAC system, and battery pack are according to the real-life specifications of Nissan Leaf S [63, 131] and automotive design and simulator tools: AMESim [9] and ADVISOR [155] (see Section 4.2.3). The values of the parameters are set and adjusted so that the CPS dynamics are verified by the experimental data gathered from the existing references. The map database generation, describing the physical equations, and implementing the algorithms in the methodology have been conducted in MATLAB/Simulink [7] and JavaScript [53]. For performance evaluation, we have driven the EV for various routes and weather, monitored, and analyzed different parameters.

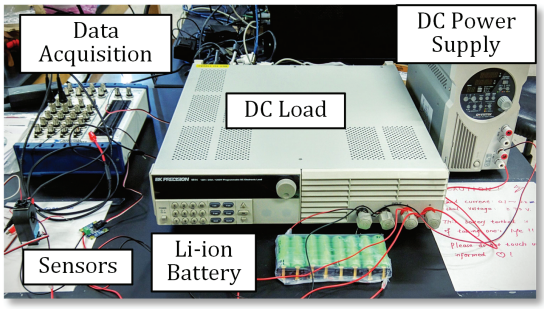

Device	Model	Description
Data Acquisition	*NI USB-6229 M ni.com*	monitor the sensor values
DC Power Supply	*Instek PSB-2400L2 gwinstek.com*	emulating the regenerative breaking system
DC Electronic Load	*BK Precision 8514 bkprecision.com*	emulating the EV power requests
Battery Cell	*NCR18650B panasonic.com*	utilized as the battery pack inside the EV
Sensors	*Current Voltage*	measuring the battery current and terminal voltage for estimating the SoC

Figure 4.7: Experimental test bed hardware.

Moreover, the test bed shown in Figure 4.7 has been utilized to validate the experiments. The required EV behavior is generated by the mentioned simulators while implementing the climate control and navigation system. Then, the test bed hardware (physical plant) uses the simulated data to emulate the EV power requests using the programmable DC power

supply and DC load while utilizing the battery cells [6] as the battery pack (scaled-down) in the EV. The required battery operating parameters, e.g. current and voltage, are monitored using the data acquisition device.

4.4.2 Results and Analysis

We compare the performance of our eco-friendly automotive climate control and navigation system methodology with the state-of-the-art methodologies:

1) ***Fastest:*** the route with the least driving time is selected [8] and the HVAC system is controlled by the fuzzy-based controller to maintain the cabin temperature around the target [67].

2) ***Energy-Aware:*** the route with the least EV energy consumption is selected [150]. The energy consumption of the HVAC for maintaining the cabin temperature is also estimated and considered in the routing. The HVAC system is controlled by the fuzzy-based controller to maintain the cabin temperature around the target [67].

3) ***Battery-Aware:*** our novel navigation system is implemented which estimates the battery lifetime and navigates accordingly. The energy consumption of the HVAC for maintaining the cabin temperature is also estimated and considered in the routing. However, the HVAC is still under control of a fuzzy-based controller [67].

4) ***Eco-Friendly:*** our novel automotive navigation system and climate control methodology is implemented thoroughly. Herein, the integration between the climate control and the navigation system is leveraged to jointly optimize the route and HVAC system for further battery lifetime and driving range improvement.

a) Time-Domain Analysis: the methodologies have been applied for multiple test cases. As shown in Figure 4.8, the EV located at UCI is being driven towards a shopping center and a beach as test cases ($30°C$ weather). The routes selected by the methodologies and driving time are labeled on the map. Each methodology optimizes the route for different goals. Hence, the driving time, EV energy consumption, and battery lifetime which are affected by route behavior also vary. You may refer to Table 4.1 for further details.

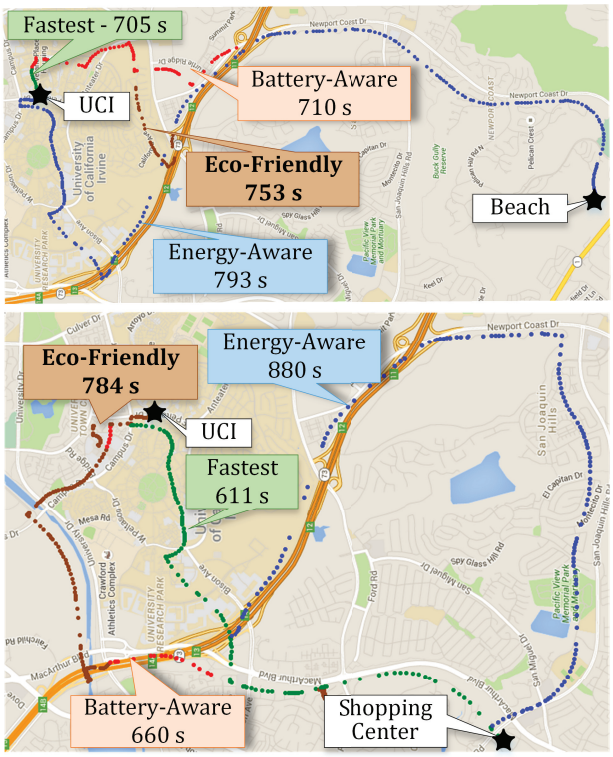

Figure 4.8: Selected routes by the navigation system methodologies. (The traces are overlapped at some points)

The behavior of the HVAC power consumption and the cabin temperature are compared for these methodologies while driving the EV from UCI to a grocery store in $35°C$ weather. As shown in Figures 4.9(a) and 4.9(b), the first three methodologies (Fastest, Energy-Aware, and Battery-Aware) implement the fuzzy-based controller in which the main target is to stabilize the cabin temperature around the target. Hence, the HVAC power consumption and the cabin temperature are almost stable and flat. However, in our eco-friendly methodology, the climate control utilizes the predicted route behavior provided from the navigation system to estimate the EV power requests and optimize the HVAC system.

As shown in Figures 4.9(a) and 4.9(b), the HVAC power consumption is adjusted so that to compensate the power consumption of the electric motor. For instance, the HVAC power consumption is reduced when the electric motor is estimated to consume more. To maintain the cabin temperature, the HVAC power consumption is increased when the electric motor is

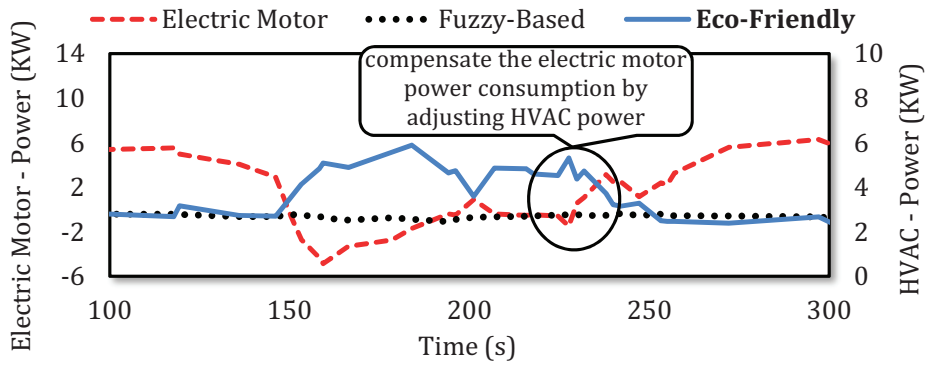

(a) HVAC power consumption.

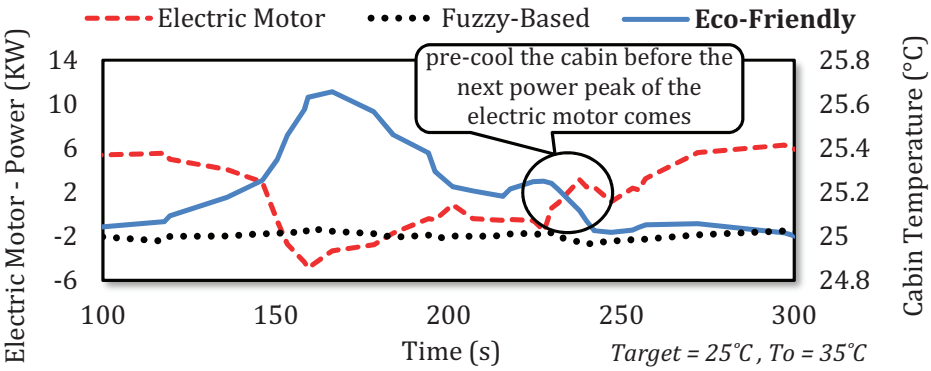

(b) Cabin temperature.

Figure 4.9: Time-domain analysis of climate control and navigation system integration.

estimated to consume less. Thereby, the battery stress is reduced which extends the battery lifetime and driving range. This behavior illustrates the integration between our automotive navigation system and climate control.

b) Ambient Temperature Analysis: the HVAC system consumes differently for various ambient temperatures. Hence, the EV energy consumption and the battery lifetime are also affected. In order to compare the performance of these methodologies, the EV has been driven from UCI to a grocery store for various ambient temperatures while under control of the four different methodologies. The target temperature for the automotive climate control has been set to $25°C$ for all the methodologies.

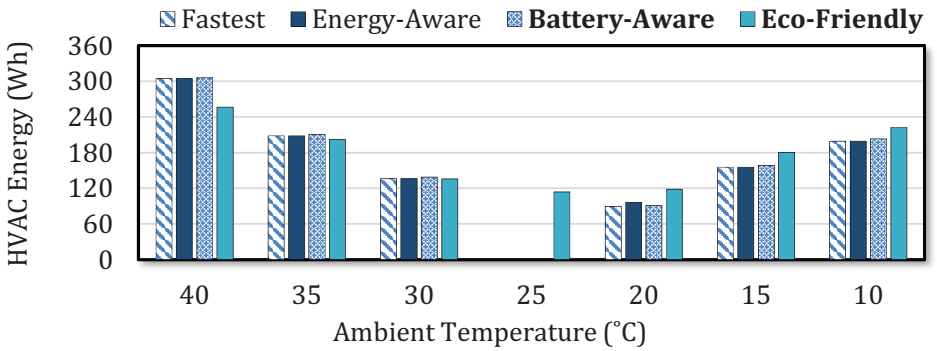

Figure 4.10: HVAC energy consumption for different ambient temperatures.

As shown in Figures 4.10 and 4.11, the HVAC energy consumption and total EV energy consumption decrease when the ambient temperature is closer to the target temperature. The energy-aware methodology attempts to reduce the EV energy consumption. However, as the temperature difference increases, the fastest and the energy-aware route methodologies perform almost the same. This is due to the fact that the HVAC energy consumption gets so significant that decreasing the driving time is more reasonable for saving energy than driving through a longer route which might save electric motor energy.

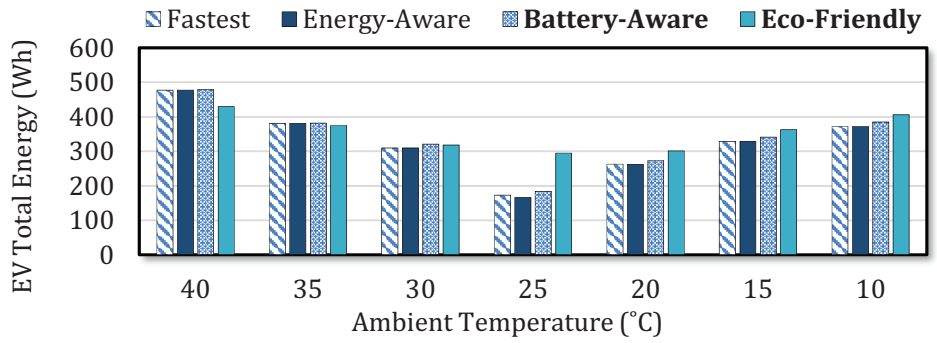

Figure 4.11: EV energy consumption for different ambient temperatures.

The battery capacity loss for the methodologies is compared with the fastest route in percentage. As shown in Figures 4.11 and 4.12, the battery capacity loss improvement is also influenced by the ambient temperature. However, by comparing the energy-aware and battery-aware methodologies, decreasing the EV energy consumption does not result in better battery capacity loss, as this is expected behavior. The battery-aware methodology has improved the

battery lifetime up to 3%, however our eco-friendly methodology has improved the battery lifetime up to 24%. The battery lifetime improvement is because of the joint optimization of the route and the HVAC system. Our eco-friendly methodology may decrease the EV energy consumption (up to 17%) for reducing the battery stress. Under certain circumstances (e.g. $T_o = 25°C$), it even increases the HVAC energy consumption in order to compensate the electric motor power consumption for reducing the battery stress. The weight parameters in the optimization algorithm affect the trade-off explained here (see Section 4.3.3).

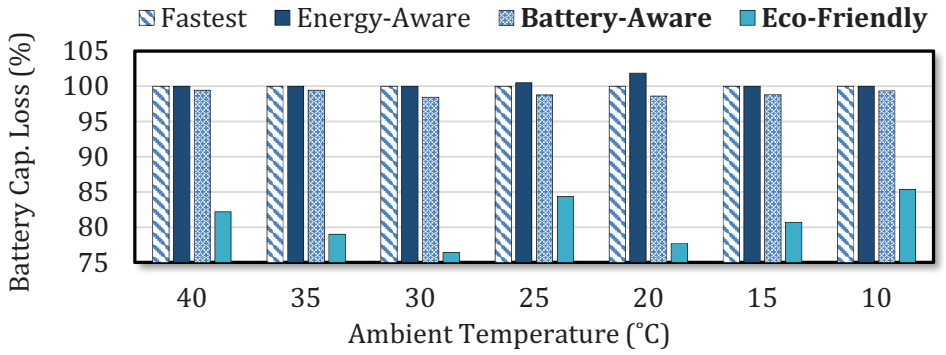

Figure 4.12: Battery capacity loss for different ambient temperatures.

c) Route Analysis: the electric motor energy consumption is influenced by the route behavior. Moreover, the HVAC system energy consumption is also dependent on the driving time. Hence, the total EV energy consumption and battery capacity loss are influenced and the methodologies may perform differently for each route. As shown in Table 4.1, the performance of these methodologies are compared for each route in details. Since, high HVAC energy consumption minimizes the influence of the route behavior on the methodologies performance, the EV has been driven in $30°C$ weather.

Table 4.1: Performance analysis of navigation system methodologies for different routes.

Start	End	Duration Time (s)				EV Energy Consumption (Wh)				Battery Cap. Loss Improvement (%)		
		Fastest	Energy-Aware	**Battery-Aware**	**Eco-Friendly**	Fastest	Energy-Aware	**Battery-Aware**	**Eco-Friendly**	Fastest	Energy-Aware	**Battery-Aware**
(1)	(2)	704.9	793.4	709.8	753.1	633.4	485.7	633.5	699.9	-1.5	-9.1	-1.1
(1)	(3)	611.4	880.3	660.4	784.1	837.6	705.0	851.7	922.0	-5.6	-25.0	-4.8
(1)	(4)	585.1	589.7	594.5	589.7	580.4	546.7	546.8	591.0	-11.8	-10.3	-9.7
(1)	(5)	336.3	336.3	341.2	341.2	309.4	309.4	321.2	318.0	-23.6	-23.6	-22.4

(1) UCI: 33.6439 °, -117.8345 ° *(2) Beach: 33.5843 °, -117.8476 °* *(3) Shopping Center: 33.6136 °, -117.8685 °*
(4) Airport: 33.6776 °, -117.8604 ° *(5) Grocery Store: 33.6637 °, -117.8263 °* *Ambient Temperature = 30°C, Target = 25°C*

The battery capacity loss resulted in our eco-friendly methodology has been compared with other methodologies and the improvements (%) have been listed in the table. The battery-aware methodology has improved the battery lifetime compared to the fastest and energy-aware methodologies by optimizing the route (up to 3% compared to the fastest). However, our eco-friendly is improving the battery lifetime further up to 24% by doing the joint optimization.

4.5 Concluding Remarks

Major design challenges in EV as automotive CPSs are mainly due to their energy-restricted and aging batteries. The battery capacity - major bottleneck of driving range - degrades over time which troubles the drivers with their daily trips. We noticed that route behavior and weather influence the electric motor and HVAC power consumption. However, existing automotive climate controls and navigation systems have not considered the trade-off between the route behavior, electric motor, and HVAC energy consumption and their influence on the battery lifetime and driving range. Hence, in this chapter, we have presented a novel jointly-optimized eco-friendly automotive climate control and navigation system methodology in which the integration of these two systems helps us to optimize the route and the HVAC for improving the battery lifetime and driving range. We conducted multiple experiments using our real-life data and models to compare the performance of our methodology with the state-of-the-arts for different weather and route behavior. We have seen up to 24% improvement in battery lifetime and 17% reduction in energy consumption.

Chapter 5

Drive Profile Optimization

5.1 Introduction and Related Work

The number of EV utilized by daily drivers is growing significantly everyday. Since EV are recharged from the power grid, their penetration into the power grid is also increasing significantly [16, 41, 132, 136, 137, 144]. The electricity load (power demanded) by the EV chargers is mainly dependent on their charging rates, e.g. Level I, Level II, and Level III chargers consume about 1.4 KW, 3.3-6.6 KW, and 50-70 KW, respectively [47]. Therefore, the increase in the EV penetration level may impact the pattern of the power grid load by increasing the daily peaks [46, 114]. This penetration has been studied thoroughly and it has been shown that it may affect the grid reliability and efficiency significantly; the components making up the power grid are designed to operate efficiently and safely in a certain range. However, by putting sudden load of EV charging on the power grid, the energy efficiency may drop due to the increased daily peaks; the components' thermal constraints may get violated; and the operating voltage may drop which causes the components to malfunction [30, 113]. Furthermore, the intermittent behavior of the EV charging process, especially using in-house EV chargers is not economical for the power grid utilities. Since the peak power demand is higher than the base power demand, the utilities have to operate more power plants in order to satisfy the peak demand for a short period of time.

On the other hand, we discussed in previous chapters that deploying EV poses new design challenges (see Chapter 1). The electrical energy in EV is mainly provided by a battery pack [92, 138]. The deliverable energy (capacity) of the battery pack restricts the driving range. The capacity is limited by stringent battery design constraints and parameters, e.g. size, weight, volume, and material. Moreover, the charging process of an EV battery pack is troublesome due to its long duration, scarcity of fast charging stations, and cost of recharging [51, 103]. The severity of driving range issue becomes more evident when comparing the fuel efficiency map of an EV with an ICE vehicle.

5.1.1 Motivational Case Study

We performed an experiment using the available data provided in manufacturers' forums and by the Environmental Protection Agency (EPA) [3, 11]. We compared the relationship between the fuel economy and speed in an EV, with an ICE vehicle. Our experiment shows that, EV and ICE vehicles have very different characteristics. As shown in Figure 5.1, the efficiency of an ICE vehicle is almost at its maximum when driving around 40-60 miles per hour (mph). However, for an EV, the efficiency drops significantly as the speed increases to more than 25 mph. Moreover, the available battery capacity decreases in higher discharge rates (rate-capacity effect) [90] (see Section 5.2.3 for more details). Therefore, if we consider this effect, the fuel economy of the EV might decrease significantly at higher speeds compared to ICE vehicles.

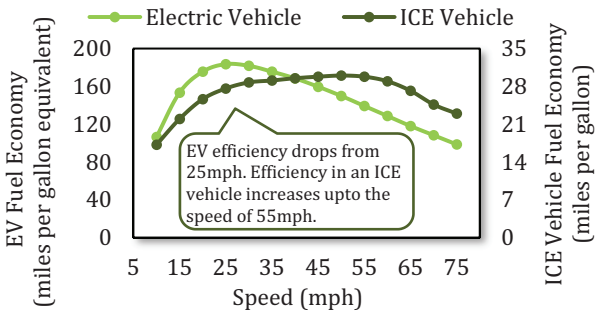

Figure 5.1: Fuel economy comparison between an EV and an ICE vehicle [3, 11].

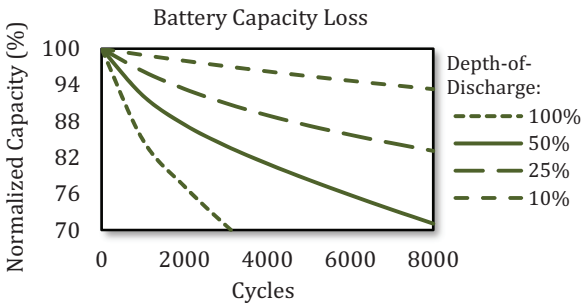

Figure 5.2: Battery capacity loss for various depths of discharge [158].

Summary and conclusion from observations: the analysis above illustrates the issue with efficiency in different speeds and how it is different for the two types of EV and ICE vehicles. Furthermore, the battery capacity degrades overtime due to the increase in the internal resistance. The battery capacity degradation causes major efficiency and reliability issues for the EV. The battery cells typically become useless after 20% of capacity degradation [98, 152]. The number of cycles a battery cell can be used to reach this point is considered as the battery lifetime. Analyzing the experimental data of battery cells shows that the battery lifetime varies significantly based on the Depth-of-Discharge (DoD) (see

Figure 5.2) [158]. This issue will enforce huge cost of battery replacement on the EV drivers or even manufacturers. For instance, the cost to replace a battery pack is more than 12,000$ for Tesla Model S 85 KWh [3] and 5,500$ for Nissan Leaf S [4]. Even though, the battery pack itself costs significantly more than the above-mentioned cost.

Moreover, the driving route on top of the driving speed (as shown in Figure 5.1) has been shown to affect the EV energy consumption in short term and the battery lifetime in long term (see Chapter 4 for further details). Hence, the time and cost for recharging and electricity load are affected by the driving route. Each daily trip also encapsulates the departure/arrival time besides the driving route which are modeled as a *drive profile* (see Section 5.2.1). The drive profile in higher level influences the driving route, energy consumption, battery lifetime, electricity cost, charging time, and electricity load.

Battery management systems are responsible for monitoring and controlling the battery cells. At run time, the BMS may monitor the status of the battery cells and control their power request in order to prevent over discharging, over charging, thermal violation, and thereby improve the driving range and battery lifetime [20, 78, 86, 131, 133, 134, 147, 151, 151, 158, 159]. Moreover, route selection algorithms are implemented that consider traffic and energy consumption in order to find the most efficient route based on the data gathered from the vehicle efficiency [54, 150] (see Chapter 4 for further details). However, the solution is limited to finding the optimum route just for avoiding the *"range anxiety"* at a particular time (short-term decision making). Furthermore, the existing drive managements do not consider battery lifetime, where it is a parameter affected by consecutive EV usages and its value cannot be estimated unless in the long run. Therefore, drivers may need to take an informed decision of their route selection everyday based on the EV and battery characteristics.

On the other hand, to address the concerns with the power grid and electricity cost, multiple EV charging algorithms for managing the power demand have been proposed. In [16], authors have analyzed the impact of in-house EV chargers on the load shape and compared

it with the case in which the Time-Of-Use (TOU) rates have been applied for load shifting [120]. Moreover, smart EV charging algorithms are proposed in which power grid load prediction and power demand estimation are conducted for optimizing the charging schedule in order to decrease the electricity cost [30, 43]. However, the existing charging algorithms do not consider the EV daily trips, their required energy, the resulting battery lifetime, and electricity cost while optimizing the charging process.

Hence, in this chapter, we model and estimate the behavior of the EV energy consumption and battery lifetime with respect to the drive profile and EV characteristics. The EV charging process and its influence on the power grid are modeled and estimated. Based on the system modeling and estimation, our novel Optimized Charge and Drive Management (OCDM) jointly optimizes the drive profile encapsulating the driving routes and departure/arrival time with the EV charging process. The optimization will improve the EV driving range and battery lifetime, decrease the charging electricity cost, and diminish the load on the power grid while scheduling the daily trips according to the driver's preferences.

5.1.2 Problem and Research Challenges

In summary, the problem of improving the EV driving range and battery lifetime, decreasing the charging cost, and diminishing the load on the power grid poses the following key challenges:

1. EV driving range and battery lifetime are significantly affected by the driving route.
2. Battery characteristics, especially rate-capacity effect influence the EV energy consumption and battery lifetime degradation.
3. The required energy and cost for recharging are dependent not only on the charge management but also on the drive management.

4. Scheduling the daily trips, e.g. departure and arrival times, may also affect the charging, driving processes, and the EV parameters.

5.1.3 Novel Contributions and Concept Review

To address the above-mentioned challenges, a novel EV charge and drive management methodology (OCDM) is proposed that employs:

1. **System Modeling and Estimation (Section 5.2):** the dynamic behavior of the system components are described and modeled using linear/non-linear and Ordinary Differential Equations (ODE).
    - **Drive Profile:** the behavior and parameters incorporated with a daily trip are modeled as a drive profile which encapsulates the driving route behavior, departure, and arrival times.
    - **Electric Vehicle:** the power generation/consumption by the electric motor in EV power train and its influence on the battery parameters are modeled and estimated according to the drive profile.
    - **Power Grid:** the EV charging process and its influence on the power grid parameters, e.g. load, are modeled and estimated.
2. **OCDM Methodology (Section 5.3):** our methodology considers and estimates EV battery lifetime, energy consumption, electricity cost, and load profile of the power grid. Then, it selects the optimized driving routes, schedules the departure/arrival time (according to driver's preferences), and optimizes the EV charging process. The optimization problem of the methodology is formulated as a Mixed Integer Linear Programming (MILP) [58, 84] (see Section 5.3.2).

3. **Experiment and Analysis of the Methodology (Section 5.4):** the performance of our methodology is compared with other state-of-the-art methodologies in terms of EV energy consumption, driving time, battery lifetime, electricity cost, and power grid parameters for various driving routes and benchmark EV. Moreover, the execution time and memory usage have been measured for different time resolutions and number of days in a charge and discharge cycle to analyze the scalability.

Figure 5.3 illustrates the data and model inputs to our OCDM and the components forming the methodology. In OCDM, the system behavior, e.g. power grid load, route behavior, EV energy consumption, etc. are modeled and estimated. Then, the behavioral estimation of the system is leveraged for optimizing the variables of driving and charging the EV using MILP. The optimized drive profile and charging process will improve the EV driving range and battery lifetime, decrease the charging cost, and diminish the load on the power grid while considering the driver's timing preference.

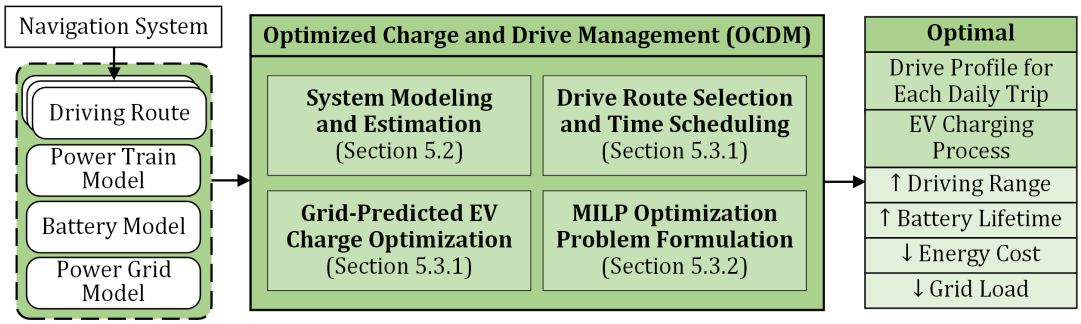

Figure 5.3: Abstract illustration of our optimized charge and drive management for EV.

5.2 System Modeling and Estimation

Adequate information about the dynamic behavior of the system components enables the charge and drive management to estimate the variables and parameters contributing to the control process. For instance, the driving route behavior (Section 5.2.1) is used to evaluate

the EV power consumption/generation and battery parameters at each instance of time. This estimation requires the modeling of the EV power train (Section 5.2.2) and battery pack (Section 5.2.3). Moreover, by knowing the power grid model and the EV charging process (Section 5.2.4), the energy consumed from the grid, the recharging cost, and power grid load are estimated.

5.2.1 Drive Profile

The driving route behavior needs to be modeled for estimating the EV power generation and consumption. The features of a driving route such as speed, acceleration, and road slope can be used to make up the drive profile. Moreover, drivers typically utilize GPS-based navigation systems for finding the route to the destination. Hence, the driving route is known before driving. Driving route features can be gathered using the existing map databases and APIs provided by the navigation systems [8]. The drivers are typically forced to maintain a certain speed according to the route condition and traffic. Gathering this information helps us to model the driving route. A drive profile encapsulates: 1) the steps to reach the destination (s); 2) the length of each step (ι_s); 3) the average speed of the vehicle at each step (υ_s); and 4) the slope of the route at each step (α_s). Therefore the drive profile is a vector of n tuples (ι_s υ_s α_s), in which n is the number of steps in the route.

Moreover, a daily trip contains departure and arrival times besides the driving route. Hence, this timing information is also encapsulated in the drive profile for each trip. Standard drive cycles (e.g. NEDC) typically used for test, simulation, and verification of vehicles performance can be used as the drive profiles [107]. However, these drive cycles lack detailed and real-life driving information such as departure, arrival times, etc. Hence, they cannot be applied to our methodology in this chapter.

5.2.2 Power Train

The power train in an EV is responsible for providing the requested propelling force by using the electrical energy from the battery pack. Given the drive profile to the EV power train model, the power requests of the EV are estimated and measured. Figure 5.4 depicts an EV architecture to help us describe our EV power train model.

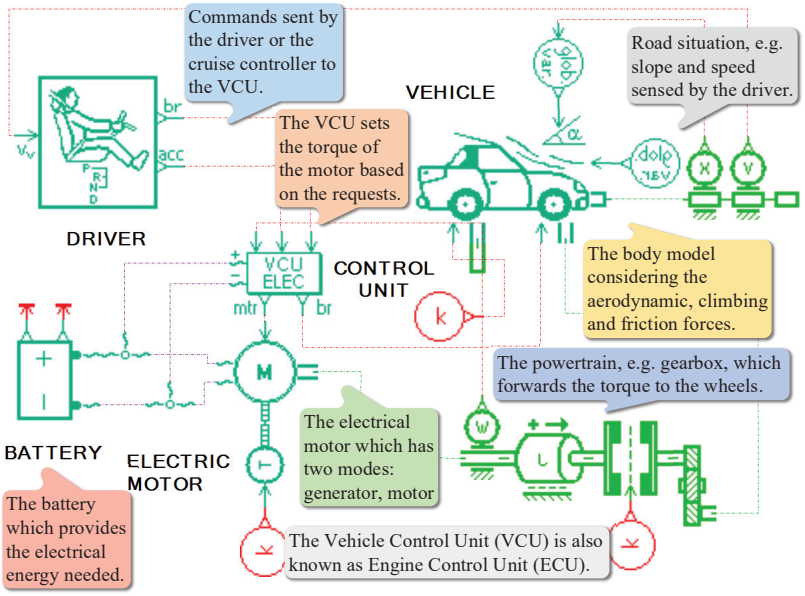

Figure 5.4: System-level EV model developed in AMESim tool [9, 147].

There are mainly three driving forces on an EV in motion: gravity force (F_{gr}), aerodynamic force (F_{aero}), and rolling resistance (F_{roll}) which affect the vehicle movement in terms of speed and acceleration. These forces are summed as the road load forces on the EV (F_{rd}) [9].

F_{gr} is the force caused by the gravity considering the road slope. The α variable in Equation 5.1 is the percentage of the road slope, e.g. 100% value for α represents the road slope of 45°. m is the vehicle mass and g is the gravitational constant.

$$F_{gr} \quad = m \times g \times \sin\left(\arctan(0.01 \times \alpha)\right) \quad (N) \tag{5.1}$$

F_{aero} is the aerodynamic drag force caused by the air striking the vehicle body. This force

depends on the vehicle speed (v), wind speed (V_{wind}), air density (ρ_{air}), penetration coefficient (C_x), and vehicle active area (S) (Equation 5.2). Since the vehicle speed affects the force quadratically, it will limit the vehicle's top speed.

$$F_{aero} = 1/2 \times \rho_{air} \times C_x \times S \times (v + V_{wind})^2 \quad (N) \tag{5.2}$$

F_{roll} is the rolling friction force resisting the motion of the wheels and tires. The equation for F_{roll} has one constant (f) and two proportional friction coefficients ($K, wind$) (Equation 5.3) which depend on the vehicle specifications.

$$F_{roll} \ = m \times g \times \left(f + K \times v + wind \times v^2\right) \quad (N) \tag{5.3}$$

The driving forces or load forces on the EV (F_{rd}) are overcome by a total force (F_{tot}) to propel the vehicle (mass m) forward at a desired speed and acceleration (a) [117].

$$F_{rd} = F_{gr} + F_{aero} + F_{roll} \tag{5.4}$$

$$F_{tot} = F_{rd} + ma \tag{5.5}$$

When F_{rd} is positive and the speed needs to be maintained, the vehicle should provide enough forward force to prevent deceleration. In this case, the force is generated only by the electric motor (F_{tr}). On the other hand, when F_{rd} is negative and the speed needs to be maintained, the vehicle needs to provide backward force to prevent acceleration. In this case, the force may be generated by the electric motor and the brakes. The later force generated by the electric motor is due to the generation mode ($F_{tr} < 0$) which is limited to F_{min} and may not provide enough backward force to neutralize the resistive force (Equation 5.6). Therefore, rest of the backward force is generated by the braking pads (Equation 5.7).

$$F_{tr} = max\,(\,F_{min}\,,\,F_{tot}\,)\quad (N) \tag{5.6}$$

$$F_{brake} = F_{tr} - F_{tot}\quad (N) \tag{5.7}$$

The mechanical power that drives the vehicle is the multiplication of F_{tr} and v (Equation 5.8). Moreover, the electric motor has an energy conversion efficiency (η_{motor}) less than 100% which varies by the torque and the rotational speed [93, 162].

$$P_{elec} = \frac{F_{tr} \times v}{\eta_{motor}}\quad (W) \tag{5.8}$$

$$I = \frac{P_{elec}}{V_{dc}}\quad (A) \tag{5.9}$$

In this chapter, the specifications for three EV (Tesla Model S 60KWh, Nissan Leaf S, and Fiat 500e) have been used to validate the power train model and to demonstrate various EV power consumption behavior while driving [3, 4, 12]. The parameters regarding the specifications are extracted from the manufacturers' forums and experimental data provided by the third-parties testing the vehicles.

5.2.3 Battery Pack

The battery pack is the main component for storing and providing the electrical energy in the EV. A battery model describes the battery energy consumption and its influence on the battery lifetime. The battery model can be specific to the material (e.g. Lithium-ion), the structure, and the connection of the battery cells in the pack.

The nominal capacity (C_n) of a battery pack depends on its structure and each battery cell capacity [102]. The battery cell nominal capacity is measured at the discharge rate of ($I_n = 0.2C$) [6]. The C rate is the discharge rate in which the battery depletes in one hour.

Lithium-ion battery cells are mostly used in EV as the main electrical energy storage because of their high energy density and adequate power density. The usable capacity of these batteries varies by the discharge rate (rate-capacity effect). This effect is empirically modeled as Peukert's Law [48]. For instance, according to [6], by increasing the discharge rate from 0.2C to 2C the discharged capacity of the battery decreases from 2857 mAh to 2500 mAh at the cut-off voltage of about 3.2 v. Peukert's Law expresses the relationship between the usable capacity and the discharge rate in Equation 5.10. pc is the Peukert Constant which can be measured for each battery type empirically. For the type of lithium-ion battery used here, the Peukert Constant is evaluated as 1.1342. This constant defines the behavior of the battery energy consumption. Although it is necessary to be evaluated, its value is orthogonal to the OCDM methodology.

The equation shows that by increasing the discharge rate, the efficiency of converting chemical energy to electrical energy decreases and more chemical reactions are needed to provide the same electrical energy. In other words, the internal resistance of the battery increases which results in more power loss. Hence, this is modeled by a larger effective current which is dependent on the discharge rate (Equation 5.11) and results in lower usable capacity.

$$C = C_n \left(I_n/I\right)^{pc-1} \quad (Ah) \tag{5.10}$$

$$I_{\mathit{eff}} = I \left(I/I_n\right)^{pc-1} \quad (A) \tag{5.11}$$

Battery State-of-Charge (SoC) shows the current available charge out of C_n. As shown in Equation 5.12, the effective current is considered for SoC estimation using columb counting [106]. Moreover, as the discharge rate increases, the SoC changing rate increases hyperbolically. SoC^0 is the initial SoC at time zero.

$$SoC^t = SoC^0 - 100 \times \int_0^t \left(I_{eff}/C_n\right) dt \tag{5.12}$$

Using the EV power train and the battery models for three EV (Nissan, Fiat, and Tesla), we have evaluated the driving range of the EV for different speeds. The results (see Figure 5.5) show that the usable capacity of the battery changes for different speeds. This verifies that considering the rate-capacity effect and having more accurate battery model in estimating the EV driving range is essential for a drive management.

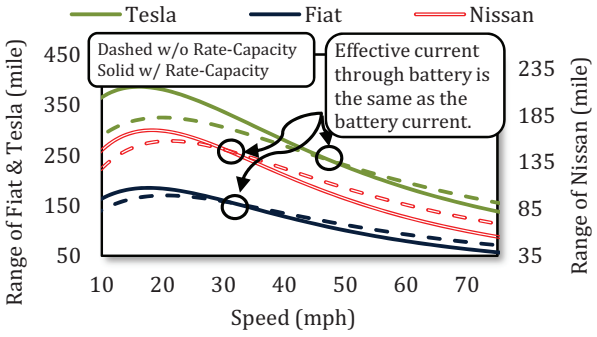

Figure 5.5: Estimated EV range w/ or w/o considering the rate-capacity effect.

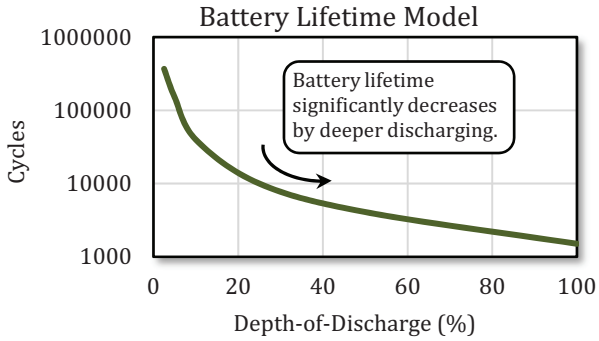

Figure 5.6: Battery lifetime cycles for various depths of discharge.

Battery DoD or depth-of-discharge shows how much capacity has been used out of C_n in one battery cycle. C_n degrades as the battery ages after each cycle. The capacity degradation rate depends on the DoD [111, 158]. After about 20% of capacity degradation, the battery will be considered useless. The battery lifetime is the number of cycles the battery can be used until the cut-off edge. The battery lifetime cycles decrease by increasing DoD as shown in Figure 5.6 [148]. Based on this observation and the data set presented in [148], the relationship between the Battery LifeTime (BLT) and the DoD is approximately modeled in Equation 5.13. The constants α and β can be measured for different types of batteries. For the type of lithium-ion battery used here, $\alpha = 330.4$ and $\beta = 1.231$ are measured.

$$BLT = \alpha \times (1/DoD)^{\beta} \quad (cycles) \tag{5.13}$$

In this battery model, it is assumed that the battery cells are utilized evenly while powering the EV. The aging effect, capacity degradation, and the decrease in usable capacity are

distributed evenly among all the battery cells. This assumption is not an overestimation as per paper [76], where the proposed configuration and scheduler evenly distribute the power on the battery cells [102, 122]. In our experiments, the chemistry of the battery cells has been assumed to behave the same for the three EV. The battery chemical characteristics have been modeled by extracting the data set presented in [148]. The specifications for the battery pack architecture, e.g. size and configuration, are extracted from the manufacturers' forums [3, 4, 12].

5.2.4 Power Grid

The EV batteries get recharged using the electrical energy provided by the power grid. There are various in-house EV chargers which provide different levels of charging. Drivers mostly use the ordinary 110 v outlet existing in the U.S. houses (Level I) or use the 220 v outlet for faster charging (Level II). Also, commercial EV charging stations provide even faster charging for EV (Level III). Each charger has its own specifications in terms of charging rate, power efficiency, and cost. The charging rate can be variable over time and get adjusted by the EV charger controller.

The utilities providing electricity are responsible for meeting the power demand by the users. They also need to maintain the reliability and efficiency of the power grid at all time. The EV chargers put a significant load on the power grid. This will increase the peak power demand which may diminish the transformer's efficiency or violate its threshold and cause thermal issues, voltage drop, and power outage.

Moreover, consuming electricity for recharging EV will cost money. The recharging electricity cost is significantly dependent on the utility pricing policy and time of charging. The utilities providing electricity have different pricing policies [13].

For instance, utilities deploy the strategy of Time-Of-Use (TOU) rate (see Table 5.1) to persuade users to shift their loads for reducing the peak power demand. In TOU policy, the users have incentive to schedule the battery charging process such that the electricity cost of recharging is minimized. Another similar incentive has been added for the weekends so that the power demand is shifted towards the weekends, if possible.

Table 5.1: Specifications of the utility pricing policy.

Time-Of-Use	12 AM ---------- 8 AM	---------- 2 PM	---------- 8 PM	------ 10 PM	------ 12 AM
Weekday	13¢/KWh	28¢/KWh			13¢/KWh
Weekend	13¢/KWh	28¢/KWh	44¢/KWh	28¢/KWh	13¢/KWh

* weekend is considered to be the last day of the weekly cycle when the EV is parked.

Drivers may decide to use the battery partially and charge it to the full state every day. Instead, others may discharge the battery completely to zero and charge it back to the full state every week. In the earlier charging schedule, the DoD is small which increases the battery lifetime [148]. Therefore, charging and discharging the battery partially decreases the charging time and may provide the driver with the flexibility of deciding on the charging schedule while possible improving the battery lifetime. For instance, the driver may choose to follow the earlier schedule and charge the vehicle during the midnight when the electricity price is lower. However, in the later schedule, the charging period is the maximum and it may overlap with the time when the electricity price is higher.

Moreover, knowing the power grid specifications and characteristics may help us to analyze and optimize the influence of the EV drive management on the power grid side, e.g. energy consumption and electricity cost. To do so, the power grid load for each day is estimated using the past statistics data. This information will be used in the OCDM as the estimated power request by the appliances in a house (excluding the EV charger). Hence, the OCDM optimizes the EV charger power in order to avoid increasing the total power demand (including the EV charger).

The power grid containing 20 houses has been modeled considering the appliances used in the house, the schedule of appliance usage, and the weather [132]. The power consumption of these houses has been evaluated for a month in order for the OCDM to estimate the daily load pattern of the house.

The power consumption estimation of the houses provides the methodology with the flexibility of scheduling the EV charger by knowing the capacity of the power grid and the electricity price. However, reactive control of the EV charger without estimation may result in underutilization of the power grid and over restricting the grid users. Moreover, an approximate estimation of the power consumption behavior is sufficient for the OCDM to reduce the peak power. Misprediction in estimated power will result in slightly sub-optimal solution and increasing the peak power.

5.3 Optimized Charge and Drive Management

5.3.1 Methodology Details

In the previous section, dynamic behavior of the system components has been described and modeled using mathematical equations. Our methodology utilizes these equations to estimate the system's parameters at each time step of the management process. These parameters include the control inputs and the state variables defining the system's operating status.

The control inputs include the parameters of the selected drive profile for each daily trip such as: selected driving route, departure time, and arrival time and the optimized EV charging rate at each time step.

The state variables include the parameters describing 1) the drive profile of each trip such as: EV energy consumption and driving time; 2) the battery operating status such as: battery power output and battery SoC; and 3) the power grid status such as: power demand by the EV charger, predicted load profile, and electricity price. Then, the relationships between these variables and control inputs are described through linear equations for the optimization purposes (described in Section 5.3.2).

In our methodology, values of the constant variables are evaluated before the optimization execution. For instance, the drive profiles for the route alternatives are modeled based on all the possible candidates offered by the Google APIs (see Section 5.2.1). The timing preferences and locations for each driver's daily trip are also assumed in the constant variables. The energy consumption of the EV while driving on each route is evaluated using the power train modeling (see Section 5.2.2). Then, battery behavioral modeling has been used to estimate the battery SoC; the rate-capacity effect is also accounted by considering EV effective energy consumption (using Peukert's Law) in estimating the SoC (see Section 5.2.3). Moreover, the power grid daily load profile is estimated and fed into the optimization problem as time-series of constant variables as the estimation (see Section 5.2.4). The physical control limitations (e.g. maximum charging rate) are also considered as the constraints of this optimization. Evaluating these constant values before optimization eliminates the influence of modeling the non-linearity behavior of the system on the methodology complexity.

The optimization problem estimates multiple state variables of the system in the future (receding horizon) and optimizes these variables and control inputs in order to reach an objective. In other words, the optimum driving route is selected from the multiple route candidates assigned statically for each daily trip; the arrival and departure time of the trips are scheduled daily while satisfying the driver's preferences; and EV charging rate at each time step is adjusted in order to charge the battery by having the statically pre-assigned estimated power grid load at that time step. The objective of the methodology

is to minimize the recharging electricity cost, reduce peak load on the power grid, and improve the battery lifetime. 1) Considering the estimated power for prediction of state variables knowing their relationships; 2) considering the influence of multiple control inputs and optimization variables on the solution simultaneously; 3) meeting hard constraints for the optimized solution; are the reasons to select MILP to formulate and solve the problem. However, selection of the approach is orthogonal to the problem and other approaches may work with different performance.

5.3.2 MILP Optimization Problem

As part of the charge and drive management, the methodology needs to optimize the driving route. For each trip, there are multiple route alternatives with their respected duration time and average power consumption. The route alternatives are extracted from all the possible routes provided by the Google APIs and modeled as the drive profiles. Then, the EV power train model has been used for estimating the power consumption values. Then, the battery model has been applied to estimate the effective average power consumption of the EV for each trip. These values are estimated before the optimization and assigned as constant variables[1]. The selection of the driving route for each of the daily trips is described by

$$t_I = \sum_{j=1}^{6} \boldsymbol{t_I}^j \ rb_I^j \qquad t_{II} = \sum_{j=1}^{6} \boldsymbol{t_{II}}^j \ rb_{II}^j \qquad t_{III} = \sum_{j=1}^{6} \boldsymbol{t_{III}}^j \ rb_{III}^j \quad (5.14)$$

$$w_I = \sum_{j=1}^{6} \boldsymbol{w_I}^j \ rb_I^j \qquad w_{II} = \sum_{j=1}^{6} \boldsymbol{w_{II}}^j \ rb_{II}^j \qquad w_{III} = \sum_{j=1}^{6} \boldsymbol{w_{III}}^j \ rb_{III}^j \quad (5.15)$$

$$1 = \sum_{j=1}^{6} rb_I^j \qquad 1 = \sum_{j=1}^{6} rb_{II}^j \qquad 1 = \sum_{j=1}^{6} rb_{III}^j \quad (5.16)$$

where t_i and w_i for $I \leq i \leq III$ are the selected driving time and average EV power consumption for each trip from the $\boldsymbol{t_i^j}$ and $\boldsymbol{w_i^j}$ alternatives. Binary values rb_i^j are optimized for the

[1]In the optimization formulation, constant variables which are known before optimization are bold in order to distinguish them with other variables. Nomenclature is provided listing and describing the variables.

route selection, and constraints in Equation 5.16 ensure that only one alternative is selected for each trip.

The departure and arrival times are constrained by the driving time of each trip:

$$t_I = t_B^a - t_A^d \qquad t_{II} = t_C^a - t_B^d \qquad t_{III} = t_A^a - t_C^d \tag{5.17}$$

where t_x^a and t_x^d are the arrival time to and departure time from $x : \{A, B, C\}$ location. It needs to be mentioned that after three trips the driver reaches the same location. The number of trips and route alternatives for each trip has been assumed to be statically three and six respectively, however other values can be applied and the number is orthogonal to the methodology.

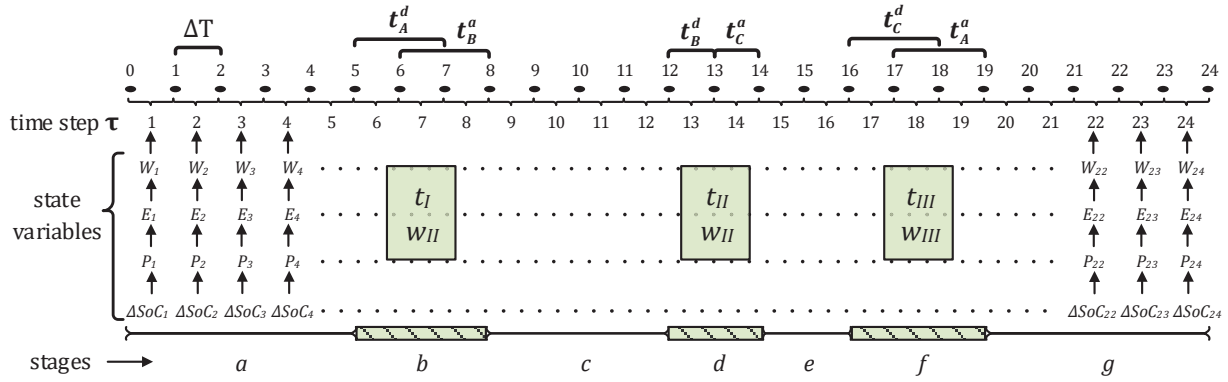

Figure 5.7: The state variables for the optimization over a day (1-hour time step duration).

The state variables of the system are defined for each time step over a day (24 hours). The number of the state variables will change based on the time step duration. 1-hour time step duration has been assumed in Figure 5.7 for easier illustration of how the methodology works over a day. The (three) daily trips divide the time horizon of a day into 7 different stages $\{a, b, c, d, e, f, g\}$. The timing of the stages changes according to the selected departure, arrival, and driving time of the trips. The number of daily trips can increase by adding more similar equations and variables while dividing the time horizon into more stages. However, this will increase the complexity while maintaining the optimality of the methodology (see Section 5.4 for further analysis).

In the following, multiple variables and linear constraints will be defined for **each time step** of the optimization:

$$b_a \; \underline{\boldsymbol{t}_{\boldsymbol{A}}^{\boldsymbol{d}}} \leq \overline{T_a} \leq b_a \; \overline{\boldsymbol{t}_{\boldsymbol{A}}^{\boldsymbol{d}}} \qquad b_a \; \mathbf{0} \leq \underline{T_a} \leq b_a \; \mathbf{0} \tag{5.18}$$

$$t_A^d - \overline{\boldsymbol{t}_{\boldsymbol{A}}^{\boldsymbol{d}}} \; (1 - b_a) \leq \overline{T_a} \leq t_A^d - \underline{\boldsymbol{t}_{\boldsymbol{A}}^{\boldsymbol{d}}} \; (1 - b_a) \qquad \mathbf{0} - \mathbf{0} \; (1 - b_a) \leq \underline{T_a} \leq \mathbf{0} - \mathbf{0} \; (1 - b_a)$$

$$b_b \; \underline{\boldsymbol{t}_{\boldsymbol{B}}^{\boldsymbol{a}}} \leq \overline{T_b} \leq b_b \; \overline{\boldsymbol{t}_{\boldsymbol{B}}^{\boldsymbol{a}}} \qquad b_b \; \underline{\boldsymbol{t}_{\boldsymbol{A}}^{\boldsymbol{d}}} \leq \underline{T_b} \leq b_b \; \overline{\boldsymbol{t}_{\boldsymbol{A}}^{\boldsymbol{d}}} \tag{5.19}$$

$$t_B^a - \overline{\boldsymbol{t}_{\boldsymbol{B}}^{\boldsymbol{a}}} \; (1 - b_b) \leq \overline{T_b} \leq t_B^a - \underline{\boldsymbol{t}_{\boldsymbol{B}}^{\boldsymbol{a}}} \; (1 - b_b) \qquad t_A^d - \overline{\boldsymbol{t}_{\boldsymbol{A}}^{\boldsymbol{d}}} \; (1 - b_b) \leq \underline{T_b} \leq t_A^d - \underline{\boldsymbol{t}_{\boldsymbol{A}}^{\boldsymbol{d}}} \; (1 - b_b)$$

$$b_c \; \underline{\boldsymbol{t}_{\boldsymbol{B}}^{\boldsymbol{d}}} \leq \overline{T_c} \leq b_c \; \overline{\boldsymbol{t}_{\boldsymbol{B}}^{\boldsymbol{d}}} \qquad b_c \; \underline{\boldsymbol{t}_{\boldsymbol{B}}^{\boldsymbol{a}}} \leq \underline{T_c} \leq b_c \; \overline{\boldsymbol{t}_{\boldsymbol{B}}^{\boldsymbol{a}}} \tag{5.20}$$

$$t_B^d - \overline{\boldsymbol{t}_{\boldsymbol{B}}^{\boldsymbol{d}}} \; (1 - b_c) \leq \overline{T_c} \leq t_B^d - \underline{\boldsymbol{t}_{\boldsymbol{B}}^{\boldsymbol{d}}} \; (1 - b_c) \qquad t_B^a - \overline{\boldsymbol{t}_{\boldsymbol{B}}^{\boldsymbol{a}}} \; (1 - b_c) \leq \underline{T_c} \leq t_B^a - \underline{\boldsymbol{t}_{\boldsymbol{B}}^{\boldsymbol{a}}} \; (1 - b_c)$$

$$b_d \; \underline{\boldsymbol{t}_{\boldsymbol{C}}^{\boldsymbol{a}}} \leq \overline{T_d} \leq b_d \; \overline{\boldsymbol{t}_{\boldsymbol{C}}^{\boldsymbol{a}}} \qquad b_d \; \underline{\boldsymbol{t}_{\boldsymbol{B}}^{\boldsymbol{d}}} \leq \underline{T_d} \leq b_d \; \overline{\boldsymbol{t}_{\boldsymbol{B}}^{\boldsymbol{d}}} \tag{5.21}$$

$$t_C^a - \overline{\boldsymbol{t}_{\boldsymbol{C}}^{\boldsymbol{a}}} \; (1 - b_d) \leq \overline{T_d} \leq t_C^a - \underline{\boldsymbol{t}_{\boldsymbol{C}}^{\boldsymbol{a}}} \; (1 - b_d) \qquad t_B^d - \overline{\boldsymbol{t}_{\boldsymbol{B}}^{\boldsymbol{d}}} \; (1 - b_d) \leq \underline{T_d} \leq t_B^d - \underline{\boldsymbol{t}_{\boldsymbol{B}}^{\boldsymbol{d}}} \; (1 - b_d)$$

$$b_e \; \underline{\boldsymbol{t}_{\boldsymbol{C}}^{\boldsymbol{d}}} \leq \overline{T_e} \leq b_e \; \overline{\boldsymbol{t}_{\boldsymbol{C}}^{\boldsymbol{d}}} \qquad b_e \; \underline{\boldsymbol{t}_{\boldsymbol{C}}^{\boldsymbol{a}}} \leq \underline{T_e} \leq b_e \; \overline{\boldsymbol{t}_{\boldsymbol{C}}^{\boldsymbol{a}}} \tag{5.22}$$

$$t_C^d - \overline{\boldsymbol{t}_{\boldsymbol{C}}^{\boldsymbol{d}}} \; (1 - b_e) \leq \overline{T_e} \leq t_C^d - \underline{\boldsymbol{t}_{\boldsymbol{C}}^{\boldsymbol{d}}} \; (1 - b_e) \qquad t_C^a - \overline{\boldsymbol{t}_{\boldsymbol{C}}^{\boldsymbol{a}}} \; (1 - b_e) \leq \underline{T_e} \leq t_C^a - \underline{\boldsymbol{t}_{\boldsymbol{C}}^{\boldsymbol{a}}} \; (1 - b_e)$$

$$b_f \; \underline{\boldsymbol{t}_{\boldsymbol{A}}^{\boldsymbol{a}}} \leq \overline{T_f} \leq b_f \; \overline{\boldsymbol{t}_{\boldsymbol{A}}^{\boldsymbol{a}}} \qquad b_f \; \underline{\boldsymbol{t}_{\boldsymbol{C}}^{\boldsymbol{d}}} \leq \underline{T_f} \leq b_f \; \overline{\boldsymbol{t}_{\boldsymbol{C}}^{\boldsymbol{d}}} \tag{5.23}$$

$$t_A^a - \overline{\boldsymbol{t}_{\boldsymbol{A}}^{\boldsymbol{a}}} \; (1 - b_f) \leq \overline{T_f} \leq t_A^a - \underline{\boldsymbol{t}_{\boldsymbol{A}}^{\boldsymbol{a}}} \; (1 - b_f) \qquad t_C^d - \overline{\boldsymbol{t}_{\boldsymbol{C}}^{\boldsymbol{d}}} \; (1 - b_f) \leq \underline{T_f} \leq t_C^d - \underline{\boldsymbol{t}_{\boldsymbol{C}}^{\boldsymbol{d}}} \; (1 - b_f)$$

$$b_g \; \mathbf{24} \leq \overline{T_g} \leq b_g \; \mathbf{24} \qquad b_g \; \underline{\boldsymbol{t}_{\boldsymbol{A}}^{\boldsymbol{a}}} \leq \underline{T_g} \leq b_g \; \overline{\boldsymbol{t}_{\boldsymbol{A}}^{\boldsymbol{a}}} \tag{5.24}$$

$$\mathbf{24} - \mathbf{24} \; (1 - b_b) \leq \overline{T_g} \leq \mathbf{24} - \mathbf{24} \; (1 - b_g) \qquad t_A^a - \overline{\boldsymbol{t}_{\boldsymbol{A}}^{\boldsymbol{a}}} \; (1 - b_b) \leq \underline{T_g} \leq t_A^a - \underline{\boldsymbol{t}_{\boldsymbol{A}}^{\boldsymbol{a}}} \; (1 - b_g)$$

$$\underline{T_a} + \underline{T_b} + \underline{T_c} + \underline{T_d} + \underline{T_e} + \underline{T_f} + \underline{T_g} \leq \boldsymbol{\tau} \leq \overline{T_a} + \overline{T_b} + \overline{T_c} + \overline{T_d} + \overline{T_e} + \overline{T_f} + \overline{T_g} \tag{5.25}$$

$$b_a + b_b + b_c + b_d + b_e + b_f + b_g = 1 \tag{5.26}$$

where b_x is the binary variable illustrating in which stage $x : \{a, b, c, d, e, f, g\}$ the driver is, at the current time step ($\boldsymbol{\tau}$). $\boldsymbol{\tau}$ in Equation 5.25 has a constant value corresponding with the current time step for which we are defining the constraints. The optimizer will select the binary variables b_x for each time step ($\boldsymbol{\tau}$) so that the stage timing boundaries are met and the current time step fits in that stage boundaries. $\overline{T_x}$ and $\underline{T_x}$ define the variable upper and lower timing boundaries of each stage. They are also optimized as part of the drive scheduling. Moreover, these upper and lower boundaries for each stage are also limited by the upper and lower boundaries of the departure and arrival times of each trip ($\overline{\boldsymbol{t_x^a}}, \underline{\boldsymbol{t_x^a}}, \overline{\boldsymbol{t_x^d}}, \underline{\boldsymbol{t_x^d}}$). The departure and arrival time boundaries are constants defined by the driver (driver's timing preferences). Equation 5.26 is added to make sure only one stage is selected at each time step.

At the driving stages, the battery power output is defined by the average EV power consumption. While at the idle stages, the battery power output is defined by the EV charger (if available). Hence, the battery power output at each time step is defined by:

$$\overline{W_a} = b_a \, \overline{\boldsymbol{w_a}} \qquad\qquad \underline{W_a} = b_a \, \underline{\boldsymbol{w_a}} \tag{5.27}$$

$$b_b \, \underline{\boldsymbol{w_b}} \leq \overline{W_b} \leq b_b \, \overline{\boldsymbol{w_b}} \qquad\qquad b_b \, \underline{\boldsymbol{w_b}} \leq \underline{W_b} \leq b_b \, \overline{\boldsymbol{w_b}} \tag{5.28}$$

$$w_I - \overline{\boldsymbol{w_b}} \, (1-b_b) \leq \overline{W_b} \leq w_I - \underline{\boldsymbol{w_b}} \, (1-b_b) \qquad\qquad w_I - \overline{\boldsymbol{w_b}} \, (1-b_b) \leq \underline{W_b} \leq w_I - \underline{\boldsymbol{w_b}} \, (1-b_b)$$

$$\overline{W_c} = b_c \, \overline{\boldsymbol{w_c}} \qquad\qquad \underline{W_c} = b_c \, \underline{\boldsymbol{w_c}} \tag{5.29}$$

$$b_d\ \underline{\boldsymbol{w_d}} \le \overline{W_d} \le b_d\ \overline{\boldsymbol{w_d}} \qquad b_d\ \underline{\boldsymbol{w_d}} \le \underline{W_d} \le b_d\ \overline{\boldsymbol{w_d}} \tag{5.30}$$

$$w_{II} - \overline{\boldsymbol{w_d}}\ (1-b_d) \le \overline{W_d} \le w_{II} - \underline{\boldsymbol{w_d}}\ (1-b_d) \qquad w_{II} - \overline{\boldsymbol{w_d}}\ (1-b_d) \le \underline{W_d} \le w_{II} - \underline{\boldsymbol{w_d}}\ (1-b_d)$$

$$\overline{W_e} = b_e\ \overline{\boldsymbol{w_e}} \qquad \underline{W_e} = b_e\ \underline{\boldsymbol{w_e}} \tag{5.31}$$

$$b_f\ \underline{\boldsymbol{w_f}} \le \overline{W_f} \le b_f\ \overline{\boldsymbol{w_f}} \qquad b_f\ \underline{\boldsymbol{w_f}} \le \underline{W_f} \le b_f\ \overline{\boldsymbol{w_f}} \tag{5.32}$$

$$w_{III} - \overline{\boldsymbol{w_f}}\ (1-b_f) \le \overline{W_f} \le w_{III} - \underline{\boldsymbol{w_f}}\ (1-b_f) \qquad w_{III} - \overline{\boldsymbol{w_f}}\ (1-b_f) \le \underline{W_f} \le w_{III} - \underline{\boldsymbol{w_f}}\ (1-b_f)$$

$$\overline{W_g} = b_g\ \overline{\boldsymbol{w_g}} \qquad \underline{W_g} = b_g\ \underline{\boldsymbol{w_g}} \tag{5.33}$$

$$\underline{W_a}+\underline{W_b}+\underline{W_c}+\underline{W_d}+\underline{W_e}+\underline{W_f}+\underline{W_g} \le W \le \overline{W_a}+\overline{W_b}+\overline{W_c}+\overline{W_d}+\overline{W_e}+\overline{W_f}+\overline{W_g} \tag{5.34}$$

where W represents the battery power output at time step $\boldsymbol{\tau}$. W is bounded by lower and upper boundaries $\underline{W_x}$ and $\overline{W_x}$ at each stage. At driving stages, the constraints will force $\underline{W_x}$ and $\overline{W_x}$ to be equal to the average EV power consumption selected for a specific trip. While at idle stages, $\underline{W_x}$ and $\overline{W_x}$ are optimized between constant parameters $\underline{\boldsymbol{w_x}}$ and $\overline{\boldsymbol{w_x}}$ which are defined by limitations of EV chargers (if available).

The energy consumed/stored in the battery and energy consumed by the EV charger at each time step are evaluated by:

$$-\boldsymbol{M}\ b_a \le W_a \le \boldsymbol{M}\ b_a \qquad -\boldsymbol{M}\ b_g \le W_g \le \boldsymbol{M}\ b_g \tag{5.35}$$

$$W - \boldsymbol{M}\ (1-b_a) \le W_a \le W + \boldsymbol{M}\ (1-b_a) \qquad W - \boldsymbol{M}\ (1-b_g) \le W_g \le W + \boldsymbol{M}\ (1-b_g)$$

$$W_x = W_a + W_g \tag{5.36}$$

$$E = W\ \mathbf{dT} \qquad\qquad E_x = W_x\ \mathbf{dT} \tag{5.37}$$

where W_a and W_g are the power outputs at stages a and g in which an EV charger exists (it is assumed that c and e stages do not have EV chargers). These variables are defined in order to evaluate the power demands by the EV chargers. They have true values only at their designated stages. Big constant variable M has been used as a dummy variable for avoiding quadratic constraints (big M method) [58]. Then, variable W_x is defined as sum of W_a and W_g to evaluate the power demands of the EV chargers at each time step. Energy change in the battery (E) and energy consumed by the EV charger (E_x) at each time step are evaluated by multiplying W and W_x by $\boldsymbol{dT}$, respectively.

The influence of the EV charger on the power grid load is evaluated by:

$$W_T = W_x + \boldsymbol{W_c} \qquad\qquad E_T = W_T\ \boldsymbol{dT} \tag{5.38}$$

$$W_T \leq \widetilde{W}_T \qquad\qquad W_x \leq \widetilde{W}_x \tag{5.39}$$

where $\boldsymbol{W_c}$ is the predicted house power consumption (excluding the EV charger) at each time step. W_T and E_T are total house power consumption and energy consumption (including the EV charger). Variables $\widetilde{W}_T$ and $\widetilde{W}_x$ define the total house peak power demand and EV charger peak power demand.

The electricity cost is estimated using variable $\boldsymbol{R}$ which is the time-varying electricity price constant pre-defined according to time step $\boldsymbol{\tau}$. The value of this constant variable is also assigned statically before the optimization for each time step.

$$P_x = E_x\ \boldsymbol{R} \qquad\qquad P_T = E_T\ \boldsymbol{R} \tag{5.40}$$

The battery behavior especially SoC estimation is defined by:

$$dSoC = E/\overline{\boldsymbol{E}} \times 100 \tag{5.41}$$

$$SoC = SoC^{\leftarrow} + dSoC \tag{5.42}$$

$$SoC \leq \widetilde{SoC} \tag{5.43}$$

where $dSoC$ is the battery SoC change due the effective energy consumed/stored (E) at time step $\boldsymbol{\tau}$. $\overline{\boldsymbol{E}}$ is the battery capacity. The current SoC gets updated using the $dSoC$ and the previous value of the SoC at the previous time step ($SoC^{\leftarrow}$). Variable $\widetilde{SoC}$ defines the peak value of the battery SoC which will be used in the cost function for reducing the average SoC. Moreover, the SoC value at the final time needs to be the same as the initial value; this is due to the fact that the management is done in daily basis and it will result in smaller DoD which prolongs the battery lifetime. The charge optimization attempts to charge the battery such that the daily battery SoC change is zero after one cycle.

The optimization cost function is defined by the following linear equation:

$$F = \beta_1 \ \widetilde{W}_x + \beta_2 \ \widetilde{W}_T + \sum_{\boldsymbol{\tau}=1}^{24} (\beta_3 \ E_x + \beta_4 \ P_x) + \beta_5 \ \widetilde{SoC} \tag{5.44}$$

where $\widetilde{W}_x$ is for reducing the peak power from the EV charger which can improve the battery lifetime by slow charging the battery. $\widetilde{W}_T$ is for minimizing the total house peak power demand which may improve the power grid energy efficiency and reliability. E_x is for reducing the energy consumption which also extends the battery lifetime by minimizing the battery DoD. P_x is for minimizing the electricity cost at each cycle. $\widetilde{SoC}$ is for maintaining low SoC average of the battery. The optimization weight variables (β) are defined manually in order to find the optimum solution in terms of the battery lifetime first, then the energy cost and energy consumption, and finally reducing the power grid load, charge rate, and SoC average. The values for the weights are as following considering the scale of the variables and their priority: $\beta_1 = 0.025, \beta_2 = 0.015, \beta_3 = 0.00015, \beta_4 = 107, \beta_5 = 1.2$.

Choosing the proper weights influences the balance and priority in the trade-off between these objectives. All these objectives are towards the benefits of the user and the utility and they all get minimized in the optimization. However, adjusting the weights can change the trade-off balance depending on the preference of the user or the utility in the importance of the objective. It needs to be noted that adjusting these weight variables is a cyber-domain design space exploration and is out of the scope of this thesis and will change the solution among the pareto-optimal points.

5.4 Experimental Results

5.4.1 Experiment Setup

Three different state-of-the-art EV (Tesla, Fiat, and Nissan) have been used as the benchmark EV to illustrate the performance of our methodology for various EV specifications and power consumption. The power consumption of the power train has been modeled using the equations specified in Section 5.2.2 and their parameters are extracted from the manufacturers' forums and experimental data provided by the third-parties testing the vehicles (see Table 5.2).

Table 5.2: Components specifications for multiple benchmark EV.

Specification		Tesla Model S	Fiat 500e	Nissan Leaf S
Battery	Energy	60 KWh	24 KWh	24 KWh
	Voltage	352 v	364 v	403.2 v
	Capacity	170.45 Ah	65.93 Ah	59.52 Ah
Body	Weight	2108 Kg	1355 Kg	1471 Kg
	Height	1.4351 m	1.57988 m	1.5494 m
	Width	1.9634 m	1.71958 m	1.7703 m
Tire	Rim Diameter	19 inch	15 inch	16 inch
	Overall Diameter	27.7 inch	23 inch	25 inch
Gear	Single Ratio	9.73	9.59	7.9377

The Google Maps Direction and Elevation APIs [8] are implemented in MATLAB [7] program to find the driving route alternatives for specific start and destination locations and generate drive profiles describing their route behaviors. Multiple drivers have also been analyzed in order to compare our OCDM methodology for various driving route conditions and environment. The locations and timing preferences for each driver's trips are selected manually and listed in Table 5.3.

Table 5.3: Driver information regarding locations and timing preferences.

Driver	Point	Address
1	A	*1301 Le Conte Ave, Montara, CA 94037*
	B	*1400 Amphitheatre Pkwy, Mountain View, CA 94043*
	C	*Hillsdale High School, 3115 Del Monte Street, San Mateo, CA 94403*
2	A	*855 Katella St, Laguna Beach, CA 92651*
	B	*Qualcomm, 8 Hughes, Irvine, CA 92618*
	C	*Engineering Hall, Irvine, CA 92617, USA*
3	A	*140 Columbia St, Seattle, WA 98104*
	B	*Microsoft Build. 42, 15590 Northeast 31st St, Redmond, WA 98052*
	C	*Univ. of Washington College of Eng., 371 Loew Hall, Seattle, WA 98195*

Time	Minimum	Maximum
t_A^d	7:30 AM	8:30 AM
t_B^a	7:50 AM	8:50 AM
t_B^d	4:00 PM	5:00 PM
t_C^a	5:00 PM	6:00 PM
t_C^d	7:00 PM	8:00 PM
t_A^a	8:00 PM	9:00 PM

The EV behavior and power consumption modeling is implemented using AMESim [9], an automotive design software and MATLAB/Simulink. The EV state estimation for each drive profile is evaluated in MATLAB. The power gird has been modeled and estimated according to [132] using GridMat [17]. The main MILP optimization problem is solved using *intlinprog* MATLAB toolbox.

5.4.2 Results and Analysis

We compare the performance of our methodology to the state-of-the-arts. Our optimized charge and drive management includes three aspects of route selection, drive scheduling, and charge optimization (see Section 5.3). We compare with the following methodologies in order to analyze each of these aspects.

1) ***Fast Drive and Dumb Charge (Fast):*** the route with the least duration time is selected manually from the route alternatives for each trip [8]. The EV is charged at the maximum current when a charger is available and as long as the electricity price is low.

2) ***Green Drive and Dumb Charge (Green):*** the route with the least energy consumption is selected manually from the route alternatives for each trip [150]. The EV is charged at the maximum current when a charger is available and as long as the electricity price is low.

3) ***Optimized Charge and Drive Management (OCDM):*** the optimal route is selected, driving is scheduled, and charging is optimized according to the methodology explained in Section 5.3. This will extend the battery lifetime, decreases the electricity cost, and diminishes power grid load. The time step duration for the optimization is set to 12 min, unless specified otherwise.

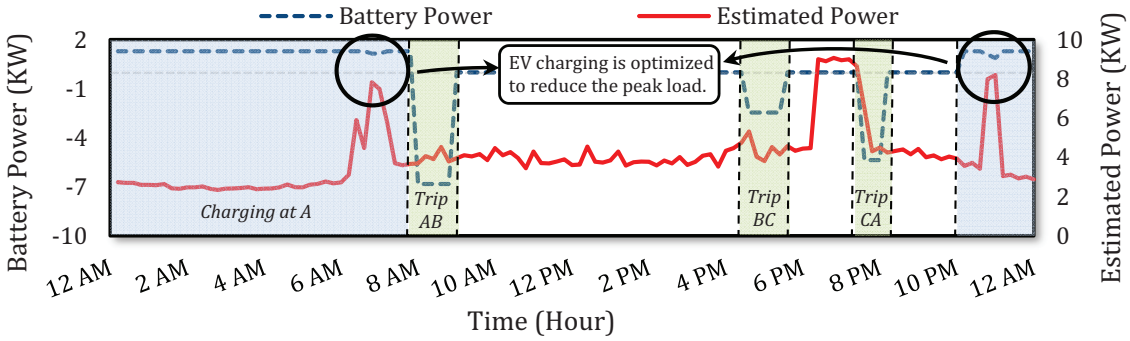

Figure 5.8: Battery power and estimated power of the house over a day when driving Tesla by Driver 1.

a) Temporal Analysis: At first, the behavior of our OCDM methodology is analyzed while driving a Tesla by driver 1 as an example. The value of the battery power output is shown in Figures 5.8 and 5.9; the negative/positive values represent that the battery is discharging/charging. The estimated power of the house (excluding the EV charger power) is also illustrated in the secondary axis of Figure 5.8. The EV charging power is optimized

and adjusted based on the estimated power of the house in order to reduce the electricity load on the power grid. Level I EV charger which is the most common one for the residential consumers is used with the maximum charging rate of 1.4 KW.

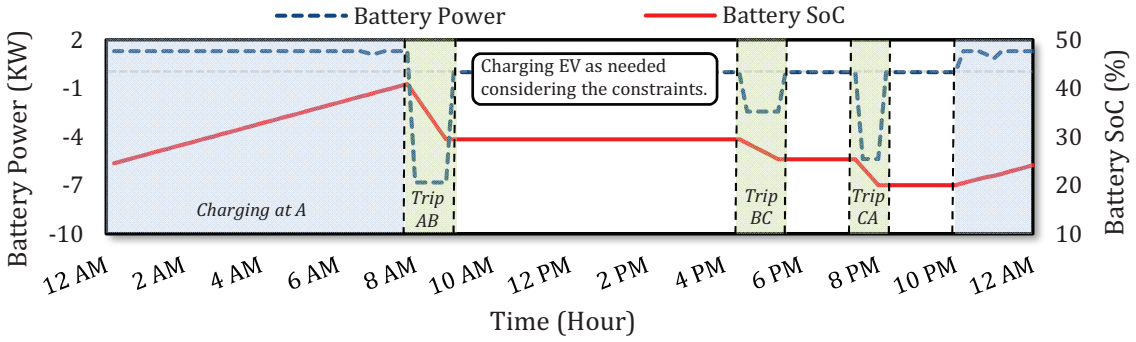

Figure 5.9: Battery SoC change regarding the discharging/charging processes when driving Tesla by Driver 1.

Figure 5.9 illustrates that the battery SoC changes while driving the EV or charging the battery. The charge optimization attempts to charge the battery such that the daily battery SoC change is zero after one cycle. In other words, the EV is charged everyday only as needed for daily driving (in one-day cycle). The charge optimization also makes sure that the battery SoC does not violate the SoC level constraints ($20\% \leq SoC \leq 80\%$). Moreover, the EV charging rate and the battery SoC average are also minimized in order to extend the battery lifetime further.

b) Driving Analysis: Each trip has its corresponding energy consumption and time duration. Hence, required energy consumption and the daily driving time are decided by the drive management. The performance of each methodology has been analyzed for thee EV types and three drivers in Figure 5.10. The daily driving time is at its least value while using the Fast methodology. However, it causes the energy consumption to increase. This verifies the fact that EV consume a lot more while driving at higher speeds. On the other hand, the energy consumption resulted from using the Green methodology is at its least value while increasing the driving time significantly.

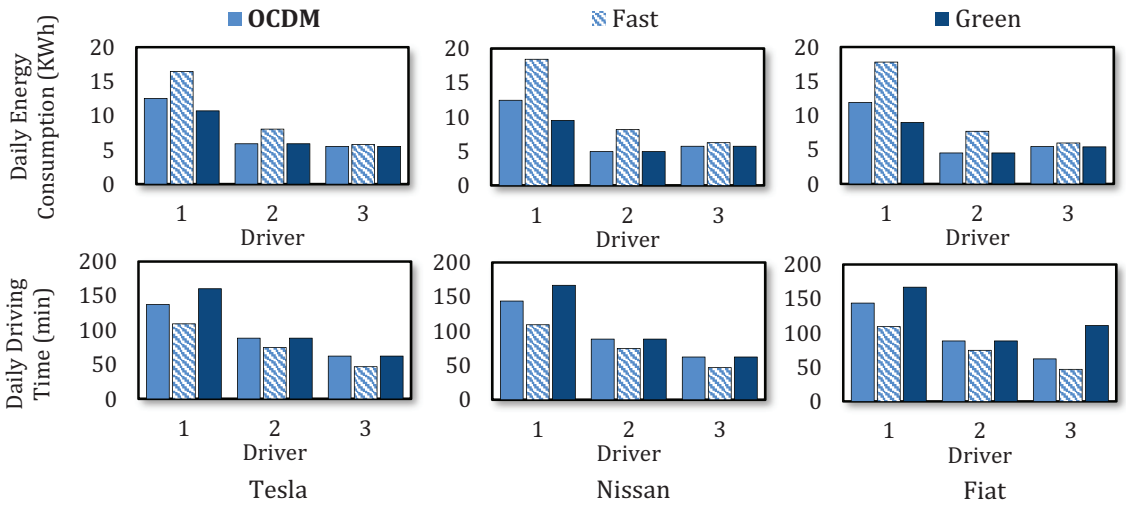

Figure 5.10: Analysis of energy consumption and driving time for each case study.

In OCDM, the optimizer selects the routes with the least energy consumption that do not violate the driver's timing preferences. This will result in more daily driving range. The OCDM has improved the required energy consumption by 27% on average compared to Fast methodology (which is commonly used) by sacrificing 20 min total driving time on average in a day. On the other hand, the OCDM has decreased the driving time by 13 min while sacrificing 12% energy consumption compared to Green methodology. As illustrated in the figure, the route selected by the Fast, Green, or OCDM methodologies for each EV is different. This is mainly because of the different characteristics, e.g. aerodynamic drag, of each EV. Compared to OCDM, the EV difference can cause drastic change in the selected route by other methods that only consider one objective, e.g. Green methodology for driver 3 in Nissan and Fiat EV.

c) Battery Analysis: The battery discharging and charging cycle affects the battery DoD and the battery lifetime. The battery lifetime cycles have been analyzed for the three EV and three drivers in Figure 5.11.

The Fast methodology results in the worst battery lifetime due to high EV energy consumption and deep discharge. The OCDM has improved the battery lifetime by 24.8% compared

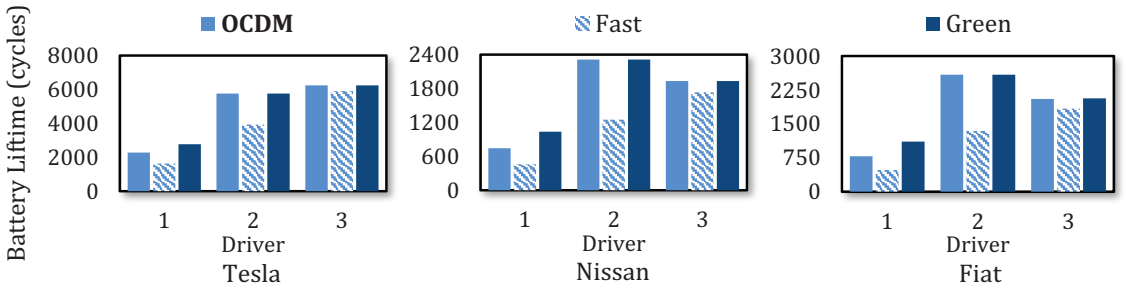

Figure 5.11: Analysis of the battery lifetime for each case study.

to the Fast methodology. On the other hand, the OCDM has decreased the battery lifetime by 4% compared to the Green methodology in the price of meeting the driving time preference. As shown in the figure, the influence of the driving routes on the battery lifetime cycles is higher for the EV with smaller battery capacity, e.g. Nissan and Fiat.

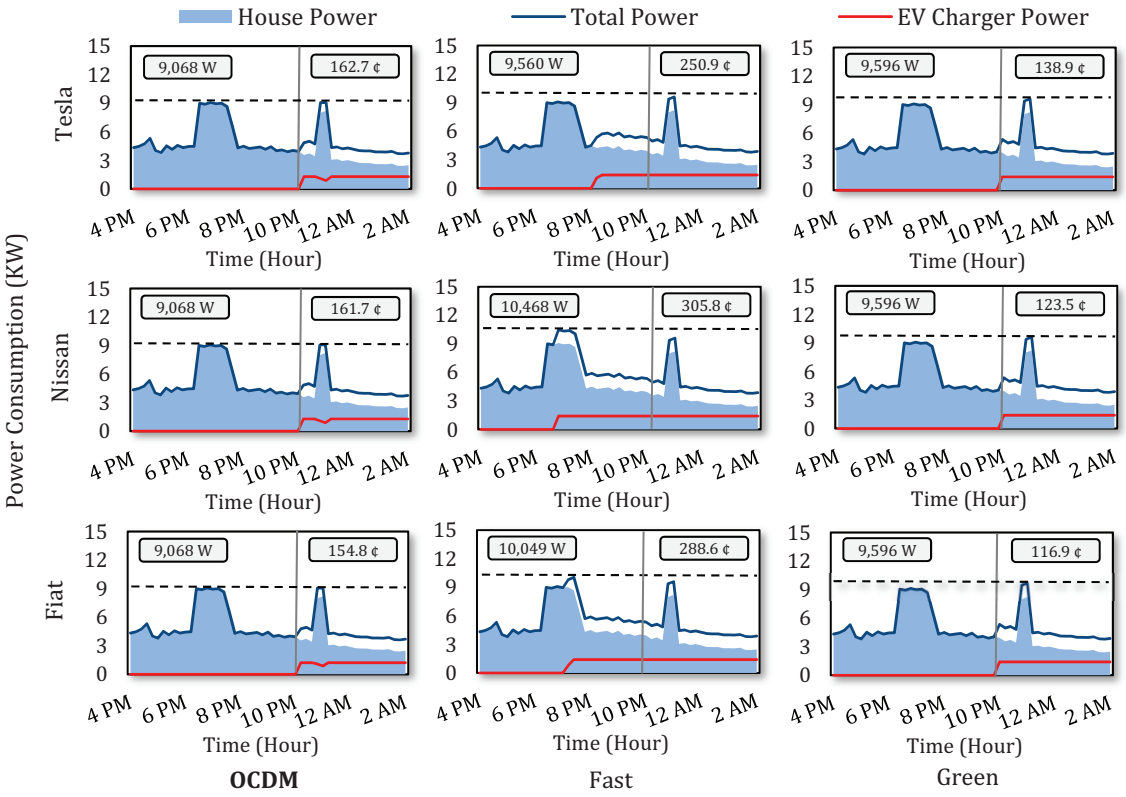

Figure 5.12: Analysis of the EV charging process and its influence on the power grid.

d) Grid Analysis: EV charging is done according to each methodology. The EV charger power, house power due to other appliances, and total power from the house including

the charger, for the time period of 4 PM to 2 AM are illustrated in Figure 5.12. The corresponding peak power demand and electricity cost for daily charge are also shown. The peak power demand has been evaluated by monitoring the power request from a house over a month using the same daily plan of charging provided by each methodology.

In the Fast and Green methodologies, the drivers charge their EV during the low electricity price tier unaware of the grid capacity and current power demand. This has resulted in up to 10.5 KW peak power demand. However, in the OCDM methodology, the peak demand has reduced to 9 KW (17% reduction) - the peak power demand of the house excluding the EV charger - by estimating the power demand of the grid.

The electricity cost has been also compared in Figure 5.13. The reduction of electricity cost resulted from OCDM is due to the energy consumption reduction and scheduling the charge process when the price is low. OCDM has reduced the electricity cost 35% compared to the Fast methodology. Compared to the Green methodology, the cost has increased by 13% in trade for meeting the timing requirements.

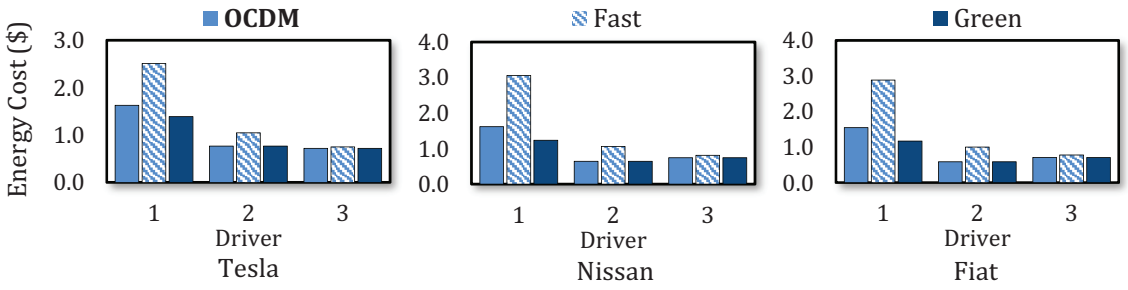

Figure 5.13: Analysis of the EV recharging cost for each case study.

It needs to be noted that the assumed EV charger is capable of providing upto 1.4 KW (Level I). By using slower EV chargers, the Fast methodology result in longer charging time. Hence, the battery cannot be charged between the time frame the electricity price is low and the driver leaves location A. This will force the driver to charge at high electric price tier which will increase the electricity cost. On the other hand, the slow charging of the EV improves the battery lifetime and charging energy efficiency further. However, although

using the faster EV chargers decrease the charging time and maybe the charging cost, it may increase the peak power demand further and reduce the battery lifetime.

Furthermore, considering the inclination of the drivers to charge their EV as soon as they reach the charger can worsen the performance of the Fast and Green methodologies in terms of peak power demand and electricity cost. However, the influence of this simultaneous charging can be eliminated in the OCDM methodology by estimating the grid load profile and scheduling the EV charger. Minimizing the peak power by implementing the power prediction as in the state-of-the-arts benefits the utilities for better energy efficiency. Although the power prediction might not be completely accurate, it is sufficient enough to provide us with the necessary information about the power grid in order to diminish the peak demand and schedule the EV charging. Moreover, without the power prediction, the EV charging rate may dynamically change with the real-time house power consumption. However, in this solution, unexpected concurrent high power consumption in the house with the EV charging may result in an undercharged vehicle for the next trip especially using slow chargers (Level I).

e) Driving Schedule Analysis: Drivers' timing preferences affect the time slack available for charging the EV at location A especially when the electricity price is low. Hence, changing the timing preferences such as setting earlier departure time from location A may increase the energy cost and the peak power demand. Moreover, giving more slack for the driving preferences enables the methodology to select another route with lower energy consumption and higher driving time. For instance, driving the Tesla by driver 1, setting the minimum t_A^d from 7:30 AM to 7 AM enables the OCDM to select a longer route with lower energy consumption reducing the energy cost from \$ 1.6 to \$ 1.3. Setting the maximum t_B^a from 8:50 AM to 8 AM forces the OCDM to select the shorter route again with higher energy consumption. However, the slack time for EV charging gets also smaller which increases the energy cost from \$ 1.6 to \$ 1.9. Earlier departure time from location A will increase

the energy cost due to the charging time overlap with the time the electricity price is high. Therefore, the drive management is required to optimize the driving schedule based on the preferences in order to decrease the energy cost and power grid load while improving the battery lifetime.

f) Methodology Scalability: Multiple parameters in the OCDM methodology, e.g. time step duration, number of trips per day, and number of days in a charge and discharge cycle, have been set manually previously. The execution time and memory usage for the optimizer have been monitored for multiple case studies (e.g. EV and driver) and time step duration (see Figure 5.14). The computing platform is comprised of an Intel Core-i7 3770 CPU with 3.4 GHz clock frequency and an 8 GB of DDR3 RAM.

Longer time steps result in higher EV average power consumption at each time step. This will increase the values of the coefficients in the optimization equations too much to converge. Longer time steps also increase the discretization error of the time in OCDM methodology. However, the optimality of the selected solution has not been compromised since the discretization is done by considering the ceiling value in order to make the timing preferences more stringent. On the other hand, smaller time steps add more equations and variables to the optimization problem. This increases the memory usage and execution time for finding the optimum solution hyperbolically.

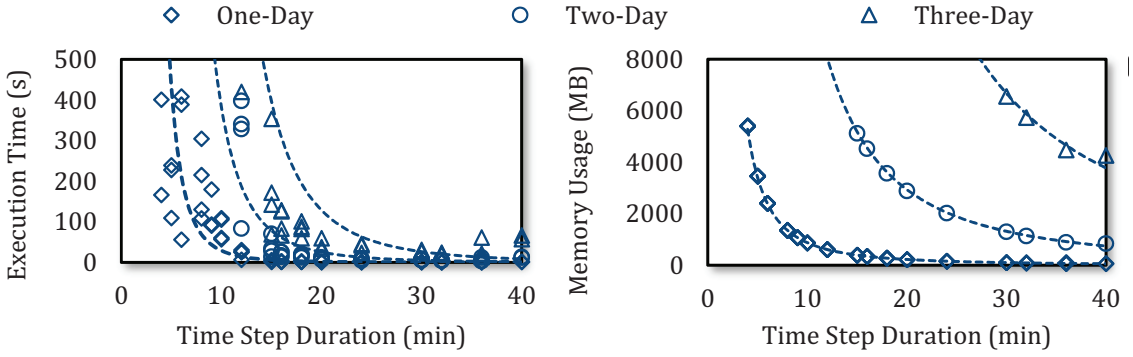

Figure 5.14: Analysis of the methodology scalability in terms of execution time and memory usage.

Adding more trips per day and increasing the number of days in a charge and discharge cycle increase the complexity of the methodology polynomially such as inverse of the time step duration. As shown in the figure, the execution time of the methodology is less deterministic than the memory usage. This is due to the fact that in the process of solving an MILP problem, multiple discrete solutions are explored heuristically and the one closest to the optimal solution gets picked. Hence, the convergence time is less predictable.

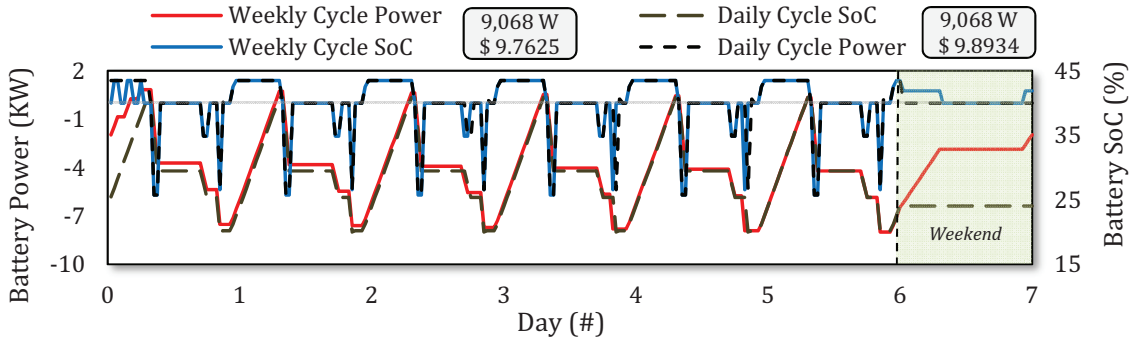

Figure 5.15: Battery power and SoC during daily and weekly cycles (energy cost and peak power shown above).

Considering multi-day cycles instead of one-day cycles adds more equations and complexity to the optimization problem (see Figure 5.14). However, if the electricity price policy and the driving routes are the same for all days, the resulted solutions are as same as the optimal solution for the one-day-cycle problem. This is due to the fact that having more days in the cycle does not add any flexibility to the optimization problem to reach better solution. On the other hand, we may consider that in the last day of the cycle (weekend in a weekly cycle), the electricity price policy changes and the EV is not used and parked at home ready to be charged (location A). Hence, more flexibility may be added for the OCDM in order to find a better solution. Depending on the pricing policy and the habit of EV utilization, the energy cost, power peak demand, EV charging rate, and SoC average may decrease. As shown in Figure 5.15, the EV charging has been more spread over the weekend decreasing the EV charging rate and SoC average. Moreover, although the weekly energy cost has decreased by 2%, it is not significant. The peak power also stays the same. This is due to the fact that in this scenario the OCDM was already using the low price tier during the week to charge.

5.5 Concluding Remarks

The EV driving range, battery lifetime, and charging process are the challenges for the EV owners and designers. The driving route, departure/arrival time of daily trips, and electricity price influence the EV energy consumption, battery lifetime, electricity cost, and the EV charger load on the power grid. Hence, we have proposed an Optimized Charge and Drive Management (OCDM) methodology in order to improve the EV driving range, extend the battery lifetime, reduce the recharging cost, and diminish the influence of EV charger on the power grid. Our methodology has three aspects of selecting the optimal driving, scheduling the daily trips, and optimizing the charging process. The optimization has been formulated in a mixed-integer linear programming using the modeling and estimation of the system components such as drive profile, EV power train, battery pack, and power grid. The performance of our methodology compared to the state-of-the-arts has been analyzed by experimenting on three benchmark EV and three drivers. Our OCDM has decreased the EV energy consumption by 27%, improved the battery lifetime by 24.8%, reduced the electricity cost by 35%, and diminished the power grid peak load by 17% while increasing less than 20 min of daily driving time. Moreover, the scalability of the methodology has been analyzed for different time resolutions and number of days and trips in a charge and discharge cycle. It has been shown that although execution time and memory usage changes by changing these variables, the optimality of the solution does not get compromised.

Chapter 6

Quality-Aware Control

6.1 Introduction and Related Work

We introduced multiple control methodologies implemented in battery-powered CPS of EV. The main responsibility of CPS controllers in any area may be abstracted into adjusting (optimizing) system variables for improving (minimizing or maximizing) an objective variable considering these (explicit or implicit) interconnections [35]. Hence, the deviation of the objective variable from the optimal value may define the controller **Quality**. The quality variable can be defined for any application domain of CPS controllers whether for cyber or physical components [22, 35, 138]. In this thesis, we focused on the area of automotive CPS by looking into EV as an example of interdisciplinary CPS to address its design challenges.

Design of high energy/power density battery cells has helped in addressing the challenges of EV. On the other hand, battery cell monitoring and control have been implemented for ensuring the battery cells' safe and efficient operation. This CPS controller described as a BMS in Chapter 2, leverages a model of the battery defined at design time to estimate its behavior at run time. Hence, it extends the battery lifetime and improves the EV driving range further by monitoring and controlling the power requests to the battery cells. Therefore, the controller quality of a BMS for a battery (physical system) can be defined by either the energy consumption or the capacity loss of the battery.

Electric motor is a major system in EV contributing to the battery power request. It is under control by a Motor Control Unit (MCU) which consumes energy in the motor mode to propel the vehicle and generates energy in the regenerative mode when braking. Its energy consumption/generation depends on the driving behavior and driving route [104, 133]. There are other auxiliary systems in EV like Heating, Ventilation, and Air Conditioning system that may also contribute to the power request [70] (see Chapter 3 for further details). The total power requests influence the battery operating behavior in terms of EV driving range and battery lifetime which are the major concerns and challenges with EV.

Furthermore, for daily drivers, driving time of a route to a destination is another major concern. Automotive Navigation System (ANS) which may be available in any vehicle especially autonomous vehicles is responsible for selecting the driving route with the least driving time. The ANS is typically equipped with a large online/offline map database of the route information. It constantly monitors the current location of the EV, looks for route alternatives to the destination, and selects the route with the minimum driving time. Therefore, the controller quality of an ANS for a driving route (physical system) can be defined by the driving time (see Chapter 4 for further details).

We introduced three of the main controllers in an EV: battery management system, motor control unit, and automotive navigation system, responsible for battery, electric motor, and driving route, respectively. Typically, these controllers only consider the behavior of their own physical systems for maintaining the quality. However, the behavior of a system and its controller is not determined only by itself and it can get affected by other systems in the CPS. In other words, due to the explicit or implicit interactions between different systems in a CPS, the controller quality of a system may get affected by another system's behavior and control. The following motivational example will illustrate this further:

6.1.1 Motivational Case Study

Consider the two physical systems of battery and driving route in a CPS of an EV. There are multiple route alternatives to a specific destination and one of them is selected by the navigation system. The selected driving route not only affects the driving time which is the controller quality of the ANS, but also affects the EV power consumption and thereby the controller quality of the BMS (e.g., energy consumption or battery capacity loss).

Figure 6.1 shows multiple route alternatives with their corresponding driving time and battery energy consumption. The BMS attempts to decrease the battery energy consumption

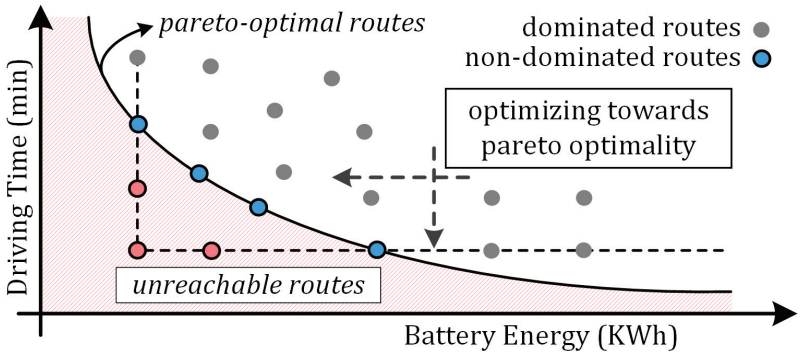

Figure 6.1: Analyzing driving routes in terms of driving time and battery energy consumption [133, 137].

(moving left on X axis) by considering the behavioral model of the battery. On the other hand, the ANS attempts to decrease the driving time (moving down on Y axis) by considering the behavioral model of the driving route. Moreover, it has been shown that driving an EV on faster highway routes may result in higher battery energy consumption. This is due to the fact that frequent braking in local driving routes may regenerate and save more energy. However, the BMS or the ANS is not aware of this implicit interaction between the driving route and battery.

Summary and conclusion from observations: since each controller has the behavioral model of its own physical system, the selected solution (driving route and battery energy) may fall into the dominated solutions which are not pareto efficient for the whole CPS. It is necessary for the controllers to have the behavioral model of each other's physical system to reach the pareto-optimal (non-dominated) solutions. This challenge is not limited to these two systems or the three above-mentioned systems in EV and may occur for any pair of systems in a CPS.

Different control designs have been presented to address the above-mentioned challenge; there are state-of-the-art system-level controllers which are equipped with a centralized behavioral model of multiple physical systems under control. They attempt to optimize the variables to reach a predefined global objective variable comprised of the objective variables for each

system. For instance, a predictive BMS in [107] has considered the driving route model for optimizing the battery utilization. An energy-aware navigation system in [137, 150] has leveraged the battery and EV power model in order to optimize the route for smaller energy consumption as well as faster driving time. However, these state-of-the-art controllers need to have a centralized behavioral model of all the other interdisciplinary influencing systems to achieve an optimal operation. This ideal embedded control design, increases the computation and memory requirements, and limits the scalability of the integration between multiple complex systems. On the other hand, the model embedded in the controller at design time is static and its accuracy is limited to the bounded knowledge available at design time. Hence, as the behavior of the physical or cyber systems changes over time - battery capacity degrades or controller ages - the controller quality and solution optimality deviate as well [35].

6.1.2 Problem and Research Challenges

In summary, the above-mentioned state-of-the-art CPS control designs suffer from the following major limitations:

1. Control in a system is limited to the behavioral knowledge of its own physical system to improve only its own quality.

2. Accuracy of the static behavioral model in a system controller is limited to the bounded information available at design time.

3. Lack of scalability to integrate multi-domain systems for optimizing a higher-level quality rather than the quality of individual systems in order to reach pareto-optimal solutions for the CPS.

6.1.3 Main Contributions and Concept Review

To address these challenges, a novel CPS control design to enable a system-level integration and optimization is proposed that employs:

1. **System Modeling and Estimation (Section 6.2):** describes the dynamic behavior of the System Under Design (SUD) using mathematical equations, e.g., modeling the electric motor using Ordinary Differential Equations (ODE) (Section 6.2.1).

2. **Adaptive Quality-Aware Control (Section 6.2.2):** monitors the controller quality of other influenced/influencing neighbor systems (e.g., battery energy consumption) in order to dynamically derive and update a data-driven behavioral model of those systems using run-time regression analysis.

3. **Cooperative Control Design (Section 6.3):** integrates the SUD controller with the data-driven model of the neighbor systems to consider their quality, adapt to their behavior, and cooperate with them by enabling a system-level optimization.

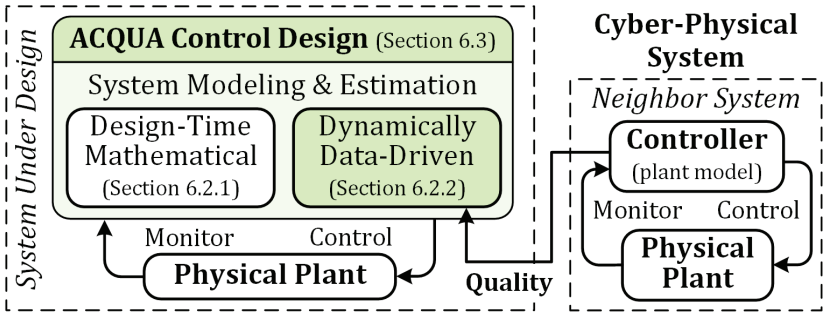

Figure 6.2: Abstract illustration of the highlighted contributions in our novel Adaptive Cooperative Quality-Aware control design for CPS.

Figure 6.2 illustrates the highlighted contributions in our Adaptive Cooperative Quality-Aware (ACQUA) control design, in abstract. Typically, a system comprises of a controller and a physical plant. The controller of the SUD may implement a design-time (centralized) mathematical model of the physical plant of its own system and any other neighbor systems,

if it is a system-level controller. However, in ACQUA control design, the need to have the complex and centralized design-time mathematical model of the neighbor systems is eliminated. This is achieved by implementing a dynamically data-driven modeling block using regression analysis. The ACQUA-based controller will monitor the controller quality of the neighbor systems, learn their behavior, and use the model to enable a system-level optimization and reach pareto-optimal solutions.

6.2 System Modeling and Estimation

During a control design process in CPS, the behavior of the physical systems are modeled. The modeling is used for the estimation of the system behavior to meet the control constraints or optimize the control inputs for minimizing a specific cost. There are different approaches to utilize this system modeling for controlling purpose, e.g., feedback control, Linear-Quadratic Regulator (LQR), and Model Predictive Control (MPC) [86, 107, 133]. We further explain details of the system modeling using the three mentioned systems in EV; we look into an automotive navigation system that selects the route with minimum driving time while cooperating with the motor control unit, and battery management system.

6.2.1 Design-Time Mathematical Modeling

There are various approaches to model and estimate the behavior of a physical system. Typically, the behavior is described using mathematical equations such as graphs, (non-)linear, and ordinary differential equations. The equations are defined by laws of physics and their parameters are evaluated by curve fitting the empirical data gathered of the system. These models are generated at design time by control designers of the system. Three physical systems of driving route, electric motor, and battery are mathematically modeled in the following as part of their corresponding controllers.

Driving Route as a physical system is modeled in map databases that are stored in the controller (ANS) or are accessible online (Google Maps [8, 60]). The databases contain geographical data for different nodes (locations) and segments (routes) between these nodes. They also provide information about the elevation of a node, length, average speed, and road slope of the connecting segments. It needs to be noted that, these databases are static from the controller perspective even if they get updated through other cyber systems (e.g., online update). Here, the databases are basically graphs or discrete mathematical modeling of the physical system (routes).

Electric motor generates the necessary force to drive the vehicle. The power consumption or generation of the electric motor in the EV is modeled and estimated by considering the motor characteristics and driving forces on the vehicle such as: gravitational (F_{gr}), aerodynamic drag (F_{aero}), and rolling resistance (F_{roll}) forces.

$$F_{tr} = F_{gr} + F_{aero} + F_{roll} + m\,a \tag{6.1}$$

The tractive force (F_{tr}) is provided by the electric motor to overcome the forces to propel the vehicle with mass (m) forward at a desired speed (v) and acceleration (a) [63]. The direction of the tractive force is defined by whether the electric motor is at the regenerative mode (regenerative braking) or motor mode.

The electric motor power consumption (P_e) is calculated as:

$$P_e = \frac{F_{tr} v}{\eta_m} \tag{6.2}$$

where η_m represents the electric motor efficiency when converting electrical to mechanical energy in the motor mode and converting mechanical to electrical energy in the regenerative mode (regenerative braking). η_m is dependent on the motor rotational speed and the

generated torque. The values of the equation parameters are evaluated at design time using empirical data [86, 93, 162].

Battery provides the power requested by the EV systems such as the electric motor and the HVAC. The influence of these power requests on the battery are estimated by models of the battery operating behavior such as State-of-Charge (SoC) and battery lifetime degradation or State-of-Health (SoH).

The usable capacity inside a lithium-ion battery decreases, by increasing the discharge rate (I) (rate-capacity effect). This effect is modeled by Peukert's Law using an effective discharge rate. Hence, the battery SoC is estimated by the coulomb counting and evaluating the effective discharge rate:

$$SoC^t = SoC^0 - \frac{100}{C_n} \times \int_0^t I \left(\frac{I}{I_n}\right)^{pc-1} dt \tag{6.3}$$

where C_n is the nominal capacity of the battery measured at nominal current (I_n) predefined by the battery manufacturer. SoC^t represents the SoC value at time t. pc is the Peukert's constant measured empirically at design time for the type of the battery cell [48, 148]. For the type of lithium-ion battery used here, the Peukert's constant is evaluated as 1.1342. This constant defines the behavior of the battery energy consumption. Although pc is necessary to be evaluated, its value is orthogonal to our methodology.

Battery capacity degrades over time (capacity-fade effect) depending on the battery utilization. The battery stress, number of discharge cycles, discharge current, and battery temperature influence this capacity loss (Q_{loss}) [64, 98]. In this chapter, Q_{loss} is modeled considering the discharge current:

$$Q_{loss} = l_1 e^{-l_2/(R\,T_{bat})} I^{l_3} \tag{6.4}$$

where R is the ideal gas constant. l_x parameters are the coefficients in the model that are measured empirically at design time [123]. Battery temperature T_{bat} is assumed to be maintained and its influence on the battery operation is out of the scope of this chapter.

6.2.2 Dynamically Data-Driven Modeling

Another approach to model the physical system is by using the data gathered while analyzing the system at run time (data-driven). In this approach, the gathered data is not fit into any physics-based equation, instead, reduced-order models or polynomial equations are utilized. This helps when the control designer of the system under design, at design time, lacks the behavioral knowledge of other neighbor systems that influence or are under influence of this system. Moreover, run-time data-driven modeling eliminates the computationally expensive offline phase required to build a centralized model at design time. Furthermore, the model dynamically updates as more data is gathered at run time. This will improve the modeling and estimation accuracy compared to the static model defined at design time, especially in the systems where their behavior changes over time, e.g., aging battery cells. In this chapter, two physical systems of electric motor and battery are going to be dynamically modeled at run time by the automotive navigation system using data-driven approach.

1) Data Collection. The first step to dynamically data-driven modeling is data collection. In our ACQUA control design, there are two pieces of data to be collected. The first piece of data ($[Y]$) that the system under design collects, is related to the controller quality of the neighbor systems. The data is provided by the controller of the neighbor systems through a predefined communication channel. The channel may be already available or can be implemented at no extra cost on an existing network connecting the systems in the CPS (e.g., CAN or FlexRay in automotive)[1]. The control designer of the SUD is not required to know

[1]Design of the communication system is out of the scope of this thesis and we assume there is at least one simplex channel available for transmitting the quality signal.

the data type or unit of the quality signal. The control designer of the neighbor systems is responsible for deciding and designating a controller quality signal, if the controller needs to be part of a cooperative system.

The second piece of data ($[X]$) to be collected is the data gathered in the SUD by monitoring its own state variables. These variables are the ones which may influence the neighbor systems directly or indirectly and may be adjusted in the controlling process to provide the adaptivity to the controller quality of the neighbor systems. Since the state variables are accessible inside the controller, there is no need for an additional communication system.

Data collection rate is decided according to the sampling time of the neighbor systems providing the data and the communication channel. The rate may be different and independent from the execution and actuation time of the SUD controller due to its intrinsic parallelism.

2) Regression Analysis. The second step to derive a dynamically data-driven model, is to fit the collected data into a general reduced-order model called ***fit model*** (F) that approximates equation $[Y = F(X) + \text{error}]$. Here, we use linear regression analysis to model the data. Mostly, the behavior of the systems is too complex to be modeled by linear regression and simple features (first-order system variables), therefore polynomial regression and higher orders of polynomial features may be used in the modeling. Since there is no prior knowledge of the relationships between the variables of the system under design and neighbor systems, different fitting regression models with various orders and features may be tested to see which one fits better. The fit models are generated using fast and efficient techniques to LASSO regression analysis using QR decomposition [24, 61]. Moreover, wider variety of machine learning models and more complex features can be added to fit the data. In other words, our ACQUA control design is applicable and orthogonal to any selection of fitting models and techniques.

The selected fit model should fit the collected data and estimate the future values with the minimum error possible. There are various techniques and metrics to evaluate if a fit model is a proper model for the given data set.

Mean Squared Error (MSE) is the average of the squared deviations that is the difference between estimated values ($\widetilde{Y} = F(X)$) from actual values (Y) for a data set. It is a measure of discrepancy between the data and the fit model (F). MSE evaluated for n samples of the collected data ($[X, Y]$) and the generated fit model (F) in ACQUA, is the fitting error (F_{MSE}) of the model:

$$F_{MSE} = 1/n \ \|Y - F(X)\|^2 \qquad (\ \|.\|^2 = l^2\text{-norm}\ ) \tag{6.5}$$

Smaller fitting error of a model (F_{MSE}) demonstrates that the model fits the collected (training) data set better. However, it is not necessarily a good model to estimate and describe the behavior of the data (e.g., controller quality) since it may over fit the data [94].

Cross validation is a technique for assessing how a fit model will generalize to an independent data set. In a k-fold cross validation, the collected data set ($[X, Y]$) is randomly partitioned into k equally-sized subsets. One of the k subsets is selected as the validation data ($[X_v, Y_v]$) for testing the model, and the remaining k - 1 subsets ($[X_t, Y_t]$) are used as the data for generating (training) the model. The cross validation process is repeated k times (number of the folds), with each of the k subsets used exactly once as the validation data to evaluate the MSE. In other words, F^i is generated (trained) using $[X_t^i, Y_t^i]$ subset and then validated using $[X_v^i, Y_v^i]$ by measuring its MSE. The MSE results for the k folds are then averaged to produce the validation error (V_{MSE}) of the model:

$$V_{MSE} = \frac{1}{k} \sum_{i=1}^{k} \|Y_v^i - F^i(X_v)\|^2 \tag{6.6}$$

Smaller validation error of a model (V_{MSE}) demonstrates that the model will probably estimate and describe the behavior of the data better. Cross validation eliminates the problem we had with the fitting error (F_{MSE}). This is due to the fact that the fit models generated at each step of the k-fold cross validation is trained and validated on separate data sets. In other words, each of the k subsets once has been considered as independent data sets and the generated fit models were not biased to those data.

The two metrics are used to assess how the generated fit model describes the collected data. The best fit model is the one which fits the data perfectly (F_{MSE}) while avoiding a biased model and over fitting (V_{MSE}). Hence, a cost function (C) is defined based on the two weighted metrics which helps in deciding the best fit model.

$$C = \alpha\ F_{MSE} + \beta\ V_{MSE} \tag{6.7}$$

where α and β are the weight parameters selected arbitrarily such that in the selected best fit model, over fitting is avoided and the model is stable and tolerable to variance and addition of data.

Pseudocode in Algorithm 5 explains the regression analysis conducted at run time to select the best fit model for the given data. Inputs to the function are the monitored SUD variables (X) and the controller quality signal (Y) from the neighbor system controller. X may be horizontally concatenated data of multiple SUD variables. Output of the function is the best fit model selected by assessing the data and all the alternatives. A pool of fit model types (*models*) specifying the order of the regression models and selection of polynomial features is defined in line 1. The number of splits for k-fold cross validation which is typically set to five, is defined in line 2. The data set ($[X, Y]$) is split to training ($[X_t, Y_t]$) and validation ($[X_v, Y_v]$) sets (lines 3-4). Each of the training and validation sets has k subsets for each iteration of k-fold cross validation. In lines 5-12, the fitting (F_{MSE}) and validation (V_{MSE})

errors for each fit model are evaluated (Equations 6.5 and 6.6). **polyfitn** is a function to generate fit model F based on the given data set and the specified fit model type; it solves the regression problem using QR decomposition. **polyvaln** is a function to evaluate the output of the fit model based on the input values; it is going to be simple matrix multiplication. In line 13, the cost function (Equation 6.7) is evaluated for the fitting and validation errors. Finally, the fit model with the minimum cost is selected as the best fit model and returned by the function.

ALGORITHM 5: Regression Analysis

Input: SUD variables X
Input: neighbor controller quality Y
Output: best fit model *bestF*

1 **define** *models* // pool of fit model types
2 **define** $k = 5$ // # of folds in cross validation

// split data to k-fold training and validation
3 $[X_t, X_v] \leftarrow$ **k-fold** (X)
4 $[Y_t, Y_v] \leftarrow$ **k-fold** (Y)

// assessing all the fit models
5 **for** $m = 1 : |models|$ **do**
6 $F\{m\} =$ **polyfitn** $(X,\ Y,\ models\{m\})$
// evaluating model fitting error
7 $F_{MSE}\{m\} = \text{norm}\ (\textbf{polyvaln}\ (F\{m\}, X) - Y)^2\ /\ |X|$
/* evaluating validation error using k-fold cross validation */
8 $V_{MSE}\{m\} = 0$
9 **for** $i = 1 : k$ **do**
10 $F^i =$ **polyfitn** $(X_t^i,\ Y_t^i,\ models\{m\})$
// evaluating model estimation error
11 $MSE^i = \text{norm}\ (\textbf{polyvaln}\ (F^i,\ X_v^i) - Y_v^i)^2\ /\ |X|$
12 $V_{MSE}\{m\} = V_{MSE}\{m\} + MSE^i/k$

// evaluating the cost function
13 $C = \alpha F_{MSE} + \beta V_{MSE}$
14 $[min\_m,\ min\_C] = \min\ (C)$
15 $bestF = F\{min\_m\}$ // select the best fit model
16 **return** $[bestF]$

6.3 ACQUA Control Design

Our adaptive cooperative quality-aware control design comprises of three modules which we describe in the following (see Figure 6.3).

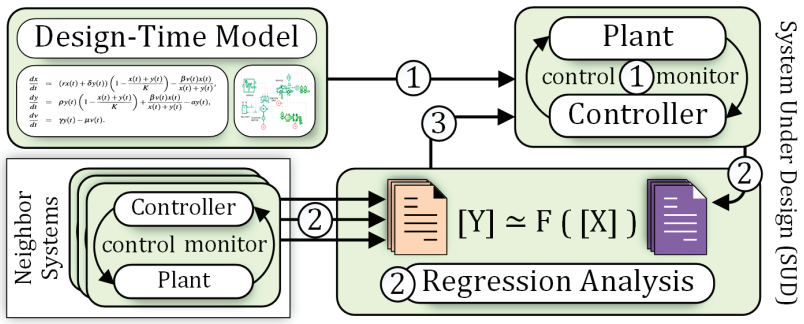

Figure 6.3: Modules of ACQUA-based control design for SUD.

1) The first module that also exists in other control designs is the main control and optimization of the system under design by considering the state variables and controller quality of the system. Different controlling approaches such as feedback control, Linear-Quadratic Regulator (LQR), and Model Predictive Control (MPC) may utilize the design-time model (see Section 6.2.1) of the SUD to estimate its behavior for optimizing the control inputs based on the feedback received from the system. The controller is responsible for ensuring the stability, optimal behavior, and controller quality of the system by adjusting the control inputs properly.

2) In second module, ACQUA learns the controller quality of the other neighbor systems (to be cooperated with) by monitoring their quality signal. ACQUA-based controller applies regression analysis to the collected data of controller quality and system variables at run time to dynamically generate a quality-aware behavioral model (see Section 6.2.2). It needs to be noted that, state-of-the-art embedded control designs implement a centralized design-time model of all these systems which can get too complex with larger CPS.

3) The third and final module is the integration of the generated quality-aware model into the existing control and optimization in order to establish a cooperative and adaptive control as we call ACQUA. The dynamically data-driven model generated at run time, provides an estimation of the controller quality of the neighbor systems which is added into the control and optimization of the SUD as an additional cost variable. It needs to be noted that the cooperation can be bi-direction and between multiple systems.

6.3.1 ACQUA-based Navigation System

In the following, we further describe how to leverage our ACQUA control design into an ANS cooperating with the MCU and the BMS. We explain how implementation of the ACQUA differs in compared to the existing ideal embedded control design.

Firstly, the BMS in EV monitors and controls the status of the battery cells. It is responsible for maintaining the battery parameters (e.g., temperature, current, and voltage) in the safe range. It may balance the load between the cells as well. This results in less energy consumption and less battery capacity loss (more battery lifetime). Therefore, in the BMS, the controller quality can be the battery energy consumption or the battery capacity loss.

Secondly, the MCU governs the performance of the electric motor. It may be responsible for selecting and regulating the speed, regulating or limiting the torque, and protecting against overloads and faults. Optimal adjusting of the electric motor torque and the power to its circuits may result in less energy consumption and degradation of the electric motor. Therefore, in the MCU, the controller quality can be the electric motor energy consumption.

On the other hand, the ANS selects the best route to a destination according to the selected controller quality which is the driving time. The controller utilizes the map database and driving route model to estimate the driving time at each route segment and thereby the

total driving time. Based on the estimated driving time, the ANS selects the fastest route. Therefore, the cost function of the control and optimization only involves the driving time.

In navigation systems, the cost function may also consider the electric motor power in order to help the MCU reduce its energy consumption. Moreover, the battery capacity loss may be added to the cost function to help the BMS improve the battery lifetime while driving. However, the behavior and characteristics of these variables need to be known at each route segment. In the state-of-the-art ideal embedded control designs (**IDEAL**), a centralized behavioral model is implemented to provide an estimation of the electric motor power and the battery capacity loss for the ANS [133].

However, the MCU and BMS may be able to provide the data for the electric motor power ($p_e \in P_e$) and the battery capacity loss ($q_b \in Q_b$). Moreover, the ANS already has the data for the driving speed ($v \in V$) and road slope ($\alpha \in A$). Hence, an ACQUA-based automotive navigation system (**ANS**) can benefit from the cooperation and retrieve the data while driving, to generate the necessary behavioral model (see Section 6.2.2). There will be two fit models F_{MCU} and F_{BMS} describing the relationships between the estimated electric motor power ($\widetilde{p}_e$) and battery capacity loss ($\widetilde{q}_b$) with the driving speed (v) and road slope (α):

$$\widetilde{p}_e = F_{MCU}\,(v, \alpha) \qquad\qquad \widetilde{q}_b = F_{BMS}\,(v, \alpha) \tag{6.8}$$

As more data is collected while driving, the fit models get updated dynamically and become more accurate and adaptive to the situation. Eventually, the dynamically data-driven models will be integrated into the cost function of the control and optimization in the ANS representing the quality of the BMS and MCU controllers (see Section 6.3). This enables system-level optimization and integration for the ANS, BMS, and MCU. It needs to be noted that there would be trade-offs between the quality of these controllers - driving time, electric motor power, and battery capacity loss.

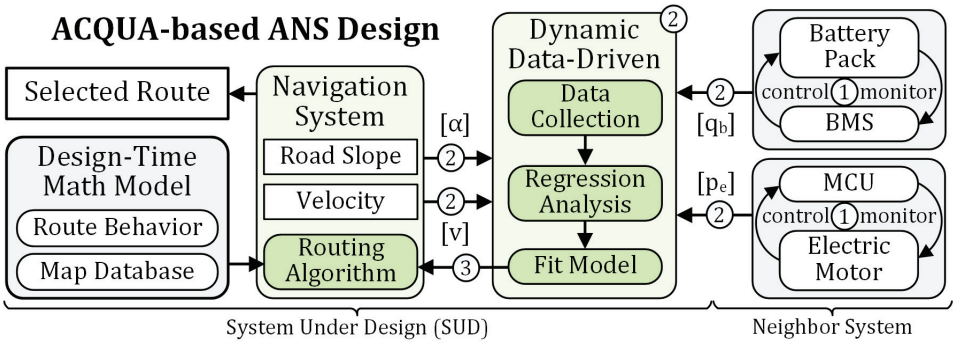

Figure 6.4: ACQUA-based navigation system cooperating with the EV motor control unit and battery management system.

Pseudocode in Algorithm 6 explains the implementation of an existing ANS and how our ACQUA control design is integrated into its control and optimization. The yellow highlighted codes are added on top of the existing control to enable the ACQUA. Inputs to the function are the current location of the EV (received from GPS), destination node, MCU quality signal, and BMS quality signal. Output of the function is the suggested direction or the selected route segment to drive on. Two arrays of $\overline{s}$ and $\overline{n}$ define the map segments and nodes stored locally in the ANS (line 1). In lines 2-5, current vehicle speed (v), road slope (α), MCU quality (p_e), and BMS quality (q_b) are added to the data sets ($[V, A, P_e, Q_b]$). In lines 6-7, the data sets are used by function **reg_analyze** to generate the best fit models (see Algorithm 5). These two lines bring the adaptivity feature to the control design. In line 8, the ANS pre-processes all the routes to the destination by solving a single-destination routing problem (**routing** function) [133]. Array of *routes* stores the fastest routes to the destination from any give node. In lines 9-20, the ANS continues searching for direction if the vehicle has not reached the destination node yet (*fid*). Segments connected to the current node are extracted and iterated to find the best one (lines 11-12). For each segment, the neighbor node is selected and the predicted route from the node is extracted from the array of *routes* (lines 13-14). In line 15, **evaluate** function uses the mathematical design-time models to estimate the driving route parameters such as the driving time in order to evaluate the cost of the driving route (see Section 6.2.1). In the ACQUA, the generated best fit models (F_{MCU}

and F_{BMS}) are also utilized to estimate the MCU and BMS controller qualities based on the predicted route and then the route cost is adjusted (line 16). This line makes the controller cooperative and quality-aware of the neighbor system controllers. Parameters α and β are set to give weights to the MCU and BMS controller qualities in trade-off with the driving time. The route with the minimum cost is selected and its segment direction is returned (lines 17-20).

ALGORITHM 6: ACQUA-based Automotive Navigation System

Input: current node *current*
Input: destination node *fid*
Input: MCU quality signal p_e
Input: BMS quality signal q_b
Output: best direction *selected_seg*

1 **define** $\overline{s}, \overline{n}$ `// stored map segments and nodes`

`// ACQUA data collection`
2 $V \leftarrow [V; v]$ `// vehicle speed`
3 $A \leftarrow [A; \alpha]$ `// road slope`
4 $P_e \leftarrow [P_e; p_e]$ `// MCU quality signal`
5 $Q_b \leftarrow [Q_b; q_b]$ `// BMS quality signal`

`// dynamically data-driven modeling`
6 $F_{MCU} =$ **reg_analyze** $([V, A], P_e)$
7 $F_{BMS} =$ **reg_analyze** $([V, A], Q_b)$

`// pre-process all the routes to destination`
8 $routes =$ **routing** $(\overline{s}, \overline{n}, fid)$
9 **if** $current \neq fid$ **then**
10 $min\_cost = \infty$
11 $attached\_segments = \{s \in \overline{s} \mid s('\text{start}') = current\}$
`// search the segments from current node`
12 **for** *seg* ***in*** *attached_segments* **do**
13 $neighbor = seg('\text{end}')$
14 $route = [current;\ routes(neighbor)]$
`// use design-time model to evaluate route driving time`
15 $cost =$ **evaluate** $('\text{time}', route)$
`// update cost to consider other qualities`
16 $cost \mathrel{+}= \alpha$ **evaluate** $(F_{MCU}, route) + \beta$ **evaluate** $(F_{BMS}, route)$
17 **if** $cost < min\_cost$ **then**
18 $min\_cost = cost$
19 $selected\_seg = seg$
20 **return** $[selected\_seg]$

6.4 Experimental Results

We experiment and analyze how ACQUA influences the performance of a controller by considering the example of an ANS cooperating with MCU and BMS.

6.4.1 Experiment Setup

A real-life EV - Nissan Leaf S [63, 133] - is considered for the experiment. The behavior of the EV electric motor and battery are modeled and simulated (see Section 6.2.1) using automotive design and simulator tools: AMESim [9] and ADVISOR [155]. The map and route behavior data (see Sections 6.2.1) for the ANS are extracted from Google Maps and OpenStreetMap real-life databases [8, 60, 133] considering the map of Orange County in California, U.S.A. We conduct the experiments by driving the EV on arbitrary selected six real-life benchmark routes listed in Table 6.1:

Table 6.1: Multiple real-life route benchmarks.

route	*A*	*B*	*C*	*D*	*E*	*F*
start	(1)	(5)	(5)	(1)	(5)	(5)
end	(3)	(6)	(2)	(2)	(4)	(3)

(1) UCI: 33.6439°, -117.8345°
(2) Cisco: 33.6921°, -117.8285°
(3) Shopping Center: 33.6136°, -117.8685°
(4) MidSchool: 33.6638°, -117.8085°
(5) Grocery Store: 33.6637°, -117.8263°
(6) Park: 33.6605°, -117.8118°

The run-time controllers and algorithms including the ANS, MCU, and BMS (see Section 6.3) are implemented in MATLAB/Simulink. Controller quality signals of the neighbor systems: MCU and BMS are passed as input variables to the ACQUA-based ANS at run time. However, a Gaussian noise with 10% variance has been added to make the behavior of the systems non-deterministic. The computing platform used for the experiment is comprised of an Intel Core-i7 3770 CPU with 2.3 GHz clock frequency and 8 GB of 1600 DDR3 RAM.

6.4.2 Results and Analysis

Regression Analysis: The ACQUA controller collects data at run time to generate the two fit models for MCU and BMS. The regression analysis algorithm evaluates various fit models to see which on is the best fit. Fitting and validation errors should be lower for the selected fit models.

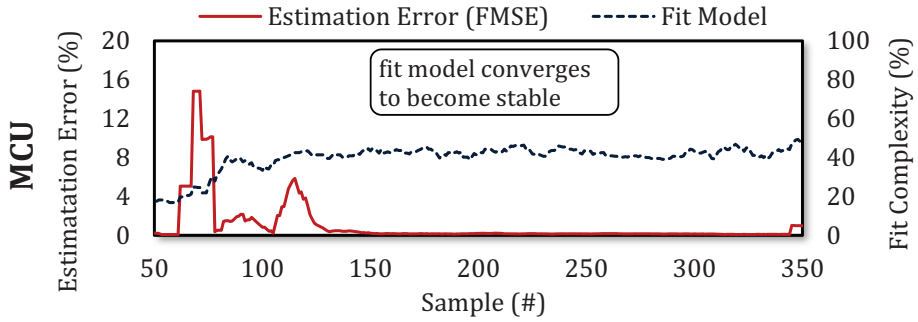

(a) Motor Control Unit

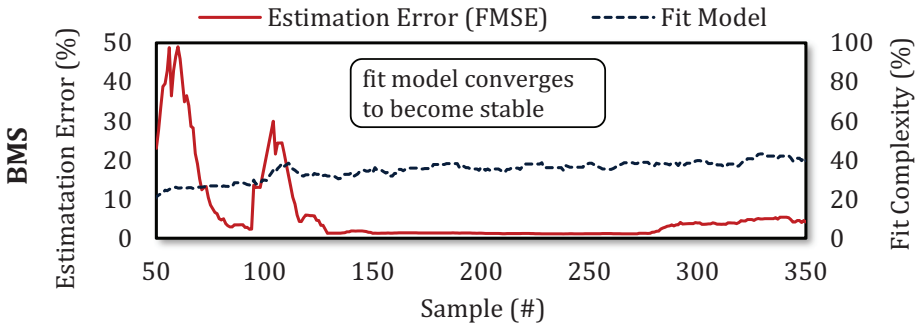

(b) Battery Management System

Figure 6.5: Model estimation error and fit model adjustment at run time.

Figures 6.5(a) and 6.5(b) show the estimation errors (F_{MSE}) of the fit models at each time step validated against the whole data set. As shown in the figures, the fit models change dynamically to adapt to the collected data. It shows that the errors decrease by updating the models as more data is collected. The validation errors does not decrease after a specific number of samples and the fit model get more stable. This is due to the fact that over fitting is avoided and having more data increases the variance and its corresponding error.

Real and estimated values of the MCU quality (Q_b) and BMS quality (P_e) are drawn in Figure 6.6. The fit models are generated based on four of the six benchmark routes ($\simeq$70%-

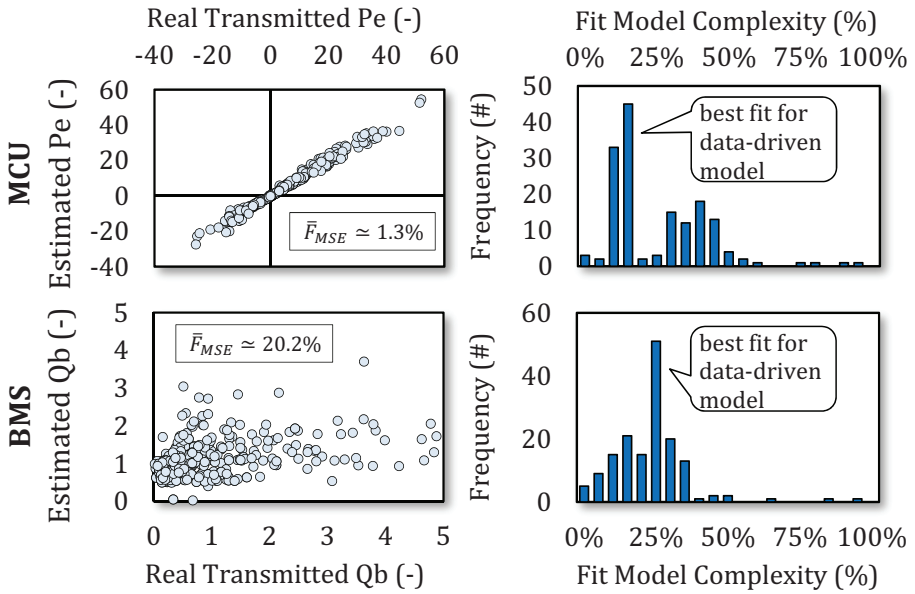

Figure 6.6: Regression accuracy and fit model histogram.

30% training-validation splits). The percentage of the validation error for F_{MCU} and F_{BMS} are 1.3% and 20.2%, respectively. It shows that the ACQUA estimates the controller qualities with adequate error; higher complexity of the battery behavior results in higher error. The regression analysis adjusts the best fit models at run time. The selection frequency of each model fit is shown in Figure 6.6. It shows that the polynomial regression models with the complexity of 21% and 26% (out of order of 8) are the best fit for MCU and BMS controller qualities. The best fit models are drawn in Figures 6.7(a) and 6.7(b) alongside the collected data values.

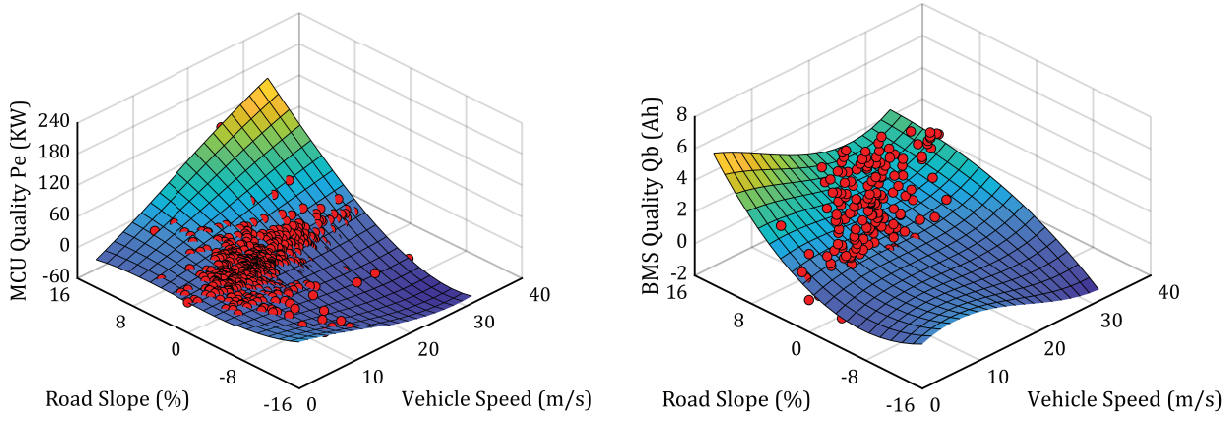

(a) Motor Control Unit

(b) Battery Management System

Figure 6.7: The best fit regression models and the data values.

We compare the performance of the control designs below in terms of EV energy consumption, battery capacity loss, and complexity:

1. ***ALONE.*** the ANS is completely independent from other systems and only considers the driving time for optimizing the route which is its controller quality.

2. ***IDEAL.*** a centralized behavioral model of the electric motor and battery is integrated into the ANS [133]. This enables an ideal system-level optimization with the MCU and BMS to consider energy consumption and battery capacity loss.

3. ***HALF-ACQUA.*** the ANS only has knowledge of the battery. It cooperates with the MCU to learn its behavior and generate a data-driven model to enable the system-level optimization.

4. ***FULL-ACQUA.*** the ANS does not have prior knowledge of the electric motor and battery. It cooperates with MCU and BMS to learn their behavior and generate data-driven models.

Table 6.2: Complexity analysis of different control designs.

Control Design	System-Level Optimization	No Centeralized Model Needed	Model Execution Time	
			Generation (µs)	Estimation (µs)
ALONE	✗	!	-	-
IDEAL	✓	✗	-	1.09
HALF-ACQUA	✓	✓	865.21	14.58
FULL-ACQUA	✓	✓	1602.45	29.24

Table 6.2 summarizes the details for the control designs in the experiment. It also shows that our ACQUA-based control design can enable system-level optimization without the need of a centralized model with low computation overhead.

Figures 6.8 and 6.9 illustrate the battery energy consumption and capacity loss for each benchmark route and each control design. The driving time (min) values for the routes

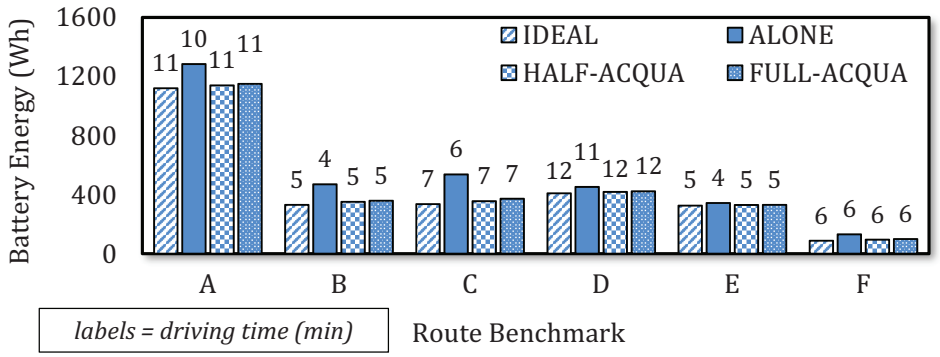

Figure 6.8: Energy consumption vs. control design and route.

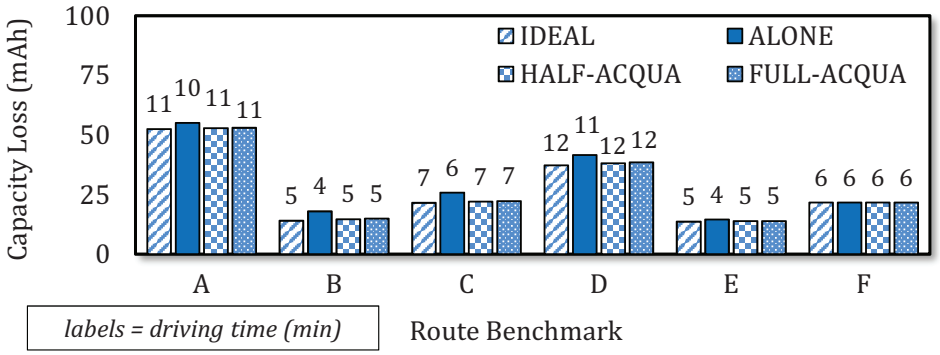

Figure 6.9: Battery capacity loss vs. control design and route.

are shown on top of each bar. **ALONE** control results in the least driving time thereby increasing the energy consumption and capacity loss. **IDEAL** control results in an pareto-optimal solution which may minimize the battery capacity loss and energy consumption with the driving time. The performance of our **ACQUA** control is in the middle of the two other controls, as it is expected. It tries to reach the solution of the **IDEAL** control by being aware of the model of the neighbor systems. The performance of **HALF-ACQUA** is closer to **IDEAL** than **FULL-ACQUA** since it has a prior knowledge of the battery. Nevertheless, the regression model in our ACQUA estimates the controller qualities with adequate accuracy such that it reaches 86% of the maximum achievable improvement by **IDEAL** control. The results show that energy consumption reduces by 18% and the battery capacity loss decreases by 12% compared to **ALONE** control.

6.5 Concluding Remarks

We observed that the state-of-the-art control designs in CPS require a centralized complex behavioral model of the influencing/influenced neighbor systems to reach a system-level pareto-optimal solution. This is challenging for the control designers who lack the knowledge of the neighbor systems. Hence, in this chapter, we proposed our ACQUA control design that learns the behavior of the neighbor systems by monitoring and modeling their controller quality with respect to the SUD variables. The dynamically generated data-driven model is then integrated into the existing controller at no cost to enable the cooperation with neighbor systems. We applied our ACQUA into a navigation system to cooperate with motor control unit and battery management system. The results illustrated that by only driving the EV once on a route, the ANS can model the MCU and BMS controller qualities with an adequate accuracy for the next trip to enable system-level optimization for both driving time and battery capacity loss. As a result, energy consumption reduces by 18% and the battery capacity loss decreases by 12% compared to the state-of-the-art on average which is 86% of the maximum achievable improvement by an ideal control.

Chapter 7

Driving Behavior Estimation

7.1 Introduction and Related Work

The electric motor is a major component in the EV that consumes energy in the motor mode and generates energy in the regenerative mode when braking. Future reactions of the driver in terms of adjustments to vehicle direction and speed, based on the driver's perception of the route and vehicle condition are described as driving behavior. The energy consumption/generation depends on the driving behavior on the route and can vary for different drivers [104, 142] (see Figure 7.1). Moreover, other accessories in EV especially Heating, Ventilation, and Air Conditioning (HVAC) system have shown to be another major contributor to battery energy consumption [20, 70, 131, 138]. The HVAC energy consumption depends on its utilization and the ambient temperature, thereby making HVAC a flexible load. The total power request in the EV influences the battery operating behavior and will be illustrated in EV driving range and battery lifetime that are the major EV design challenges [134].

Design challenges in EV have been addressed by designing more efficient and robust battery cells, device-level battery management systems, or system-level battery and energy managements. The device-level methodologies monitor or control the cells in order to maintain their safe and efficient operation [115]. Moreover, as we focused in this thesis, system-level methodologies are implemented to optimize the battery utilization by adjusting higher-level power requests in order to improve the battery lifetime and driving range given the future driving route [86, 151] (see Chapters 2-5).

For instance, it has been shown that the driving route influences the EV energy, thereby the EV driving range and battery lifetime. This is in addition to the fact that the driving route also affects driving time and distance. Hence, navigation systems have been implemented to optimize and select the best route for a specific EV [133, 137, 147, 150] (see Chapter 4). In another work, route prediction has helped in optimizing the energy split between battery and

ultracapacitor in Hybrid Electrical Energy Storage (HEES) [29, 152]. Moreover, a predictive thermal and energy management methodology has been implemented for Hybrid Electrical Energy Storage (HEES) in order to optimize the ultracapacitor and battery utilization while maintaining the battery temperature in the safe range (see Chapter 2). Furthermore, a battery lifetime-aware automotive climate control has been implemented which considers the driving route in the future to predict the EV power requests and optimize the HVAC operation while maintaining passenger thermal comfort (see Chapter 3).

The above-mentioned system-level battery and energy management methodologies require information regarding the future EV power requests for optimizing the control inputs. Hence, they have assumed that the driving route - which can be provided by the navigation system - is known before hand for estimating future EV states. However, the driving route is not the only factor affecting the EV power. The driving behavior of a driver regarding the driving route condition is also influential. Experiments have been conducted to illustrate how driving behavior affects the power consumption.

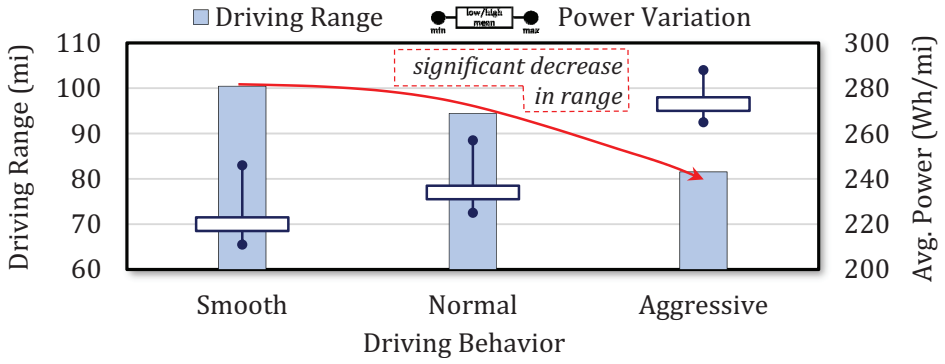

Figure 7.1: Impact of different driving behavior on EV power consumption variation and driving range tested on Nissan Leaf [104].

7.1.1 Motivational Case Study

The impact of different aggressiveness levels of driving behavior on the EV power has been analyzed using historical data. Figure 7.1 shows the power consumption and estimated driving range evaluated for a Nissan Leaf simulated in FASTSim [104, 142].

Summary and conclusion from observations: we realized that the driving behavior may significantly affect the EV acceleration and speed, and thereby the power consumption. Hence, the driving behavior should be accounted into the energy management as well. However, current EV power prediction has been limited to the knowledge of only the driving route. This limitation significantly decreases the estimation accuracy required for the EV battery and energy managements.

Driving behavior modeling has been investigated and exploited for driver assistant systems, especially for vehicle safety purposes [82, 83]. These models attempt to eliminate the driver's decision-making lag of 0.5-1.5 seconds [21, 22, 126] and predict the future reactions up to a few seconds. For instance, in the state-of-the-art modeling methodologies using Hidden Markov Model (HMM), Neural Network (NN), and graph modeling, the driver's behavior in terms of the vehicle speed is predicted up to the next 3 seconds with accuracy of up to 99.5% [37, 68, 119]. These controllers need to be triggered within a few seconds before an event for safety purposes. Hence, we consider their prediction as short-term (< 5 seconds). However, these short-term predictions are not sufficient for battery and energy management methodologies. They require more accurate and longer-term predictions of at least more than 5 seconds to perform well. The requirement for longer prediction time is mainly due to the fact that the physical process involved is much slower. We consider their prediction as long term when the prediction time is comparable to the duration of driving segments.

7.1.2 Problem and Research Challenges

The problem of driving behavior modeling and estimation for EV energy management poses the following challenges:

1. Energy and battery managements in EV do not account driving behavior for optimization, although it affects the operating parameters - driving range and battery lifetime.

2. Accuracy of the EV power consumption estimation has been at stake due to lack of driving behavior consideration.

3. Driving behavior modeling methodologies focus only on very recent input information and current state (visible environment around the car) for short-term prediction. This leads to failure of the prediction for longer period of time.

7.1.3 Main Contributions and Concept Review

To address the above-mentioned challenges, a novel methodology of driving behavior modeling and estimation for EV energy management is proposed which employs:

1. **Electric Vehicle Modeling (Section 7.2.1):** main EV components such as electric motor, HVAC, and battery are modeled using Ordinary Differential Equations (ODE) and operating parameters such as power consumption and battery lifetime are estimated for various driving conditions.

2. **Driving Behavior Modeling (Section 7.2.2):** driving behavior is modeled using a variation of Artificial Neural Networks (ANN) by training a novel context-aware Nonlinear AutoRegressive model with eXogenous Inputs (NARX) [97, 125] based on historical behavior of the drivers, their recent reactions, and the average speed of the route reported by Google Maps. This context-aware model estimates the driving behavior of a specific driver in terms of the vehicle speed for up to 30 seconds (long term).

3. **Integration into EV Energy Management (Section 7.3):** the estimated future maneuvers of the driver in terms of vehicle speeds are utilized in the battery and energy management methodologies for improving the battery lifetime and driving range. In this chapter, a battery lifetime-aware automotive climate control is implemented and its performance has been analyzed using our novel context-aware driving behavior modeling and estimation methodology.

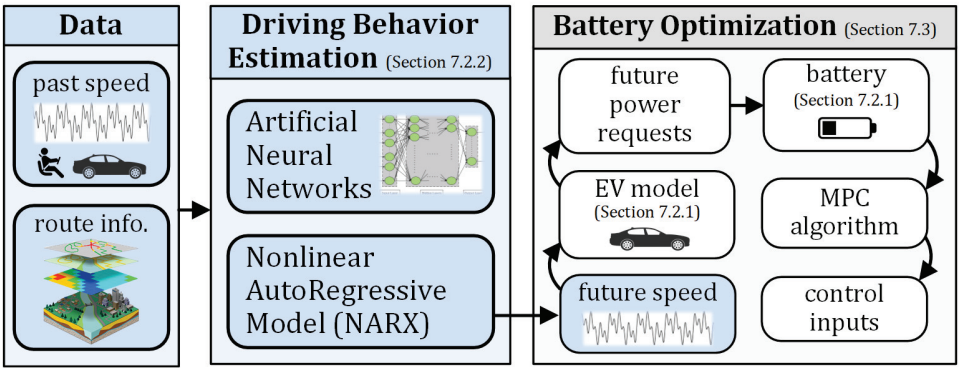

Figure 7.2: Illustration of our novel context-aware driving behavior modeling and estimation for energy management (contributions highlighted).

Figure 7.2 illustrates our proposed methodology to estimate the driving behavior. In this chapter, the EV driving dynamics are modeled given the driving behavior. Moreover, a context-aware NARX model (variation of ANN) is generated and trained using driving route information and corresponding real data of the driver's behavior. Our novel model is self-adaptive with respect to specific driver behavior and is able to predict the driving behavior for long-term up to 30 seconds. We integrate our context-aware model into a newly adjusted energy management methodologies. Hence, their control inputs are adjusted given the future vehicle speeds and EV power requests to minimize power variation, energy consumption, and extend the battery lifetime.

7.2 System Modeling and Estimation

Recent energy management methodologies deployed in EV, as in the battery lifetime-aware automotive climate control, require modeling of the EV components for predicting their dynamic behavior and power requests (see Section 7.2.1). Moreover, estimation of the driving behavior and vehicle speed (see Section 7.2.2) is required for accurate estimation of the EV power request. The system modeling and estimation is then used for optimizing and adjusting the control inputs in order to improve the EV driving range and battery lifetime.

7.2.1 Electric Vehicle

EV as an automotive Cyber-Physical System (CPS) consists of many interconnected subsystems with various functionalities and responsibilities. There are two subsystems in EV (electric motor and HVAC) which are the main contributors to energy consumption/generation (i.e. battery utilization). Their functional behavior needs to be investigated and modeled, for estimating the EV power request at each instance of time.

Electric motor generates the necessary force to drive the vehicle. The power consumption or generation of the electric motor in the EV is modeled and estimated by considering the motor characteristics and driving forces on the vehicle such as: gravitational (F_{gr}), aerodynamic drag (F_{aero}), and rolling resistance (F_{roll}) forces.

$$F_{tr} = F_{gr} + F_{aero} + F_{roll} + ma \tag{7.1}$$

The tractive force (F_{tr}) is provided by the electric motor to overcome the forces to propel the vehicle with mass (m) forward at a desired speed (v) and acceleration (a) [117]. The direction of F_{tr} is defined by whether the electric motor is in regenerative mode (regenerative braking) or motor mode.

The electrical motor power consumption (P_e) is calculated as:

$$P_e = \frac{F_{tr} v}{\eta_m} \tag{7.2}$$

where η_m represents the electric motor efficiency when converting electrical to mechanical energy in the motor mode and converting mechanical to electrical energy in the regenerative mode (regenerative braking). η_m is dependent on the motor rotational speed and the generated torque; its values are provided as the electric motor specifications [86, 93, 162].

HVAC system is monitored and controlled by the automotive climate control to maintain the cabin temperature. The cabin temperature (T_z) is influenced by the supply air temperature (T_s), flow rate ($\dot{m}_z$), the cabin heat capacity (M_c), and the heat capacity of the air (c_p). The relationships between these variables and parameters are defined by ordinary differential equations describing thermodynamics in the HVAC system [131].

The HVAC system power consumption consists of: 1) cooling power, 2) heating power, and 3) fan power. The cooling and heating power consumption is due to the energy difference between their inlet and outlet air flow:

$$P_c = \frac{c_p}{\eta_c}\dot{m}_z(T_m - T_c) \tag{7.3}$$

$$P_h = \frac{c_p}{\eta_h}\dot{m}_z(T_s - T_c) \tag{7.4}$$

where P_c and P_h are cooling and heating power consumption. η_c and η_h are the efficiency parameters of the cooling and heating processes. Moreover, the heat exchange between the coolant/evaporator and air is modeled as efficiency parameters. The air returned from the cabin (T_z) and the outside air (T_o) are mixed and recirculated back into the cooling coil. T_m is the temperature of the mixed air and d_r is the mixture fraction [$T_m = (1-d_r)T_o + d_r T_z$]. T_c is the temperature of the outlet air after cooling before heating. The fan power consumption (P_f) is quadratically related to $\dot{m}_z$ and k_f is a parameter that captures the fan efficiency and the duct pressure losses.

$$P_f = k_f(\dot{m}_z)^2 \tag{7.5}$$

The parameters for the model are set based on an HVAC specifications and to accurately describe the thermodynamic behavior in different conditions [66, 131].

Battery provides the power requested by the EV systems such as the electric motor and the HVAC. The influence of these power requests on the battery are estimated by models of the battery operating behavior such as State-of-Charge (SoC) and battery lifetime degradation or State-of-Health (SoH).

The usable capacity inside a lithium-ion battery decreases with higher discharge rate (I) (rate-capacity effect). This effect is modeled by the Peukert's Law using the effective current. Hence, the SoC of the battery is estimated by the coulomb counting and measuring the effective discharge rate:

$$SoC^{t} = SoC^{0} - \frac{100}{C_n} \times \int_0^t I \left(\frac{I}{I_n}\right)^{pc-1} dt \tag{7.6}$$

where C_n is the nominal capacity measured at nominal current (I_n) predefined by the manufacturer. SoC^{t} represents the SoC value at time t. pc is the Peukert's constant typically measured empirically for the type of lithium-ion battery cell [48, 148]. For the battery type used here, pc is evaluated as 1.1342. Although this constant is necessary to capture the battery consumption behavior, our methodology is not influenced by its value.

Ratio of current capacity to nominal capacity (SoH) degrades over time in lithium-ion batteries (capacity-fade effect). The SoH degradation ($\bigtriangledown SoH$) is mainly influenced by the stress on the battery cell which is modeled by SoC deviation (SoC_{dev}) and SoC average (SoC_{avg}). $\bigtriangledown SoH$ is related to the pattern of SoC values over a time period [98] following Equation 7.7:

$$\bigtriangledown SoH = f\ (SoC_{dev}, SoC_{avg}) = \ \ (a_1 e^{\alpha SoC_{dev}} + a_2)(a_3 e^{\beta SoC_{avg}}) \tag{7.7}$$

where α, β, a_1, a_2, and a_3 are the parameters for estimating $\bigtriangledown SoH$ accurately based on the battery type. Thorough evaluation of the battery temperature influence on $\bigtriangledown SoH$ is out of the scope of the chapter. Hence, we have modeled it as a constant in Equation 7.7.

The EV components are modeled using the above-mentioned equations. Moreover, their parameters are extracted from the manufacturers' forums and experimental data provided by the third-parties testing the vehicle (see Table 7.1).

Table 7.1: Components specifications of the Nissan Leaf EV.

Specification		Nissan Leaf S
Battery	Energy	24 KWh
	Voltage	403.2 v
	Capacity	59.52 Ah
Body	Weight	1471 Kg
	Height	1.5494 m
	Width	1.7703 m
Wheel	Rim Diameter	16 inch
	Overall Diameter	25 inch
Gear	Single Ratio	7.9377

7.2.2 Driving Behavior

The driving forces on the vehicle are evaluated by knowing the driving behavior given the EV model (see Section 7.2). The driving behavior depends on the driving route and reactions of the driver to specific route condition. Although the driving behavior estimation is leveraged in the battery optimization, they operate independently of each other. In the following, we describe state-of-the-art methodologies to model the driving behavior in terms of the future vehicle speed that will be used for EV power request prediction in the battery optimization:

1) Ideal (IDL). In this model, we are able to predict the vehicle speed at any given time with perfect accuracy. In other words, a controller would have access not only to the previous and current vehicle speeds, but also to the future vehicle speeds.

2) Motion-Preserving (MP). Typically, in rule-based or optimization-based methodologies [112, 127], either there is no assumption about the future, or the assumption is

that the vehicle is going to preserve its current motion. In other words, in this model, the future vehicle speed after h seconds, is assumed to be determined by the following physics-based equation,

$$v_{t|k} = v_{t|0} + a_{t|0} \times k \tag{7.8}$$

where $v_{t|0}$ and $a_{t|0}$ are the speed and acceleration values at time t. $v_{t|k}$ is the speed for time $t+k$ predicted at time t.

3) Statistical Modeling. In this approach, the future vehicle speed is predicted using past speeds, current speed, and information of any other factors that can affect the vehicle speed. Since the correlation between the current speed and predicted speed decreases for further future time instances, the estimation error increases. In order to address this, as part of our novel methodology, statistical information of the average speed for each road segment ($\widetilde{v}$) extracted from Google Maps APIs [8] is also fed to the model providing the future context and condition of the driving route. Given the current location of the vehicle, the future trajectory of the vehicle and the average speed values can be determined using the map database. The average speed at a specific time is a feature and information that is provided that can represent and model the uncertainty, route condition and traffic of a segment. Therefore, accounting them into the model will further reduce the prediction error. More features can be used to improve the accuracy, however, the available data of the route is limited.

To model and predict the driving behavior, we evaluate $V_t^{+h} = \{v_{t|k} : 1 \leqslant k \leqslant h\}$, which are the predicted values of the vehicle speeds for the next $h \geqslant 1$ future seconds at time t. The problem of statistical modeling is formulated as a challenge to estimate the function f in Equation 7.9,

$$V_t^{+h} = f\ (V_t^{-d}, \widetilde{V}_t^{-d'}, \widetilde{V}_t^{+h'}) + E_t^{+h} \tag{7.9}$$

where $V_t^{-d} = \{v_\tau | t-d \leqslant \tau \leqslant t-1\}$ and $\widetilde{V}_t^{-d'} = \{\widetilde{v}_\tau | t-d' \leqslant \tau \leqslant t-1\}$ represents the values for the past d and d' real speeds and average speeds before time t. $\widetilde{V}_t^{+h'} = \{v_{t|k} : 1 \leqslant k \leqslant h'\}$ represent the values for the future h' average speeds since time t. $E_t^{+h} = \{e_\tau | t+1 \leqslant \tau \leqslant t+h\}$ represent the error introduced to the system due to other factors influencing the future speeds (V_t^{+h}) such as weather, etc. However, other influencing factors have been considered to be the same for all the data and are avoided in the modeling and estimation. Hence, $\hat{V}_t^{+h} = \hat{f}\ (V_t^{-d}, \widetilde{V}_t^{-d'}, \widetilde{V}_t^{+h'})$ is predicted using $\hat{f}$, the approximation of function f. We have investigated three machine learning and modeling techniques for approximation: Random Forests, FeedForward Neural Network, and NARX.

3.a) Random Forests (RF). Multiple regression Decision Trees (DT) are combined to make an RF [26]. Each of these regression decision trees chooses a random set of input variables (features such as past, current speeds, and future average speeds) and works independently on a subset of data to model a particular aspect of the driving behavior. In a regression decision tree, instead of making deterministic decisions in the leaves as in a binary decision tree, a statistical distribution model specifies the probability of each output value. Singular decision trees easily over fit the training data. However, this is addressed in RF by randomly selecting the input features for each decision tree and combining the results. A single probability distribution is generated by weighted averaging of the probability distribution outputs of the trees based on the frequency of occurrence of a particular driver behavior in the training data set. The most probable value of the final distribution is reported as the final result of the random forests.

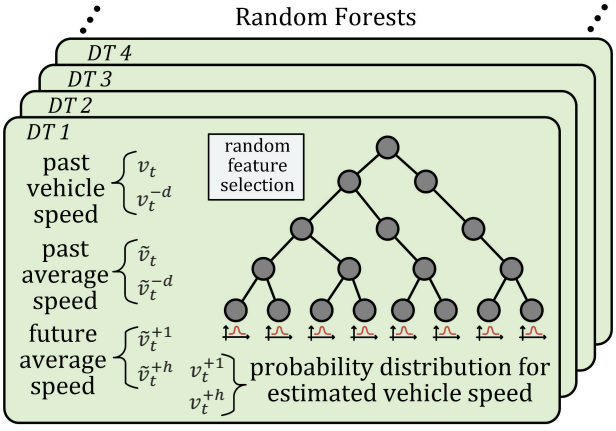

Figure 7.3: RF architecture to predict each of the future speed values.

3.b) FeedForward Neural Network (FFNN). Artificial Neural Networks (ANN) are a family of models that are mostly used to estimate nonlinear functions with large number of inputs and outputs. They consist of connected artificial neurons which mimic biological neural network behavior under different topologies. In order to model driving behavior and estimate future vehicle speed (approximate function $\hat{f}$), considering limited processing power, we initially chose FFNN, the simplest, fastest, and the most common variation of ANNs [23, 160]. In an FFNN architecture, neurons in one layer are connected via directed weighted edges to only the neurons in their adjacent layer and there is no interconnection between neurons inside one layer. Moreover, as the name FFNN suggests, there are no feedback edges in this architecture of neurons (see Figure 7.4).

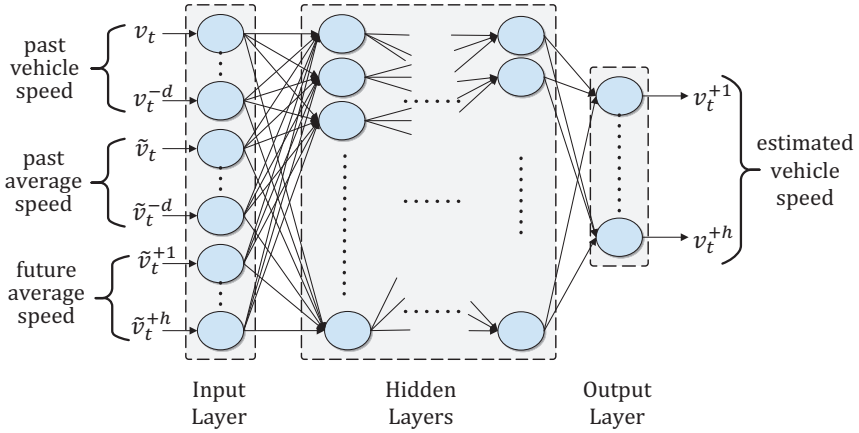

Figure 7.4: FFNN architecture to predict future speed values.

The output signal of neuron i in layer $l+1$ is calculated by:

$$z_i^{l+1} = f\ (w_{0i}^l + \sum_{j=1}^{n^l} w_{ji}^l z_j^l) \tag{7.10}$$

where n^l is the number of neurons in layer l, w_{ji}^l is the weight of the edge between neuron j in layer l and neuron i in layer $l+1$, and w_{0i}^l is the inherent threshold of neuron i in layer $l+1$ (treated as a normal weight with the input signal being one). f is a transfer function which is (typically) chosen to be a logistic sigmoid function, $f(x) = \frac{1}{1+e^{-x}}$. Weight of the edges are calculated by a Back Propagation (BP) algorithm [100] to train the model and

minimize the following performance function:

$$MSE = \frac{1}{P}\sum_{p=1}^{P}\sum_{k=1}^{K}(d_k^p - o_k^p)^2 \tag{7.11}$$

where MSE is the global mean sum squared error between the estimated outputs o^p and the targets d^p where p and k are indices for the training sample p and for the component k of the output vector, respectively.

3.c) Nonlinear AutoRegressive model with eXogenous Inputs. NARXs are one of the simplest architectures of Recurrent Neural Networks (RNN) that includes feedback edges between two different layers of nodes. RNNs are a very promising family of Neural Networks which have the capability to adapt to changes in the input/output, and typically they are much more stable in compare to FFNNs. In this work, we have chosen to focus on NARXs which inherit the adaptivity properties of their architecture family and have been proven to carry out good results in long-term prediction applications [97, 125].

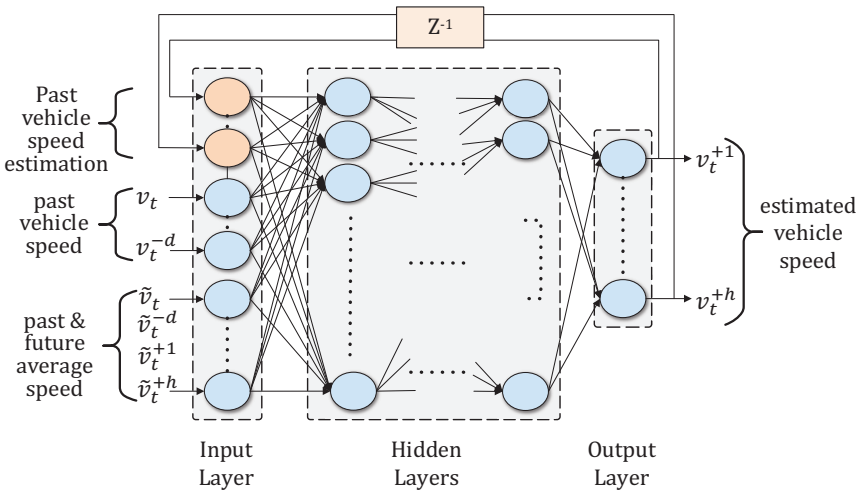

Figure 7.5: NARX architecture to predict future speed values.

As shown in Figure 7.5, the architecture is similar to FFNN's and the only difference is that the output of the architecture is connected to its input by a delay of one-second. In other words, to train a NARX-based model, function $\hat{f}$ in $\hat{V}_t^{+h} = \hat{f}\ (V_t^{-d}, \widetilde{V}_t^{-d'}, \widetilde{V}_t^{+h'}, \hat{V}_{t-1}^{+h})$

is estimated to minimize the effect of E_t^{+h} in Equation 7.9. The feedback loop in this architecture helps in capturing the behavior of a specific driver. It needs to be noted that the NARX model adapts to the specific driver behavior at the training phase (offline) with no extra time spent online. In other words, the pre-trained NARX model has the ability to adapt its output to each individual driver's behavior, at the cost of a limited amount of processing power thanks to the feedback from its estimated outputs to its inputs.

Although RFs are known to easily achieve high accuracy for a wide range of problems, ANNs can be more accurate if their parameters are tuned for the given problem. Moreover, NARXs, as a fast recurrent architecture of ANNs, are more suitable for time-series prediction since they can memorize and utilize the recent observations in the time-series data. It needs to be noted that any technique that can reach the same accuracy is also applicable to our methodology. In this chapter, our context-aware NARX model with 8 layers is used to predict 30 seconds ($h = 30$) of future vehicle speeds. The number of input features is $d = 35$, $d' = 5$, and $h' = 35$ (total 76 features). These values were decided based on the data and validation error to avoid over fitting.

7.3 Driving Behavior within Energy Management

We elaborated on how our methodology models and estimates the driving behavior in terms of the future vehicle speeds (Section 7.2.2). The estimated future values of the vehicle speed are used by the battery and energy managements in order to predict the EV power requests and optimize their control inputs. In this chapter, we consider a battery lifetime-aware automotive climate control as an example of how to deploy this driving behavior estimation for improving the driving range and battery lifetime while maintaining the thermal comfort for the passengers. It needs to be noted that any control methodology that uses the future driving behavior for its optimization purpose can benefit from our model.

As detailed in Algorithm 7, our driving behavior modeling methodology implemented as the function $\hat{f}$, uses the past vehicle speeds (V^{-d}), past average vehicle speeds ($\widetilde{V}^{-d'}$), and future average vehicle speeds ($\widetilde{V}^{+h'}$) (by Google Maps) in order to estimate the future vehicle speeds ($\hat{V}^{+h}$) (line 1). The future vehicle speeds ($\overline{v}$) are derived to evaluate the future vehicle acceleration ($\overline{a}$) (lines 2-3). Moreover, the future road slopes ($S^{+h'}$) are retrieved and saved in $\overline{\alpha}$ from Google to predict the driving forces on the EV such as the gravitational force (line 4). In line 5, the electric motor model is utilized to predict the power requests based on the driving behavior (see Section 7.2.1). Then, the battery lifetime-aware automotive climate control implements a Model Predictive Control (MPC) (lines 6-9) that considers the pattern of the electric motor power requests to adjust HVAC control inputs and optimize its utilization. The objective of the optimization is to maintain the temperature and reduce the battery stress by decreasing the SoC deviation (Equation 7.12). Finally, the optimal control inputs are applied to the HVAC (lines 10-11).

ALGORITHM 7: Driving Behavior Integration with Climate Control

Input: past vehicle speeds V^{-d}
Input: past average vehicle speeds $\widetilde{V}^{-d'}$
Input: future average vehicle speeds $\widetilde{V}^{+h'}$
Input: future road slopes $S^{+h'}$
Input: current state T_z
Output: control inputs $[P_f, P_c, P_h]$

`// estimate future vehicle speeds`
1 $\hat{V}^{+h} \leftarrow \hat{f}\ (V^{-d},\ \widetilde{V}^{-d'},\ \widetilde{V}^{+h'})$
2 $\overline{v} \leftarrow \hat{V}^{+h}$ `// future vehicle speed`
3 $\overline{a} \leftarrow d\hat{V}^{+h}/dt$ `// future vehicle acceleration`
4 $\overline{\alpha} \leftarrow S^{+h'}$ `// future road slope`
`// predict electric motor power consumption`
5 $P_e \leftarrow$ **electric motor** $(\overline{v}, \overline{a}, \overline{\alpha})$
`/* define state variables and control inputs */`
6 $x^0 \leftarrow T_z$ `// initial cabin temperature`
7 $z \leftarrow [x, i, u, x^+]'$ `// control window variables`
8 **init** c_{eq}, c_{neq}, c `// define constraints, cost func.`
9 $\widetilde{z} \leftarrow$ **optimize** (z, c_{eq}, c_{neq}, c) `// call optimizer`
10 $[P_f, P_c, P_h] \leftarrow \widetilde{z}\ \{control\ inputs\}$
11 **return** $[P_f, P_c, P_h]$

In the MPC optimization problem, the dynamic behavior of the EV including the HVAC, electric motor, and battery subsystems is modeled using linear and non-linear equations (see Section 7.2.1), multiple state variables $x = \{T_z, SoC\}$, control inputs $i = \{T_s, T_c, d_r, \dot{m}_z\}$, and auxiliary variables $u = \{T_m, P_h, P_c, P_f, P_e\}$. The values of these variables and inputs are estimated and evaluated for a future prediction horizon using the modeling equations. The controller utilizes an optimizer to adjust the HVAC control inputs such as heating and cooling coil temperature set points and fan speed in the prediction horizon while considering the EV power requests. The solver optimizes these variables to improve the battery lifetime, reduce the HVAC power influence, and maintain the cabin temperature around a specific target temperature. The relationships between the variables and control inputs are defined by equality and non-equality constraints (C_{eq}, C_{neq}). Moreover, there are certain constraints on the control inputs and state variables of the MPC problem that should be satisfied during the optimization and control process for safe operation and stable control. The cost function for the optimization problem at time t is formulated as in Equation 7.12; $(T_z^{k|t} - T_{target})^2$ is the thermal comfort cost for minimizing the deviation of the temperature from target temperature (T_{target}); $T_z^{k|t}$ is the temperature for time $t+k$ predicted at time t. $(SoC^{+k|t} - SoC^{k|t})^2$ is the battery SoC cost for minimizing the SoC deviation; $SoC^{k|t}$ and $SoC^{+k|t}$ are the current and final SoC values for time $t+k$ predicted at time t. This function will result in extending the battery lifetime and decreasing the energy consumption for further driving range.

$$
\begin{aligned}
min. \sum_{k=1}^{N} \quad & \frac{w_1}{\gamma_1} (T_z^{k|t} - T_{target})^2 + \frac{w_2}{\gamma_2} (SoC^{+k|t} - SoC^{k|t})^2 \\
s.t. \quad & C_{eq} \quad \text{discretized modeling equations [Equations 7.1-7.6]} \\
& C_{neq} \quad \text{limits on control inputs and variables } [x, i, u] \\
& \quad \text{constrained cabin temperature } [\underline{T}_z \leq T_z \leq \overline{T}_z]
\end{aligned} \tag{7.12}
$$

The constraint on the cabin temperature already ensures the required thermal comfort by limiting the temperature variance. Hence, a higher priority is given to the battery SoC devi-

ation in order to extend the battery lifetime and reduce the energy consumption. Therefore, we evaluate optimization coefficients (w_x and γ_x) accordingly to find the optimum solution in terms of the battery lifetime first, then thermal comfort cost.

Experiments on the HVAC system and its behavior analysis showed that ($\triangle T_z = 1°C$) temperature variance results in an energy consumption equivalent to ($\triangle SoC = 0.04\%$) battery SoC reduction per second on average. Hence, coefficients ($\gamma_1 = \triangle {T_z}^2 = 1$) and ($\gamma_2 = \triangle SoC^2 = 0.0016$) are evaluated to normalize the objective terms considering the range of their values. Moreover, weight coefficients ($w_1 = 0.1, w_2 = 0.128$) are defined to prioritize each term accordingly. It needs to be noted that the values for weight coefficients are decided arbitrarily by trial and error, to ensure the desired battery performance. Furthermore, they can be adjusted by the designer's preferences for the trade-offs between battery lifetime and thermal comfort regardless of the estimation methodology.

Adjusting the constraints and the weight coefficients will help in finding the best optimal solution to the problem. However, the driving behavior estimation methodology is independent of the optimization process. Moreover, the optimization may be implemented using Sequential Quadratic Programming (SQP) to achieve better solution [131].

7.4 Experimental Results

7.4.1 Experiment Setup

The EV electric motor, HVAC, and battery subsystems are modeled and implemented in MATLAB/Simulink. The experiments are conducted using part of the SHRP 2 Naturalistic Driving Study [1] database. We use the driving data of three drivers in 17, 19, and 20 trips with duration of 3 to 138 minutes, each. The driving data is divided into training ($\approx 70\%$), validation ($\approx 15\%$), and test ($\approx 15\%$) splits. Each split is divided such that they include short, medium, and long distance trips on highway and local areas. The training and prediction of the NARX model have been done using the "*train*" and "*predict*" functions in Neural Network toolbox of MATLAB. The optimization problem has been formulated as matrices in MATLAB and has been solved using "*fmincon*" function in Optimization toolbox. The computing platform used for the experiments has an Intel Core-i7 3770 CPU with 2.3 GHz clock frequency and 8 GB of 1600 DDR3 RAM.

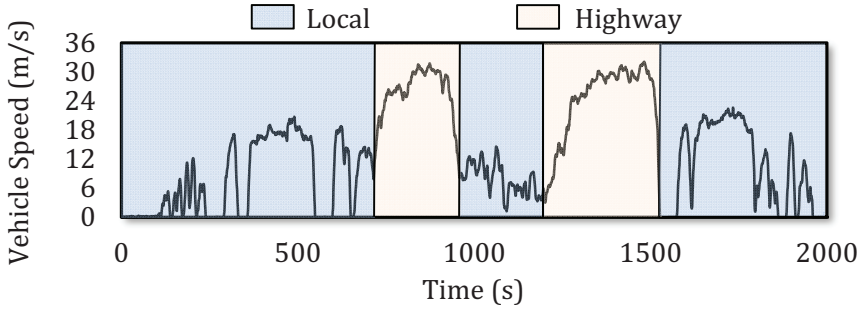

Figure 7.6: Portion of the real-life vehicle speed data for two route conditions.

The data is sampled every second and the simulation time step is considered to be one second as well. For instance, Figure 7.6 illustrates a small portion ($\approx$ 33 min = 2000 samples) of the recorded vehicle speed of a real driver that we used for training. The figure shows the behavior of the vehicle speed both in highway and local driving areas (highlighted in the figure). These contexts are used in the training for improving the vehicle speed prediction.

7.4.2 Results and Analysis

We compare the performance of the following methodologies in terms of complexity, estimation accuracy, and resulting performance of the battery/energy optimization:

1. ***IDL:*** in ideal methodology, the values of the future vehicle speeds are known, which is the most ideal scenario.

2. ***MP:*** the vehicle is assumed to basically preserve its current motion for a specific future period. It is typically utilized for fast path prediction and collision avoidance [112, 127].

3. ***RF:*** the vehicle speed is predicted using random forests model [26] trained by real data. The future prediction is based on the past and current speed values while knowing the context of the road condition defined by the average speeds in the past and future (Section 7.2.2).

4. ***FFNN:*** the vehicle speed is predicted using an FFNN architecture with 8 layers [160] trained by real data. The prediction is based on the past and current speed values while knowing the context of the road condition defined by the average speeds in the past and future (Section 7.2.2). This architecture does not have any feedback loop which limits the ability to adapt to a specific driver behavior.

5. ***NARX:*** our novel context-aware modeling is implemented using an 8-layer nonlinear autoregressive model with exogenous inputs [97, 125] trained by real data. The prediction is based on the past and current speed values while knowing the context of the road condition defined by the average speeds in the past and future (Section 7.2.2). The feedback loop in the architecture makes it self-adaptive and driver-specific resulting in better speed prediction.

a) Complexity analysis: the execution time of each methodology is different due to their various architecture and complexity. Ideal (**IDL**) and motion-preserving (**MP**) methodologies do not require any training phase, while the other statistical model-based methodologies (**RF**, **FFNN**, and **NARX**) implement machine learning models that should be trained.

Table 7.2: Complexity of the driving behavior estimation.

Methodolgy	Acronym	Context-Aware	Execution Time	
			Training (s)	Prediction (ns)
Ideal	IDL	✗	0.00	0.67
Motion-Preserving	MP	✗	0.00	1.87
Random Forests	RF	✓	3685.17	30923.88
FeedForward Neural Network	FFNN	✓	2459.88	316.90
Nonlinear AutoRegressive with eXogenous Inputs	**NARX**	✓	9240.23	631.10

The time needed for the training and prediction phases in each methodology is shown in Table 7.2. It needs to be noted that the training phase is done offline and it is not considered as a bottleneck for the controller. The prediction phase is more important since it is integrated into the controller for energy management. The ideal (**IDL**) and motion-preserving (**MP**) methodologies require inconsiderable time since they implement just one equation. However, the statistical models take more time to predict in the interest of having smaller error for longer-term prediction. The prediction time for NN-based models are the smallest as they implement constant number of equations to predict a value as opposed to random forests (**RF**) which requires traversing through multiple decision trees.

b) Estimation accuracy: the accuracy of different methodologies is compared in terms of Mean Absolute Error (MAE) and Delay (D). For n-second future vehicle speed prediction, $MAE(n)$ and $D(n)$ are calculated as follows:

$$MAE\,(n) = \frac{1}{M}\sum_{i=1}^{M} |SP_n(i) - S_n(i)| \tag{7.13}$$

$$D\,(n) = \textbf{argmax}\ \rho\,(\hat{SP}_n, \hat{S}_n) \tag{7.14}$$

where SP_n is the vector of the estimated n-second future speeds and S_n is the vector of the real speeds during that time. M is the number of samples for validation or test. Function ρ calculates the correlation between the two normalized signals $\hat{SP}_n$ and $\hat{S}_n$. Due to the nature of our control optimization, the value of error in the prediction is not the major factor affecting the output of the optimization and control performance. The more valuable aspect is the model ability to predict the changing trend of the vehicle speed. The model should be able to predict whether the speed is going to increase or decrease. The MAE represents how close the predictions are to the real values, however, it does not show correctness of the model in predicting the direction and changing trend of speed. Meanwhile, $D\ (n)$ shows the agility of the model to catch up with the changing trend of speed (not execution time). For instance, $D\ (23) = 12$ demonstrates that if a changing trend is going to occur in 23 seconds, it might not be predictable by the model up to 12 seconds (on average) before its occurrence.

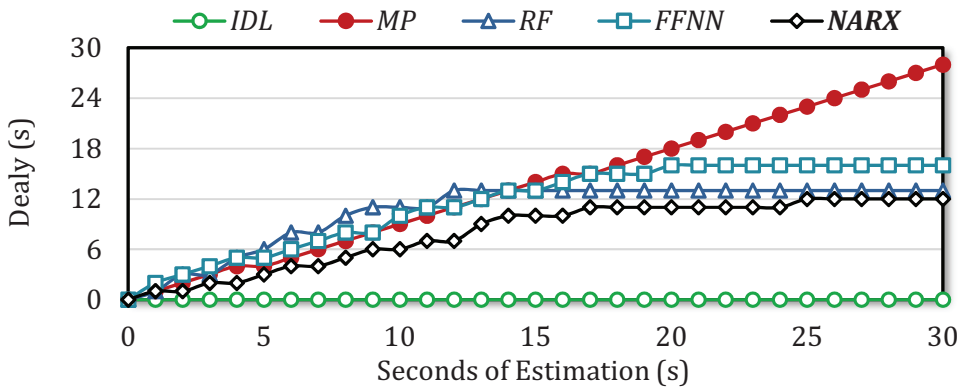

Figure 7.7: Estimation delay for different methodologies for various window sizes.

Figures 7.7 and 7.8 illustrate mean absolute error and delay for the methodologies for n-second ($n = 1 : 30$) future speed prediction. Longer term estimation increases the error except for the ideal (**IDL**) methodology. The error and delay of our novel context-aware methodology (**NARX**) is less than the other methodologies especially for longer estimation ($n > 15$). This is due to the intrinsic feedback in our context-aware NARX enabling self-adaptive model which adjusts to the specific driver behavior resulting in lower delay and estimation error, as opposed to the other statistical models (**RF** and **FFNN**).

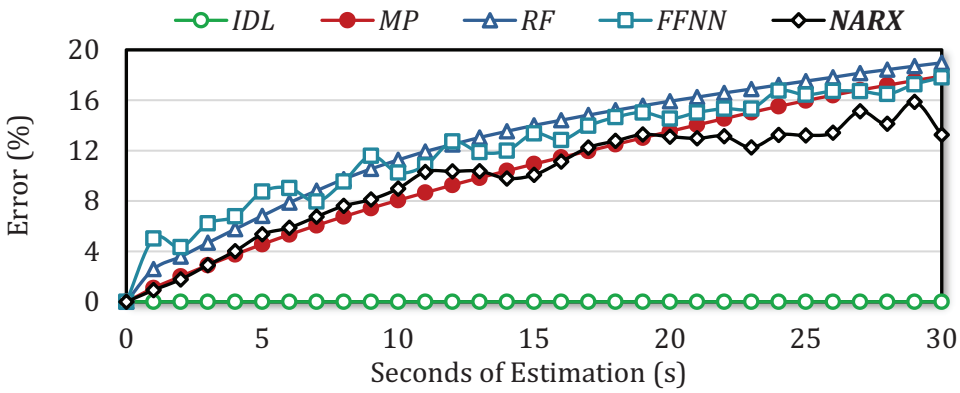

Figure 7.8: Estimation error for different methodologies for various window sizes.

c) Optimization cost: the vehicle speed prediction is integrated into the battery lifetime-aware automotive climate control. Hence, the prediction accuracy and delay may influence the MPC optimization and control performance. The optimization cost includes the thermal comfort and battery lifetime costs (Equation 7.12 in Section 7.3). It has been shown that the optimization cost decreases by having the future EV power requests, compared to the traditional climate control (which only considers the cabin temperature). However, this has been previously done when the real future vehicle speeds were given (**IDL** methodology). The results prove the statements mentioned in Section 7.2.2 about the performance of **NARX**; the **NARX** model has smaller prediction time, estimation error, and average delay for the model compared to other models (**RF** and **FFNN**). Hence, in the following, we select our context-aware **NARX** model as the best statistical modeling.

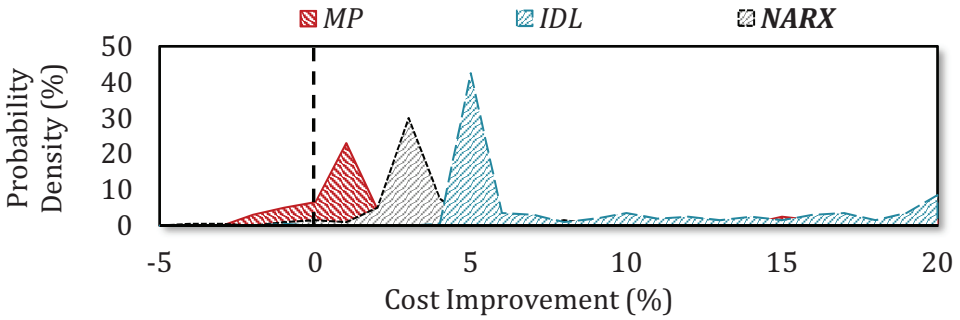

Figure 7.9: Distribution of total cost improvement for different methodologies.

Figure 7.9 shows the distribution of the optimization cost improvement over the traditional climate control. In other words, it shows how these methodologies improve the control quality compared to the the traditional climate control. The ideal (**IDL**) methodology illustrates the maximum improvement 11% (larger mean and smaller variance values). Our context-aware **NARX** can reach up to 6.9% improvement (on average) which is higher than the state-of-the-art methodology of motion-preserving (**MP**). This is mainly achieved because of the lower estimation error and average delay of the model.

d) EV performance: driving range and battery lifetime are the important factors in EV. Hence, the optimization performance in the battery lifetime-aware climate control is analyzed.

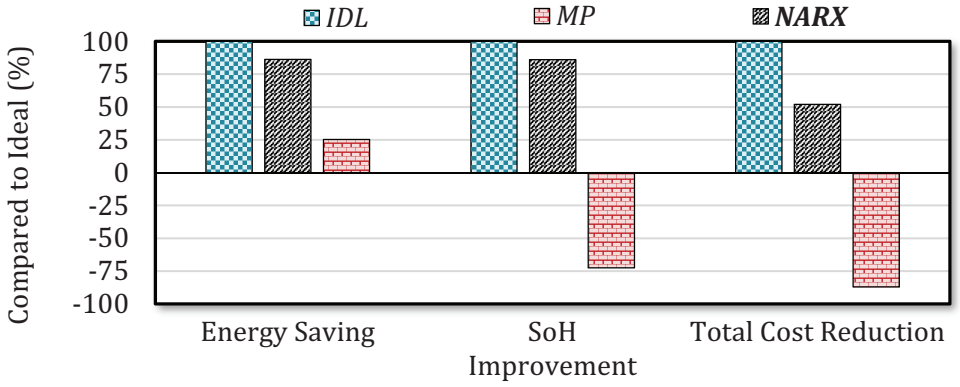

Figure 7.10: Energy saving, battery lifetime improvement, and total optimization cost reduction compared to ideal case.

Figure 7.10 shows the energy saving, battery lifetime (SoH) improvement, and total optimization cost reduction achieved, compared to the ideal methodology in percentage. For instance, using **IDL** methodology, the SoC deviation reduced by 11% to improve the battery lifetime. However, using context-aware **NARX** methodology, SoC deviation reduced by 9.5% and there was no improvement in **MP** methodology. It is shown that our context-aware **NARX** can help the battery lifetime-aware automotive climate control to improve the driving range and battery lifetime up to 82% of the maximum improvement achievable (by **IDL** methodology). Small degradation in the improvement is due to the estimation error and misprediction

of the future vehicle speeds and EV power requests. However, our context-aware **NARX** methodology is much better than the motion preserving (**MP**) methodology especially in terms of the battery lifetime. The poor performance of the **MP** is due to the fact that it does not capture the uncertainty in driving behavior for long term prediction. Hence, the mispredicted future vehicle speeds and EV power requests cause the energy management to decide wrong control inputs which do not help the performance.

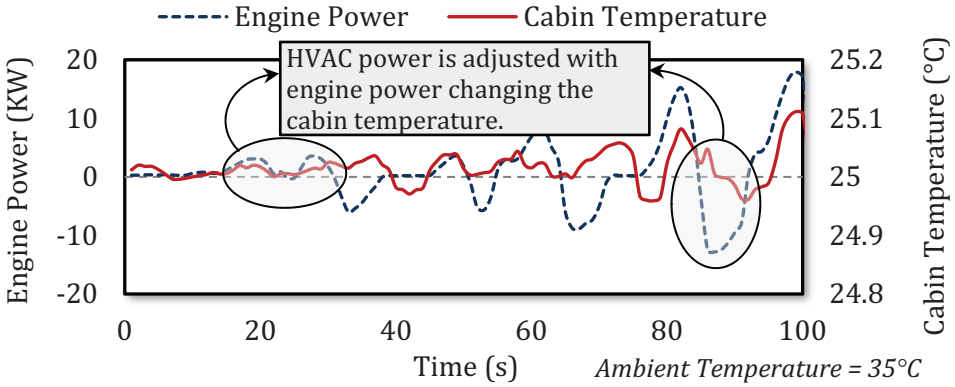

Figure 7.11: Temperature variation when integrating driving behavior estimation into battery lifetime-aware automotive climate control.

e) Thermal comfort: the automotive climate control has been set to maintain the cabin temperature around the target temperature (25°C) with the variation of up to 1°C (≈4%) The ambient temperature is assumed to be 35°C. Since the constraint is very stringent, no thermal comfort degradation has been seen in terms of temperature variation (see Figure 7.11) compared to the ideal methodology. The figure illustrates how the HVAC power and cabin temperature are adjusted by the climate control according to the estimated EV power requests such that the battery stress is minimized. It needs to be noted that deciding the set points for the cabin temperature (variation of 2°C) is a very costly decision for the climate control in terms of the power consumption required by the HVAC system to maintain that temperature. Therefore, it becomes important for the climate control methodology to exploit the variation of the cabin temperature around the target temperature to improve the battery lifetime and energy consumption.

f) Estimation window: having more knowledge of the future vehicle speeds and EV power requests might help the performance of the battery lifetime-aware automotive climate control. We have analyzed its performance in terms of the optimization cost improvement for different estimation window sizes. We have changed the time step duration and the number of steps in the window size of the prediction horizon:

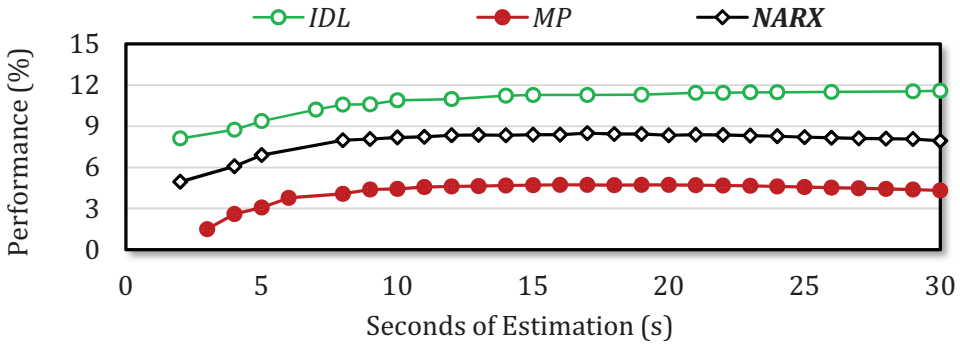

Figure 7.12: Impact of estimation window size on climate control performance.

Figure 7.12 shows that in **IDL** methodology, the performance (total optimization cost improvement) always increases by having more future information. In other words, longer-term prediction improves the performance of the energy and battery management; it results in more battery lifetime (SoH) improvement and energy saving. In our context-aware **NARX** methodology, the performance also increases for longer predictions, but it saturates after more than 17-second future estimation. This is due to the fact that the estimation error increases for the time instances further away from the immediate present causing the misprediction of the future vehicle speeds and EV power requests. Higher misprediction rate and average delay for the methodologies like motion-preserving (**MP**) result in lower performance compared to our methodology and definitely ideal methodology. That is due to the uncertainty in the driving behavior that will result in poor performance of the controller compared to the **IDL**. The uncertainty is modeled and further eliminated in our context-aware **NARX** model by using average vehicle speed data to represent the route condition.

7.5 Concluding Remarks

State-of-the-art EV battery and energy managements leverage long-term power prediction to optimize their control inputs and improve the EV driving range and battery lifetime. However, they have only considered the driving route which is not enough for accurate modeling and estimation of the EV power requests. Moreover, the state-of-the-art driving behavior modeling and estimation methodologies focus on short-term prediction and fail to predict for long term. In this chapter, we proposed a novel context-aware methodology using NARX architecture to model and estimate the driving behavior in terms of future vehicle speeds for up to 30 seconds. Our methodology shows only 12% estimation error for up to 30-second speed prediction which is improved by 27% compared to the state-of-the-art. Moreover, we showed in our results that our novel context-aware NARX model can help an energy management methodology like a battery lifetime-aware automotive climate control to improve its control performance up to 82% of the maximum performance achievable in the ideal methodology where all the future vehicle speeds are assumed to be known.

Chapter 8

Self-Secured Control

8.1 Introduction and Related Work

Electronic Design Automation (EDA) has helped with addressing the challenges towards design and development of the CPS. Controllers are integrated within these systems that compromise of: sensors to monitor the environment and state of the physical system; micro controllers to process the data and make decisions; and actuators to apply the control actions to the physical system [116]. Sophisticated control algorithms are implemented that make decisions based on phsyical state and given a complex model. For instance, a Battery Management System (BMS) utilizes a model of the battery in order to decide how much each cell can provide power and energy at this current state of the system. The BMS is responsible to prevent over loading, over charging, and over discharging the battery cells considering any power request received from the system, e.g. EV. Moreover, resource management and scheduling algorithms may be implemented using Model Predictive Control (MPC) or Reinforced Learning to distribute the power among the battery cells or even other types of energy storage such as ultracapacitor [107, 151]. Hence, the main objective of the BMS has always been to improve the available capacity and energy efficiency while minimizing the battery lifetime degradation that may happen in lithium-ion battery cells [124, 131].

All the decisions made at run time by the controller depend on the observed state of the physical system or the environment and the control inputs are adjusted based on the model. However, the arising challenge is that whether the controller can trust the sensed data and/or the model. There are many scenarios that the control loop can be compromised. The corrupted loop will cause the controller to make wrong decisions and thereby sway the state of the physical system to unwanted or unstable states [52, 153].

8.1.1 Motivational Case Study

Control loops can be compromised from different aspects such as data sensing, the physical system, or the model (see Figure 8.1). For instance, the sensed data can become unreliable by directly or indirectly attacking the sensors to give wrong data, no data, or misplaced data (e.g. Denial-of-Service or Delay Attacks). Example of this attack has been seen in navigation systems by altering the data received from the GPS or IMU sensors [57, 129]. Moreover, the physical system which is the main module of the control loop can be attacked. This may seem less frequent and easily detectable. However, a battery may be replaced with a low-quality battery and cause the whole CPS to catch on fire since the BMS is unaware of the alteration of the physical system. Furthermore, biased machine learned models in the controllers have been seen to give wrong decisions by changing the control inputs slightly not visible to naked eyes. For instance, an image classifier model in an autonomous driving control may detect a "STOP" sign as a "Speed Limit" sign [44].

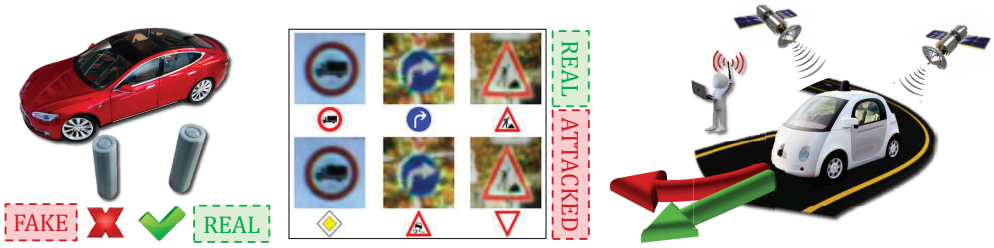

Figure 8.1: Examples of different attacks on the control in a compromised CPS. [79]

Summary and conclusion from observations: according to the observation and experiments, the state-of-the-art controllers are not intelligent enough to capture any anomaly in the control loop. In other words, the controller makes the decision based on the current observed state of the physical system and the given model without considering that the behavior of the control loop is not normal. Moreover, the controller does not have any mechanism to secure the control loop to prevent a compromise and to recover from the attack.

8.1.2 Novel Contributions and Concept Review

In order to address the challenges with vulnerabilities existing in control, we propose a novel self-secured machine learning architecture by employing the following.

1. **Control Loop Vulnerabilities (Section 8.2):** are described in details for the current controllers of the automotive CPS. Different aspects that the control loop can be compromised and our solution to the issues are explained.

2. **Self-Secured Machine Learning (Section 8.3):** architecture is proposed that utilizes a novel Conditional Generative Adversarial Network (CGAN) to capture the behavior of the control loop and detect any anomaly at the run time [55]. Moreover, a novel secure prediction technique will recover the control loop from the attack.

3. **Self-Secured BMS (Section 8.4):** is implemented where the self-secured machine learning architecture is integrated into an existing BMS and tested against multiple existing attack models.

Figure 8.2 illustrates the highlighted modules of our novel self-secured machine learning architecture that will be integrated into an existing automotive CPS, e.g. battery management system. Moreover, it abstracts how the modules are related to each other to detect a vulnerability and recover from it.

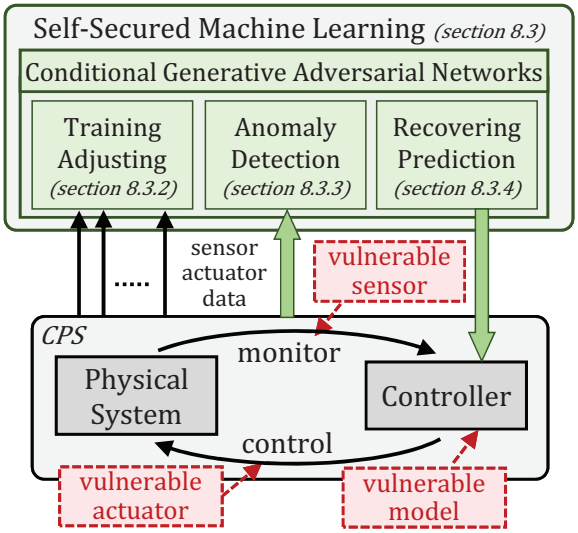

Figure 8.2: Self-secured machine learning architecture integrated into automotive CPS.

8.2 Control Loop Vulnerabilities

Cyber-physical systems in every domain typically implement controllers that are responsible for interacting with one or more physical systems to reach an objective and maintain a certain control quality [80]. In other words, controller seeks to maintain physical variables at certain set points in spite of unmeasured disturbances. The interaction between the physical systems and the controller is abstracted as a closed-loop feedback control.

8.2.1 Control Loop Design

Control loops comprise of multiple components of sensors, microcontrollers, and actuators, interacting with a physical system (see Figure 8.3).

Sensors are devices that measure and convert certain types of energy in terms of a physical parameter to an electrical output. Sensors are mostly used to monitor the state of a physical system or the environment. For instance, a BMS may implement thousands of sensors on a battery module attached to each cell to measure their voltage, current, or temperature.

Microcontrollers periodically retrieve the data from the sensors and process them to reach a decision for the controllable variables. Typically, Proportional Integral Derivative (PID) controllers are responsible to accomplish this task. However, PIDs have very limited knowledge of the physical system and its dynamic behavior. Hence, Model Predictive Control (MPC) is a more advanced method of control that relies on dynamic models of the physical system. They achieve better control stability and quality of control by optimizing the control process for a certain time horizon in the future. For instance, the BMS may process the data to evaluate the battery cell State-of-Charge (SoC) or battery lifetime - State-of-Health (SoH) [85]. The BMS will then find the optimal control actions considering the battery lifetime and energy efficiency.

Actuators are devices that convert an electrical signal to the required physical parameter, e.g. current, voltage, physical motion, etc. The electrical signal to the actuators are decided by the microcontrollers. For instance, the BMS may adjusts the current drawn from the battery cells as the control actions, as the results from the BMS algorithm. Furthermore, there may be relay switches to change the battery structure for better battery operation [64].

Physical System dynamics will then change by triggering the actuators and applying the control actions decided by the microcontroller. The control process will continue and the physical system will continuously react to the control inputs. Meanwhile, the control loop is triggered periodically to maintain the required set points. For instance, due to the intrinsic variations in battery cells, they may discharge differently from each other. Hence, the BMS observing the state of these cells will adjust its controllable variables (current drawn from the cells) to maintain a balance among them to increase the available capacity of the battery.

8.2.2 Physical System Attack

Physical system dynamics change slowly overtime depending on the values of its controllable variables. Typically, the behavior of the physical system is described using mathematical equations such as Ordinary Differential Equations (ODE) or Finite-State Machines (FSM). These modeling equations can be used in MPC algorithms for estimating the state of the system and evaluating optimum control actions. Physical systems may have unique behavior when applying the control inputs.

Battery cells have different performances and dynamic behavior. In other words, they will illustrate different current-voltage (I-V) behavior during charge and discharge cycles. Moreover, their thermal behavior and their internal generated heat are different due to the various materials used in the production. High performance battery cells are typically required for high-power or high-energy applications. However, they cost much more than the low perfor-

mance ones. Hence, middle-man-attack may replace or alter the cells with the counterfeit ones without the BMS being aware of the altercation. The BMS interacting with the new counterfeit physical system may not operate properly resulting in unstable states, e.g. fast draining battery cells or cells catching on fire [149]. Currently, there exist multiple mechanisms to distinguish between these cells. For instance, the appearance and packing can be used to tell the difference or an embedded RFID tags can be used. However, the current approaches can be hacked easily leaving the control loop vulnerable.

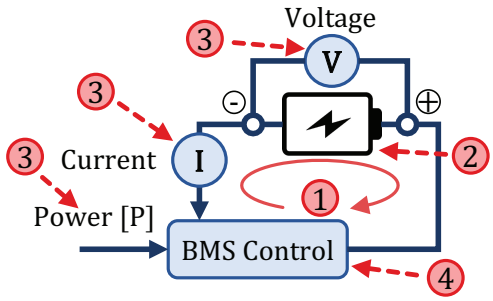

Figure 8.3: Control loop design (1) in a BMS controller and its vulnerabilities within automotive CPS: physical attack (2), sensor attack (3), and vulnerable model (4).

8.2.3 Sensor Attack

The performance of a sensor is typically decided by the control designer at the design time. It defines how the sensor reacts the physical parameter it is measuring. The electrical signal is provided for the microcontroller in order to be processed. Nowadays, to maintain scalability of the sensor network with the growing number of sensors implemented in CPS, the connections are becoming wireless, e.g. Bluetooth, Zigbee. The wireless network can bring more weak points and add more vulnerabilities to a control loop. Therefore, the sensor data can be under multiple attacks, e.g. man-in-the-middle, fuzz attack, replay attack. Therefore, the controller may not be able to trust the data to observe the state of the physical system and make decisions. For instance, a compromised voltage sensor of a battery may cause the BMS to over charge or over discharge the battery resulting in shorter battery

lifetime or in the worst case explosion. Cryptography algorithms are typically used to secure the communication channel for data. However, they have their own challenges in terms of complexity scalability. Furthermore, they will not be effective against physical attacks to the sensors, leaving the control loop vulnerable.

8.2.4 Vulnerable Model

Physical system models are the major part of decision making of a controller. The models utilized by the algorithms will help the controller identify the current state of the physical system given the observed data. For instance, an object detection algorithm classifies the recorded image from the camera based on a pre-trained machine learning model. The BMS estimates the SoC of the battery cell given the measured current drawn from the battery. However, the reliability of the model and decisions made by the controller are unknown without testing. In other words, the attacker has the option of remaining in a stealth mode wherein it spoofs some sensor but only by an amount that is indistinguishable from noise. However, the attacker can force the system to get into an unsafe region [99]. For instance, the object detection algorithm can be fooled to classify an image completely wrong with the highest probability by slightly tweaking the image (not visible to naked eye) [79]. On the other hand, the BMS may be attacked to consumer more energy from the battery cells [95].

8.3 Self-Secured Control

We explained the security and vulnerability challenges with the current controls. Hence, in this chapter, we propose a novel machine learning architecture using Conditional Generative Adversarial Network (CGAN) that will be integrated in parallel to the control loop (see Section 8.3.1). It is responsible to capture and learn the normal behavior of the physical

system interacting with the controller (see Section 8.3.2). The architecture is trained by running the CPS and monitoring the control loop at run time by the manufacturer, before any attack can happen, at ***train-only*** phase. Afterwards, at ***detect-n-predict*** phase, the architecture will monitor the control loop to detect any anomaly or attack (see Section 8.3.3) and recover from them (see Section 8.3.4) at run time. Moreover, it will also get updated and learn new dynamics, if the rate of attacks detected are low in a certain time window.

8.3.1 Machine Learning Architecture

Typically, the dynamic behavior of the control loop containing the physical system and the control components can be modeled using mathematical equations and deterministic modeling. However, the behavior of the physical systems can get too complex to be modeled by equations. Moreover, there may be many unknown factors influencing the behavior that make it challenging to model. For instance, a battery manufacturing process is not completely deterministic that will result in various battery cells with different performance and behavior. Modeling and capturing the exact behavior of the battery cells is very challenging problem. Hence, data-driven statistical modeling (machine learning) is applied to describe the behavior. However, machine learning models may suffer from unknown biases and sometimes significant prediction errors. Therefore, we propose a novel conditional generative adversarial network to capture the behavior. Moreover, it will also help in enabling a self-secured control.

Generative Adversarial Networks (GAN) is a recently-introduced neural networks architecture that helps with generating a more stable machine learning model without dealing with the complex distribution of the data [55]. By the definition of GAN, there will be two neural networks 1) *generator* (G) and 2) *discriminator* (D) (see Figure 8.4); the *generator* attempts to generate data resembling a physical process; and the *discriminator* attempts to tell the

difference between the real data of the physical process and the fake data generated by the *generator*. The output of the *discriminator* is a scalar representing the probability of the data being real.

GAN creates a situation for both neural networks that can be modeled as a minimax game in game theory. Hence, for the *generator* to be successful, it needs to learn to generate the distribution of the real data for the physical process very well, such that the *discriminator* cannot distinguish. On other hand, for the *discriminator* to be successful, it needs to learn the distribution of the real data for the physical process very well, such that the *generator* cannot fool it. Therefore, in order to compete with each other to get better in this game, both will become the best to generate and discriminate. Hence, at the equilibrium point, which is the optimal point in minimax game, the *generator* will model the real data, and the *discriminator* will output probability of 0.5 as the output of the *generator* equals real data.

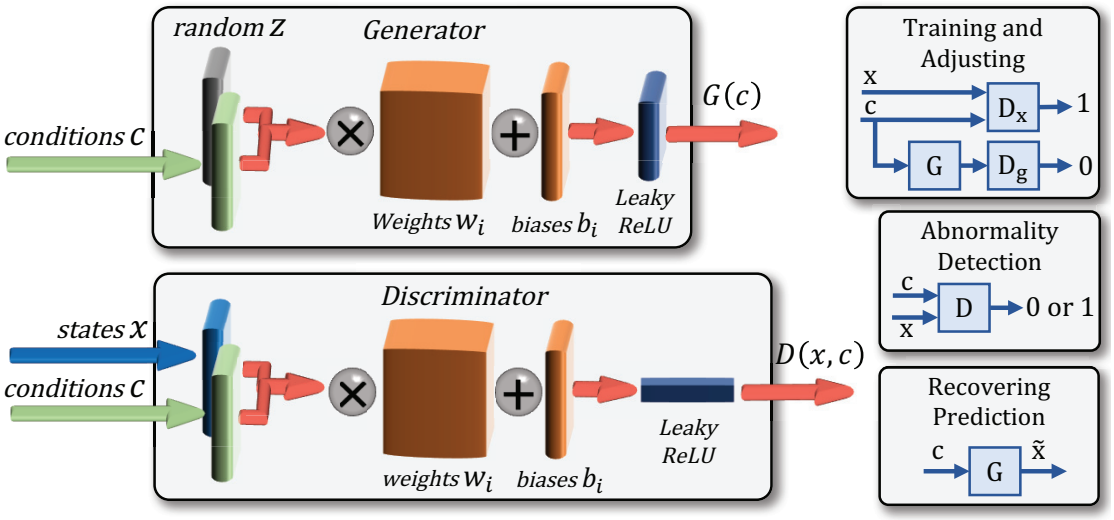

Figure 8.4: Detailed architecture of our novel conditional generative adversarial network for self-secured control.

Selection of GAN architecture for the control design would be mainly due to the following factors: 1) competition between two networks can provide faster convergence; 2) two networks are already being trained for purposes required for a secured control design; 3) the model will be more robust towards any attack model especially adversarial examples.

Here in this chapter, both neural networks need to learn the physical process of the control loop for a limited number of time steps ($T = 6$). The data is sampled from the signals of the sensors and actuators in the control loop. The *discriminator* verifies whether the physical process data for the period of T is real or fake (compromised). On the other hand, the *generator* attempts to generate similar data to fool the discriminator.

To capture the current state of the physical system and make the decisions more aware of the context, a Conditional GAN (CGAN) is implemented. Here in, the beginning portion of the time steps ($T_c = 4 < T$) is given as the condition data to both networks. Therefore, both networks will predict based on the given condition. Furthermore, the conditional prediction will help the *generator* to later do recovery prediction that will be discussed in Section 8.3.4.

8.3.2 Training and Adjusting

The main challenge of the CGAN machine learning architecture is training two neural networks. Both networks need to converge to an equilibrium point where none of them are too much stronger than the other. Otherwise, the *discriminator* always tells the difference between the real or fake data or the *generator* always generates very closely to real data.

Hence, at the ***train-only*** phase, the manufacturer is responsible to run the controller for a certain period of time in order to train the CGAN with real data. During the training process, two optimizations will be conducted to minimize their loss functions.

$$G_{loss} = \frac{1}{N} \sum_{i=1}^{N} H\left(D\left(G\left(c_i\right), c_i\right), 1\right) \tag{8.1}$$

where G_{loss} loss function is to minimize the mean of the cross entropy between label one (1) and the output of the *discriminator* given the fake generated data based on condition c_i over N batch size. In other words, training the *generator* to fool the *discriminator*.

$$D_{loss}^{real} = \frac{1}{N}\sum_{i=1}^{N} H\left(D\left(x_i, c_i\right), 1\right) \tag{8.2}$$

$$D_{loss}^{fake} = \frac{1}{N}\sum_{i=1}^{N} H\left(D\left(G\left(c_i\right), c_i\right), 0\right) \tag{8.3}$$

$$D_{loss} = D_{loss}^{real} + D_{loss}^{fake} \tag{8.4}$$

On the other hand, D_{loss} loss function of is to minimize the mean of the cross entropy between label zero (0) and the output of the *discriminator* given the real data and condition c_i, plus the cross entropy between label one (1) and the output of the *discriminator* given the fake generated data based on condition c_i.

After training the CGAN, both entropies will reach small stable values. However, the training will not stop after the ***train-only*** phase. The CGAN will be further trained at the ***detect-n-predict*** phase given the new batches of data sampled at run time. However, only the consecutive batches are used for training that their probability of having no anomaly is higher than an arbitrary defined thrust threshold (α_{real}) for a large period of time. Meanwhile, at the ***detect-n-predict*** phase, the CGAN is used for anomaly detection and recovering prediction as will be discussed in the following.

8.3.3 Anomaly Detection

Trained CGAN includes a *discriminator* neural networks that is used for distinguishing between real or fake data of the physical process. The trained *discriminator* captures the real dynamic behavior of the control loop for T time steps given the conditional data for T_c time steps. Due to competition with the *generator*, it does not get adapted to fake or corrupted data and it is less biased and more tolerant to adversarial attacks.

Any attack to the vulnerable physical system, sensor, or model will corrupt the physical process of the control loop (see Section 8.2). Therefore, the *discriminator* can give a probability of detecting an anomaly in the period of the given data x and condition c. The conditional anomaly detection helps in capturing the state of the physical system for the last T_c time steps to make more deterministic decision. When the probability of having no anomaly within the given batch is smaller than the fake threshold $[D(x, c) < \alpha_{fake}]$, the batch will be labeled as an anomaly. In other words, the control loop is compromised.

Many defensive mechanisms can be implemented in case of detecting an anomaly, e.g. triggering default control actions. However, we introduce a recovering prediction mechanism that can complement or replace the current mechanisms.

8.3.4 Recovering Prediction

Trained CGAN includes a *generator* neural networks that is used for generating data (fake) resembling the real data of the physical process. The trained *generator* captures the real dynamic behavior of the control loop for T time steps given the conditional data for T_c time steps. Therefore, using the *generator* model, the dynamic behavior of the physical system can be predicted, when needed.

When an anomaly is detected, the current conditional data can be given to the *generator* network to generate the rest of the physical data. Although the data is fake, it is very close to the real data that might have happened when there was no anomaly. The first estimated physical data: $\tilde{x}[T_c + 1] \leftarrow \tilde{x} = G(c)$ will be applied to the control loop.

8.4 Self-Secured BMS

We apply our novel CGAN machine learning architecture to an existing battery management system to enable self-security against various attacks and vulnerabilities.

8.4.1 Attack Models

Multiple attack models are applied to the control loop of a BMS to observe the changing dynamic behavior of the physical system.

a) Physical Attack: in this attack model, the physical system is altered, for instance the battery cell is replaced with lower performance battery cell. The internal resistance and capacitance of the battery cell will be higher. The behavior is not detectable by normal BMS since the cell may still provide enough power required

b) Denial-of-Service Attack: the data retrieved from the sensors are tampered with uniform distribution noise that is randomly generated with the probability of 20%. This attack will directly fool the controller to observe a wrong (random) state of the system, e.g. higher SoC or lower voltage than actually available.

8.4.2 Integrating Novel Architecture

We apply our novel CGAN machine learning architecture to an existing BMS. Voltage, current, and power sensor values are sampled every second. They will represent the dynamic behavior of the control loop (physical process). They will represent the I-V characteristics of a battery cell. Moreover, the relationships between these data values should follow the correct behavior of the control loop (without a compromised control or sensor).

8.5 Experimental Results

To test the functionality and performance of our novel self-secured control using CGAN, the self-secured BMS is experimented on multiple attack scenarios and the performance is compared with a normal BMS and single generator trained individually for both anomaly detection and recovery prediction.

8.5.1 Experiment Setup

The battery, sensors, and actuators are modeled in MATLAB. Lithium-ion battery cell 18650 has been used for the experiment. A Nissan Leaf S EV has been driven on a standard driving cycle *NEDC* and *ECE* [107, 131] as case studies. The training and prediction of the CGAN machine learning model has been implemented using TensorFlow in python [15]. Hence, the control algorithms of the self-secured BMS is running in python and communicating with MATLAB to retrieve sensor data and transmit control actions.

8.5.2 Results and Analysis

We analyze and compare the performance of the self-secured BMS in terms of model accuracy of CGAN for training data, anomaly detection performance of the *discriminator* networks, and estimation error of the *generator* network in prediction.

a) CGAN Model Accuracy: at the ***train-only*** phase, the CGAN model is trained on 10,000 samples of data by driving the Nissan Leaf S EV on a standard driving cycle *NEDC* and *ECE*. The loss function of the both networks are shown in Figure 8.5. It is shown that after a while, the value of cross entropy for both loss functions reaches a stable value, when they have captured the physical process thoroughly. There might be new data samples at run

time that the models have not captured and there should be a peak in the error. However, these will not be detected as anomaly since they are higher than the fake threshold.

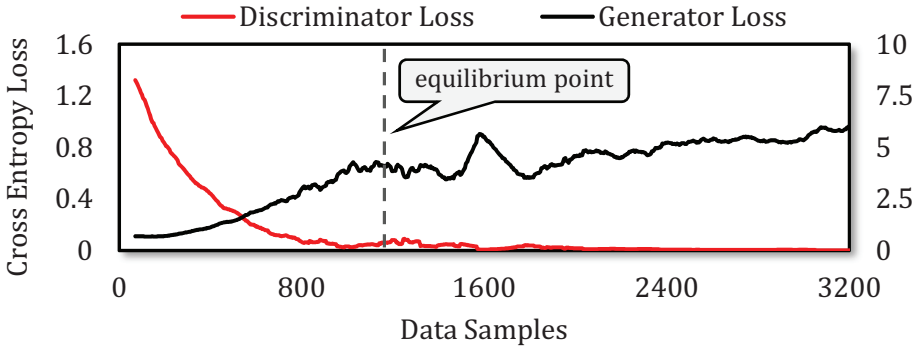

Figure 8.5: CGAN *generator* and *discriminator* loss function at *train-only* phase reaching equilibrium point.

The performance shown in this chapter is the result after tuning the CGAN machine learning networks by optimizing multiple hyper parameters. The size of the inputs the networks are $T_c = 4$ and $T - T_c = 2$ multiplied by the number of sensors (3). The *discriminator* has one hidden layer with 360 neurons and the *generator* has one hidden layer with 1200 neurons. The dimension of added noise in the *generator* is 15. These parameters are adjusted such that the models do not over fit the data and can reach equilibrium point.

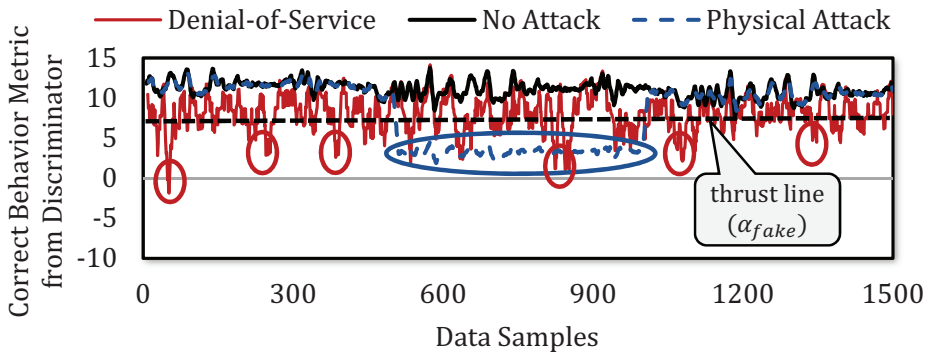

Figure 8.6: Performance of the *discriminator* in detecting DoS and physical attack.

b) Anomaly Detection: at the ***detect-n-predict*** phase, we apply two attack models (see Section 8.4.1) and observe how the self-secured BMS detects them. Figure 8.6 illustrates the metric that the discriminator predicts the behavior to be correct. When there is no attack it is in a normal range. However, when the behavior is corrupted in a compromised

control, the values fall below the threshold as shown in the figure. The threshold is defined based on the minimum value achieved in the ***train-only*** phase. The denial-of-service attack happens 20% of the time with a uniform distribution. It is shown that 83% of the attacks are detected. The physical attack is much harder since the behavior is complex to capture. However, our self-secured control is able to detect the attack by identifying the fake behavior. It has been seen that the single generator technique would not be able to detect more 65% of the attacks. Since the decision is mainly based on the error of the prediction and current state, it does not capture behavior change when there is anomaly.

c) Prediction Recovering Error: at the ***detect-n-predict*** phase, we apply two attack models (see Section 8.4.1) and observe how the self-secured BMS recovers from the detected anomalies by predicting. The error of the predicted values from the *generator* is compared with the real values of the physical system at the run-time ***detect-n-predict*** phase. Figure 8.7 shows the probability density of the prediction error. As shown in the figure, the estimation error when a physical attack happens, is more deterministic than DoS. This is due to the fact that the physical behavior is compromising the system in a more deterministic way than a random number jamming a data (DoS). The average prediction error resulted from the *generator* is about 21% which is significantly good for a model which has no prior knowledge of the system. The error has decreased compared to a single generator which was 29%.

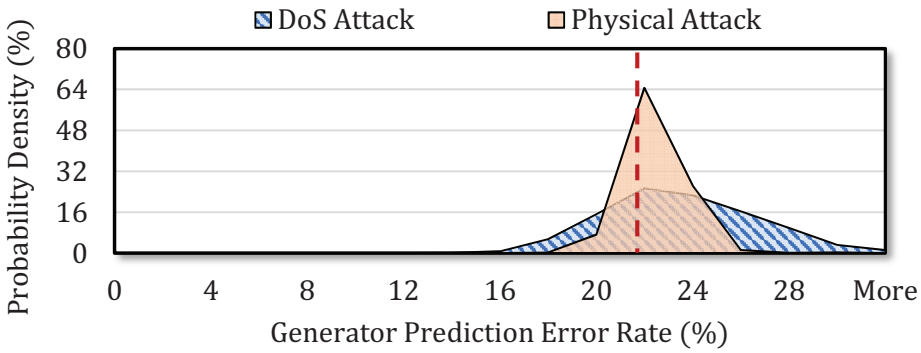

Figure 8.7: Performance of the *generator* in terms of the prediction error when an attack happens.

8.6 Concluding Remarks

Current CPS and their control loops are vulnerable to attacks from sensors/actuators, unknown biases. and predictions in the control models. These vulnerabilities may cause the state of the physical system to sway to an unstable state, e.g. battery catching on fire. Current security solutions such as cryptography do not address these attacks from the physical domain. Hence, in this chapter, we have proposed a novel machine learning architecture using CGAN to enable a self-secured control. CGAN containing of two neural networks will capture the dynamic behavior of the control loop in order to detect any anomaly resulted from the attacks, and to recover from the attack by predicting the correct state of system. We experimented our novel architecture on a self-secured BMS by driving a Nissan Leaf S on *NEDC*, *ECE* driving cycles. The self-secured BMS could detect the added attacks to the system with 83% accuracy and the recovering prediction error has been 21% on average which improved by 28% and 8%, respectively.

Bibliography

[1] Transportation Research Board of the National Academy of Sciences. "The 2nd Strategic Highway Research Program Naturalistic Driving Study Dataset. Available from the SHRP 2 NDS InSight Data Dissemination". `insight.shrp2nds.us`., 2013.

[2] United States Environmental Protection Agency "Sources of Greenhouse Gas Emissions". `www.epa.gov`., 2015.

[3] Tesla, Tesla Motors Inc. "Tesla Model S Spec". `www.teslamotors.com`., 2015.

[4] Nissan. "Nissan Leaf S Spec". `www.nissanusa.com`., 2015.

[5] Maxwell "BC Series Ultracapacitors Datasheet". `maxwell.com`., 2015.

[6] Panasonic "Li-ion NCR18650B". `panasonic.com`., 2015.

[7] MathWorks "MATLAB, Simulink". `www.mathworks.com`., 2015.

[8] Google Inc. "Google Maps Web API". `developers.google.com`., 2015.

[9] SIEMENS "LMS Imagine.Lab Amesim". `plm.automation.siemens.com`., 2015.

[10] Automotive Energy Supply Co. "Li-ion Battery for EV". `www.eco-aesc-lb.com/en`., 2015.

[11] EPA, United States Environmental Protection Agency. "Fuel Economy Guide 2008". `www.fueleconomy.gov/feg/FEG2008.pdf`., 2015.

[12] Fiat. "Fiat 500e Spec". `www.fiatusa.com`., 2015.

[13] SCE, Southern California Edisson. "Time-Of-Use Residential Rate Plans". `www.sce.com`., 2016.

[14] EPA, United States Environmental Protection Agency. "Test Drive Cycles". `www.epa.gov/vehicle-and-fuel-emissions-testing/dynamometer-drive-schedules`., 2017.

[15] M. Abadi, A. Agarwal, and Others. Tensorflow: Large-scale machine learning on heterogeneous distributed systems. *arXiv preprint arXiv:1603.04467*, 2016.

[16] F. Ahourai and M. A. Al Faruque. Grid Impact analysis of a Residential Microgrid under Various EV Penetration Rates in GridLAB-D. *Technical Report, TR 13-08, July, 2013*.

[17] M. A. Al Faruque and F. Ahourai. A model-based design of Cyber-Physical Energy Systems. In *2014 19th Asia and South Pacific Design Automation Conference (ASP-DAC)*, pages 97–104. IEEE, jan 2014.

[18] M. A. Al Faruque, L. Dalloro, S. Zhou, H. Ludwig, and G. Lo. Managing Residential-Level EV Charging Using Network-as-Automation Platform (NAP) Technology. *IEEE International Electric Vehicle Conference (IEVC)*, 2012.

[19] M. A. Al Faruque and K. Vatanparvar. Energy Management-as-a-Service over Fog Computing Platform. *IEEE Internet of Things Journal*, 3(2):161–169, 2016.

[20] M. A. Al Faruque and K. Vatanparvar. Modeling, Analysis, and Optimization of Electric Vehicle HVAC Systems. *Asia and South Pacific Design Automation Conference (ASP-DAC)*, pages 1–6, 2016.

[21] M. Amir and T. Givargis. HES Machine: Harmonic Equivalent State Machine Modeling for Cyber-Physical Systems. In *International High Level Design Validation and Test Workshop (HLDVT)*, pages 31–38. IEEE, 2017.

[22] M. Amir and T. Givargis. Hybrid State Machine Model for Fast Model Predictive Control: Application to Path Tracking. *IEEE/ACM International Conference on Computer-Aided Design (ICCAD)*, 2017.

[23] R. R. Andrawis and Others. Forecast combinations of computational intelligence and linear models for the NN5 time series forecasting competition. *International Journal of Forecasting*, 27:672–688, 2011.

[24] T. B. Arnold and R. J. Tibshirani. Efficient Implementations of the Generalized Lasso Dual Path Algorithm. *Journal of Computational and Graphical Statistics*, 25(1):1–27, 2016.

[25] R. Baheti and H. Gill. Cyber-physical Systems. *The impact of control technology*, pages 161–166, 2011.

[26] L. Breiman. Random Forests. *Machine learning*, 45(1):5–32, 2001.

[27] M. Busl, T. Sattelmayer, and W. Polifke. Design of an Energy-Efficient Climate Control Algorithm for Electric Cars. *Department of Automatic Control, Lund University, Sweden*, 2011.

[28] E. F. Camacho and C. B. Alba. *Model predictive control*. Springer Science & Business Media, 2013.

[29] J. Cao and A. Emadi. A new battery/ultracapacitor hybrid energy storage system for electric, hybrid, and plug-in hybrid electric vehicles. *Power Electronics, IEEE Transactions on*, 27(1):122–132, 2012.

[30] Y. Cao, S. Tang, C. Li, P. Zhang, Y. Tan, Z. Zhang, and J. Li. An Optimized EV Charging Model Considering TOU Price and SOC Curve. *IEEE Transactions on Smart Grid*, pages 388–393, 2012.

[31] M. Casale-Rossi, P. Palella, M. Anton, O. Galzur, R. Hum, R. Kress, and P. Lo. The World Is Going... Analog & Mixed-Signal! What about EDA? *Proceedings of the Conference on Design, Automation & Test in Europe*, page 37, 2014.

[32] S. Chakraborty, M. A. Al Faruque, W. Chang, D. Goswami, M. Wolf, and Q. Zhu. Automotive Cyber–Physical Systems: A Tutorial Introduction. *IEEE Design & Test*, 33(4):92–108, 2016.

[33] S. Chakraborty, M. Lukasiewycz, C. Buckl, S. Fahmy, P. Leteinturier, and H. Adlkofer. Embedded Systems and Software Challenges in Electric Vehicles. In *DATE '12 Proceedings of the Conference on Design, Automation and Test in Europe*, pages 424–429, 2012.

[34] W. Chang, M. Lukasiewycz, S. Steinhorst, and S. Chakraborty. Dimensioning and Configuration of EES Systems for Electric Vehicles with Boundary-Conditioned Adaptive Scalarization. In *9th International Conference on Hardware/Software Codesign and System Synthesis*, number 26, page 26. IEEE Press, sep 2013.

[35] W. Chang, A. Pröbstl, D. Goswami, M. Zamani, and S. Chakraborty. Battery-and Aging-Aware Embedded Control Systems for Electric Vehicles. *Real-Time Systems Symposium (RTSS)*, pages 238–248, 2014.

[36] C. Chen, A. Seff, A. Kornhauser, and J. Xiao. DeepDriving: Learning Affordance for Direct Perception in Autonomous Driving. *Proceedings of the IEEE International Conference on Computer Vision*, pages 2722–2730, 2015.

[37] S.-W. Chen, C.-Y. Fang, and C.-T. Tien. Driving behaviour modelling system based on graph construction. *Transportation research part C: emerging technologies*, 26:314–330, 2013.

[38] K. W. E. Cheng, B. P. Divakar, H. Wu, K. Ding, and H. F. Ho. Battery-management system (BMS) and SOC development for electrical vehicles. *IEEE Transactions on Vehicular Technology*, 60(1):76–88, 2011.

[39] K.-T. Cho, K. G. Shin, and T. Park. CPS Approach to Checking Norm Operation of a Brake-by-Wire System. *6th International Conference on Cyber-Physical Systems (ICCPS)*, pages 41–50, 2015.

[40] Y. Choi, N. Chang, and T. Kim. DC-DC converter-aware power management for low-power embedded systems. *IEEE Transactions on Computer-Aided Design of Integrated Circuits and Systems*, 26(8):1367–1381, 2007.

[41] G. Ciwei and Z. Liang. A Survey of Influence of Electrics Vehicle Charging on Power Grid. *Power System Technology*, pages 128–130, 2011.

[42] T. H. Cormen. Introduction to algorithms. *MIT press*, 2009.

[43] T. Cui, Y. Wang, S. Chen, Q. Zhu, S. Nazarian, and M. Pedram. Optimal Control of PEVs for Energy Cost Minimization and Frequency Regulation in the Smart Grid Accounting for Battery State-of-Health Degradation. *Proceedings of the Design Automation Conference (DAC'15)*, page 134, 2015.

[44] N. Das, M. Shanbhogue, S.-T. Chen, F. Hohman, L. Chen, M. E. Kounavis, and D. H. Chau. Keeping the Bad Guys Out: Protecting and Vaccinating Deep Learning with JPEG Compression. *arXiv preprint arXiv:1705.02900*, 2017.

[45] J. De Santiago, H. Bernhoff, and Others. Electrical Motor Drivelines in Commercial All-Electric Vehicles: A Review. *IEEE Transactions on Vehicular Technology*, pages 475–484, 2012.

[46] S. Deilami, A. S. Masoum, P. S. Moses, and M. A. S. Masoum. Real-Time Coordination of Plug-In Electric Vehicle Charging in Smart Grids to Minimize Power Losses and Improve Voltage Profile. *IEEE Transactions on Smart Grid*, pages 456–467, 2011.

[47] L. Dickerman and J. Harrison. A New Car, a New Grid. *IEEE Power and Energy Magazine*, page 55, 2010.

[48] D. Doerffel and S. A. Sharkh. A critical review of using the Peukert equation for determining the remaining capacity of lead-acid and lithium-ion batteries. *Journal of Power Sources*, 155:395–400, 2006.

[49] U. S. D. o. T. DOT. National Transportation Statistics, 2015.

[50] A. Du Pasquier, I. Plitz, and Others. A comparative study of Li-ion battery, supercapacitor and nonaqueous asymmetric hybrid devices for automotive applications. *Journal of Power Sources*, pages 171–178, 2003.

[51] U. Eberle and R. von Helmolt. Sustainable transportation based on electric vehicle concepts: a brief overview. *Energy & Environmental Science*, pages 689–699, 2010.

[52] H. Fawzi, P. Tabuada, and S. Diggavi. Secure Estimation and Control for Cyber-Physical Systems Under Adversarial Attacks. *IEEE Transactions on Automatic Control*, 59(6):1454–1467, 2014.

[53] D. Flanagan. JavaScript: The Definitive Guide. *O'Reilly Media, Inc.*, 2006.

[54] R. K. Ganti, N. Pham, H. Ahmadi, S. Nangia, and T. F. Abdelzaher. GreenGPS: A participatory sensing fuel-efficient maps application. *Proceedings of the 8th international conference on Mobile systems, applications, and services*, pages 151–164, 2010.

[55] I. Goodfellow, J. Pouget-Abadie, M. Mirza, B. Xu, D. Warde-Farley, S. Ozair, A. Courville, and Y. Bengio. Generative Adversarial Nets. *Advances in neural information processing systems*, pages 2672–2680, 2014.

[56] J. Gould and T. F. Golob. Clean air forever? A longitudinal analysis of opinions about air pollution and electric vehicles. *Transportation Research Part D: Transport and Environment*, 3(3):157–169, 1998.

[57] A. Grant, P. Williams, N. Ward, and S. Basker. GPS jamming and the impact on maritime navigation. *The Journal of Navigation*, 62(2):173–187, 2009.

[58] I. Griva, S. G. Nash, and A. Sofer. Linear and Nonlinear Optimization. *Siam*, 2009.

[59] M. M. Haghighi. *Controlling Energy-Efficient Buildings in the Context of Smart Grid: A Cyber Physical System Approach*. University of California, Berkeley, 2013.

[60] M. Haklay and P. Weber. OpenStreetMap: User-Generated Street Maps. *IEEE Pervasive Computing*, 7:12–18, 2008.

[61] F. Harrell. *Regression Modeling Strategies: With Applications to Linear Models, Logistic and Ordinal Regression, and Survival Analysis*. Springer, 2015.

[62] T. R. Hawkins, B. Singh, G. Majeau-Bettez, and A. H. Strømman. Comparative Environmental Life Cycle Assessment of Conventional and Electric Vehicles. *Journal of Industrial Ecology*, pages 53–64, 2013.

[63] J. G. Hayes, R. P. R. de Oliveira, S. Vaughan, M. G. Egan, R. P. R. De Oliveira, S. Vaughan, and M. G. Egan. Simplified Electric Vehicle Power Train Models and Range Estimation. *2011 IEEE Vehicle Power and Propulsion Conference*, pages 1–5, 2011.

[64] L. He, Y. Gu, T. Zhu, C. Liu, and K. G. Shin. SHARE: SoH-Aware Reconfiguration to Enhance Deliverable Capacity of Large-Scale Battery Packs. *6th International Conference on Cyber-Physical Systems (ICCPS)*, pages 169–178, 2015.

[65] A. Heinig, M. Dietrich, and Others. System Integration - The Bridge between More than Moore and More Moore. *Proceedings of the Conference on Design, Automation & Test in Europe*, page 132, 2014.

[66] K. D. Huang, S. C. Tzeng, T. M. Jeng, and W. D. Chiang. Air-conditioning system of an intelligent vehicle-cabin. *Applied Energy*, 83:545–557, 2006.

[67] B. Ibrahim and Others. Fuzzy-based Temperature and Humidity Control for HVAC of Electric Vehicle. *Procedia Engineering*, pages 904–910, 2012.

[68] A. Jain, H. S. Koppula, S. Soh, B. Raghavan, A. Singh, and A. Saxena. Brain4Cars: Car That Knows Before You Do via Sensory-Fusion Deep Learning Architecture. *arXiv preprint arXiv:1601.00740*, 2016.

[69] F. R. Kalhammer, B. M. Kopf, D. H. Swan, V. P. Roan, and M. P. Walsh. Status and Prospects for Zero Emissions Vehicle Technology. *Report of the ARB Independent Expert Panel*, page 25, 2007.

[70] K. R. Kambly and T. H. Bradley. Estimating the HVAC energy consumption of plug-in electric vehicles. *Journal of Power Sources*, 259:117–124, 2014.

[71] G. Karimi and X. Li. Thermal management of lithium-ion batteries for electric vehicles. *International Journal of Energy Research*, 37(1):13–24, 2013.

[72] D. E. Kaufman and R. L. Smith. Fastest paths in time-dependent networks for intelligent vehicle-highway systems application. *Journal of Intelligent Transportation Systems*, pages 1–11, 1993.

[73] A. Kelman and F. Borrelli. Bilinear Model Predictive Control of a HVAC System Using Sequential Quadratic Programming. In *International Federation of Automatic Control World Congress*, pages 9869–9874, 2011.

[74] E. Kim, J. Lee, and K. G. Shin. Real-time prediction of battery power requirements for electric vehicles. In *2013 ACM/IEEE International Conference on Cyber-Physical Systems, ICCPS 2013*, pages 11–20, 2013.

[75] E. Kim, K. G. K. Shin, J. Lee, K. G. K. Shin, and J. Lee. Real-Time Battery Thermal Management for Electric Vehicles. *5th International Conference on Cyber-Physical Systems (ICCPS)*, pages 72–83, 2014.

[76] H. Kim and K. G. Shin. Scheduling of battery charge, discharge, and rest. In *Proceedings - Real-Time Systems Symposium*, pages 13–22, 2009.

[77] L. D. Knibbs, R. J. D. Dear, and S. E. Atkinson. Field study of air change and flow rate in six automobiles. *Indoor air*, pages 303–313, 2009.

[78] K. Knoedler, J. Steinmann, S. Jones, A. Huss, E. Kural, O. Bringmann, J. Zimmermann, S. Laversanne, and D. Sanchez. Optimal energy management and recovery for FEV. In *2012 Design, Automation & Test in Europe Conference & Exhibition (DATE)*, pages 683–684, 2012.

[79] A. Kurakin, I. Goodfellow, and S. Bengio. Adversarial examples in the physical world. *arXiv preprint arXiv:1607.02533*, 2016.

[80] S. Lampke, S. Schliecker, D. Ziegenbein, and A. Hamann. Resource-Aware Control-Model-Based Co-Engineering of Control Algorithms and Real-Time Systems. *SAE International Journal of Passenger Cars-Electronic and Electrical Systems*, 8(2015-01-0168):106–114, 2015.

[81] E. A. Lee. Cyber Physical Systems: Design Challenges. In *2008 11th IEEE International Symposium on Object and Component-Oriented Real-Time Distributed Computing (ISORC)*, pages 363–369, 2008.

[82] S. Lefèvre, D. Vasquez, and C. Laugier. A survey on motion prediction and risk assessment for intelligent vehicles. *Robomech Journal*, 1(1):1, 2014.

[83] T. Levermore and Others. A Review of Driver Modelling. *UKACC International Conference on Control (CONTROL)*, pages 296–300, 2014.

[84] C.-W. Lin, B. Zheng, Q. Zhu, and A. Sangiovanni-Vincentelli. Security-Aware Design Methodology and Optimization for Automotive Systems. *Transactions on Design Automation of Electronic Systems (TODAES)*, 21(1):1–26, dec 2015.

[85] H.-T. Lin, T.-J. Liang, and S.-M. Chen. Estimation of Battery State of Health Using Probabilistic Neural Network. *IEEE Transactions on Industrial Informatics*, 9(2):679–685, 2013.

[86] X. Lin, P. Bogdan, N. Chang, and M. Pedram. Machine Learning-Based Energy Management in a Hybrid Electric Vehicle to Minimize Total Operating Cost. *IEEE/ACM International Conference on Computer-Aided Design (ICCAD)*, pages 627–634, 2015.

[87] X. Lin, D. Gorges, and S. Liu. Eco-Driving Assistance System for Electric Vehicles based on Speed Profile Optimization. In *IEEE Conference on Control Applications (CCA)*, pages 629–634, 2014.

[88] A. B. Lopez, K. Vatanparvar, A. P. D. Nath, S. Yang, S. Bhunia, and M. A. Al Faruque. A Security Perspective on Battery Systems of the Internet of Things. *Journal of Hardware and Systems Security*, 1(2):188–199, 2017.

[89] M. Lorenz and Others. A Coupled Numerical Model to Predict Heat Transfer and Passenger Thermal Comfort in Vehicle Cabins. *SAE Technical Paper*, 2014.

[90] L. Lu, X. Han, J. Li, J. Hua, and M. Ouyang. A review on the key issues for lithium-ion battery management in electric vehicles. *Journal of Power Sources*, 226:272–288, 2013.

[91] M. M. Lukasiewycz, S. S. Steinhorst, S. Andalam, F. Sagstetter, P. Waszecki, W. Chang, M. Kauer, P. Mundhenk, S. Shanker, S. Fahmy, and S. Chakraborty. System Architecture and Software Design for Electric Vehicles. In *DAC '13 Proceedings of the 50th Annual Design Automation Conference*, 2013.

[92] S. Lukic, R. Bansal, F. Rodriguez, and A. Emadi. Energy Storage Systems for Automotive Applications. *IEEE Transactions on Industrial Electronics*, 55:2258–2267, 2008.

[93] S. M. Lukic and A. Emadi. Effects of Drivetrain Hybridization on Fuel Economy and Dynamic Performance of Parallel Hybrid Electric Vehicles. *IEEE Transactions on Vehicular Technology*, pages 385–389, 2004.

[94] S. Marsland. *Machine Learning: An Algorithmic Perspective*. CRC press, 2015.

[95] T. Martin, M. Hsiao, D. Ha, and J. Krishnaswami. Denial-of-Service Attacks on Battery-powered Mobile Computers. *Pervasive Computing and Communications (PerCom)*, pages 309–318, 2004.

[96] M. Maurer, J. C. Gerdes, B. Lenz, and H. Winner. *Autonomous Driving: Technical, Legal and Social Aspects*. Springer Publishing Company, Incorporated, 2016.

[97] J. M. P. Menezes and G. A. Barreto. Long-term time series prediction with the NARX network: An empirical evaluation. *Neurocomputing*, 71(16):3335–3343, 2008.

[98] A. Millner. Modeling Lithium Ion Battery Degradation in Electric Vehicles. *Conference on Innovative Technologies for an Efficient and Reliable Electricity Supply (CITRES)*, pages 349–356, 2010.

[99] Y. Mo and B. Sinopoli. On the Performance Degradation of Cyber-Physical Systems Under Stealthy Integrity Attacks. *IEEE Transactions on Automatic Control*, 61(9):2618–2624, 2016.

[100] M. F. Møller. A Scaled Conjugate Gradient Algorithm for Fast Supervised Learning. *Neural networks*, 6(4):525–533, 1993.

[101] R. Montgomery. Fundamentals of HVAC control systems. *Elsevier*, 2008.

[102] S. Narayanaswamy, S. Steinhorst, M. Lukasiewycz, M. Kauer, and S. Chakraborty. Optimal dimensioning of active cell balancing architectures. In *Design, Automation and Test in Europe Conference and Exhibition (DATE), 2014*, pages 1–6, 2014.

[103] J. Neubauer and E. Wood. The impact of range anxiety and home, workplace, and public charging infrastructure on simulated battery electric vehicle lifetime utility. *Journal of Power Sources*, pages 12–20, 2014.

[104] J. Neubauer and E. Wood. Thru-life impacts of driver aggression, climate, cabin thermal management, and battery thermal management on battery electric vehicle utility. *Journal of Power Sources*, 259:262–275, 2014.

[105] M. Nilsson. Electric Vehicles: The phenomenon of range anxiety. *ELVIRE Report, June*, 2011.

[106] S. Pang, J. Farrell, J. Du, and M. Barth. Battery State-of-Charge Estimation. *American Control Conference*, pages 1644–1649, 2001.

[107] S. Park, Y. Kim, and N. Chang. Hybrid Energy Storage Systems and Battery Management for Electric Vehicles. In *DAC '13 Proceedings of the 50th Annual Design Automation Conference*, pages 1–6, 2013.

[108] M. Pedram, N. Chang, Y. Kim, and Y. Wang. Hybrid electrical energy storage systems. *Proceedings of the 16th ACM/IEEE international symposium on Low power electronics and design - ISLPED '10*, page 363, 2010.

[109] A. A. Pesaran. Battery Thermal Management in EVs and HEVs: Issues and Solutions. *Advanced Automotive Battery Conference*, page 10, 2001.

[110] S. B. Peterson, J. F. Whitacre, and J. Apt. The economics of using plug-in hybrid electric vehicle battery packs for grid storage. *Journal of Power Sources*, 195(8):2377–2384, 2010.

[111] M. Petricca, D. Shin, A. Bocca, A. Macii, and Others. Automated Generation of Battery Aging Models from Datasheets. *International Conference on Computer Design (ICCD)*, pages 483–488, 2014.

[112] A. Polychronopoulos, M. Tsogas, and Others. Sensor Fusion for Predicting Vehicles' Path for Collision Avoidance Systems. *IEEE Transactions on Intelligent Transportation Systems*, pages 549–562, 2007.

[113] G. Putrus, P. Suwanapingkarl, D. Johnston, E. Bentley, and M. Narayana. Impact of electric vehicles on power distribution networks. *2009 IEEE Vehicle Power and Propulsion Conference*, 2009.

[114] K. Qian, C. Zhou, M. Allan, and Y. Yuan. Modeling of load demand due to EV battery charging in distribution systems. *IEEE Transactions on Power Systems*, 26:802–810, 2011.

[115] H. Rahimi-Eichi, U. Ojha, F. Baronti, and M. Chow. Battery Management System: An Overview of Its Application in the Smart Grid and Electric Vehicles, 2013.

[116] R. R. Rajkumar, I. Lee, L. Sha, and J. Stankovic. Cyber-Physical Systems: The Next Computing Revolution. *47th Design Automation Conference (DAC)*, pages 731–736, 2010.

[117] K. Reif. Fundamentals of Automotive and Engine Technology. *Springer: Bosch professional automotive information*, 2014.

[118] A. Y. Saber and G. K. Venayagamoorthy. One Million Plug-in Electric Vehicles on the Road by 2015. *12th International IEEE Conference on Intelligent Transportation Systems (ITSC)*, pages 1–7, 2009.

[119] A. Sathyanarayana, P. Boyraz, and Others. Driver Behavior Analysis and Route Recognition by Hidden Markov Models. *International Conference on Vehicular Electronics and Safety (ICVES)*, pages 276–281, 2008.

[120] S. Shao, T. Zhang, M. Pipattanasomporn, and S. Rahman. Impact of TOU rates on distribution load shapes in a smart grid with PHEV penetration. In *2010 IEEE PES Transmission and Distribution Conference and Exposition: Smart Solutions for a Changing World*, 2010.

[121] D. Shin, Y. Kim, J. Seo, N. Chang, Y. Wang, and M. Pedram. Battery-supercapacitor hybrid system for high-rate pulsed load applications. In *2011 Design, Automation & Test in Europe*, pages 1–4, 2011.

[122] D. Shin, E. Macii, and M. Poncino. Statistical Battery Models and Variation-Aware Battery Management. *Proceedings of the Design Automation Conference (DAC'14)*, pages 1–6, 2014.

[123] D. Shin, M. Poncino, and E. Macii. Thermal Management of Batteries Using a Hybrid Supercapacitor Architecture, mar 2014.

[124] D. Shin, M. Poncino, E. Macii, and N. Chang. A Statistical Model-Based Cell-to-Cell Variability Management of Li-ion Battery Pack. *IEEE Transactions on Computer-Aided Design of Integrated Circuits and Systems*, 34(2):252–265, 2015.

[125] H. T. Siegelmann and Others. Computational Capabilities of Recurrent NARX Neural Networks. *IEEE Transactions on Systems, Man, and Cybernetics, Part B: Cybernetics*, 27(2):208–215, 1997.

[126] H. Summala. Brake Reaction Times and Driver Behavior Analysis. *Transportation Human Factors*, 2(3):217–226, 2000.

[127] L. Sun, K. Feng, C. Chapman, and N. Zhang. An Adaptive Power Split Strategy for Battery-Supercapacitor Powertrain Design, Simulation and Experiment . *IEEE Transactions on Power Electronics*, 2017.

[128] S. F. Tie and C. W. Tan. A review of energy sources and energy management system in electric vehicles. *Renewable and Sustainable Energy Reviews*, pages 82–102, 2013.

[129] T. Trippel, O. Weisse, W. Xu, and Others. WALNUT: Waging doubt on the integrity of mems accelerometers with acoustic injection attacks. *IEEE European Symposium on Security and Privacy (EuroS&P)*, pages 3–18, 2017.

[130] K. Umezu and H. Noyama. Air-Conditioning system For Electric Vehicles (i-MiEV). In *SAE Automotive Alternate Refrigerant Systems Symposium*, 2010.

[131] K. Vatanparvar and M. A. Al Faruque. Battery Lifetime-Aware Automotive Climate Control for Electric Vehicles. In *ACM/IEEE Design Automation Conference (DAC'15)*, pages 1–6, 2015.

[132] K. Vatanparvar and M. A. Al Faruque. Design Space Exploration for the Profitability of a Rule-Based Aggregator Business Model Within a Residential Microgrid. *IEEE Transactions on Smart Grid*, 6(3):1167–1175, 2015.

[133] K. Vatanparvar and M. A. Al Faruque. Eco-Friendly Automotive Climate Control and Navigation System for Electric Vehicles. In *2016 ACM/IEEE 7th International Conference on Cyber-Physical Systems, ICCPS 2016 - Proceedings*, 2016.

[134] K. Vatanparvar and M. A. Al Faruque. OTEM: Optimized Thermal and Energy Management for Hybrid Electrical Energy Storage in Electric Vehicles. *Conference on Design, Automation & Test in Europe (DATE)*, pages 1–6, 2016.

[135] K. Vatanparvar and M. A. Al Faruque. ACQUA: Adaptive and Cooperative Quality-Aware Control for Automotive Cyber-Physical Systems. *IEEE/ACM International Conference on Computer-Aided Design (ICCAD)*, pages 1–8, 2017.

[136] K. Vatanparvar and M. A. Al Faruque. Application-Specific Residential Microgrid Design Methodology. *ACM Transactions on Design Automation of Electronic Systems (TODAES)*, 22(3):44, 2017.

[137] K. Vatanparvar and M. A. Al Faruque. Electric Vehicle Optimized Charge and Drive Management. *ACM Trans. Des. Autom. Electron. Syst.*, 23(1):3:1—-3:25, aug 2017.

[138] K. Vatanparvar and M. A. Al Faruque. Path to Eco-Driving: Electric Vehicle HVAC and Route Joint Optimization. *IEEE Design & Test*, 2017.

[139] K. Vatanparvar and M. A. Al Faruque. Control-as-a-Service in Cyber-Physical Energy Systems over Fog Computing. In *Fog Computing in the Internet of Things*, pages 123–144. Springer, 2018.

[140] K. Vatanparvar and M. A. Al Faruque. Design and Analysis of Battery-Aware Automotive Climate Control for Electric Vehicles. *ACM Transactions on Embedded Computing Systems (TECS)*, 2018.

[141] K. Vatanparvar, Q. Chau, and M. A. A. Faruque. Home energy management as a service over networking platforms. In *Innovative Smart Grid Technologies Conference (ISGT), 2015 IEEE Power Energy Society*, pages 1–5, 2015.

[142] K. Vatanparvar, S. Faezi, I. Burago, M. Levorato, and M. A. Al Faruque. Driving Behavior Modeling and Estimation for Battery Optimization in Electric Vehicles: Work-in-progress. *International Conference on Hardware/Software Codesign and System Synthesis Companion*, pages 15:1—-15:2, 2017.

[143] K. Vatanparvar, S. Faezi, I. Burago, M. Levorato, and M. A. Al Faruque. Extended Range Electric Vehicle with Driving Behavior Estimation in Energy Management. *IEEE Transactions on Smart Grid*, 2018.

[144] K. Vatanparvar, S. Fakhouri, M.-A. Siddika, and M. A. Al Faruque. Compartmentalisation-based design automation method for power grid. *IET Cyber-Physical Systems: Theory & Applications*, 2(1):20–27(7), apr 2017.

[145] K. Vatanparvar and M. A. Faruque. Demo Abstract: Energy Management as a Service over Fog Computing Platform. *Aicps.Eng.Uci.Edu*, pages 4–5, 2015.

[146] K. Vatanparvar and R. Sharma. Battery Optimal Approach to Demand Charge Reduction in Behind-The-Meter Energy Management Systems. *IEEE Power and Energy Society General Meeting (PES GM)*, 2018.

[147] K. Vatanparvar, J. Wan, and M. A. Al Faruque. Battery-Aware Energy-Optimal Electric Vehicle Driving Management. In *Proceedings of the International Symposium on Low Power Electronics and Design*, volume 2015-Septe, pages 353–358, 2015.

[148] J. Wang, P. Liu, J. Hicks-Garner, E. Sherman, S. Soukiazian, M. Verbrugge, H. Tataria, J. Musser, and P. Finamore. Cycle-life model for graphite-LiFePO4 cells. *Journal of Power Sources*, 196:3942–3948, 2011.

[149] Q. Wang, P. Ping, X. Zhao, G. Chu, J. Sun, and C. Chen. Thermal runaway caused fire and explosion of lithium ion battery. *Journal of power sources*, 208:210–224, 2012.

[150] Y. Wang, J. Jiang, and T. Mu. Context-aware and energy-driven route optimization for fully electric vehicles via crowdsourcing. *IEEE Transactions on Intelligent Transportation Systems*, 14:1331–1345, 2013.

[151] Y. Wang, X. Lin, M. Pedram, N. Chang, and Others. Joint Automatic Control of the Powertrain and Auxiliary Systems to Enhance the Electromobility in Hybrid Electric Vehicles. *Proceedings of the Design Automation Conference (DAC'15)*, pages 1–6, 2015.

[152] Y. Wang, X. Lin, Q. Xie, N. Chang, and M. Pedram. Minimizing State-of-Health Degradation in Hybrid Electrical Energy Storage Systems with Arbitrary Source and Load Profiles. In *DATE '14 Proceedings of the conference on Design, Automation & Test in Europe*, pages 1–4, New Jersey, 2014. IEEE Conference Publications.

[153] A. Wasicek, P. Derler, and E. A. Lee. Aspect-oriented Modeling of Attacks in Automotive Cyber-Physical Systems. *51st Design Automation Conference (DAC)*, pages 1–6, 2014.

[154] J. Wei, J. M. Snider, J. Kim, J. M. Dolan, R. Rajkumar, and B. Litkouhi. Towards a Viable Autonomous Driving Research Platform. *IEEE Intelligent Vehicles Symposium (IV)*, pages 763–770, 2013.

[155] K. B. Wipke, M. R. Cuddy, and S. D. Burch. ADVISOR 2.1: A user-friendly advanced powertrain simulation using a combined backward/forward approach. *IEEE Transactions on Vehicular Technology*, 48(6):1751–1761, 1999.

[156] W. Wolf. Cyber-physical systems. *Computers*, 42(3):88–89, 2009.

[157] D. Work, A. Bayen, and Q. Jacobson. Automotive Cyber Physical Systems in the Context of Human Mobility. *National Workshop on High-Confidence Automotive Cyber-Physical Systems*, pages 3–4, 2008.

[158] Q. Xie, X. Lin, Y. Wang, and Others. State of Health Aware Charge Management in Hybrid Electrical Energy Storage Systems. *Design Automation and Test in Europe (DATE)*, pages 1060–1065, 2012.

[159] Q. Xie, Y. Wang, Y. Kim, M. Pedram, and N. Chang. Charge allocation in hybrid electrical energy storage systems. *IEEE Transactions on Computer-Aided Design of Integrated Circuits and Systems*, 32(7):1003–1016, 2013.

[160] B. Yegnanarayana. *Artificial Neural Networks*. PHI Learning Pvt. Ltd., 2009.

[161] M. Yilmaz and P. T. Krein. Review of Battery Charger Topologies, Charging Power Levels, and Infrastructure for Plug-In Electric and Hybrid Vehicles. *IEEE Transactions on Power Electronics*, pages 2151–2169, 2013.

[162] M. Zeraoulia, M. E. H. Benbouzid, and D. Diallo. Electric Motor Drive Selection Issues for HEV Propulsion Systems: A Comparative Study. *IEEE Transactions on Vehicular Technology*, pages 1756–1764, 2006.